

Copyright

by

Wade Sterling Bonzon

1996

**THERMAL GRADIENTS IN SEGMENTALLY  
CONSTRUCTED HOLLOW BOX BRIDGE PIERS**

APPROVED BY

SUPERVISING COMMITTEE:

---

John E. Breen

---

Michael E. Kreger

*to my parents, who encouraged me to explore the world with wide-open eyes*

**THERMAL GRADIENTS IN SEGMENTALLY  
CONSTRUCTED HOLLOW BOX BRIDGE PIERS**

by

Wade Sterling Bonzon, B.S.C.E.

Thesis

Presented to the Faculty of the Graduate School

of The University of Texas at Austin

in Partial Fulfillment

of the Requirements

for the Degree of

Master of Science in Engineering

The University of Texas at Austin

December 1996

## ACKNOWLEDGEMENTS

A work of this magnitude is never truly completed by one person alone. As such, I want to thank a varied group of individuals who, whether they knew it or not, all came together to encourage and support this effort.

I will never forget the phone call John Breen made to me while I was still considering graduate school. His offer to work on the U.S. 183 Instrumentation Project changed my view of structural engineering and set me on a career path for which I will be forever grateful.

Tom Rummel at TxDOT was always available to give suggestions and answer questions. Dean Van Landuyt provided new perspectives on aesthetics in bridge design which I will carry with me during my career. From Eby Construction Joe Lee, Ron Fletcher, "T. Ray", and Enos Saiz dealt patiently with our field work.

Rodney Davis and Brian Wood answered literally hundreds of my questions about segmental construction during the course of the project. Valerie Andres suffered with me on top of a cold and windy superstructure. Keith Thompson listened to my constant complaints about this thesis and provided many good ideas. April Jenkins sorted out many complicated tuition problems, while Laurie Golding was a procurement officer of the highest caliber. Sharon Cunningham provided valuable guidance during thesis production. Willy Ramirez and Chris Gilchrist deserve thanks for their help with the finite element portion of the project.

Heather Jobson, Derek Watkins, Kristin Grubb, and the other members of "the dinner group" kept me alive with good food and great company. Pete Schönwetter never failed to debate me on any subject of my choosing.

Finally, I would not have survived without the care and support of Michelle Parsley. She let me forget about the world, at least for a short while, and that made all the difference to me.

December, 1996

# **THERMAL GRADIENTS IN SEGMENTALLY CONSTRUCTED HOLLOW BOX BRIDGE PIERS**

by

Wade Sterling Bonzon, M.S.E.

The University of Texas at Austin, 1996

SUPERVISOR: John E. Breen

Temperature-induced stresses in hollow concrete bridge superstructures such as those commonly used in precast segmental construction are well known and recognized by bridge design codes. However, very little is known about the effect of non-linear temperature gradients on hollow concrete bridge piers.

Strain gauges and thermocouples were installed in a segmentally constructed concrete bridge pier as part of an ongoing investigation of the construction and performance of the new U.S. 183 segmental viaduct currently being built in Austin, Texas. Temperature and strain data were acquired continuously over the course of the first four months of the pier's service life.

Data concerning temperature gradients across the pier's cross-section, thermally-induced strains, and post-tensioning stresses are presented. Temperature gradient data and the induced thermal strains are analyzed to determine the effects of temperature changes on the pier. Calculations with measured temperature data, including a finite element analysis, are also compared to those made with temperature gradients published in current bridge design codes. Comparisons of calculated and measured strains are made to confirm the accuracy of the calculation methods. Recommendations concerning design thermal gradients and the design of hollow concrete piers for temperature gradient effects are presented.

## TABLE OF CONTENTS

|   |            |
|---|------------|
| <b>List of Tables .....</b>                                 | <b>xi</b>  |
| <b>List of Figures.....</b>                                 | <b>xii</b> |
| <b>1 Introduction.....</b>                                  | <b>1</b>   |
| 1.1 General.....  | 1          |
| 1.2 U.S. 183 Project.....                                   | 1          |
| 1.2.1 Project Location.....                                 | 1          |
| 1.2.2 Project Description.....                              | 3          |
| 1.3 Large Ramp Pier Description.....                        | 6          |
| 1.4 Problem Statement and Objectives.....                   | 9          |
| 1.5 Scope of Work.....                                      | 10         |
| <b>2 Background and Previous Studies.....</b>               | <b>11</b>  |
| 2.1 General.....  | 11         |
| 2.2 Non-Linear Thermal Gradients.....                       | 12         |
| 2.2.1 Gradient Shape.....                                   | 12         |
| 2.2.2 Gradient Effects.....                                 | 14         |
| 2.2.2.1 Generalized Members.....                            | 14         |
| 2.2.2.2 Effects on Bridge Piers.....                        | 22         |
| 2.3 Development of Current AASHTO Code Provisions.....      | 24         |
| 2.3.1 Potgieter and Gamble [8].....                         | 25         |
| 2.3.2 NCHRP Report 276 [5].....                             | 25         |
| 2.3.3 AASHTO LRFD Specifications [11] Requirements.....     | 29         |
| 2.3.4 AASHTO Segmental Specification [12] Requirements..... | 31         |
| 2.3.5 Roberts [7].....                                      | 32         |
| 2.4 Previous Bridge Pier Temperature Studies.....           | 34         |
| 2.4.1 General.....  | 34         |
| 2.4.2 Stephenson [14].....                                  | 34         |
| 2.4.3 Andres [1].....                                       | 36         |
| 2.5 Precast Segmental Piers in North America.....           | 38         |
| 2.5.1 Long Key Bridge.....                                  | 38         |
| 2.5.2 Seven-Mile Bridge.....                                | 39         |
| 2.5.3 Dauphin Island Bridge [18].....                       | 39         |
| 2.5.4 Sunshine Skyway Approaches.....                       | 41         |
| 2.5.5 Neches River Bridge [2].....                          | 41         |
| 2.5.6 Linn Cove Viaduct.....                                | 42         |
| 2.5.7 Wando River Bridge [23].....                          | 43         |
| 2.5.8 James River Bridge [24].....                          | 44         |
| 2.5.9 Chesapeake and Delaware Canal Bridge [25].....        | 44         |
| 2.5.10 Louetta Road Overpass.....                           | 45         |
| 2.5.11 Northumberland Strait Crossing.....                  | 46         |

|   |           |
|---|-----------|
| <b>3 Pier Instrumentation .....</b>                               | <b>49</b> |
| 3.1 Instrumentation Objectives .....                              | 49        |
| 3.2 Pier Selection .....  | 50        |
| 3.3 Gauge Types .....   | 51        |
| 3.3.1 Concrete Strain Gauges .....                                | 51        |
| 3.3.2 Steel Strain Gauges .....                                   | 54        |
| 3.3.3 Thermocouples .....   | 55        |
| 3.4 Overall Instrumentation Plan .....                            | 55        |
| 3.5 “Base” Segment PC16-1 Gauge Locations .....                   | 57        |
| 3.5.1 Concrete Strain Gauges .....                                | 57        |
| 3.5.2 Thermocouples .....   | 60        |
| 3.6 “Gradient” Segment PC16-5 Gauge Locations .....               | 62        |
| 3.6.1 Concrete Strain Gauges .....                                | 62        |
| 3.6.2 Thermocouples .....   | 63        |
| 3.7 “Top” Segment PC16-7 Gauge Locations .....                    | 64        |
| 3.7.1 Concrete Strain Gauges .....                                | 64        |
| 3.7.2 Thermocouples .....   | 64        |
| 3.8 Capital PC16-8 Gauge Locations .....                          | 65        |
| 3.8.1 Force Path Evaluation .....                                 | 65        |
| 3.8.2 Concrete Strain Gauges .....                                | 67        |
| 3.8.3 Steel Strain Gauges .....                                   | 69        |
| 3.8.4 Thermocouples .....   | 72        |
| 3.9 Data Acquisition System .....                                 | 75        |
| <b>4 Pier and Ramp Superstructure Construction Sequence .....</b> | <b>77</b> |
| 4.1 Introduction .....  | 77        |
| 4.2 Segmental Pier Construction .....                             | 77        |
| 4.2.1 Segment Casting Operations .....                            | 77        |
| 4.2.2 Pier Erection .....   | 86        |
| 4.3 Balanced-Cantilever Superstructure Erection .....             | 91        |
| 4.3.1 Phase I .....   | 91        |
| 4.3.2 Phases II and III .....                                     | 92        |
| 4.3.3 Phase IV .....  | 93        |
| 4.3.4 Phases V and VI .....                                       | 93        |
| 4.3.5 Phase VII .....   | 94        |
| <b>5 Data Presentation .....</b>                                  | <b>95</b> |
| 5.1 General Temperature Trends .....                              | 95        |
| 5.1.1 Daily Cycles .....  | 95        |
| 5.1.2 Seasonal Characteristics .....                              | 98        |
| 5.1.3 Effects of Cover .....                                      | 101       |
| 5.1.4 Effects of Shading .....                                    | 103       |
| 5.2 Thermal Gradients .....                                       | 104       |
| 5.2.1 Pier Shaft Gradients .....                                  | 104       |
| 5.2.2 Capital Gradients .....                                     | 111       |



|   |            |
|---|------------|
| 5.2.3 Capital Curing Gradients .....                        | 116        |
| 5.3 Concrete Strain Gauge Measurements.....                 | 120        |
| 5.3.1 Axial Strains .....                                   | 120        |
| 5.3.2 Transverse Strains.....                               | 125        |
| 5.4 Pier Post-Tensioning Strains.....                       | 128        |
| 5.4.1 General.....  | 128        |
| 5.4.2 Axial Strains .....                                   | 129        |
| 5.4.3 Transverse Strains.....                               | 132        |
| <b>6 Temperature Stress Analysis .....</b>                  | <b>137</b> |
| 6.1 Maximum Observed Temperature Gradients.....             | 137        |
| 6.1.1 Maximum Gradient Selection Process.....               | 137        |
| 6.1.1.1 Maximum Positive Gradient Determination .....       | 137        |
| 6.1.1.2 Maximum Negative Gradient Determination .....       | 139        |
| 6.1.2 Octagonal Shell Projection Method.....                | 139        |
| 6.1.3 Maximum Temperature Gradients .....                   | 143        |
| 6.1.3.1 Maximum Positive Gradients .....                    | 143        |
| 6.1.3.2 Maximum Negative Gradients.....                     | 145        |
| 6.2 Stress/Strain Analyses - Hand Calculation Methods ..... | 148        |
| 6.2.1 Classical Method.....                                 | 148        |
| 6.2.1.1 Positive Gradients .....                            | 149        |
| 6.2.1.2 Negative Gradients .....                            | 154        |
| 6.2.2 Primary Bending Axis Method .....                     | 158        |
| 6.2.2.1 Positive Gradients .....                            | 162        |
| 6.2.2.2 Negative Gradients .....                            | 165        |
| 6.2.3 Transverse Stresses .....                             | 166        |
| 6.2.3.1 Positive Gradients .....                            | 169        |
| 6.2.3.2 Negative Gradients .....                            | 171        |
| <b>7 Finite Element Analysis.....</b>                       | <b>173</b> |
| 7.1 General.....  | 173        |
| 7.2 Model Input.....  | 174        |
| 7.2.1 Pier Geometry .....                                   | 174        |
| 7.2.2 Material Properties.....                              | 175        |
| 7.2.3 Temperature Loading.....                              | 176        |
| 7.2.2.1 General.....  | 176        |
| 7.2.2.1 Maximum Observed Gradients .....                    | 178        |
| 7.2.2.2 Design Temperature Gradients .....                  | 179        |
| 7.3 Analysis Results.....                                   | 180        |
| 7.3.1 Longitudinal Strains.....                             | 180        |
| 7.3.1.1 Positive Gradients .....                            | 180        |
| 7.3.1.2 Negative Gradients .....                            | 183        |
| 7.3.2 Transverse Strains.....                               | 187        |
| 7.3.2.1 Positive Gradients .....                            | 187        |
| 7.3.2.2 Negative Gradients .....                            | 189        |

|  |            |
|--|------------|
| 7.3.3 Comments .....   | 192        |
| <b>8 Comparison of Results.....</b>                              | <b>193</b> |
| 8.1 Longitudinal Strains.....                                    | 193        |
| 8.1.1 Strain Projection Plots .....                              | 193        |
| 8.1.1.1 Positive Gradients .....                                 | 194        |
| 8.1.1.2 Negative Gradients .....                                 | 198        |
| 8.1.2 Measured Strain Comparisons .....                          | 200        |
| 8.1.2.1 Positive Gradient.....                                   | 202        |
| 8.1.2.2 Negative Gradient .....                                  | 211        |
| 8.1.3 Comments on Longitudinal Strains .....                     | 217        |
| 8.2 Transverse Strains.....                                      | 218        |
| 8.2.1 Positive Gradient.....                                     | 219        |
| 8.2.2 Negative Gradient .....                                    | 228        |
| 8.2.3 Comments on Transverse Strains.....                        | 236        |
| 8.3 General Comments.....  | 237        |
| <b>9 Design Implications.....</b>                                | <b>240</b> |
| 9.1 Sample Load Cases .....                                      | 240        |
| 9.1.1 Construction Loads .....                                   | 240        |
| 9.1.2 Service Load Cases .....                                   | 249        |
| 9.1.3 Comments on Load Cases.....                                | 260        |
| 9.2 Suggested Revisions to AASHTO Guide Specification [12] ..... | 261        |
| 9.2.1 Thermal Gradients .....                                    | 261        |
| 9.2.2 Application of Thermal Gradients to Substructures .....    | 263        |
| 9.3 Suggestions for Future Study.....                            | 265        |
| <b>10 Summary, Conclusions, and Recommendations.....</b>         | <b>267</b> |
| 10.1 Summary .....   | 267        |
| 10.2 Conclusions.....  | 270        |
| 10.3 Recommendations .....                                       | 272        |
| <b>Appendix - Calculations .....</b>                             | <b>275</b> |
| <b>References.....</b>   | <b>304</b> |
| <b>Vita .....</b>  | <b>307</b> |

## LIST OF TABLES

|     |   |     |
|-----|---|-----|
| 2.1 | <i>Proposed temperature coefficient magnitudes for positive gradients<br/>(after Imbsen, et al [5])</i> .....     | 27  |
| 2.2 | <i>Proposed temperature coefficient magnitudes for negative gradients<br/>(after Imbsen, et al [5])</i> .....     | 28  |
| 2.3 | <i>Proposed design values for concrete coefficient of thermal expansion<br/>(after Imbsen, et al [5])</i> .....   | 28  |
| 2.4 | <i>Excerpt from AASHTO LRFD Specification [11] “Table 3.4.1-1 - Load<br/>Combinations and Load Factors”</i> ..... | 29  |
| 2.5 | <i>AASHTO LRFD Code [11] positive gradient magnitude values</i> .....   | 30  |
| 4.1 | <i>Construction and instrumentation sequence for pier P16</i> .....   | 91  |
| 7.1 | <i>Maximum tensile and compressive strains by load case: positive gradients...</i>                                | 182 |
| 7.2 | <i>Maximum tensile and compressive strains by load case: negative gradients...</i>                                | 186 |

## LIST OF FIGURES

|      |   |    |
|------|---|----|
| 1.1  | <i>U.S. 183 segmental viaduct location</i> .....  | 2  |
| 1.2  | <i>U.S. 183 viaduct mainlane superstructure</i> .....   | 4  |
| 1.3  | <i>Typical access ramp superstructure</i> .....   | 5  |
| 1.4  | <i>(a) Mainlane “Y” pier; (b) small ramp pier; (c) large ramp pier</i> .....  | 5  |
| 1.5  | <i>Typical large ramp pier: elevation view</i> .....  | 7  |
| 1.6  | <i>Typical sections: large ramp pier</i> .....  | 8  |
| 2.1  | <i>Factors affecting thermal gradients (after Roberts [7])</i> .....  | 13 |
| 2.2  | <i>A statically determinate member under a linear temperature gradient (after Roberts [7])</i> .....  | 15 |
| 2.3  | <i>Arbitrary section with a non-linear temperature distribution</i> .....   | 16 |
| 2.4  | <i>(a) Non-linear strain distribution assuming no interaction between section fibers, (b) final linear strain distribution because plane sections remain plane (after Imbsen [5])</i> ..... | 16 |
| 2.5  | <i>Thermal gradient and stress distribution in a fully restrained member</i> .....  | 17 |
| 2.6  | <i>Temperature-induced stress distributions (after Roberts [7])</i> .....   | 18 |
| 2.7  | <i>Application of thermal gradients to a two-span beam (after Potgieter and Gamble [8])</i> .....   | 20 |
| 2.8  | <i>Application of thermal gradients to a three-span beam (after Roberts [7])</i> .....  | 21 |
| 2.9  | <i>Temperature-induced response in a free-standing single pier bent</i> .....   | 22 |
| 2.10 | <i>Temperature-induced response in a fully restrained single pier bent</i> .....  | 23 |
| 2.11 | <i>Temperature-induced response in a partially-restrained single pier bent</i> .....  | 23 |
| 2.12 | <i>Temperature-induced response of a multiple-pier bent</i> .....   | 24 |
| 2.13 | <i>Proposed maximum solar radiation zones (after Imbsen, et al [5])</i> .....   | 26 |
| 2.14 | <i>Proposed positive vertical temperature gradient (after Imbsen, et al [5])</i> .....  | 26 |
| 2.15 | <i>Proposed negative vertical temperature gradient (after Imbsen, et al [5])</i> .....  | 27 |
| 2.16 | <i>AASHTO LRFD Code [11] vertical positive gradient shape</i> .....   | 30 |
| 2.17 | <i>Unusually-shaped mainlane pier, U.S. 183 segmental viaduct</i> .....   | 36 |
| 2.18 | <i>Bronze-encased steel bolt undergoing uniform temperature change</i> .....  | 37 |
| 2.19 | <i>Concrete pier model undergoing differential temperature change</i> .....   | 37 |
| 2.20 | <i>Unusual V-shaped piers, Long Key Bridge</i> .....  | 39 |
| 2.21 | <i>Cross-section of precast segmental piers, Dauphin Island Bridge</i> .....  | 40 |
| 2.22 | <i>Segmental pylon cross-sections, Neches River Bridge</i> .....  | 42 |
| 2.23 | <i>Segmental approach pier cross-section, Neches River Bridge</i> .....   | 42 |
| 2.24 | <i>Pier cross-section, Linn Cove Viaduct</i> .....  | 43 |
| 2.25 | <i>Cross-sectional dimensions of approach-span piers, Chesapeake and Delaware Canal cable-stayed bridge</i> .....   | 45 |
| 2.26 | <i>Segmental pier cross-section, Louetta Road Overpass</i> .....  | 46 |
| 2.27 | <i>Elevation view of pier components, Northumberland Strait Crossing</i> .....  | 48 |
| 3.1  | <i>Map showing location of research facilities relative to U.S. 183 viaduct</i> .....   | 49 |
| 3.2  | <i>Bridge layout in the U.S. 183 and IH-35 interchange area</i> .....   | 51 |

|      |  |    |
|------|--|----|
| 3.3  | <i>An electronic strain gauge .....</i>  | 53 |
| 3.4  | <i>Concrete strain gauge .....</i>   | 53 |
| 3.5  | <i>Installation of an electronic strain gauge directly onto the reinforcing bar .....</i>  | 54 |
| 3.6  | <i>Diagram of a Type T thermocouple.....</i>   | 55 |
| 3.7  | <i>Instrumented areas of pier P16 relative to surrounding structures' locations... 57</i>  | 57 |
| 3.8  | <i>Concrete gauge locations in base segment PC16-1 .....</i>   | 58 |
| 3.9  | <i>Concrete gauges tied onto rebar cage of base segment PC16-1 .....</i>   | 59 |
| 3.10 | <i>Access blackout and conduit for gauge wires, base segment PC16-1 .....</i>  | 59 |
| 3.11 | <i>Blockout and instrument wires after casting, base segment PC16-1 .....</i>  | 60 |
| 3.12 | <i>Thermocouple locations in base segment PC16-1 .....</i>   | 61 |
| 3.13 | <i>Typical thermocouple placement in rebar cage, base segment PC16-1 .....</i>   | 61 |
| 3.14 | <i>Concrete strain gauge positions, "gradient" segment PC16-5 .....</i>  | 62 |
| 3.15 | <i>Thermocouple locations in the "gradient" segment PC16-5.....</i>  | 63 |
| 3.16 | <i>Concrete gauge locations in "top" segment PC16-7.....</i>   | 64 |
| 3.17 | <i>Thermocouple locations in "top" segment PC16-7.....</i>   | 65 |
| 3.18 | <i>Fixed moment connection during superstructure erection achieved with<br/>DYWIDAG post-tensioning bars.....</i>                                  | 66 |
| 3.19 | <i>Plan view of concrete strain gauges located in top half of capital segment.....</i>   | 67 |
| 3.20 | <i>Elevation view of concrete strain gauges in top half of capital segment.....</i>  | 68 |
| 3.21 | <i>Concrete strain gauge placement in compression strut between tie-down<br/>anchor plates and tendon anchorages .....</i>                         | 68 |
| 3.22 | <i>Two layers of concrete strain gauges located near bottom face of capital<br/>segment coinciding with gauge locations in segment PC16-7.....</i> | 69 |
| 3.23 | <i>Location of steel strain gauges at the bottom face of the capital.....</i>  | 70 |
| 3.24 | <i>Locations of steel strain gauges near top face of the capital.....</i>  | 71 |
| 3.25 | <i>Locations of strain gauges attached to DYWIDAG post-tensioning tie-downs ..</i>   | 72 |
| 3.26 | <i>Temperature gradient thermocouples located near base of capital segment .....</i>   | 73 |
| 3.27 | <i>Thermocouples located near top face of capital segment .....</i>  | 74 |
| 3.28 | <i>Thermocouples placed in compression strut areas .....</i>   | 74 |
| 3.29 | <i>Data recording equipment in place at top of pier .....</i>  | 76 |
| 4.1  | <i>Location of precasting facility and bridge site.....</i>  | 78 |
| 4.2  | <i>Completed pier segments in storage at the casting yard .....</i>  | 79 |
| 4.3  | <i>Typical segment-per-day casting sequence.....</i>   | 80 |
| 4.4  | <i>Casting bed with steel support frame for formwork.....</i>  | 82 |
| 4.5  | <i>Hydraulic jacks used to align the bulkhead pier segment.....</i>  | 83 |
| 4.6  | <i>Match cast segments fit together perfectly.....</i>   | 83 |
| 4.7  | <i>Application of bond breaker to bulkhead segment top face .....</i>  | 84 |
| 4.8  | <i>Pier segment outer form and scaffolding .....</i>   | 84 |
| 4.9  | <i>Placement of 50 mm thick cinder blocks under reinforcement cage.....</i>  | 85 |
| 4.10 | <i>Rebar chair used to ensure adequate clear cover.....</i>  | 85 |
| 4.11 | <i>Removal of outer formwork.....</i>  | 86 |
| 4.12 | <i>"U-turns" in tendon ducts located in pier foundation.....</i>   | 87 |
| 4.13 | <i>Steel support frame for segment prior to cast-in-place base construction .....</i>  | 87 |

|      |   |     |
|------|---|-----|
| 4.14 | <i>Cast-in-place base forming a rigid moment connection between base segment PC16-1 and foundation.....</i>                               | 88  |
| 4.15 | <i>Hydraulic ram stressing temporary post-tensioning bars.....</i>  | 89  |
| 4.16 | <i>Sequence of final post-tensioning of pier P16 tendons .....</i>  | 89  |
| 4.17 | <i>Phase I, cantilevering from pier P14 .....</i>   | 92  |
| 4.18 | <i>Phases II and III, cantilever construction from piers P15 and P16 .....</i>  | 92  |
| 4.19 | <i>Phase IV, completion of the 43.3-meter central span .....</i>  | 93  |
| 4.20 | <i>Phases V and VI, cantilevering of segments from P17, placement of temporary truss, and erection of 38.1-meter Span E. ....</i>         | 94  |
| 4.21 | <i>Phase VII, completion of Span D and installation of continuity tendons .....</i>   | 94  |
| 5.1  | <i>Temperature gradient orientations at different times in the day .....</i>  | 96  |
| 5.2  | <i>Typical daily temperature cycle of selected outside-layer thermocouples in gradient segment PC16-5.....</i>                            | 97  |
| 5.3  | <i>Datalogger panel temperatures recorded during April 1996 .....</i>   | 100 |
| 5.4  | <i>Datalogger panel temperatures recorded during May 1996 .....</i>   | 100 |
| 5.5  | <i>Datalogger panel temperatures recorded during June 1996.....</i>   | 100 |
| 5.6  | <i>Datalogger panel temperatures recorded during July 1996.....</i>   | 101 |
| 5.7  | <i>Comparison of temperatures recorded through the thickness of the west wall on June 17, 1996 .....</i>                                  | 102 |
| 5.8  | <i>Comparison of temperatures at locations along the height of pier P16 .....</i>   | 104 |
| 5.9  | <i>One day cycle of thermal gradients along the north-south axis of the pier P16 cross-section on June 17, 1996.....</i>                  | 105 |
| 5.10 | <i>One day cycle of thermal gradients along the northeast-southwest axis of the cross-section: June 17, 1996.....</i>                     | 107 |
| 5.11 | <i>One day cycle of thermal gradients along the east-west axis of the cross-section, June 17, 1996.....</i>                               | 109 |
| 5.12 | <i>One day cycle of thermal gradients along the northwest-southeast axis of the pier's cross-section, June 17, 1996 .....</i>             | 110 |
| 5.13 | <i>One day cycle of thermal gradients occurring along the north-south axis of the capital segment cross-section on June 17, 1996.....</i> | 112 |
| 5.14 | <i>One day cycle of thermal gradients along the northeast-southwest axis, capital segment PC16-7, June 17, 1996 .....</i>                 | 113 |
| 5.15 | <i>One day cycle of thermal gradients along the east-west axis, capital segment PC16-8, June 17, 1996.....</i>                            | 114 |
| 5.16 | <i>One day cycle of thermal gradients along the northwest-southeast axis, capital segment PC16-8, June 17, 1996 .....</i>                 | 115 |
| 5.17 | <i>Mechanism for cracking of large monolithic members during curing.....</i>  | 116 |
| 5.18 | <i>Comparison of internal curing temperature to ambient air temperature, capital segment PC16-8.....</i>                                  | 117 |
| 5.19 | <i>Maximum gradient shape during curing of capital.....</i>   | 118 |
| 5.20 | <i>Map of cracks found during curing of capital segment PC16-8.....</i>   | 119 |

|      |   |     |
|------|---|-----|
| 5.21 | Temperature and strain changes on June 17, 1996: outer gauge locations, north-south sectional axis.....   | 121 |
| 5.22 | Temperature and strain changes on June 17, 1996: outer gauge locations, east-west sectional axis.....   | 122 |
| 5.23 | Comparison of longitudinal strains on June 17, 1996: eastern face gauge locations in segment PC16-1, PC16-5, and PC16-7 .....                             | 123 |
| 5.24 | Temperature and strain changes on June 17, 1996: outer and inner gauges, north wall of pier P16.....  | 124 |
| 5.25 | Temperature and strain changes on June 17, 1996: outer and inner gauges, west wall of pier P16.....   | 124 |
| 5.26 | Temperature and strain changes on June 17, 1996: north and south faces, horizontal gauges.....  | 126 |
| 5.27 | Comparison of transverse strains near north face of the pier, segments PC16-1, PC16-5, and PC16-7 .....   | 127 |
| 5.28 | Temperature and strain changes on June 17, 1996: horizontally oriented gauges, east and west faces.....   | 127 |
| 5.29 | Pressure transducer readings during pier post-tensioning.....   | 128 |
| 5.30 | Selected axial strains in segment PC16-1 during post-tensioning, north and south axis locations .....   | 129 |
| 5.31 | Selected axial strains in segment PC16-1 during pier post-tensioning, east-west axis locations.....   | 131 |
| 5.32 | Comparison of strains along length of pier during post-tensioning .....   | 132 |
| 5.33 | Comparison of axial and transverse strains during post-tensioning, north-south axis locations.....  | 133 |
| 5.34 | Comparison of axial and transverse strains during post-tensioning, east-west axis locations.....  | 133 |
| 5.35 | Comparison of transverse strains near the south face of each segment .....  | 134 |
| 5.36 | Comparison of transverse strains near the north face of each segment .....  | 135 |
| 5.37 | Comparison of transverse strains near the east face of each segment .....   | 135 |
| 5.38 | Comparison of transverse strains near the west face of each segment.....  | 136 |
| 6.1  | Gradient shapes plotted using average temperatures at each depth .....  | 140 |
| 6.2  | Independent octagonal "shells" .....  | 141 |
| 6.3  | Projection of temperature gradient shape onto a single axis .....   | 142 |
| 6.4  | Maximum measured monthly positive temperature gradients .....   | 143 |
| 6.5  | Design code positive temperature gradients .....  | 144 |
| 6.6  | Maximum measured monthly negative temperature gradients .....   | 146 |
| 6.7  | Design code negative temperature gradients.....   | 147 |
| 6.8  | Calculation of self-equilibrating stresses induced by the maximum positive temperature gradient, April 1996 .....   | 150 |
| 6.9  | Longitudinal strains due to self-equilibrating stresses induced by monthly maximum positive gradients, plotted on the east-west cross-sectional axis..... | 152 |

|      |  |     |
|------|--|-----|
| 6.10 | Longitudinal strains due to self-equilibrating stresses induced by design positive gradients, plotted on the east-west cross-sectional axis .....  | 153 |
| 6.11 | Calculation of self-equilibrating stresses induced by the maximum negative temperature gradient, April 1996 .....  | 155 |
| 6.12 | Longitudinal strains due to self-equilibrating stresses induced by monthly maximum negative gradients, plotted on the east-west cross-sectional axis.....  | 156 |
| 6.13 | Longitudinal strains due to self-equilibrating stresses induced by design negative gradients, plotted on the east-west cross-sectional axis .....  | 157 |
| 6.14 | Final planar section orientation is dependent on temperature loading .....   | 159 |
| 6.15 | Areas and assigned temperatures used for stress calculations.....  | 160 |
| 6.16 | (a) Primary bending axes through the pier cross-section (b) Summation of volumes to determine $\phi$ angle .....   | 160 |
| 6.17 | Distance of each subdivided area's centroid to the bending axis B-B.....   | 161 |
| 6.18 | Longitudinal strains due to self-equilibrating stresses induced by monthly maximum positive gradients, calculated by the primary bending axis method and plotted on the east-west cross-sectional axis ..... | 163 |
| 6.19 | Orientation of primary bending axis B-B calculated for each monthly maximum positive gradient load case.....   | 164 |
| 6.20 | Longitudinal strains due to self-equilibrating stresses induced by monthly maximum negative gradients, calculated by the primary bending axis method and plotted on the east-west cross-sectional axis ..... | 165 |
| 6.21 | Orientation of primary bending axis B-B calculated for each monthly maximum negative gradient load case.....   | 166 |
| 6.22 | Application of non-linear thermal gradient to individual pier walls.....   | 167 |
| 6.23 | Frame model of pier cross-section used for redistribution of forces by computer frame analysis program .....   | 168 |
| 6.24 | Temperature distributions and self-equilibrating transverse strains caused by positive temperature gradients for (a) April, (b) May, (c) June, (d) July .....  | 170 |
| 6.25 | Temperature distributions and self-equilibrating transverse strains caused by negative temperature gradients for (a) April, (b) May, (c) June, (d) July .....  | 172 |
| 7.1  | (a) Actual pier geometry, (b) finite element model geometry, (c) element mesh longitudinal geometry, (d) actual cross-section geometry, and (e) element mesh cross-section geometry.....                     | 175 |
| 7.2  | "Octagonal shell" method of temperature estimation.....  | 177 |
| 7.3  | Maximum positive gradient load case: April 23, 1996 .....  | 178 |
| 7.4  | Nodal temperature assignments: NCHRP 276 [5] positive design gradient....  | 179 |
| 7.5  | Contour plots of temperature and longitudinal strain, April maximum positive gradient load case .....  | 180 |
| 7.6  | Finite element analyses strain projection plots on east-west cross-sectional axis from maximum monthly positive temperature gradients .....  | 181 |



|      |   |     |
|------|---|-----|
| 7.7  | <i>Finite element analyses strain projection plots on east-west cross-sectional axis from positive design temperature gradients.....</i>                                    | 182 |
| 7.8  | <i>Contour plots of temperature and longitudinal strain, April maximum negative gradient load case .....</i>  | 184 |
| 7.9  | <i>Finite element analyses strain projection plots on east-west cross-sectional axis from maximum monthly negative temperature gradients.....</i>                           | 185 |
| 7.10 | <i>Finite element analyses strain projection plots on east-west cross-sectional axis from negative design temperature gradients.....</i>                                    | 186 |
| 7.11 | <i>Temperature loading and transverse strain from finite element analysis of monthly positive temperature gradients during (a) April, (b) May, (c) June, (d) July .....</i> | 189 |
| 7.12 | <i>Temperature loading and transverse strain from finite element analysis of monthly negative temperature gradients during (a) April, (b) May, (c) June, (d) July .....</i> | 191 |
| 8.1  | <i>Comparison of calculated strains projected on the east-west axis for the April 1996 maximum positive temperature distribution.....</i>                                   | 195 |
| 8.2  | <i>Comparison of calculated strains projected on the east-west axis for the June 1996 maximum positive temperature distribution.....</i>                                    | 197 |
| 8.3  | <i>Comparison of calculated strains projected on the east-west axis for the April 1996 maximum negative temperature distribution.....</i>                                   | 198 |
| 8.4  | <i>Comparison of calculated strains projected on the east-west axis for the June 1996 maximum negative temperature distribution.....</i>                                    | 200 |
| 8.5  | <i>Temperature changes along the east-west cross-sectional axis recorded by thermocouples in segment PC16-5 .....</i>   | 203 |
| 8.6  | <i>Calculated strain changes and strain changes recorded by concrete strain gauges in segment PC16-1, east-west cross-sectional axis.....</i>                               | 204 |
| 8.7  | <i>Temperature changes along the north-south cross-sectional axis recorded by thermocouples in segment PC16-5 .....</i>   | 205 |
| 8.8  | <i>Calculated strain changes and strain changes recorded by concrete strain gauges in segment PC16-1, north-south cross-sectional axis.....</i>                             | 205 |
| 8.9  | <i>Calculated strain changes and strain changes recorded by concrete strain gauges in segment PC16-5, east-west cross-sectional axis.....</i>                               | 206 |
| 8.10 | <i>Comparison of C433 and C458 during several daily cycles of temperature ....</i>  | 208 |
| 8.11 | <i>Calculated strain changes and strain changes recorded by concrete strain gauges in segment PC16-5, north-south cross-sectional axis .....</i>                            | 208 |
| 8.12 | <i>Calculated strain changes and strain changes recorded by concrete strain gauges in segment PC16-7, east-west cross-sectional axis.....</i>                               | 209 |
| 8.13 | <i>Nearly identical daily strain cycles for gauges in segment PC16-7 and their locations and orientations in the cross-section .....</i>                                    | 210 |
| 8.14 | <i>Calculated strain changes and strain changes recorded by concrete strain gauges in segment PC16-7, north-south cross-sectional axis .....</i>                            | 211 |
| 8.15 | <i>Temperature changes along the east-west cross-sectional axis recorded by thermocouples in segment PC16-5 .....</i>   | 212 |

|      |  |     |
|------|--|-----|
| 8.16 | <i>Calculated strain changes and strain changes recorded by concrete strain gauges in segment PC16-1, east-west cross-sectional axis</i> .....   | 212 |
| 8.17 | <i>Temperature changes along the north-south cross-sectional axis recorded by thermocouples in segment PC16-5</i> .....                          | 213 |
| 8.18 | <i>Calculated strain changes and strain changes recorded by concrete strain gauges in segment PC16-1, north-south cross-sectional axis</i> ..... | 214 |
| 8.19 | <i>Calculated strain changes and strain changes recorded by concrete strain gauges in segment PC16-5, east-west cross-sectional axis</i> .....   | 215 |
| 8.20 | <i>Daily cycles of strain recorded by C435 and C454</i> .....  | 215 |
| 8.21 | <i>Calculated strain changes and strain changes recorded by concrete strain gauges in segment PC16-5, north-south cross-sectional axis</i> ..... | 216 |
| 8.22 | <i>Calculated strain changes and strain changes recorded by concrete strain gauges in segment PC16-7, east-west cross-sectional axis</i> .....   | 217 |
| 8.23 | <i>Calculated strain changes and strain changes recorded by concrete strain gauges in segment PC16-7, north-south cross-sectional axis</i> ..... | 217 |
| 8.24 | <i>Transverse strain comparison in the south wall of segment PC16-1</i> .....  | 220 |
| 8.25 | <i>Transverse strain comparison in the west wall of segment PC16-1</i> .....   | 221 |
| 8.26 | <i>Transverse strain comparison in the north wall of segment PC16-1</i> .....  | 221 |
| 8.27 | <i>Transverse strain comparison in the east wall of segment PC16-1</i> .....   | 222 |
| 8.28 | <i>Several daily cycles of strain changes recorded by gauge C416</i> .....   | 223 |
| 8.29 | <i>Transverse strain comparison in the south wall of segment PC16-5</i> .....  | 224 |
| 8.30 | <i>Transverse strain comparison in the west wall of segment PC16-5</i> .....   | 224 |
| 8.31 | <i>Transverse strain comparison in the north wall of segment PC16-5</i> .....  | 225 |
| 8.32 | <i>Transverse strain comparison in the east wall of segment PC16-5</i> .....   | 225 |
| 8.33 | <i>Transverse strain comparison in the south wall of segment PC16-7</i> .....  | 226 |
| 8.34 | <i>Transverse strain comparison in the west wall of segment PC16-7</i> .....   | 227 |
| 8.35 | <i>Transverse strain comparison in the north wall of segment PC16-7</i> .....  | 227 |
| 8.36 | <i>Transverse strain comparison in the east wall of segment PC16-7</i> .....   | 228 |
| 8.37 | <i>Transverse strain comparison in the south wall of segment PC16-1</i> .....  | 229 |
| 8.38 | <i>Transverse strain comparison in the west wall of segment PC16-1</i> .....   | 230 |
| 8.39 | <i>Transverse strain comparison in the north wall of segment PC16-1</i> .....  | 230 |
| 8.40 | <i>Transverse strain comparison in the east wall of segment PC16-1</i> .....   | 231 |
| 8.41 | <i>Transverse strain comparison in the south wall of segment PC16-5</i> .....  | 232 |
| 8.42 | <i>Transverse strain comparison in the west wall of segment PC16-5</i> .....   | 232 |
| 8.43 | <i>Transverse strain comparison in the north wall of segment PC16-5</i> .....  | 233 |
| 8.44 | <i>Transverse strain comparison in the east wall of segment PC16-5</i> .....   | 233 |
| 8.45 | <i>Transverse strain comparison in the south wall of segment PC16-7</i> .....  | 234 |
| 8.46 | <i>Transverse strain comparison in the west wall of segment PC16-7</i> .....   | 235 |
| 8.47 | <i>Transverse strain comparison in the north wall of segment PC16-7</i> .....  | 235 |
| 8.48 | <i>Transverse strain comparison in the east wall of segment PC16-7</i> .....   | 236 |
| 9.1  | <i>Unbalanced segment construction load case</i> .....   | 242 |
| 9.2  | <i>Stress components for load case excluding temperature effects</i> .....   | 243 |

|      |   |     |
|------|---|-----|
| 9.3  | <i>Additional sectional stresses due to the application of the April maximum measured positive temperature gradient .....</i> | 245 |
| 9.4  | <i>Additional sectional stresses due to the application of the NCHRP 276 positive design gradient .....</i>                   | 246 |
| 9.5  | <i>Additional sectional stresses due to the application of the April maximum measured negative temperature gradient .....</i> | 247 |
| 9.6  | <i>Additional sectional stresses due to the application of the NCHRP 276 negative design gradient .....</i>                   | 248 |
| 9.7  | <i>Dead loads at several phases during construction .....</i>   | 250 |
| 9.8  | <i>Relative contributions of dead and live loads to stress at the base of the pier P16 for the service limit state .....</i>  | 251 |
| 9.9  | <i>Service load case IV with maximum measured positive gradient effects .....</i>   | 253 |
| 9.10 | <i>Service load case IV with NCHRP positive design gradient effects .....</i>   | 254 |
| 9.11 | <i>Additional thermal case with measured positive gradient effects .....</i>  | 255 |
| 9.12 | <i>Additional thermal case with NCHRP positive design gradient effects .....</i>  | 256 |
| 9.13 | <i>Service load case IV with maximum measured negative gradient effects .....</i>   | 257 |
| 9.14 | <i>Service load case IV with NCHRP negative design gradient effects .....</i>   | 258 |
| 9.15 | <i>Additional thermal case with measured negative gradient effects .....</i>  | 259 |
| 9.16 | <i>Additional thermal case with NCHRP negative design gradient effects .....</i>  | 260 |

# CHAPTER 1

## *INTRODUCTION*

### *1.1 GENERAL*

The U.S. 183 elevated freeway is a precast segmental post-tensioned box girder viaduct currently under construction in Austin, Texas. Researchers from the Phil M. Ferguson Structural Engineering Laboratory of The University of Texas at Austin are conducting field instrumentation operations on the bridge. These studies began in 1994 and will be continuing through 1997. Phases I and II of the research program involved the instrumentation of one precast segmental mainlane superstructure span constructed by the span-by-span method and one cast-in-place mainlane pier [1] respectively. This thesis presents the results of Phase III, the instrumentation and monitoring of a segmentally constructed hollow box bridge pier. A future phase will study a ramp superstructure span to be built by the balanced-cantilever method.

This chapter contains information concerning the U.S. 183 segmental viaduct. A full description of the segmentally constructed ramp pier is presented, and the scope and objectives of its instrumentation are outlined.

### *1.2 U.S. 183 PROJECT DESCRIPTION*

#### **1.2.1 Project Location**

The route of U.S. Highway 183 runs north-south from southern South Dakota through several plains states, bisects central Texas, and ends just short of the Texas coast of the Gulf of Mexico near Corpus Christi. Its path jogs to the southeast as it passes through the northern end of Austin, and forms one segment of a loop of heavily traveled arteries around the central part of Austin (see Figure 1.1). The U.S. 183

segmental viaduct project constitutes one of the last legs of this loop of limited-access freeway. Other major sections of the loop freeway include Interstate Highway 35, Loop 1 (MoPac Expressway), and U.S. Highway 71/290 (Ben White Boulevard).

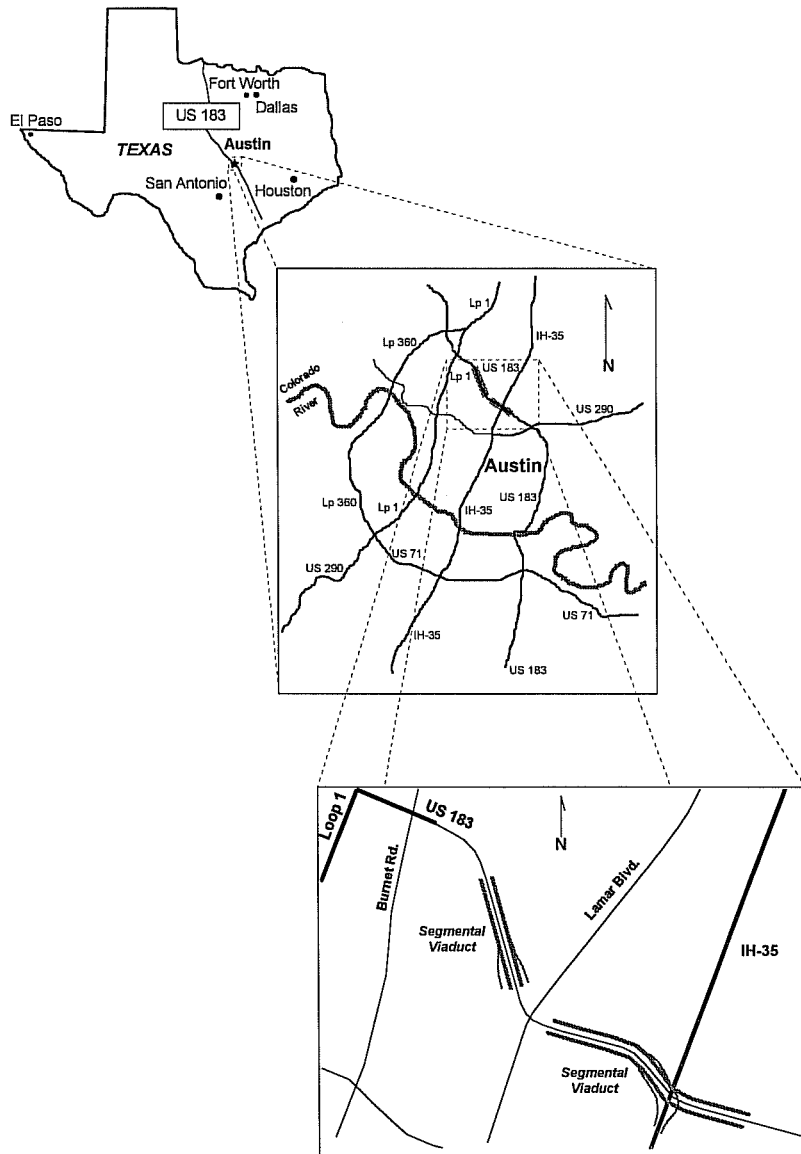


Figure 1.1: U.S. 183 segmental viaduct location.

### **1.2.2 Project Description**

At present, U.S. 183 consists of six lanes of full-access arterial in the area of the new viaduct. When construction is complete, these existing lanes will serve as the frontage roads for the new limited-access elevated freeway. Limited right-of-way, extreme narrowness of the U.S. 183 corridor, the need to mitigate traffic delays, and the desire to minimize construction time were crucial design considerations. Much of the new bridge was required to overhang existing traffic lanes; therefore, overhead construction was a prime consideration as well. During the design process, engineers at the Texas Department of Transportation (TxDOT) were allowed a great deal of freedom to create an aesthetically pleasing viaduct structure. Precast segmental construction methods fit these requirements well, and public attention to and acceptance of the new elevated freeway has been unusually positive.

The mainlanes of the new viaduct consist of twin bridge structures built using the span-by-span method of precast segmental construction. Each bridge carries three full lanes of traffic with provisions for a wide 3-meter outside shoulder and a narrow 1.2 meter inside shoulder (see Figure 1.2). The mainlane girders typically span 36 meters to 41 meters between piers. On average, each span consists of 14 superstructure segments weighing approximately 490 kN apiece. Anchorage segments located at the piers weigh approximately 620 kN. The mainlane superstructure segments feature unusually wide wings rather than the more traditional box girder design consisting of a wide box and short wings. This configuration is more appropriate for the single column supports chosen due to the limited right-of-way.

Four access ramp structures carrying one lane of traffic each complete the viaduct (see Figure 1.3). Three of the ramps are being constructed span-by-span, while the high flyover ramp located at the interchange of U.S. 183 and Interstate Highway 35 will be partly built in balanced-cantilever (see Chapter 4 for an outline of the balanced-cantilever construction sequence). Span lengths for the ramp structures vary between

30 meters and 41 meters. The two longest spans located on the balanced-cantilever ramp reach 55 meters.

A total of 3300 precast segments were produced at the contractor's casting yard. The total bid cost for the viaduct was approximately \$74 million. For comparison, this figure translates into about \$480/m<sup>2</sup> of bridge deck. The average cost of highway bridges in the state of Texas is about \$380/m<sup>2</sup> while the national average for the United States is approximately \$750/m<sup>2</sup>. These numbers by no means represent a comparison of typical segmental bridge costs to other types of construction. However, the U.S. 183 price and the average figure for Texas do reflect the availability of good quality concrete, lack of seismic design requirements, and the large number of working days per year (i.e., good weather) typical of bridges constructed in Texas.

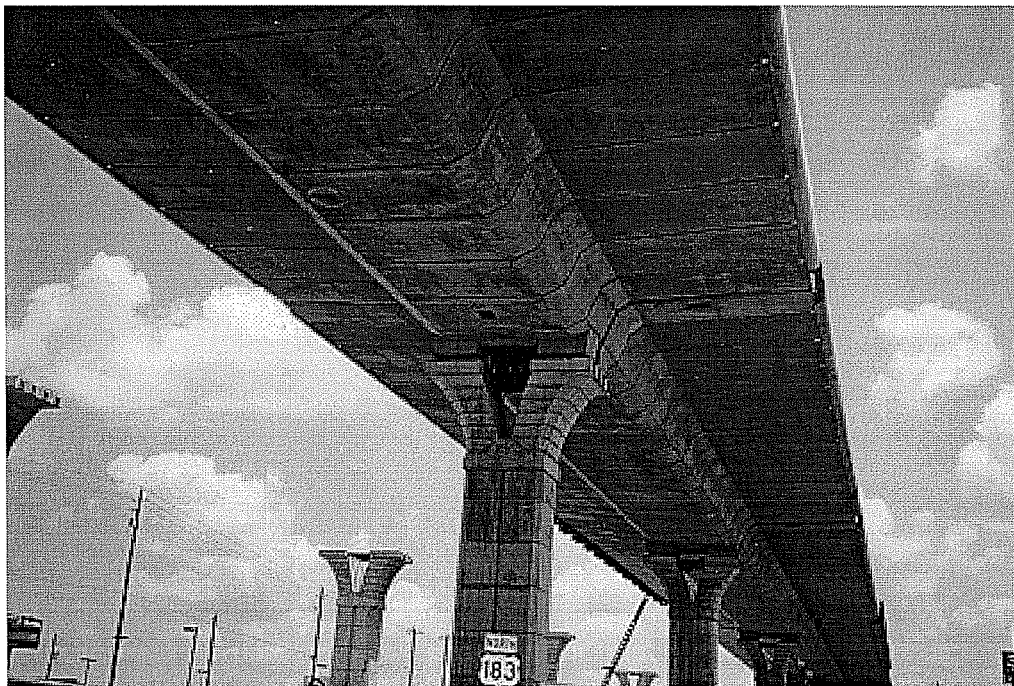


*Figure 1.2: U.S. 183 viaduct mainlane superstructure.*

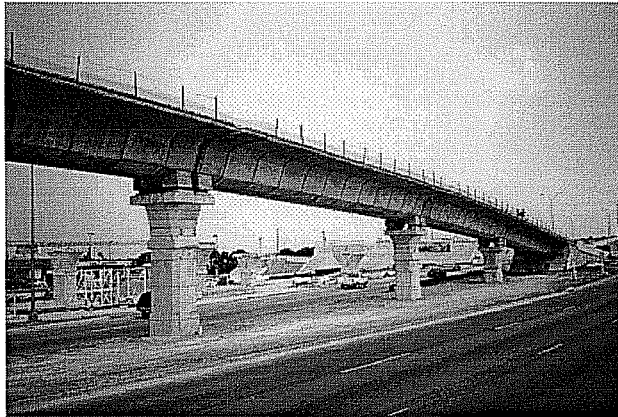


*Figure 1.3: Typical access ramp superstructure.*

The U.S. 183 segmental viaduct project was originally designed with three types of segmentally constructed piers covering 100% of the piers in the project (see Figure 1.4). However, the general contractor, Martin K. Eby, Inc., opted to cast in place two of the three pier types [2]. One of these cast-in-place types, the “Y” shaped mainlane pier (see Figure 1.4a), was instrumented in a previous study [1]. The second type, the small ramp pier (see Figure 1.4b), was not instrumented. The third type, known as the large ramp pier (see Figure 1.4c), was the only type to be constructed with precast segments.

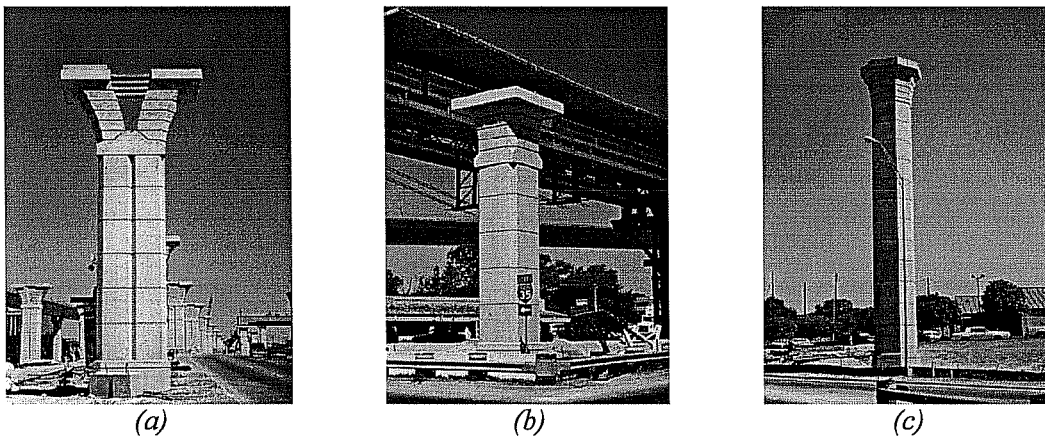


*Figure 1.4: (a) Mainlane “Y” pier; (b) small ramp pier; (c) large ramp pier.*



The contractor's decision to cast most of the piers on the project in place rather than use precast segmental construction was made due to several factors. First, the vast majority of the piers were relatively short (below 10 meters in height) and easy to reach with only small cranes. Also, access to the piers for construction vehicles was relatively simple: most of the mainlane piers were located in the median of the existing roadway where ground conditions were excellent (this fact can also be advantageous for segmentally constructed piers). Principally, contractor constraints on the precasting yard were decisive. The contractor had great difficulty locating a suitable facility with existing noise- and air-pollution control certification in the environmentally sensitive Austin area. The actual site selected was very cramped and priority was given to casting and storage facilities for the superstructure segments. The decision was made to use the large amount of land provided as the bridge right-of-way as the construction preparation area for the pier reinforcement cages.

### *1.3 LARGE RAMP PIER DESCRIPTION*

The large ramp pier was designed as a hollow, octagonal column cross-section with 406-mm thick walls. The column's shaft consisted of precast segments of 2.44-meter and 1.22-meter lengths. The hollow section reduced foundation costs and facilitated the transportation and erection of the pier segments. A solid "capital" segment located at the top of the column provided an anchorage zone for post-tensioning tendons. The capital also served as a bearing area for the ramp superstructure and an anchorage for tie-down bars connecting the superstructure to the capital during balanced-cantilever erection. Figure 1.5 and Figure 1.6 show the general configuration of the large ramp pier.

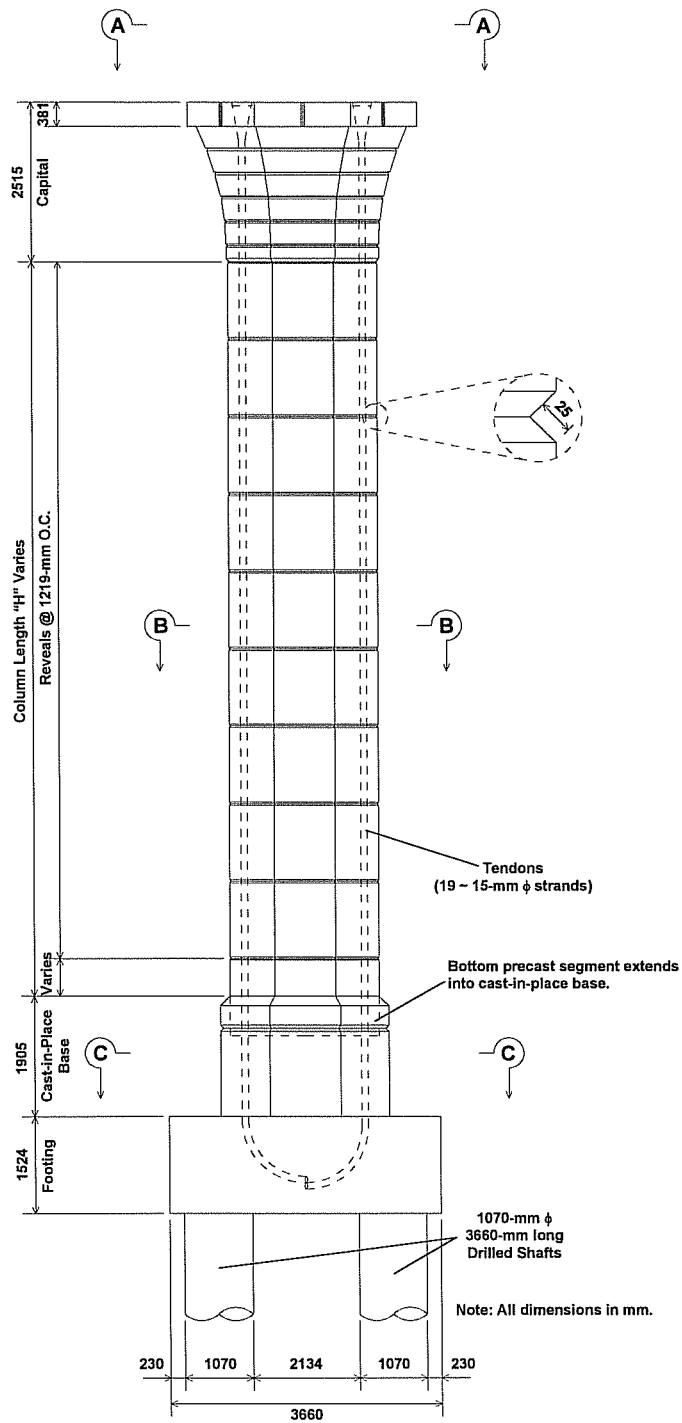
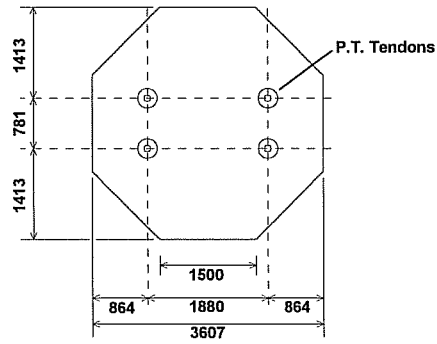
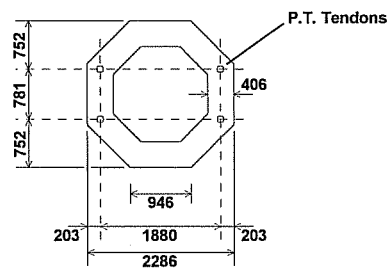


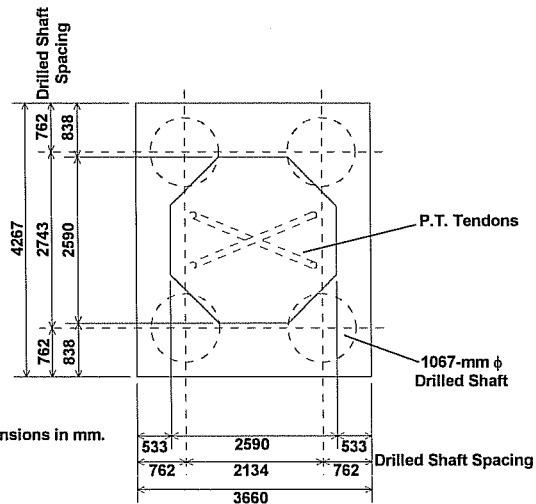
Figure 1.5: Typical large ramp pier: elevation view.



**SECTION A-A**



**SECTION B-B**



Note: All dimensions in mm.

**SECTION C-C**

Figure 1.6: Typical sections: large ramp pier.

#### *1.4 PROBLEM STATEMENT AND OBJECTIVES*

The effects of temperature gradients on concrete superstructure members with hollow cross-sections are well known and recognized by bridge design codes. However, present United States (U.S.) codes offer no provisions for the application of thermal gradients in bridge piers. The increasing use of precast segmental substructures both in the U.S. and worldwide coupled with the lack of guidance available to designers highlights the need for a closer examination of the shapes and magnitudes of the actual gradients that occur in order to provide input data for broader analytical studies. Such studies will indicate what types of substructures might be sensitive to differential temperature gradients. From the outset it was recognized that the effects of thermal gradients would be much less in a single-pier bent than in a multiple-pier substructure. However, only single-pier bents were available. It was felt that the opportunity to obtain measured temperatures in a hollow section justified the program even if the overall effects might be limited. The instrumentation of the large ramp pier will be used to determine whether design codes should treat hollow concrete substructures differently and whether differential temperature gradients should be applied to bridge piers. The objectives of this project are as follows:

1. To comprehensively instrument a precast segmental bridge pier with a hollow cross-section.
2. To determine the maximum differential temperature gradient across the pier's cross-section and the frequency of its occurrence during the service life of the pier.
3. To determine the typical shape of the differential temperature gradient.
5. To track the behavior of the pier due to changes in temperature gradients over time.
6. To measure the induced stresses in the pier caused by applied temperature gradients and determine their importance to the overall behavior of the pier.
7. To make recommendations for changes or additions to current bridge design codes.

### *1.5 SCOPE OF WORK*

The scope of this project included the thorough instrumentation of a precast, segmentally-constructed bridge pier with a hollow cross-section. Instruments were monitored hourly during the first 5 months of the service life of the pier. A finite element model was used to confirm measured response of the pier to applied temperature gradients. Analytical studies were performed to extend the results to multiple-column bents. Comparisons of measured pier gradients to those specified for bridge superstructures in current bridge design codes were used to determine recommendations for modifications in current design practice.

## CHAPTER 2

### *BACKGROUND AND PREVIOUS STUDIES*

#### *2.1 GENERAL*

Engineers have long known of the effects of ambient temperature variations on the superstructures of bridges. This fact is reflected in bridge designs which account for axial shortening and elongation in the superstructure through the use of elastomeric bearing pads, rollers, and expansion joints [3]. Recently, some sophisticated bridge designs eliminated such devices; more accurate analysis methods allowed designers to accommodate superstructure movements through deflections of the substructure [4].

The increased use of monolithic systems with restrained members highlighted a second and potentially serious environmentally-induced effect: strains due to temperature gradients through member cross-sections. The poor thermal conductivity of concrete tends to create large temperature differentials on opposite sides of members as they are heated and cooled in daily cycles [3]. These differentials in turn cause a corresponding strain distribution which can develop a significant amount of tensile stress in the member. The problem became especially apparent in bridge superstructures with hollow cross-sections: the Jagst bridge in Germany and several cast-in-place bridges in the State of Colorado exhibited cracking attributable in part to thermal differences between the top and bottom flanges [5].

To date, however, no investigations into the effects of non-linear thermal gradients on concrete bridge piers have been performed. According to a survey performed by Poston, Diaz, and Breen [6] in 1984 regarding 155,000 bridge bents, approximately 17% were single pier bent configurations. Of these, about 11% were designed with a hollow cross-section. Of the 129,000 bent configurations built with multiple piers, 1% were hollow in cross-section. Thus, in the period of 20 years

between 1960 and 1980, approximately 2950 single-pier and 1420 multiple-pier bent configurations were built with hollow cross-sections. Furthermore, respondents to the survey indicated that the number of single-pier bents (where hollow cross-sections are more often used) would likely increase to 20% of the planned total for the period from 1980 to 1990. Therefore it would seem that the use of hollow cross-sections is increasing in bridge piers built in North America. Additional anecdotal evidence of the increasing use of segmentally constructed hollow bridge piers is presented later in this chapter. Clearly, there exists a need for clarification of the code requirements concerning the effects of temperature gradients on hollow bridge piers.

## *2.2 NON-LINEAR THERMAL GRADIENTS*

### **2.2.1 Gradient Shape**

Many factors influence the shape of thermal gradients across a member's cross-section. Environmental variations, material properties, and time all greatly affect the distribution of temperatures (see Figure 2.1).

In general, the environmental influences on a bridge structure include radiation, convection, and conduction [4,5]. The most important of these is solar radiation [5,7,8], which causes significant increases in temperature on surfaces directly exposed to sunlight, even on days when the ambient air temperature is relatively low. In addition to direct solar radiation, re-radiation of heat back into the surrounding environment can also occur, primarily at night [5]. Convection and conduction occur between the structure and the ambient air [4,5]. These two processes are directly related to the difference in temperature between the air and concrete and can be affected by wind speed. Roberts [7] reported that air stirring caused by vehicular motion on the decks of bridges can influence temperatures near the top surface.

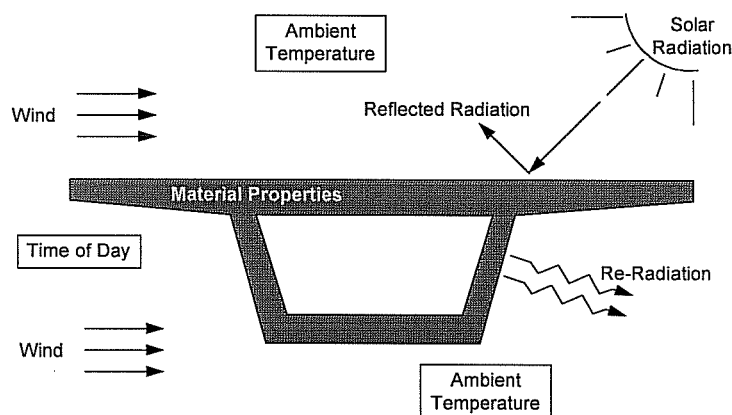


Figure 2.1: Factors affecting thermal gradients (after Roberts [7]).

Weather patterns during certain times of the year and at particular geographic locations affect temperature distributions as well. During the months of March and April, the city of Austin, Texas typically experiences unstable weather patterns. Warm and cool fronts tend to arrive alternately every few days, causing large variations in the ambient air temperature on a day-to-day basis. Potgieter and Gamble [8] suggest that such variations in weather patterns can produce large temperature differences through bridge members. A warm weather pattern that immediately follows cold weather can produce a large “positive” gradient in bridge decks (i.e., the temperature of the bridge deck is higher than that of the soffit.) Cool weather following a warm front can have the opposite effect, producing “negative” gradients. The same researchers also cite ambient humidity as an important factor. In desert regions air temperature during the night can fall dramatically, whereas daytime temperatures can rise to very high levels. This large daily fluctuation can cause severe gradients in bridge structures. However, the effect may be less pronounced in humid climates where nighttime ambient air temperature drops relatively little; the bridge members never cool down sufficiently to create large temperature gradients when the sun rises the following morning.



The material properties of concrete greatly influence the distribution of temperatures through the bridge cross-section. Moorty and Roeder [4] cite density, specific heat, and conductivity as important factors in determining heat flow. The low conductivity of concrete is the most important material property which contributes to the shapes of measured gradients in bridges [3,7,8]. Heat absorbed into the outer layer of a concrete member will transfer through the section over a period of many hours. During thermal tests on concrete frame models, Vecchio and Sato [9] reported that steady-state temperature conditions finally occurred in the 300 mm thick sections of their models after 18 hours of constantly-applied thermal load. It can be concluded that the daily radiation and temperature fluctuations in the environment surrounding bridges will seldom if ever allow the structures to achieve steady-state equilibrium.

### **2.2.2 Gradient Effects**

#### ***2.2.2.1 Generalized Members***

The effects of temperature gradients on a structure are a function of the shape of the gradient and the determinacy of the structure [5]. In order to investigate the effects of thermal gradients, several assumptions must be made (from Imbsen, et al[5]):

1. The material is homogeneous and isotropic.
2. Material properties are independent of temperature changes.
3. The material behaves elastically (i.e., superposition is valid).
4. Plane sections remain plane.
5. Temperature varies only with depth of the member.

The first and third assumptions limit the discussion of thermal response in concrete members to those in an uncracked state. The fifth assumption was confirmed experimentally by Hoffman, McClure, and West [10] during a thermal study on a model span in Pennsylvania.

The requirement that plane sections remain plane is the basis of all thermal gradient effects. As shown in Figure 2.2, when a statically determinate member undergoes a linear temperature distribution across its cross-section it will experience bending and elongation related to the slope of the linear gradient. No induced stresses will occur due to the linearity of the gradient [7].

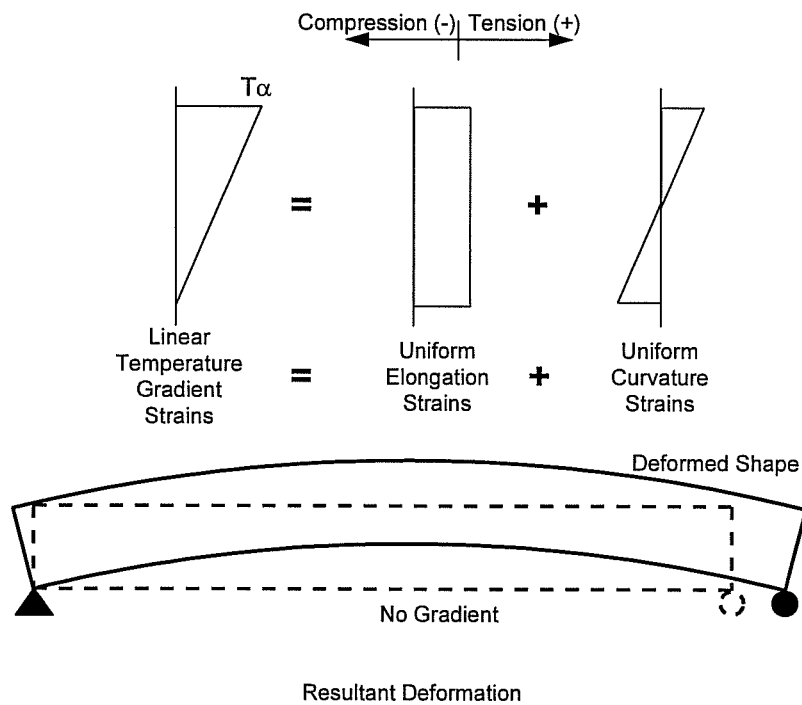


Figure 2.2: A statically determinate member under a linear temperature gradient (after Roberts [7]).

The problem becomes more complicated with the application of a non-linear temperature gradient (see Figure 2.3). Temperature induced strain is a function of the temperature at any distance from the neutral axis of the member and the coefficient of thermal expansion  $\alpha$ :

$$\varepsilon_t(Y) = \alpha T(Y) \quad (2.1)$$

where  $Y$  is measured from the neutral axis of the member.

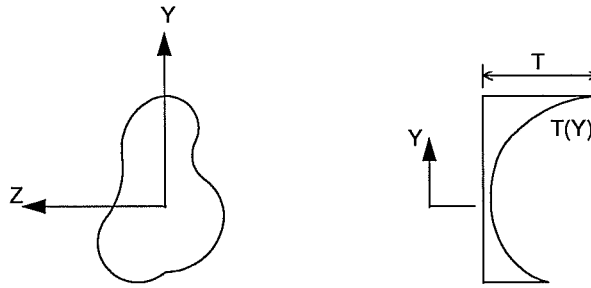


Figure 2.3: Arbitrary section with a non-linear temperature distribution.

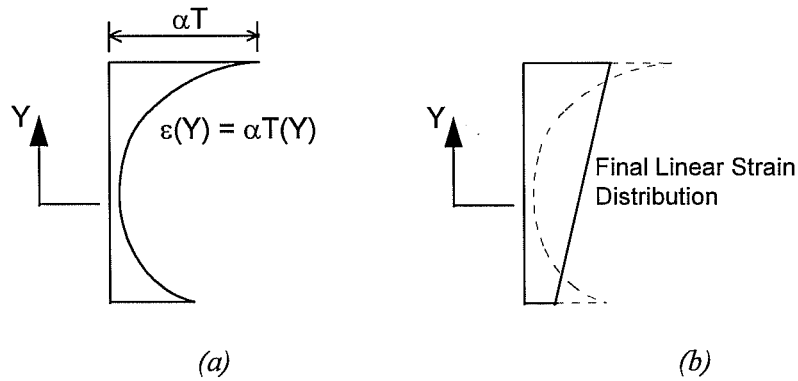


Figure 2.4: (a) Non-linear strain distribution assuming no interaction between section fibers (b) final linear strain distribution because plane sections remain plane (after Imbsen[5]).

Figure 2.4a illustrates the strain distribution across the arbitrary section with a non-linear temperature gradient if plane sections do not remain plane and the section's fibers do not influence one another. In a monolithic structure this cannot be the case; there is an interaction and shear transfer between fibers and the actual strain distribution has been shown to be linear as shown in Figure 2.4b. The induced stress

distribution in a fully restrained member due to the non-linear gradient can be calculated as (see Figure 2.5):

$$\sigma_t(Y) = E \alpha T(Y) \quad (2.2)$$

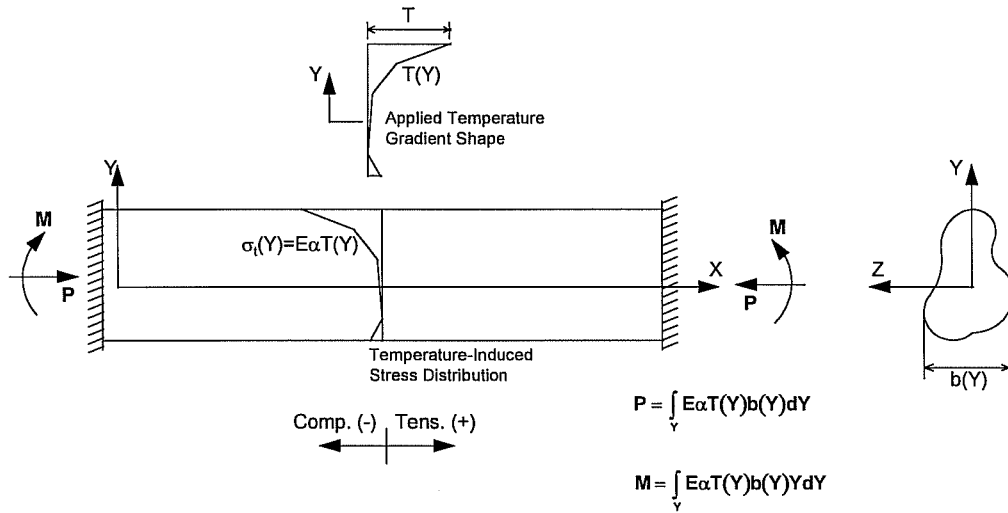


Figure 2.5: Thermal gradient and stress distribution in a fully restrained member.

The internal stresses needed to satisfy the requirement that plane sections remain plane are referred to as *self-equilibrating* stresses. They arise from the interaction of the member's fibers with one another and are analogous to residual stresses present in hot-rolled steel shapes [5,8]. To calculate their magnitude, one must first assume that the member is fully restrained [7]. The temperature-induced stress distribution (i.e. Equation 2.2) represents the sum of the self-equilibrating stresses and *artificial* stresses which represent the axial force and bending moment required to fully restrain the member [5]. Figure 2.6 illustrates this concept.

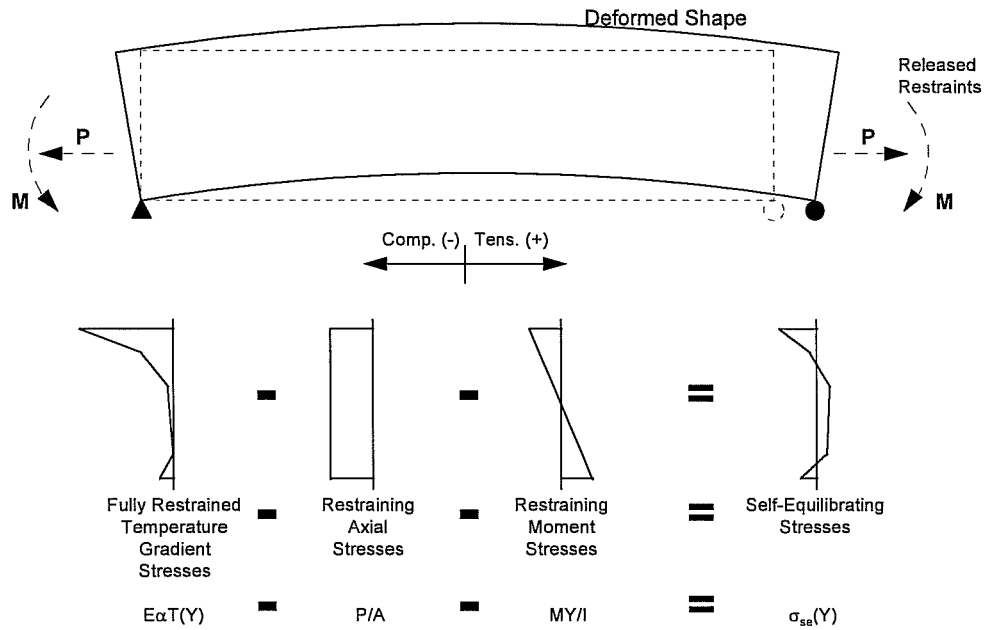


Figure 2.6: Temperature-induced stress distributions (after Roberts [7]).

The restraining axial force is expressed as:

$$P = \int_Y E \alpha T(Y) b(Y) dY = \int_Y \sigma_t b(Y) dY \quad (2.3)$$

where  $b(Y)$  is the section width at any distance  $Y$  from the neutral axis [5,7]. The axial stress can be written as:

$$\sigma_p(Y) = \frac{P}{A} \quad (2.4)$$

where  $A$  is the cross-sectional area of the member. It follows that the restraining moment is calculated as:

$$M = \int_Y E \alpha T(Y) b(Y) Y dY = \int_Y \sigma_t(Y) b(Y) Y dY \quad (2.5)$$

and the bending stresses are:

$$\sigma_m(Y) = \frac{MY}{I} \quad (2.6)$$

where  $I$  is the moment of inertia of the section about the neutral axis. Self-equilibrating stresses are then calculated by the following:

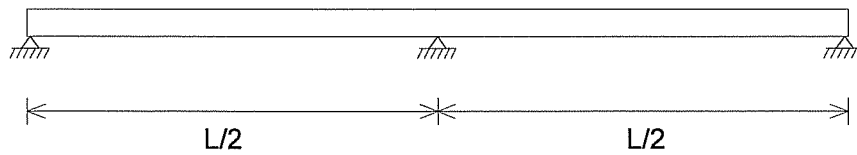
$$\sigma_{se} = \sigma_t - \sigma_p - \sigma_m = E\alpha T(Y) - \frac{P}{A} - \frac{MY}{I} \quad (2.7)$$

In summary, self-equilibrating stresses in a statically determinate member are determined in these steps:

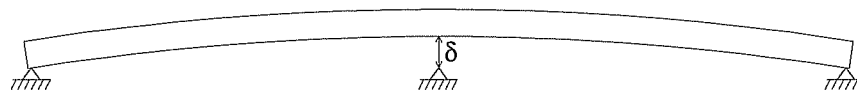
- Artificially restrain the member
- Calculate the fully restrained stress distribution (Equation 2.2)
- Calculate the artificial moments and axial forces (Equations 2.4 and 2.6)
- Remove the artificial stresses from the total stress distribution (Equation 2.7)

The member's curvature can then be found by converting the sum of the stresses found in Equations 2.4 and 2.6 into strains and solving for the slope of the linear strain distribution [8].

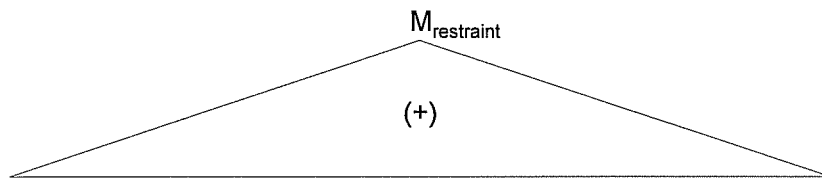
Stress distributions in statically indeterminate members are found similarly. Potgieter and Gamble [8] present the example of a two span continuous beam (see Figure 2.7). As before, the fully restrained axial and bending stresses are calculated, and the member's curvature is found as stated above. Using the calculated value for curvature, the beam's unrestrained deflection (cambered upwards for positive gradients) can be found. A force is then applied at the middle support to satisfy boundary conditions, and the new restraint stresses (i.e., bending moment) are added to the self-equilibrating stresses found earlier.



**Example Two-Span Structure**



**Unrestrained Deformation with Uniform Curvature**



**Moments Due to Restraining Force at Center Support**

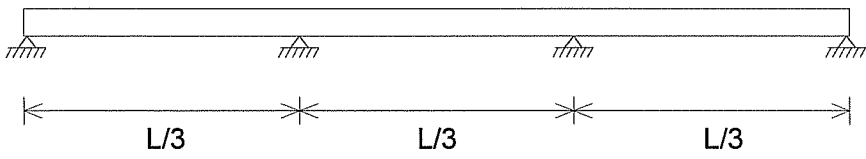


**Actual Deformation**

*Figure 2.7: Application of thermal gradients to a two-span beam (after Potgieter and Gamble [8]).*

Roberts [7] illustrates the concept with a three-span continuous beam using the same process (see Figure 2.8). The temperature stresses are more critical in this

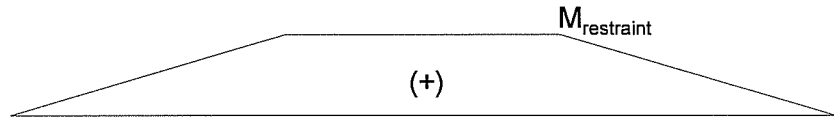
example: the three-span beam undergoes a positive moment due to temperature stresses in the middle span, thus acting in concert with live load moments.



**Example Three-Span Structure**



**Unrestrained Deformation with Uniform Curvature**



**Moments Due to Restraining Force at Center Support**



**Actual Deformation**

*Figure 2.8: Application of thermal gradients to a three-span beam (after Roberts [7]).*



### 2.2.2.2 Effects on Bridge Piers

The effects on hollow bridge piers due to temperature gradients are assumed to be similar to those for the beam members in the previous section. However, different deflection patterns are possible due to the differences in support conditions. Figure 2.9 shows the expected deflection due to self-equilibrating stresses on the statically determinate free-standing single pier bent.

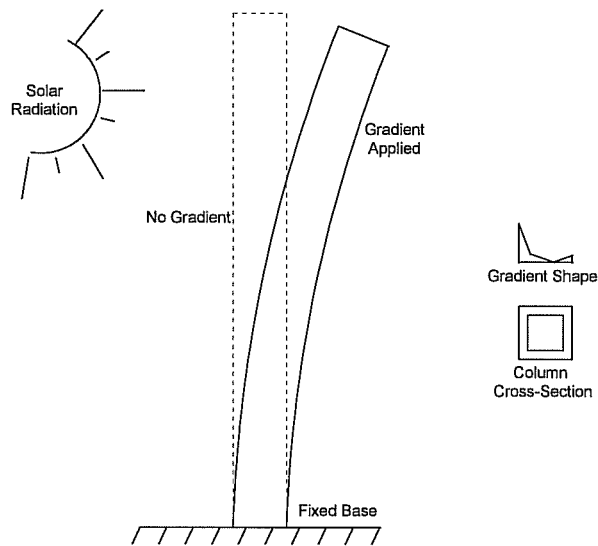


Figure 2.9: Temperature-induced response in a free-standing single pier bent.

Restraint conditions would be imposed on the pier in various degrees depending on the type of interface between the pier and the superstructure. A simplistic idealization would be to model the pier as a fully restrained member (see Figure 2.10). This assumption requires that both the superstructure and the foundation exhibit infinite stiffness. Modeling the pier in this manner would produce an overly conservative estimate of the axial and flexural stresses induced by the non-linear temperature gradient.

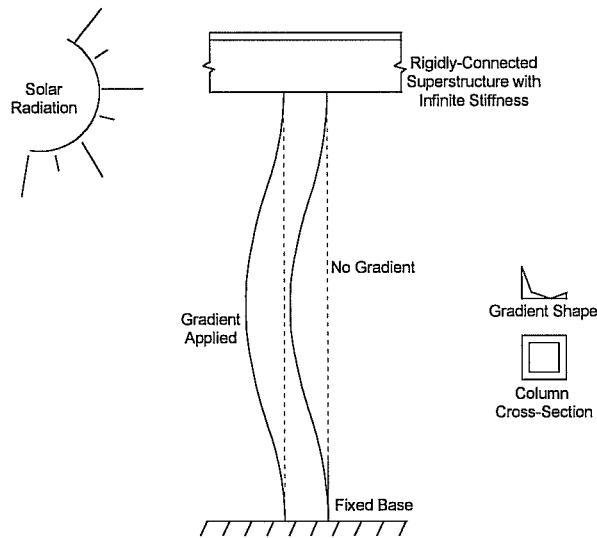


Figure 2.10: Temperature-induced response in a fully restrained single pier bent.

Modeling the pier as partially restrained by the superstructure and the foundation would give a more accurate representation of the induced stresses. The stiffness at each end of the pier could be modeled as finite. Therefore, some movement would be possible at the column's ends as shown in Figure 2.11.

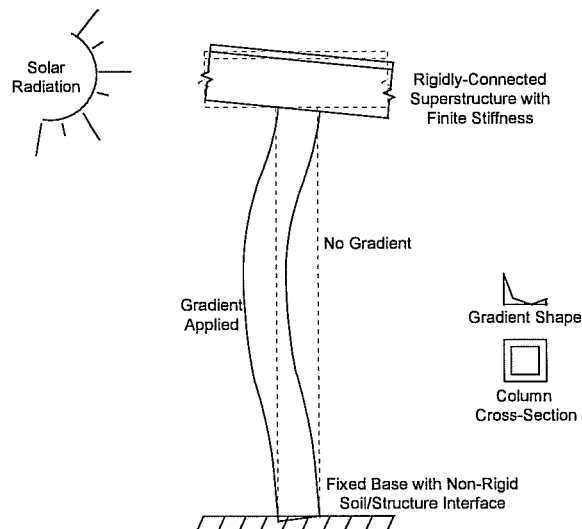


Figure 2.11: Temperature-induced response in a partially-restrained single pier bent.

Although their use is rare, bents consisting of multiple piers with hollow cross-sections would also respond to thermal gradients according to restraint conditions. For a bent with no superstructure attached, the response would be highly dependent on the orientation of the applied maximum temperature difference (see Figure 2.12). Various levels of rigidity in the superstructure-to-bent and foundation-to-column connections along with the temperature gradient orientation would also influence any induced stresses. Finally, the bent configuration itself would affect the response. The number of piers and horizontal braces would determine the magnitudes of strains and stresses induced by temperature.

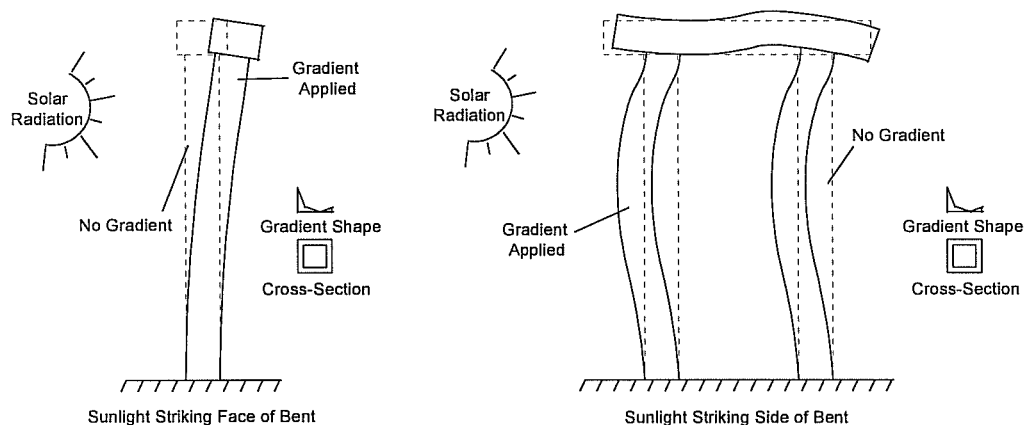


Figure 2.12: Temperature-induced response of a multiple-pier bent.

### 2.3 DEVELOPMENT OF CURRENT AASHTO CODE PROVISIONS

A comprehensive literature review of studies related to thermal gradient effects in bridge superstructures was performed by Roberts [7]. However, it is necessary to discuss two important studies [5,8] that had a direct impact on the thermal effects provisions as stated in the American Association of State Highway and Transportation Officials (AASHTO) *LRFD Bridge Design Specifications* [11] and the *AASHTO Guide Specifications for the Design and Construction of Segmental Concrete Bridges* [12]. Findings indicated by a new study [7] are discussed in a subsequent section.

### **2.3.1 Potgieter and Gamble [8]**

Researchers from the University of Illinois used a one-dimensional heat flow computer model to predict temperature distributions in concrete box-girder bridges. The program was run with a variety of cross-sectional shapes. Temperature data taken over a period of two days from the Kishwaukee River Bridge in northern Illinois were used to confirm the results found by the computer program.

In addition, measurements of solar radiation levels from 26 weather stations throughout the country were used as input for the computer model. From these data, researchers attempted to quantify the maximum possible gradient and the frequency of its occurrence in particular regions in the continental United States.

Potgieter and Gamble [8] noted that temperature-induced stresses were primarily a serviceability problem. The effects of these stresses on the ultimate strength of a structure were minimal. The authors found temperature stresses to be of the same order of magnitude as those caused by service live loads. Most importantly, the authors recommended the use of additional mild reinforcement to control crack widths, rather than additional prestressing to prevent the occurrence of tensile stresses.

### **2.3.2 NCHRP Report 276 [5]**

This study's main objective was to develop specific guidelines intended for adoption into the AASHTO bridge design code. This extremely informative report provided an overview of (then) current design code provisions for temperature gradients from a variety of foreign sources. Case studies were examined to determine the magnitude of thermal effects on typical bridge types and configurations. Also, a comprehensive list of references was cited to aid designers. Several complete examples of calculations to determine temperature-induced stresses were included as well.

Design guidelines for the applications of thermal gradients in bridge superstructures were proposed that relied heavily on the research performed by Potgieter and Gamble [8]. The United States was divided into four zones of solar radiation intensity (see Figure 2.13). Both positive and negative temperature gradient shapes were proposed that varied in magnitude according to the radiation zone in which a particular project was located (see Figures 2.14 and 2.15). The temperature magnitudes corresponding to the gradient coefficients can be found in Tables 2.1 and 2.2. NCHRP Report 276 also recommended design values for the concrete coefficient of thermal expansion based on aggregate type (see Table 2.3).

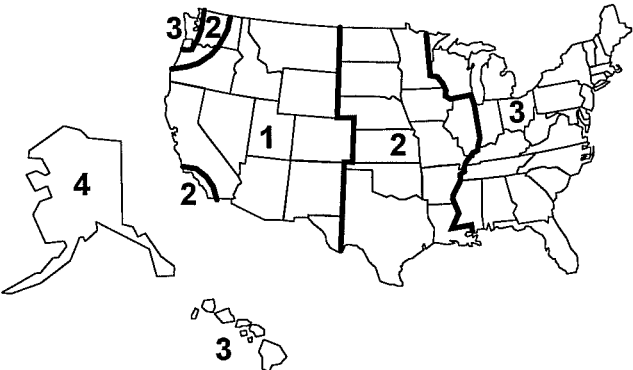
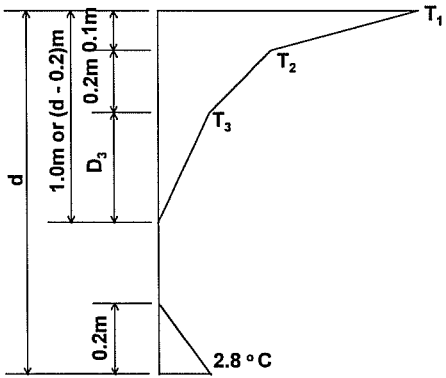


Figure 2.13: Proposed maximum solar radiation zones (after Imbsen, et al [5]).



Note: For superstructure depths greater than 0.61m

Figure 2.14: Proposed positive vertical temperature gradient (after Imbsen, et al [5]).

| Positive Gradients     |                     |                     |                     |
|------------------------|---------------------|---------------------|---------------------|
| Plain Concrete Surface |                     |                     |                     |
| Zone                   | T <sub>1</sub> (°C) | T <sub>2</sub> (°C) | T <sub>3</sub> (°C) |
| 1                      | 30                  | 8                   | 2.8                 |
| 2                      | 26                  | 7                   | 2.2                 |
| 3                      | 23                  | 6                   | 2.2                 |
| 4                      | 21                  | 5                   | 1.7                 |

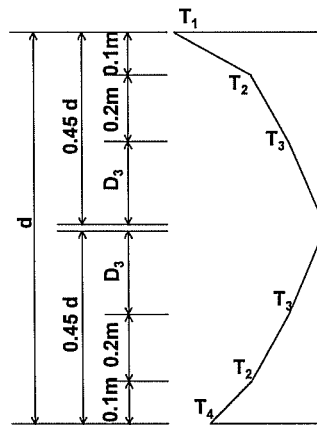
  

| 50 mm Blacktop |                     |                     |                     |
|----------------|---------------------|---------------------|---------------------|
| Zone           | T <sub>1</sub> (°C) | T <sub>2</sub> (°C) | T <sub>3</sub> (°C) |
| 1              | 24                  | 8                   | 2.2                 |
| 2              | 20                  | 7                   | 2.2                 |
| 3              | 18                  | 6                   | 1.7                 |
| 4              | 16                  | 5                   | 1.0                 |

| 100 mm Blacktop |                     |                     |                     |
|-----------------|---------------------|---------------------|---------------------|
| Zone            | T <sub>1</sub> (°C) | T <sub>2</sub> (°C) | T <sub>3</sub> (°C) |
| 1               | 17                  | 5                   | 1.7                 |
| 2               | 14                  | 5.6                 | 1.7                 |
| 3               | 13                  | 6                   | 1.1                 |
| 4               | 12                  | 6                   | 1.1                 |

Table 2.1: Proposed temperature coefficient magnitudes for positive gradients (after Imbsen, et al [5]).



Note: For superstructure depths greater than 0.6 meters

Figure 2.15: Proposed negative vertical temperature gradient (after Imbsen, et al [5]).

**Negative Gradients**

| Plain Concrete Surface |                     |                     |                     |                     |
|------------------------|---------------------|---------------------|---------------------|---------------------|
| Zone                   | T <sub>1</sub> (°C) | T <sub>2</sub> (°C) | T <sub>3</sub> (°C) | T <sub>4</sub> (°C) |
| 1                      | 15.0                | 3.9                 | 1.1                 | 7.8                 |
| 2                      | 12.8                | 3.3                 | 1.1                 | 5.6                 |
| 3                      | 11.7                | 3.3                 | 1.1                 | 4.4                 |
| 4                      | 10.6                | 2.8                 | 1.1                 | 3.3                 |

| 50 mm Blacktop |                     |                     |                     |                     |
|----------------|---------------------|---------------------|---------------------|---------------------|
| Zone           | T <sub>1</sub> (°C) | T <sub>2</sub> (°C) | T <sub>3</sub> (°C) | T <sub>4</sub> (°C) |
| 1              | 12.2                | 3.9                 | 1.1                 | 8.3                 |
| 2              | 10.0                | 3.3                 | 1.1                 | 6.1                 |
| 3              | 9.4                 | 3.3                 | 1.1                 | 5.6                 |
| 4              | 8.3                 | 2.8                 | 0.6                 | 4.4                 |

| 100 mm Blacktop |                     |                     |                     |                     |
|-----------------|---------------------|---------------------|---------------------|---------------------|
| Zone            | T <sub>1</sub> (°C) | T <sub>2</sub> (°C) | T <sub>3</sub> (°C) | T <sub>4</sub> (°C) |
| 1               | 8.9                 | 2.8                 | 0.6                 | 6.7                 |
| 2               | 7.2                 | 2.8                 | 0.6                 | 5.0                 |
| 3               | 6.7                 | 3.3                 | 0.6                 | 4.4                 |
| 4               | 6.1                 | 3.3                 | 0.6                 | 4.4                 |

*Table 2.2: Proposed temperature coefficient magnitudes for negative gradients (after Imbsen, et al [5]).*

| Aggregate Type | Thermal Coefficient of Concrete (0.000001 per °C) |
|----------------|---|
| Quartzite      | 12.8  |
| Quartz         | 11.5  |
| Sandstone      | 11.7  |
| Gravel         | 12.4  |
| Granite        | 9.5   |
| Dolerite       | 9.5   |
| Basalt         | 9.0   |
| Marble         | 4.3 to 7.4  |
| Limestone      | 7.2   |

*Table 2.3: Proposed design values for concrete coefficient of thermal expansion (after Imbsen, et al [5]).*

### 2.3.3 AASHTO LRFD Specification [11] Requirements

According to the 1994 edition of the *AASHTO LRFD Bridge Design Specification* temperature gradient effects are to be examined on a case-by-case basis under six different load combinations as shown in Table 2.4. The load factor  $Y_{TG}$  is to be chosen for each individual project. The commentary suggests basing the load factor on two items: the type of structure and the limit state being investigated. It suggests considering a lower factor for the strength limit states, but gives no example values.

| AASHTO LRFD Load Combinations and Load Factors |                                  |                                  |      |      |      |      |                |          |          |                            |    |    |    |
|--|----------------------------------|----------------------------------|------|------|------|------|----------------|----------|----------|----------------------------|----|----|----|
| Load Combination                               | DC<br>DD<br>DW<br>EH<br>EV<br>ES | LL<br>IM<br>CE<br>BR<br>PL<br>LS | WA   | WS   | WL   | FR   | TU<br>CR<br>SH | TG       | SE       | Use One of These at a Time |    |    |    |
|  |                                  |                                  |      |      |      |      |                |          |          | EQ                         | IC | CT | CV |
| Limit State                                    |                                  |                                  |      |      |      |      |                |          |          |                            |    |    |    |
| STRENGTH-I                                     | $Y_p$                            | 1.75                             | 1.00 | -    | -    | 1.00 | 0.50/1.20      | $Y_{TG}$ | $Y_{SE}$ | -                          | -  | -  | -  |
| STRENGTH-II                                    | $Y_p$                            | 1.35                             | 1.00 | -    | -    | 1.00 | 0.50/1.20      | $Y_{TG}$ | $Y_{SE}$ | -                          | -  | -  | -  |
| STRENGTH-III                                   | $Y_p$                            | -                                | 1.00 | 1.40 | -    | 1.00 | 0.50/1.20      | $Y_{TG}$ | $Y_{SE}$ | -                          | -  | -  | -  |
| STRENGTH-V                                     | $Y_p$                            | 1.35                             | 1.00 | 0.40 | 0.40 | 1.00 | 0.50/1.20      | $Y_{TG}$ | $Y_{SE}$ | -                          | -  | -  | -  |
| SERVICE-I                                      | 1.00                             | 1.00                             | 1.00 | 0.30 | 0.30 | 1.00 | 1.00/1.20      | $Y_{TG}$ | $Y_{SE}$ | -                          | -  | -  | -  |
| SERVICE-III                                    | 1.00                             | 1.00                             | 1.00 | -    | -    | 1.00 | 1.00/1.20      | $Y_{TG}$ | $Y_{SE}$ | -                          | -  | -  | -  |

Table 2.4: Excerpt from AASHTO LRFD Specification [11] "Table 3.4.1-1 - Load Combinations and Load Factors"

The AASHTO Code's positive gradient shape is based on that of NCHRP Report 276 [5]. The code specifies the same solar radiation zones as the report, but the gradient shape is simplified to some extent (see Figure 2.16 and Table 2.5).



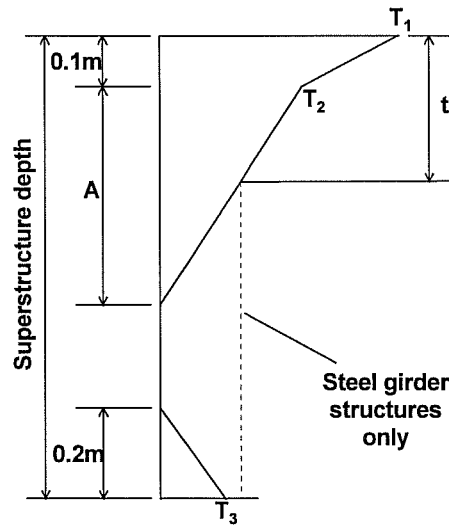


Figure 2.16: AASHTO LRFD Code [11] vertical positive gradient shape.

| Plain Concrete Surface |            | 50mm Asphalt |            | 100mm Asphalt |            |            |
|------------------------|------------|--------------|------------|---------------|------------|------------|
| Zone                   | $T_1$ (°C) | $T_2$ (°C)   | $T_1$ (°C) | $T_2$ (°C)    | $T_1$ (°C) | $T_2$ (°C) |
| 1                      | 30.0       | 7.8          | 23.9       | 7.8           | 17.2       | 5.0        |
| 2                      | 25.6       | 6.7          | 20.0       | 6.7           | 13.9       | 5.6        |
| 3                      | 22.8       | 6.1          | 18.3       | 6.1           | 12.8       | 6.1        |
| 4                      | 21.1       | 5.0          | 16.1       | 5.0           | 12.2       | 6.1        |

Table 2.5: AASHTO LRFD Code [11] positive gradient magnitude values.

The negative gradient shape values specified by AASHTO are the values in Table 2.5 multiplied by -0.5. For both positive and negative gradients, the dimension “A” is specified as:

- 300mm for concrete superstructures that are 400mm or greater in depth
- 100mm less than the actual depth for concrete sections shallower than 400mm
- 300mm for steel superstructures, where  $t$  = concrete deck thickness

Furthermore, the code specifies that the “temperature value  $T_3$  shall be taken as 0.0, unless a site-specific study is made to determine an appropriate value, but shall not exceed 2.8°C” for positive gradients and 1.4°C for negative gradients. There are no code provisions or commentary relating to the use of thermal gradients of any kind in the design of bridge substructures.

### **2.3.4 AASHTO Segmental Specification [12] Requirements**

The AASHTO specification relating to concrete segmental bridges contains the following provision for thermal gradients:

#### **7.4.4 Differential Temperature**

Positive and negative differential superstructure temperature gradients shall be considered in accordance with Appendix A of National Cooperative Highway Research Program Report 276 “Thermal Effects in Concrete Bridge Superstructures” [5].

It also amends the *AASHTO Standard Specifications* [13] load cases by adding the following service load condition:

$$(DL + SDL + EL) + \beta_E E + B + SF + R + S + (DT) \quad (2.8)$$

where: loads in parentheses from the AASHTO segmental specification, all others from *AASHTO Standard Specifications* [13].

DL = structure dead load

B = buoyancy

SDL = superimposed dead load

SF = stream flow pressure

EL = erection loads at end of construction

R = rib shortening

E = earth pressure

S = shrinkage

$\beta_E$  = earth pressure coefficient

DT = thermal gradient loading

The segmental specification states that for any load combination that includes full live load with impact the load DT may be reduced by 50%. Also, the load T (temperature loading) in the standard specification is redefined as:

$$T = (TRF + DT) \quad (2.9)$$

where TRF is equivalent to the original T loading. There are no provisions for the application of temperature gradient loading to substructures in the AASHTO segmental specification.

### **2.3.5 Roberts [7]**

A comprehensive set of temperature measurements were made with thermocouples installed in several segments of the downtown San Antonio “Y” segmental viaduct project. Readings were taken continuously from July 1992 through July 1993. Roberts reported a maximum positive gradient magnitude of 50% of the AASHTO segmental specification for a segment with no asphalt topping, and 78% of design values with a 50 mm thick asphalt layer. The general shapes of the measured positive gradients were quite similar to those of the code specifications. The maximum measured negative gradient magnitude was about 65% of the design value for an untopped segment, but was reduced to only 50% after the addition of the 50 mm topping. Again, the shape of the measured negative gradient was similar to that of the design gradient.

Based on this large set of measured temperatures, Roberts suggested the following temporary provisions to the AASHTO segmental specification requirements (with changes in italics):

#### **7.4.4 Differential Temperature**

Positive and negative differential superstructure temperature gradients *shall be taken as 80% of the values represented* in Appendix A of National Cooperative Highway Research Program Report 276 “Thermal Effects in Concrete Bridge Superstructures” [5]. *Alternatively, site specific thermal gradients, developed based on the climatic conditions in the area and the actual material properties of the structure, may be substituted for the current design gradients.*

Roberts also suggested an addition to the commentary section 7.4.4. as follows:

*The currently recommended design thermal gradients, both positive and negative, have not been substantiated with field data. The data collected to date indicate that the design gradients may be overly conservative.*

In addition to this new wording, Roberts also outlined suggested changes in allowable stress requirements. Current allowable stress levels force designers to use additional post-tensioning to eliminate small areas of tension in the top and bottom flanges of a member subjected to self-equilibrating stresses from negative temperature gradients. Roberts’ proposed changes would relieve designers of the requirement to account for these stresses.

Finally, Roberts recommended that stresses due to temperature gradients be eliminated from all ultimate strength load cases by the application of a load factor of

zero to the DT term defined previously. Roberts highlighted the need for additional field temperature measurements as well as thermal studies on cracked sections. However, no suggestions were made for the application of thermal gradients to hollow bridge piers.

## 2.4 PREVIOUS BRIDGE PIER TEMPERATURE STUDIES

### 2.4.1 General

A literature search performed by the author provided no indication that studies on the effects of non-linear temperature gradients on hollow concrete piers have ever been performed in the United States. However, at least two previous authors addressed temperature effects on bridge piers with solid cross-sections.

### 2.4.2 Stephenson [14]

An early model for the flow of heat through a tall slender concrete pier and the induced forces it caused was provided by Stephenson [14]. From observations of solar radiation, Stephenson suggested that the variation of solar energy in a daily cycle was basically sinusoidal. Thus, the heat flow, H, varied according to:

$$H = \sqrt{\omega \frac{C}{R}} \quad (2.10)$$

where:  $\omega = \frac{2\pi}{T}$

T = period of oscillation

C = thermal capacity per unit area

R = thermal resistance per unit area

The quantity  $\frac{C}{R}$  was a multiple of density, specific heat, and thermal conductivity.

Stephenson suggested that the sinusoidal variation of heat flow also involved a phase angle (given as 45° for good quality concrete) representing the time lag between a

change in temperature and the flow of heat through the column. Surface absorptivity was also accounted for in the model.

Stephenson also suggested that the temperature through the column's section (i.e., the non-linear temperature gradient) could be described as an exponential function:

$$T(x) = T_0 e^{-ax} \quad (2.11)$$

where:  $T_0$  = variation of temperature from the mean temperature at the irradiated surface

$x$  = distance from the irradiated surface of the column

$$a = \sqrt{\frac{\omega CR}{2}}$$

The strain at any point in the column was then calculated using the equation:

$$\frac{\partial L}{L} = T\alpha = T_0 \alpha e^{-ax} \quad (2.12)$$

Stephenson also recognized that plane sections must remain plane under strains induced by the exponential temperature distribution. This was accounted for by equating the moment of the strain diagram about the shaded side of the column's cross-section with depth "d":

$$T_0 \alpha \int_0^d e^{-ax} (d - x) dx \quad (2.13)$$

with the moment of the area of the final, triangular strain distribution:

$$\alpha T_1 \frac{d^2}{3} \quad (2.14)$$

where  $T_1$  is the temperature at the irradiated side. This equation yielded an expression for the radius of curvature of the unrestrained member:

$$d \frac{L}{\partial L} = \frac{d}{T_1 \alpha} \quad (2.15)$$

Stephenson then found the column tip deflection with:

$$\Delta_{\text{tip}} = \frac{H^2}{2r} \quad (2.16)$$

where  $r$  was the radius of curvature of the column under differential thermal load and  $H$  was the height of the column. The induced stress due to a longitudinal restraint at the top of the column could then be calculated as:

$$f_{\text{bc}} = \frac{3\Delta_{\text{tip}}yE}{H^2} \quad (2.17)$$

### **2.4.3 Andres [1]**

Although primarily concerned with the flow of forces through an unusually-shaped concrete pier (see Figure 2.17), Andres also tracked the temperature characteristics and resulting stresses induced in that pier. The work was part of the first phase of the U.S. 183 Instrumentation Project.

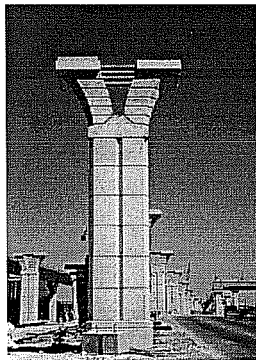


*Figure 2.17: Unusually-shaped mainlane pier, U.S. 183 segmental viaduct.*

Andres described one model of the stresses induced in a monolithic pier section as analogous to the bronze-encased steel bolt shown in Figure 2.18. Each material responds differently to uniform temperature changes due to their differing coefficients of thermal expansion. Similarly, the pier's shaft can be described with two different material responses due to the extreme differences in temperature between the "core" and "shell" concrete (see Figure 2.19).

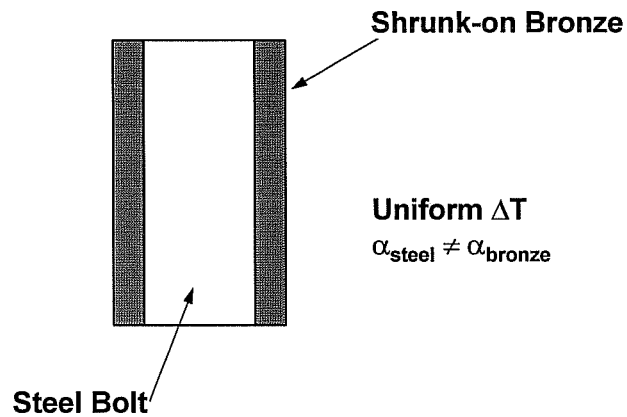


Figure 2.18: Bronze-encased steel bolt undergoing uniform temperature change.

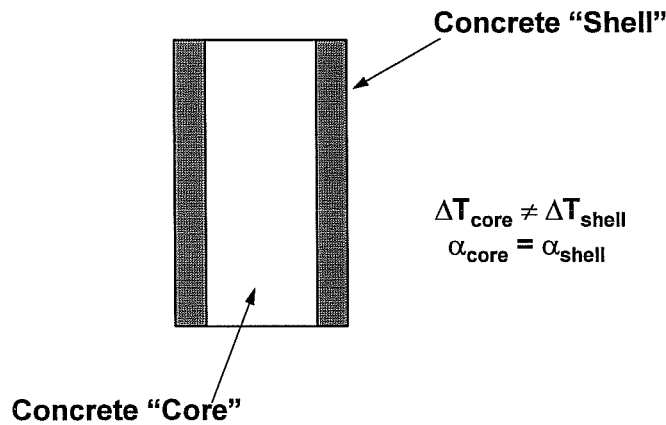


Figure 2.19: Concrete pier model undergoing differential temperature change.



The outer shell will tend to expand due to heating, pulling the core along with it. Compressive stresses then occur in the shell while tension develops in the core area. Using this approach, Andres found that compressive stresses induced in the shell concrete due to temperature were of the same order of magnitude as those induced by the viaduct's superstructure dead load.

The data indicated large temperature gradients across the monolithic cross-section of the pier, but thermocouples were installed in only one quadrant of the pier's cross section, making determination of the gradient shape impossible.

## 2.5 *PRECAST SEGMENTAL PIERS IN NORTH AMERICA*

Although no research into the effects of temperature gradients on hollow, precast bridge piers has been performed, construction of bridges with substructures of this type is increasing. An overview of projects involving precast, segmentally constructed bridge piers is presented here as anecdotal evidence of their importance. This list is representative but not inclusive.

### **2.5.1 Long Key Bridge**

The Long Key Bridge, designed by Figg and Muller Engineers of Tallahassee, Florida, was completed in 1980 and featured 3701 meters of bridge deck consisting of 36-meter spans built by the span-by-span method. It is located 145 km south of Miami in the Florida Keys [15]. The structure stands out as one of the first long over-water applications of precast segmental construction in North America. The piers had an unusual "V" shape and were precast at the contractor's casting yard (see Figure 2.20). The V-piers were post-tensioned to the bridge superstructure and were designed to act monolithically with it. Precasting the unusually shaped piers enhanced construction quality and eliminated the need for complex formwork to be installed over the water.

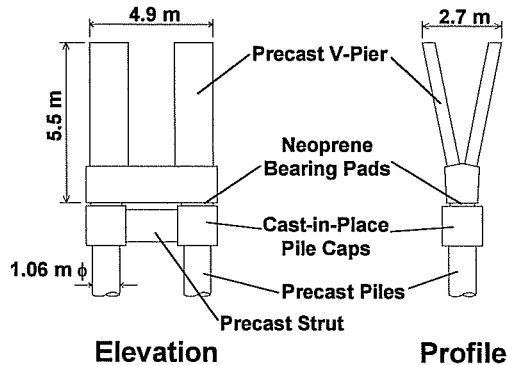


Figure 2.20: Unusual V-shaped piers, Long Key Bridge

### **2.5.2 Seven-Mile Bridge**

The Seven-Mile Bridge, also designed by Figg and Muller Engineers, was completed in 1982. It featured 41-meter spans constructed by the span-by-span method. In an unusual move, the contractor decided to partially post-tension each span on a barge before erection and then lift the entire span into place. This lengthy project stretched 10.9 km between two islands in the Florida Keys.

Most of the project's substructure consisted of cast-in-place twin-shaft units. Higher level piers on the project were constructed from precast concrete segments with rectangular cross-sections and post-tensioned vertically [16,17]. Pier segments featured five voided cells in their cross-sections. Pier heights for the segmentally constructed piers ranged from 8.2 meters to 19.8 meters.

### **2.5.3 Dauphin Island Bridge [18]**

The Dauphin Island bridge is a 5430-meter long structure located about 80 km south of Mobile, Alabama. It serves to connect Dauphin Island in the Gulf of Mexico with the mainland United States, and replaced a 24-year-old bridge that was destroyed in a hurricane that struck the area in 1979. The new bridge was completed in 1982

after two years of construction. About 80% (4240 m) of the bridge's length consists of short-span (20 m) monolithically precast girder-and-deck segments. The bridge also features a 250-meter three-span unit built in balanced-cantilever with precast segments with a middle main span reaching 120 meters. The approaches for the main unit consist of twenty-six spans of 36 meters each built span-by-span with precast segments.

The designer, Figg and Muller Engineers, elected to use hollow, rectangular precast pier segments for the substructure of the segmentally constructed approach spans. Altogether, 174 precast box pier segments were used to construct piers ranging in height from 7 to 27 meters. Each pier segment was 4.88 x 2.44 x 2.74 meters high with 250 mm thick walls (see Figure 2.21). They were vertically match cast at the project's precasting plant located in Mandeville, Louisiana and barged to the bridge site. Epoxy was placed in the joints between segments during erection of the precast piers, which were then post-tensioned vertically.

The designers chose to use precast pier segments to hasten construction. Pier segments could be precast in the yard and readied for erection concurrent with construction of the shorter monolithic spans. Also, shipment of precast segments was quite economical by barge, and prevented the need to transport large amounts of fresh concrete over water to the site.

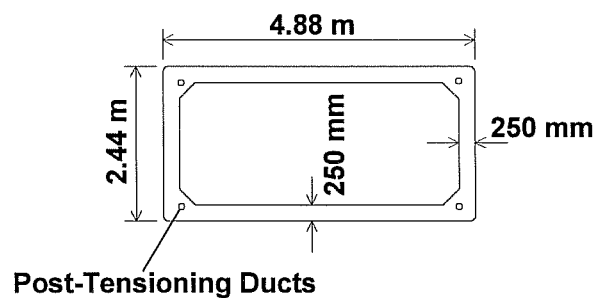


Figure 2.21: Cross-section of precast segmental piers, Dauphin Island bridge.

#### **2.5.4 Sunshine Skyway Approaches**

The Sunshine Skyway Bridge is a cable-stayed structure featuring a concrete, trapezoidal box girder and a main clear span of 366 meters. It was designed by Figg and Muller Engineers. Construction of the 6.7 km long bridge was completed in 1987. It links St. Petersburg with Bradenton across Tampa Bay on the west coast of the Florida peninsula.

Most of the approaches to the cable-stayed main span were constructed with AASHTO girders, but higher level approaches were built with trapezoidal-box precast segments. The piers supporting these 41-meter spans were precast box segments. A total of 606 substructure segments were produced and used in piers ranging in height from 8 to 41 meters. All segments were cast at Port Manatee and barged approximately 6.4 km to the bridge site [19].

#### **2.5.5 Neches River Bridge [2]**

The Neches River Bridge is a cable-stayed structure located in southeastern Texas. It was originally designed as a box girder bridge by the Texas Department of Transportation but was redesigned for the contractor by Figg and Muller as a cable-stayed bridge which incorporated precast segmental piers. Several of the piers were only used temporarily during construction, and were therefore easier to dismantle than cast-in-place piers when the bridge was completed in 1986. Due to the remote location of the bridge site, precast substructures eliminated the need to build a large scale concrete batch plant on-site. Typical segments were 3 meters long, with approach pier heights reaching 40 meters. The main pylons were 96.6 meters high. The cross-sections for the pylons and the approach piers are shown in Figures 2.22 and 2.23.

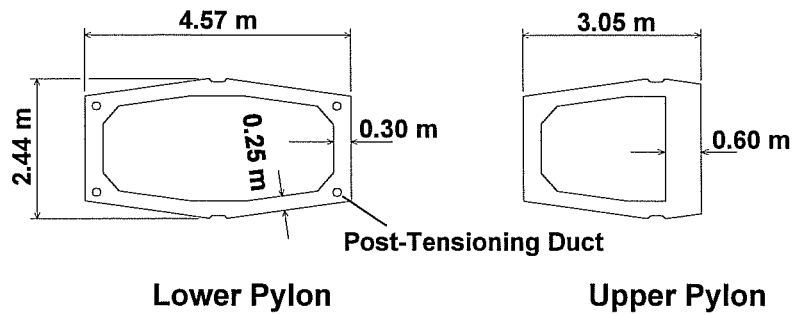


Figure 2.22: Segmental pylon cross-sections, Neches River Bridge.

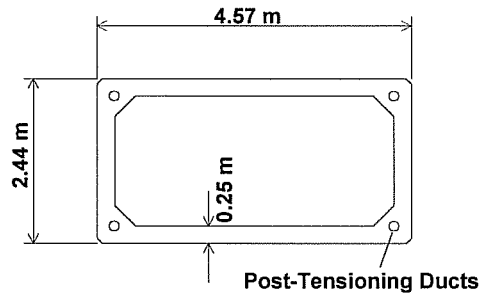


Figure 2.23: Segmental approach pier cross-section, Neches River Bridge.

### **2.5.6 Linn Cove Viaduct**

Completed in 1983, the Linn Cove Viaduct formed the last link in the Blue Ridge Parkway located in a popular recreation area in North Carolina. The 379-meter long structure winds along the face of Grandfather Mountain, an environmentally-sensitive area in the Blue Ridge Mountains [20]. The bridge was designed by Figg and Muller Engineers and was constructed using the method of progressive placement. This method involved cantilevering the front of the bridge forward along the route by the addition of superstructure segments. When the location of a pier was reached, precast pier segments were placed by a crane located at the cantilevered tip of the bridge superstructure. Because of the 55-meter length of several of the spans,

temporary bents were placed in the same manner when the bridge superstructure reached midspan to reduce moments due to cantilever bending [21].

The pier segments were precast with an unusual cross-sectional shape (see Figure 2.24). The segments were match cast at a facility located at one end of the bridge. Segments were cast in both 1.8- and 2.7-meter lengths, and were bonded with epoxy during erection. After placement of the cap segment was complete, the pier was post-tensioned with eight tendons consisting of 12 ~ 13mm strands each. The tendons followed ducts from the top of the pier through and out the side of the cast-in-place footing [22].

The use of precast pier segments greatly reduced the environmental impact of the construction activity. It also enabled the constructor to work completely from the top of the bridge during pier erection.

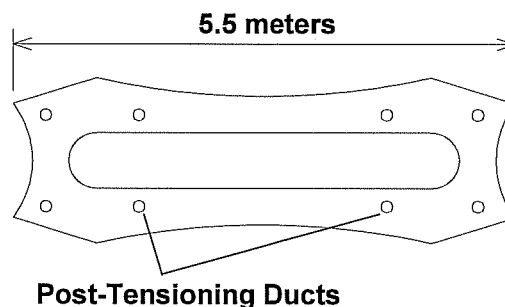


*Figure 2.24: Pier cross-section - Linn Cove Viaduct*

### **2.5.7 Wando River Bridge [23]**

The Wando River Bridge is located on Interstate 526 near Charleston, South Carolina. It was designed by Figg and Muller. Construction of this 2500 meter long dual-span bridge was completed in 1988. Typical approach spans were 46 meters in length while the cantilevered main spans were 122 meters long.

The piers consisted of rectangular precast segments typically 3 meters in length. They were built in heights up to 41 meters to provide navigable clearance for ship traffic on the river. For piers located in the river, the hollow sections were filled with concrete in the bottom 15 meters. This provided additional resistance to ship impact. All precast segments were barged directly to the bridge site and lifted into place with a barge-mounted crane. For this project, the use of precast piers mitigated potential environmental problems in the surrounding wetlands.

#### **2.5.8 James River Bridge [24]**

This 1426 meter long bridge is located near Richmond, Virginia and was completed in 1989. This innovative cable-stayed structure features a 192-meter main span with 46-meter approach spans. Span-by-span construction was used to erect the approach spans, and the deck was cantilevered from the pylons outward during construction of the main span.

Precast, segmental piers with rectangular cross-sections were used for the approaches. Each segment had dimensions 2.4 x 5.5 x 4.3 meters high, and pier heights ranged from 19.5 to 43.9 meters. In addition, the main pylons were cast in place up to the level of the deck, with the remaining height comprised of precast segments.

#### **2.5.9 Chesapeake and Delaware Canal Bridge [25]**

This major new concrete cable-stayed bridge was completed in late 1995. It crosses the Chesapeake and Delaware Canal near St. Georges, Delaware on State Route 1. The main span is 229 meters in length, and the entire structure is 1417 meters long. The bridge consists of precast segmentally constructed 46 meter long approach spans built using the span-by-span method with an overhead gantry, as well as the main cable-stayed span comprised of the same trapezoidal segments.

While the main pylons were cast-in-place, the piers for the approach spans were constructed of precast rectangular box segments. The pier segments were 2.44 x 5.50 meters in size and were built in 1.22, 1.52, 1.83, and 3.05 meter lengths. Two pier segments were match-cast per day at the casting yard located 290 km to the south in Cape Charles, Virginia. Segments were barged directly to the bridge site. The approach span piers used a total of 463 precast segments and ranged in height up to 42 meters. The piers were post-tensioned after erection with 12 and 19 ~13 mm strand tendons (see Figure 2.25).

The use of precast segmental piers enabled constructors to take advantage of the relatively inexpensive barging costs to transport segments. They also served to speed up erection time. The hollow cross-section of the piers allowed designers to reduce the number of precast piles supporting the piers and the size and cost of the foundations.

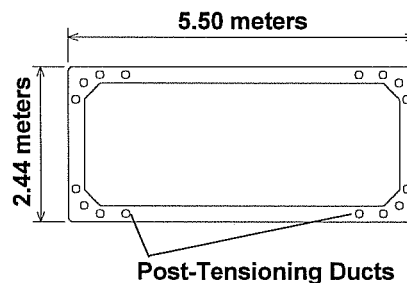


*Figure 2.25: Cross-sectional dimensions of approach-span piers, Chesapeake and Delaware Canal cable-stayed bridge.*

### **2.5.10 Louetta Road Overpass**

The Louetta Road Overpass of State Highway 249, located in Houston, Texas, is an experimental bridge with several unique characteristics. Designed by the Texas Department of Transportation (TxDOT), it is scheduled for completion in 1996. The



bridge features the new “U54” precast, prestressed trapezoidal beam developed by TxDOT to increase span lengths and enhance aesthetics of urban highway bridges. In addition, the overpasses use precast, hollow, segmentally constructed piers. The entire project features extra-high-strength concrete with compressive strengths ranging from 70 to 90 MPa to decrease material usage and increase durability and impermeability [26].

The precast segmental piers consist of a small cast-in-place base, several 1.5-meter high column segments, and a 1.1-meter high ornamental capital segment. Pier heights range from 5.5 to 6.0 meters. The typical cross section of the pier is shown in Figure 2.26 [27]. According to Ralls and Carrasquillo [26], the use of this hollow section with thin walls was necessary to take full advantage of the extremely high concrete strength required for the project. In addition, this structure presented an opportunity for TxDOT to explore the feasibility of precast segmental piers in commonly used highway overpasses [2].

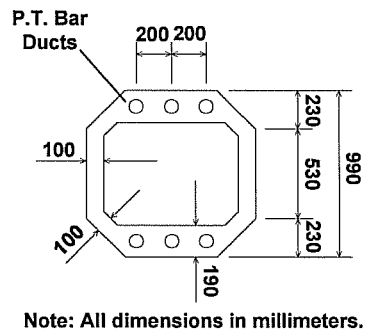


*Figure 2.26: Segmental pier cross-section, Louetta Road Overpass.*

### **2.5.11 Northumberland Strait Crossing**

This 12.9-km long structure is located between Prince Edward Island and the mainland at New Brunswick, in eastern Canada. The bridge was designed in a joint venture with J. Muller International and SLG/Stamley. When completed in 1997, it will

be one of the longest over-water crossings ever built using precast segmental technology. The bridge was constructed with twenty-one precast segmental approach spans averaging about 90 meters in length and built in balanced-cantilever. Also, the main bridge consists of 43 spans of 250 meters in length. The main spans were built using cast-in-place balanced cantilever techniques in the precasting yard, and lifted and placed as entire cantilever girder units weighing nearly 79,600 kN by a special floating crane supplied by Dutch contractors [28].

The piers were match-cast in the precasting yard in three large units: the pier base, the pier shaft with a conical ice shield, and a special “template” segment. Pier bases were cast in two separate sizes depending on the water depths at their locations and had maximum heights of 42 meters. The pier shafts were precast in heights up to 50 meters. They consisted of a 20-meter diameter conical ice shield located at the bottom of the shaft and a variable height shaft section. The pier shaft varied from an octagonal section at the ice shield to a rectangular section at the top. A rectangular “template” segment was match cast between the pier shaft and the massive cantilever girder unit described above. In this way, constructors could control the alignment of the bridge superstructure by simply varying the geometry of the template segment (see Figure 2.27). The piers were post-tensioned after their erection in the strait to provide structural continuity [29].

The use of precast components for this massive structure enabled constructors to continue work even during the eight months of the year that the strait is icebound. The relatively short four-month window of opportunity for erection in the strait could therefore be used in an efficient manner. The entire bridge is projected to be completed within only four years in this particularly harsh construction environment [28].

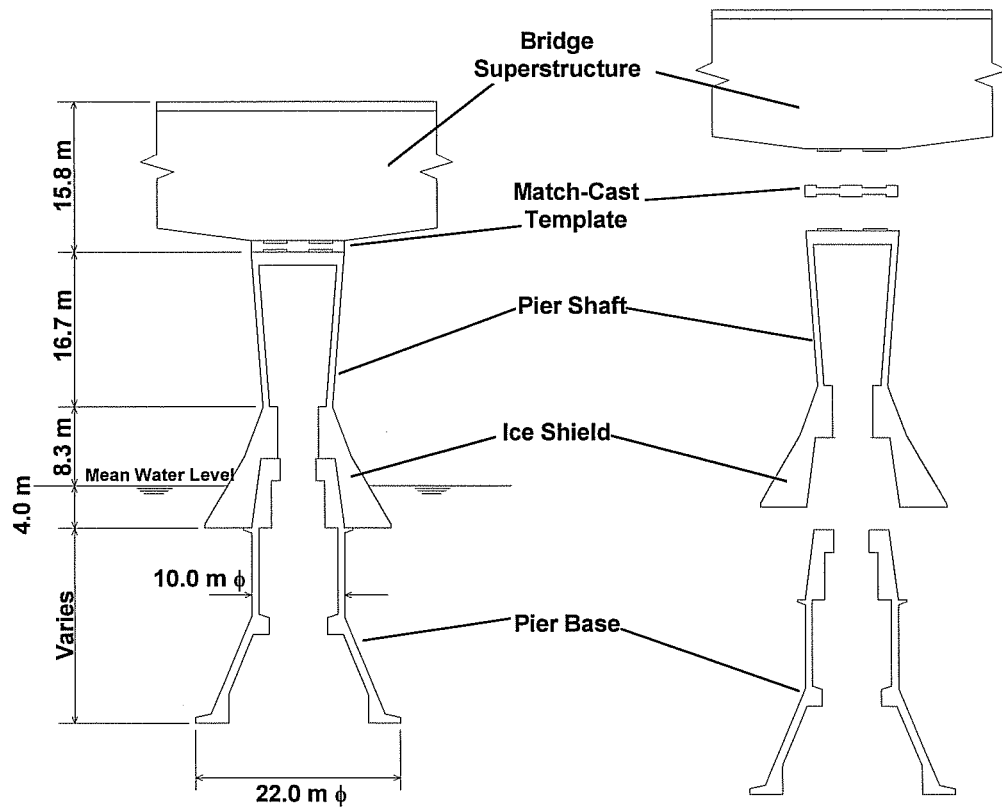


Figure 2.27: Elevation view of pier components, Northumberland Strait Crossing.

## CHAPTER 3

### *PIER INSTRUMENTATION*

#### *3.1 INSTRUMENTATION OBJECTIVES*

The location of the U.S. 183 segmental viaduct in close proximity to The University of Texas at Austin's Phil M. Ferguson Structural Engineering Laboratory provided researchers there with an excellent opportunity to instrument and monitor a major concrete segmental bridge (see Figure 3.1). Furthermore, the U.S. 183 project provided an unusual opportunity to conduct research on a precast, segmentally constructed, hollow box, concrete bridge pier. The segmental piers on the U.S. 183 viaduct will support a portion of one flyover access ramp to be built using the balanced-cantilever method of construction. Thus, instrumenting one of these piers will enable researchers to measure pier strains induced by this construction method.

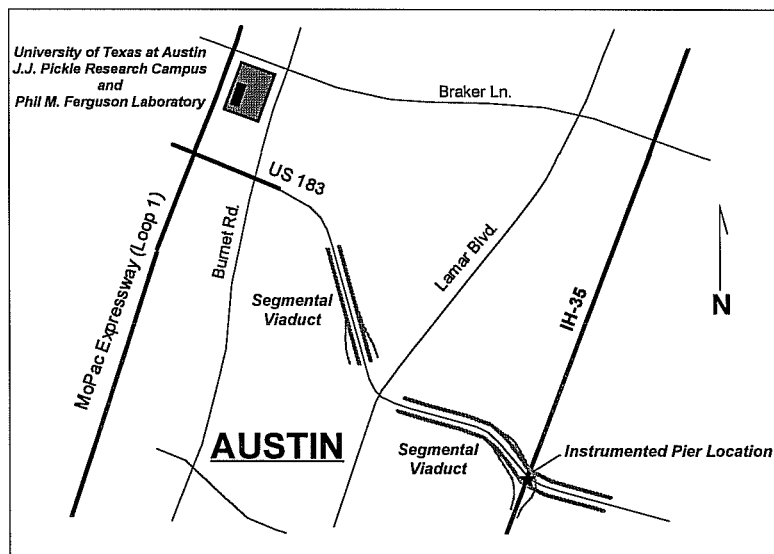


*Figure 3.1: Map showing location of research facilities relative to U.S. 183 viaduct.*

The main objectives of the instrumentation of a segmental pier were as follows:

1. Measure the sunlight-induced temperatures across the hollow-box cross section.
2. Measure the corresponding strain changes due to the temperature gradients.
3. Determine the flow of forces from the post-tensioning of the pier.
4. Measure the strain changes in the pier during balanced-cantilever superstructure erection.
5. Determine the dead load and post-tensioning force paths through the capital segment into the column during superstructure erection.

### *3.2 PIER SELECTION*

The only part of the U.S. 183 project using the large ramp pier was ramp “P”, a high flyover ramp to be built using the balanced-cantilever method of construction. The highlight of the ramp was a 5-span unit with spans of 38.1m - 54.9m - 43.3m - 54.9m - 38.1m. As shown in Figure 4.2, pier P15 was located between a 54.9-meter span and the center 43.3 meter span, and was originally selected for instrumentation in order to track the most critical construction loads. However, pier P15 was not the optimal choice for temperature gradient effects because of its location between the north- and south-bound viaducts of the U.S. 183 mainlanes; the new bridges would prevent most of the sunlight from striking the pier.

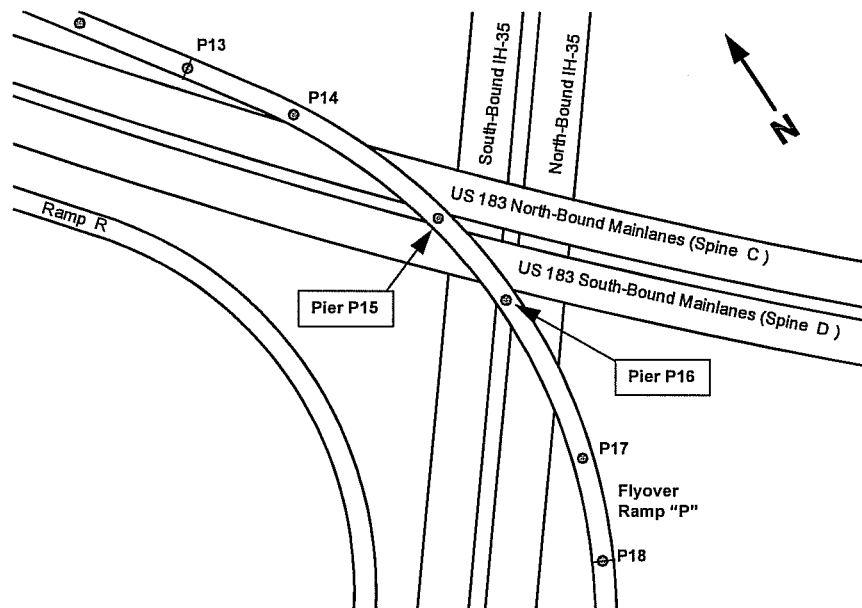


Figure 3.2: Bridge layout in the U.S. 183 and IH-35 interchange area.

Selection of the pier to be instrumented therefore involved a compromise between a location best for construction stresses and a location ideal for temperature gradients. Pier P16 was selected because it satisfied this compromise. It was located between the other 54.9-meter span and the middle 43.3-meter span where high bending moments would be introduced during balanced-cantilever erection of the ramp superstructure. It was situated just south of the south-bound U.S. 183 mainlane viaduct, where sunlight could strike most of the length of the pier unhindered, providing the maximum possible temperature gradients.

### 3.3 GAUGE TYPES

#### **3.3.1 Concrete Strain Gauges**

In areas where the concrete is not expected to crack, such as in the column or compression struts, strains could be measured using a prefabricated concrete strain

gauge. Development of this type of gauge and a more detailed description of several types of concrete strain devices was performed by Arréllaga [30].

The concrete strain gauge was simply an electronic strain gauge mounted on a small diameter steel rod and embedded in the concrete. A series of tests was performed at an earlier stage of the U.S. 183 instrumentation project to determine the most effective and accurate concrete strain gauge possible. This series of tests was described by Andres [1]. The type of concrete strain gauge described below has been found to be extremely durable and accurate.

The concrete gauges used for instrumenting the large ramp pier P16 were prefabricated at the Ferguson Structural Engineering Laboratory. They consisted of a cold-rolled steel round approximately 235mm in length and 4.75mm in diameter. A length of approximately 20mm on each end of the round was threaded so that a small washer and nuts could be attached. These washers provided positive anchorage in the concrete and ensured strain compatibility between the steel round and the concrete surrounding it. The washers were placed such that the effective gauge length was 203.2mm. At the middle of the gauge length, a small  $350\Omega$  electronic strain gauge was carefully attached to the steel round, which was previously cleaned of any corrosion products.

An electronic strain gauge works on the principle that changing the length of a wire also changes the resistance across that wire. As shown in Figure 3.3, as the gauge is loaded, the wire in the gauge elongates, causing the resistance across the gauge to increase. This change in resistance can be measured by data recording instruments.

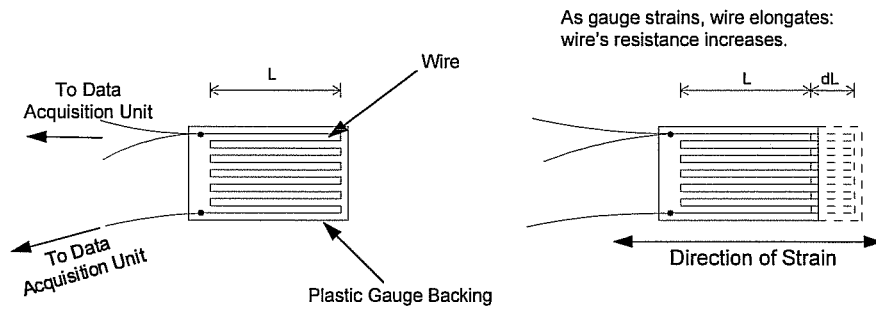


Figure 3.3: An electronic strain gauge.

Electronic strain gauges and their leadwires tend to be extremely fragile: great care was taken to prevent the infiltration of water or corrosive agents and to protect the gauge from impact. Each electronic gauge was painted with a layer of acrylic and covered by a piece of pliable butyl rubber. Most of the steel rod was then wrapped in plastic shrink-tube to interrupt the steel-to-concrete bond to control the 203.2-mm gauge length. In order to prevent infiltration of moisture, each end of the shrink tube was coated in watertight Sikadur™ segmental bridge epoxy. Figure 3.4 illustrates the concrete strain gauge.

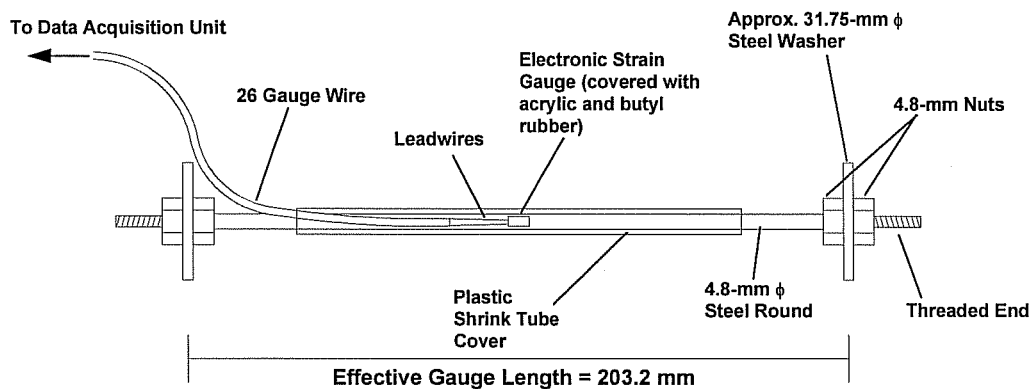


Figure 3.4: Concrete strain gauge.



### **3.3.2 Steel Strain Gauges**

Concrete strain gauges of the type described above are not as accurate for strain measurements in areas where the concrete is in tension and may crack. Therefore, in some tension areas of the pier, electronic gauges were installed directly onto the reinforcing steel cage at the casting yard. This technique was used previously in the project with success [1].

For each instrument a small, flat area on the surface of the reinforcing bar was polished clean to ensure a good bond between the electronic gauge and the steel. After attaching the leadwires to the gauge, the entire gauge was painted with a protective acrylic coating. This coating helped to prevent a short in the gauge by ensuring that no contact was made between the metal of the leadwires and the steel reinforcement. Finally, a protective piece of butyl rubber coated by a layer of segmental bridge epoxy covered the gauge, giving it some measure of impact resistance. Figure 3.5 shows part of the process of installing steel strain gauges.

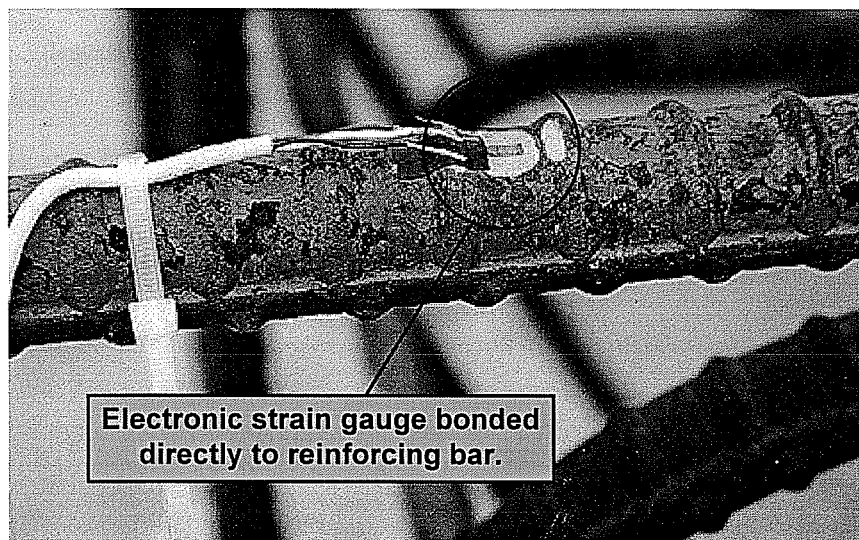


*Figure 3.5: Installation of an electronic strain gauge directly onto the reinforcing bar.*

### 3.3.3 Thermocouples

The measurement of temperature in the concrete was achieved by the use of thermocouples. The accuracy and ease of installation of these instruments made them ideal for use in sometimes harsh field conditions.

A thermocouple consists of a wire with two dissimilar metals shielded from each other (see Figure 3.6). When the two metals are brought into contact with one another, the voltage drop across the connection varies as the temperature surrounding the connection changes. However, a standard voltmeter cannot be used to read the voltage across the connection because the connection at the voltmeter itself would alter the apparent temperature reading [30]. The data acquisition systems used on this project provided connections with known reference temperatures and automatically compensated for the second connection. Several types of thermocouple wire are available, but type T wire was chosen for this project. The two dissimilar metals in type T wire are copper and constantan, both of which hold up relatively well in the corrosive environment of curing concrete [1].

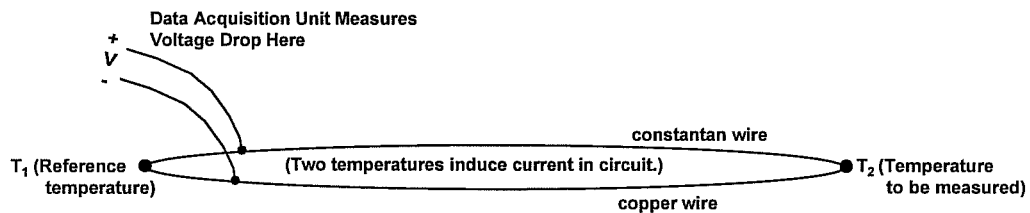


Figure 3.6: Diagram of a Type T thermocouple.

### 3.4 OVERALL INSTRUMENTATION PLAN

In order to assess the axial and bending stresses associated with both temperature fluctuations and construction loads, strain gauges were placed at three column sections along the pier's height and were distributed throughout the capital

segment PC16-8. All three column sections contained concrete strain devices oriented vertically. With these instruments, one can track the bending strains due to balanced-cantilever construction moments, axial forces, and nonlinear stress distributions caused by temperature gradients across the pier's box section.

In addition to the longitudinal gauges, concrete strain devices were placed normal to the pier's primary axis at all three shaft sections. Arranged regularly around the outside face of the pier, these gauges were meant to capture any strains that might occur under axial loading due to the Poisson effect. Gauges were also oriented horizontally in some areas to measure strains in tensile ties that were expected to occur during post-tensioning.

Thermocouples were placed in all three shaft sections and the capital. However, only the middle section located in segment PC16-5 has a sufficient distribution of thermocouples to measure temperature gradients across the pier section. This placement was the most practicable for assessing the maximum possible temperature gradient. A lower section would have had sunlight blocked by the IH-35 overpasses nearby; a higher section would have sunlight blocked by the balanced-cantilever ramp superstructure. Figure 3.7 illustrates the sections of the pier that were instrumented and their relative positions to other structures nearby.

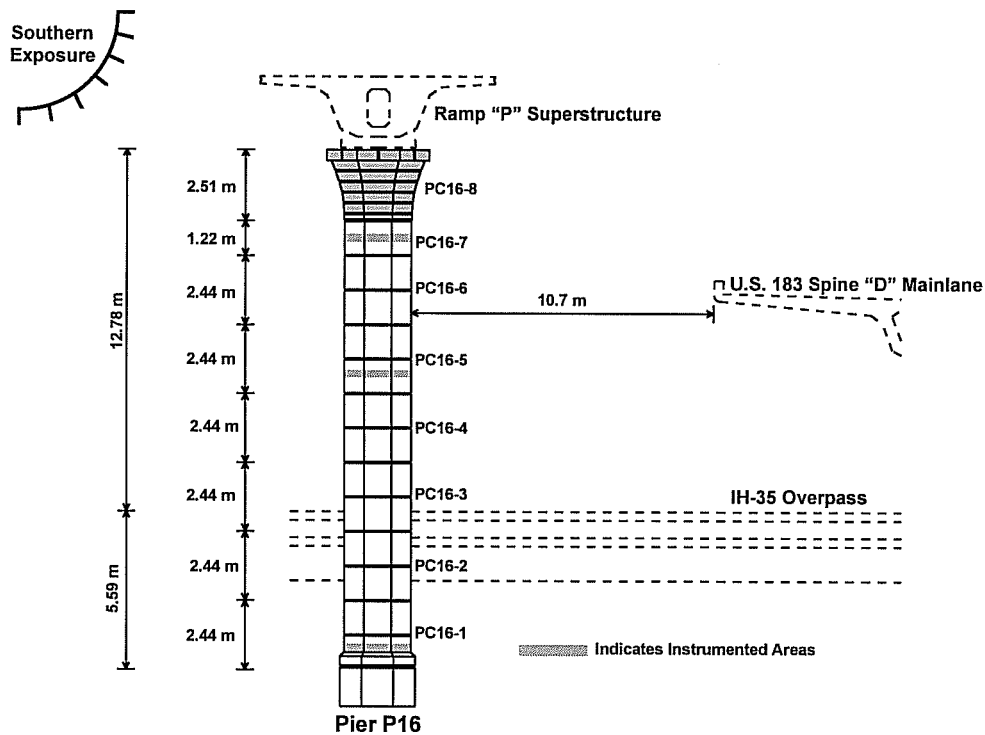


Figure 3.7: Instrumented areas of pier P16 relative to surrounding structures' locations.

### 3.5 "BASE" SEGMENT PC16-1 GAUGE LOCATIONS

#### 3.5.1 Concrete Strain Gauges

Concrete strain gauges were placed in the base segment PC16-1 in the configuration shown in Figure 3.8. Segment PC16-1 concrete gauges were numbered using the designation Cxxx where "C" denotes "Concrete Strain Gauge" and the corresponding number is the gauge number. In this case, gauges were numbered C400 through C419. The set of gauges was located just above the upper edge of the cast-in-place concrete base. The vertically oriented gauges, such as C400, C402, C409, etc. were installed to measure the strains due to bending moment and axial force at the base of the pier. Base moments would be critical during the balanced-cantilever erection of

the ramp superstructure. The horizontally oriented gauges C401, C406, C411, and C416 were added to measure any “hoop”-type stresses that may occur under axial loads such as post-tensioning loads and superstructure dead loads.

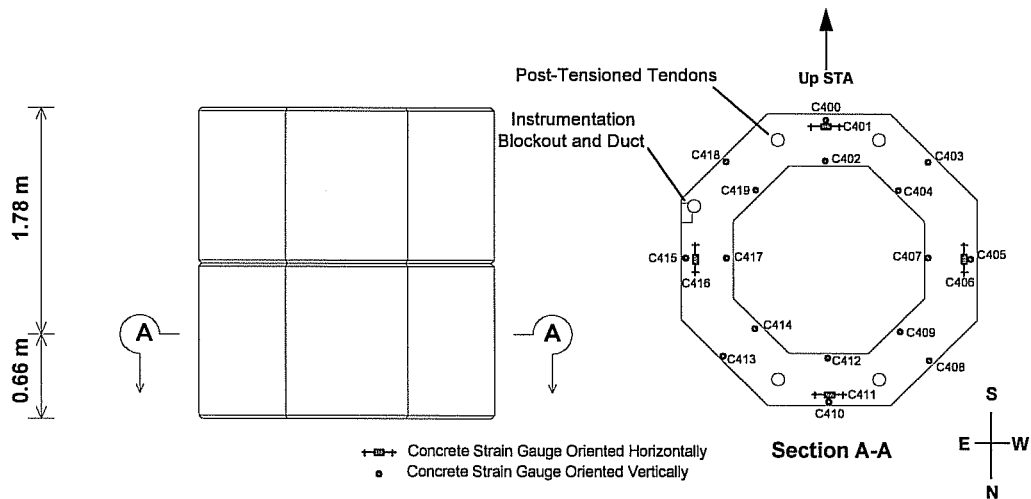
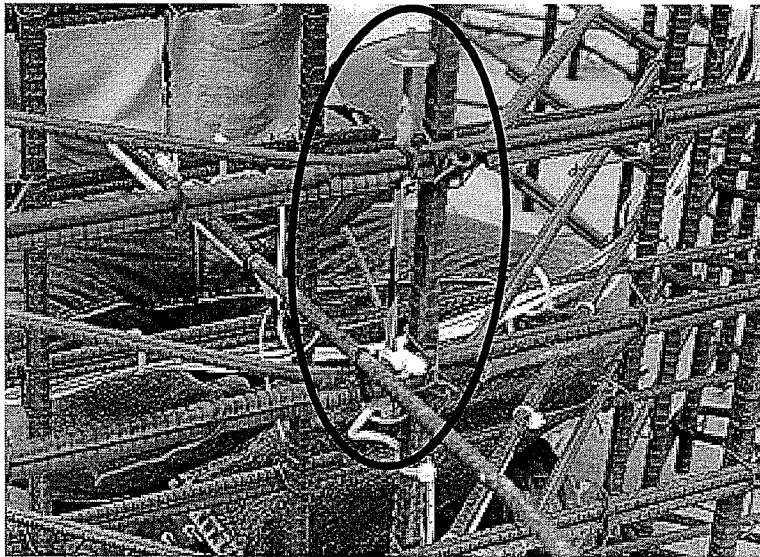


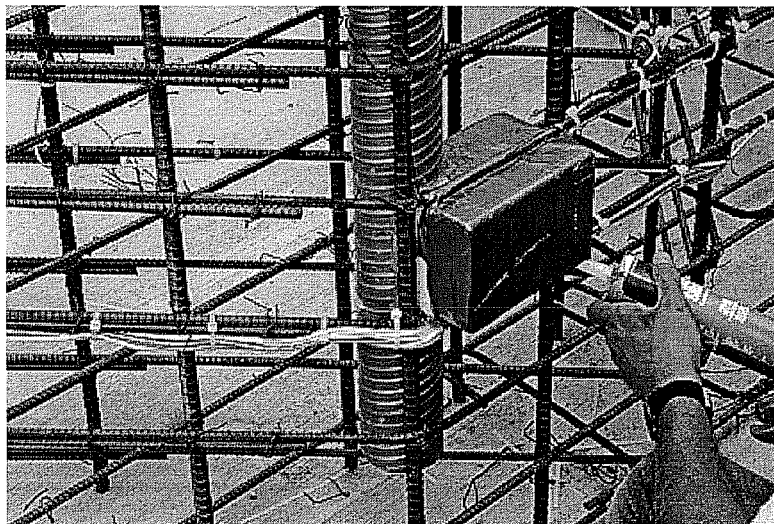
Figure 3.8: Concrete gauge locations in base segment PC16-1.

Figure 3.9 illustrates concrete gauges as they appear installed in the segment’s rebar cage. Concrete gauges were tied directly to the reinforcement. In this case, the reinforcement pattern was conducive to the gauge placements desired, and very few extra bars were needed to place the gauges. However, in some situations, gauges were required in areas where no bars could be used to attach them. In these cases, small bars or welded wire mesh were installed as a platform for the concrete gauges. After gauge placement, each gauge’s wires were securely tied to the rebar cage and routed to a small blockout at one corner of the segment, following the rebar cage along the way. In this way, researchers could access the wire ends to splice wires capable of reaching to dataloggers at a later time. After casting was complete the segments were stored in the casting yard for as long as ten months. Figures 3.10 and 3.11 show the blockout before and after segment casting. In Figure 3.10, note the metal conduit running

vertically from the blockout. After pier erection, the instrument wires for all the segments were routed up through this conduit to the top of the pier. For a detailed description of the pier erection sequence see Chapter 4.



*Figure 3.9: Concrete gauges tied onto rebar cage of base segment PC16-1.*



*Figure 3.10: Access blockout and conduit for gauge wires, base segment PC16-1.*

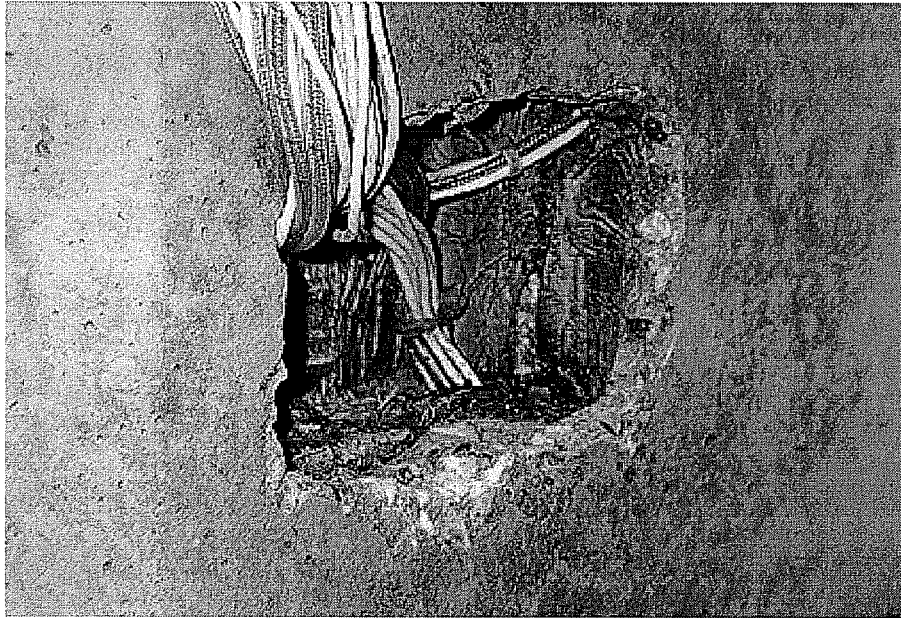


*Figure 3.11: Blockout and instrument wires after casting, base segment PC16-1.*

### **3.5.2 Thermocouples**

Thermocouples were numbered similarly to the concrete gauges. Thermocouples T400 through T407 were located in the base segment PC16-1 as shown in Figure 3.12. While this set of thermocouples would not be able to fully measure a temperature gradient across the pier's section, they would be useful for extrapolating temperature distributions found at other sections. These thermocouples would also be useful for comparing strains at different sections; dissimilar thermal effects due to differing exposures could be determined and separated from other strains at each section. The fully shaded location of this instrument set was not conducive to measuring maximum temperature gradients.

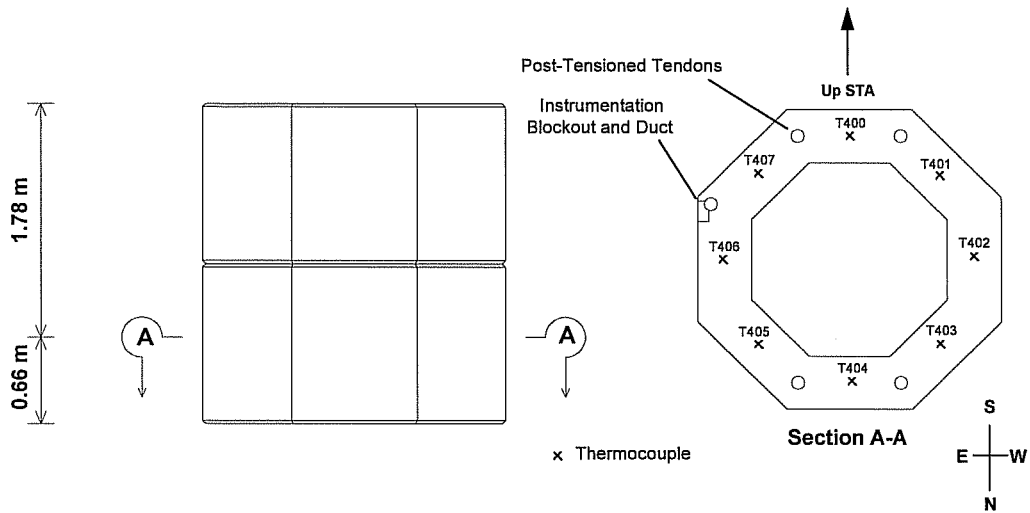


Figure 3.12: Thermocouple locations in base segment PC16-1.

Thermocouples were attached to the segment's reinforcement cage in a manner similar to the concrete gauges. Figure 3.13 shows a thermocouple tied to one of the cage's bars. The thermocouples were placed such that they were always at least one inch from any rebar's surface.

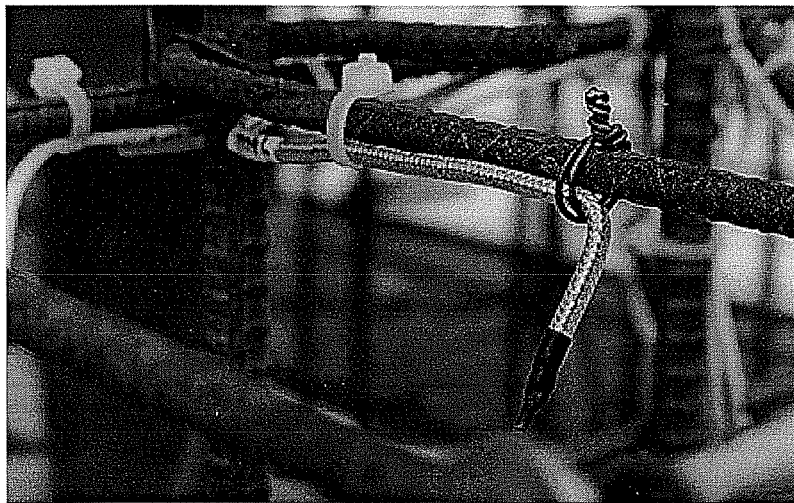


Figure 3.13: Typical thermocouple placement in rebar cage, base segment PC16-1.



### 3.6 "GRADIENT" SEGMENT PC16-5 GAUGE LOCATIONS

#### 3.6.1 Concrete Strain Gauges

In the "gradient" segment PC16-5, concrete gauge locations resembled those of the base segment. Gauges were numbered in the same manner as well, running from C430 to C441, as shown in Figure 3.14. However, to reduce the number of gauges in this area, and due to their somewhat redundant nature, the off-axis gauges were omitted. Axial- and bending-strain gauges were retained along the axes of the pier cross section coinciding with and normal to the longitudinal axis of the ramp superstructure. Transverse strain gauges were included to measure Poisson-type strains. These measurements are useful when subtracting out "hoop"-type strains present in both the bottom and mid-height segments.

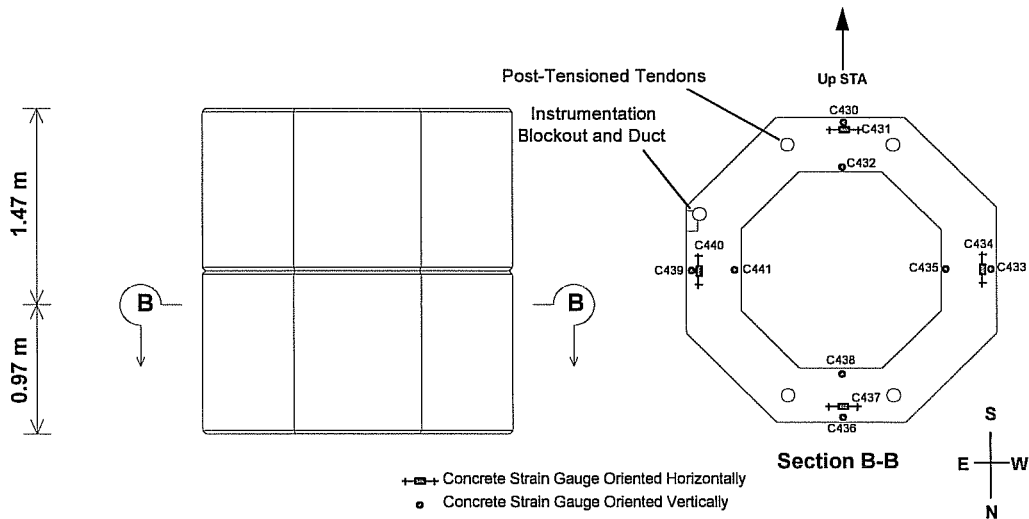


Figure 3.14: Concrete strain gauge positions, "gradient" segment PC16-5.

### 3.6.2 Thermocouples

The instrument cluster in segment PC16-5 was specifically positioned to measure the maximum possible temperature gradients occurring in the pier. For this reason, a section was chosen located at an elevation midway between the elevation of the top edge of the barrier wall on the IH-35 overpasses and the elevation of the bottom of the capital segment (see Figure 3.7). This location assured unobstructed sunlight at the level of the full gradient thermocouple set.

As shown in Figure 3.15, three thermocouples were installed on every side of the octagonal pier cross-section. The outer gauges were located at a cover of one inch, about the closest to the surface of the concrete as was thought possible and safe. The next ring of thermocouples was located at the middle of the 406mm thickness of the pier walls. The these locations correspond with those thermocouples located in segment PC16-1 and PC16-7. Finally the inner ring was located again at a cover of 25mm from the inside faces of the pier walls. These 24 instruments were numbered T410 through T433.

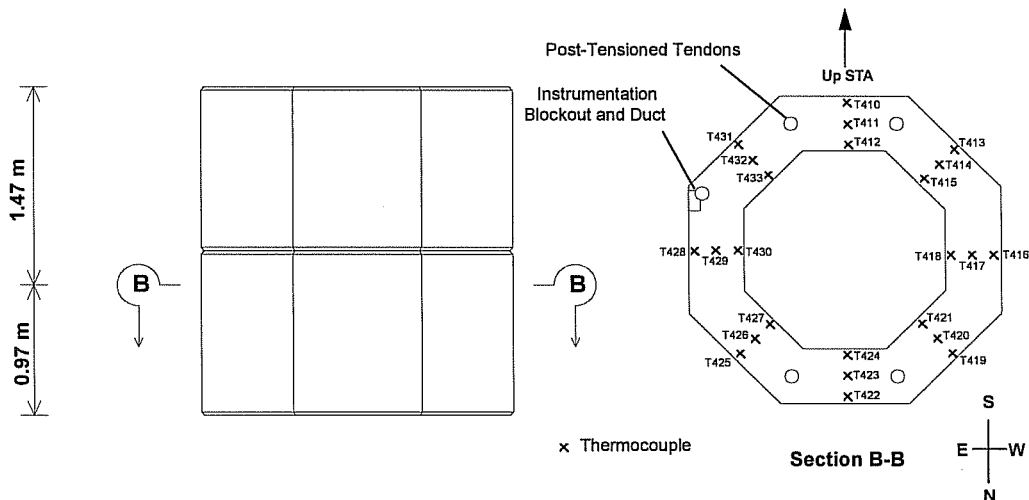


Figure 3.15: Thermocouple locations in the "gradient" segment PC16-5.

### 3.7 "TOP" SEGMENT PC16-7 GAUGE LOCATIONS

#### 3.7.1 Concrete Strain Gauges

The locations of instruments in this segment were identical to those in the base segment PC16-1. Concrete gauges in this segment were numbered C450 through C469 (see Figure 3.16).

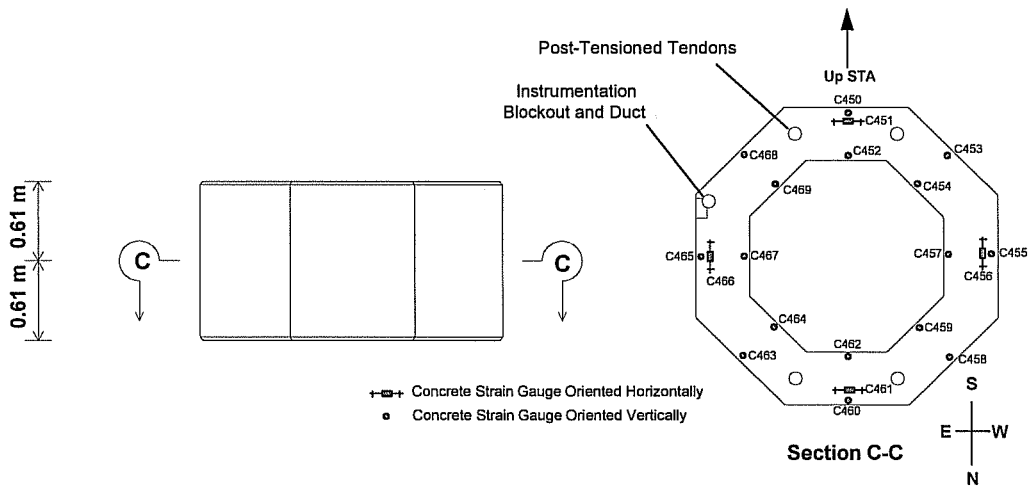


Figure 3.16: Concrete gauge locations in "top" segment PC16-7.

#### 3.7.2 Thermocouples

Like the concrete gauges, thermocouple placement in this segment was identical to the base segment. However, this instrument section was located in an exposure to full sunlight. Figure 3.17 shows the locations of thermocouples T440 through T447.

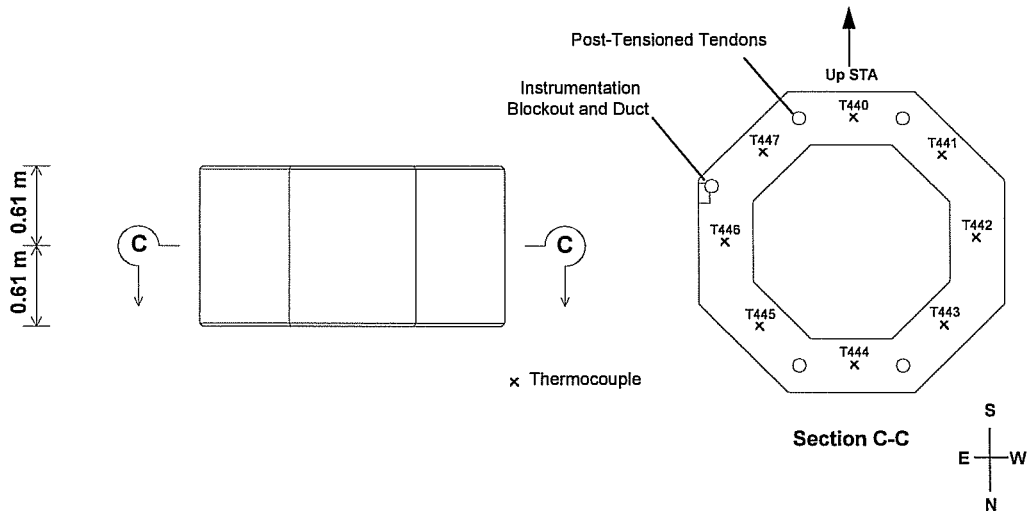
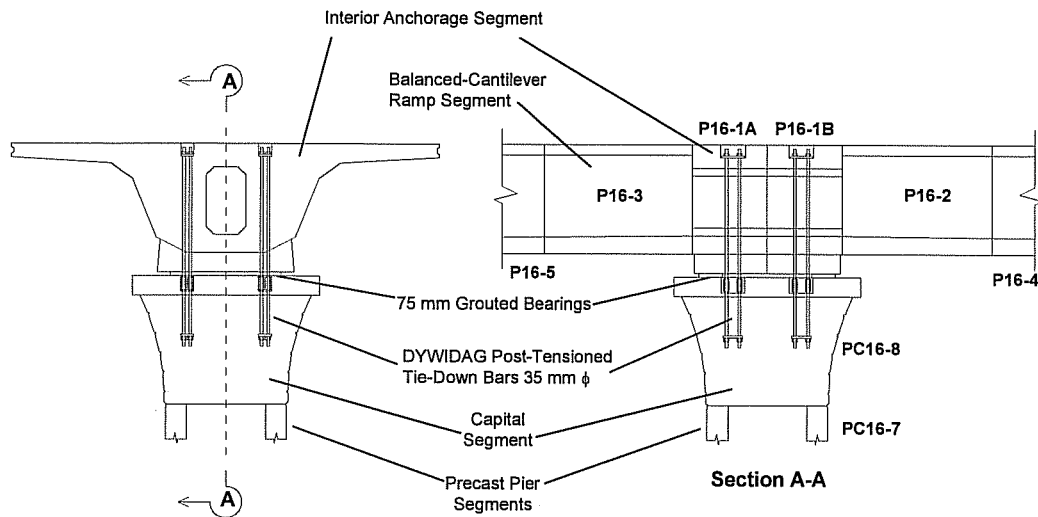


Figure 3.17: Thermocouple locations in “top” segment PC16-7.

### 3.8 CAPITAL PC16-8 GAUGE LOCATIONS

#### 3.8.1 Force Path Evaluation

The capital segment PC16-8 serves as an anchorage zone for this post-tensioned segmental pier. In addition to its primary function, the capital also provides anchorage for post-tensioned “tie-down” bars used during the balanced-cantilever construction of the ramp superstructure. These bars provide the clamping force required to maintain a full moment connection between the superstructure and the pier during cantilevering (see Figure 3.18).



*Figure 3.18: Fixed moment connection during superstructure erection achieved with DYWIDAG post-tensioned bars.*

Extremely high construction loads could be generated in the capital by the unbalanced erection process, and the strain distributions during this loading would probably not be linear. Thus, the capital provides an ideal opportunity for the use of strut-and-tie modeling to predict the flow of forces. A comprehensive illustration of the strut-and-tie modeling concept including many design examples was performed by Bergmeister, Breen, Jirsa, and Kreger [31].

The primary goal of instruments located in the capital segment was to measure and evaluate the possible force paths in this complex area. Both concrete and steel strain gauges were installed to measure strains coinciding with these force paths. In addition to this, thermocouples were installed throughout the capital. These instruments were installed to provide information on temperature gradients during the curing of this large monolithic segment and after the pier was erected and in service. They were also to be used to extract any thermally induced strains present during post-tensioning and superstructure cantilevering operations. In total, 168 instruments were

installed in the capital segment. In contrast, the rest of the pier shaft (segments PC16-1, PC16-5, and PC16-7) only contained 92 instruments.

### **3.8.2 Concrete Strain Gauges**

Concrete gauges located in the capital were numbered from C501 through C544 (see Figures 3.19 through 3.21). Gauges C533 through C544 were primarily located in areas where compression struts between anchor plates were predicted to form. C541 through C544 were placed such that their longitudinal axes coincided with the predicted compression struts' axes between the tie-down bar anchor plates and the anchor plates of the pier post-tensioning tendons (see Figure 3.21).

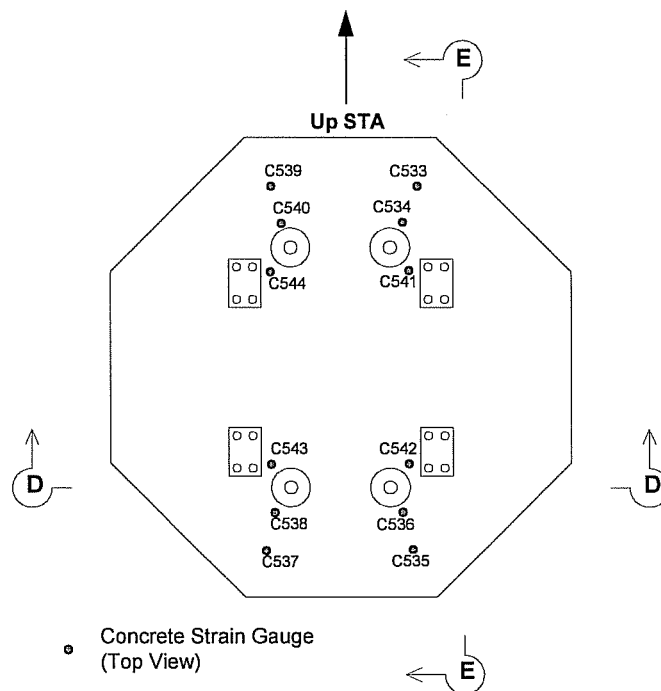
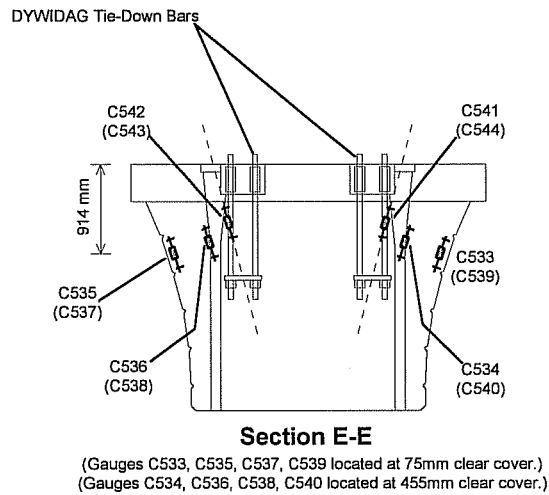


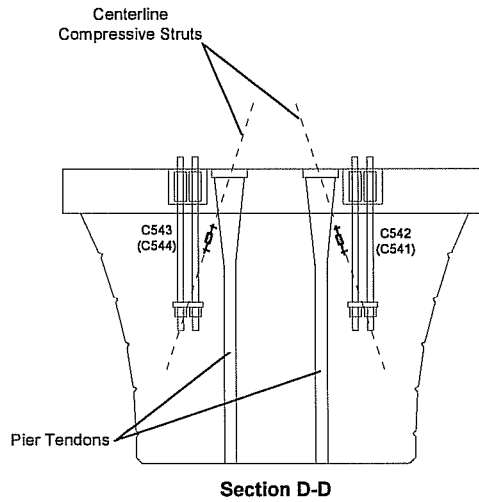
*Figure 3.19: Plan view of concrete strain gauges located in top half of capital segment.*



Concrete Strain Gauge  
 (Oriented Along Compressive Struts)

Note: Gauges denoted by ( ) located "behind" gauges shown.

Figure 3.20: Elevation view of concrete strain gauges in top half of capital segment.



Concrete Strain Gauge  
 (Oriented Along Compressive Struts)

**Notes:**

Gauges denoted by ( ) located "behind" gauges shown.  
 Gauges C533-C540 omitted for clarity.

Figure 3.21: Concrete strain gauge placement in compression strut between tie-down anchor plates and tendon anchorages.

In addition to concrete gauges located in high compression struts, two sections of gauges were located near the bottom of the capital that reflected gauge positioning in the pier segment PC16-7. Figure 3.22 shows the distribution of these gauges.

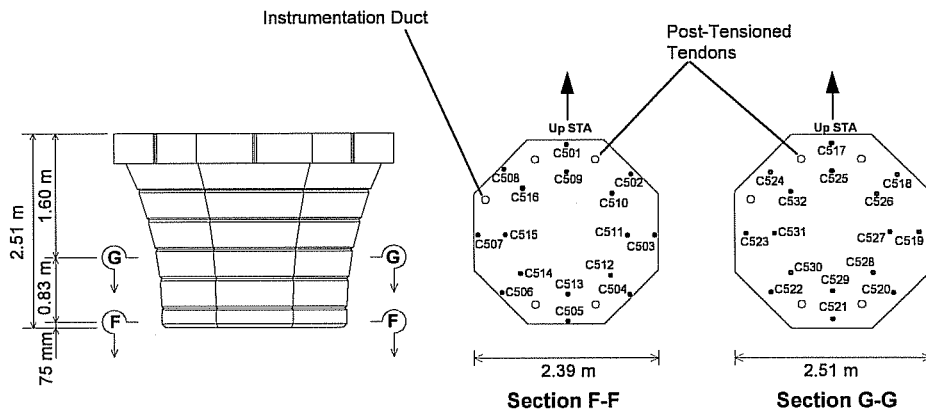


Figure 3.22: Two layers of concrete strain gauges located near bottom face of capital segment coinciding with gauge distributions in segment PC16-7.

### 3.8.3 Steel Strain Gauges

Strain gauges located directly on reinforcing steel were installed in the capital to coincide with possible tension ties predicted by strut-and-tie modeling. Steel gauges were numbered from S500 to S552.

Steel strain gauges were installed in a section located about 75mm clear cover from the capital's bottom face (see Figure 3.23). The design required tensile steel reinforcement across the bottom face of the segment. Gauges S509 through S516 were attached to these tensile ties to determine their contribution to the flow of forces through the pier. Gauges S501 through S508 were also placed along the perimeter steel at this section. These gauges were intended to measure any hoop stresses present at the



interface between the monolithic capital and the hollow, octagonal segment PC16-7 located just below it.

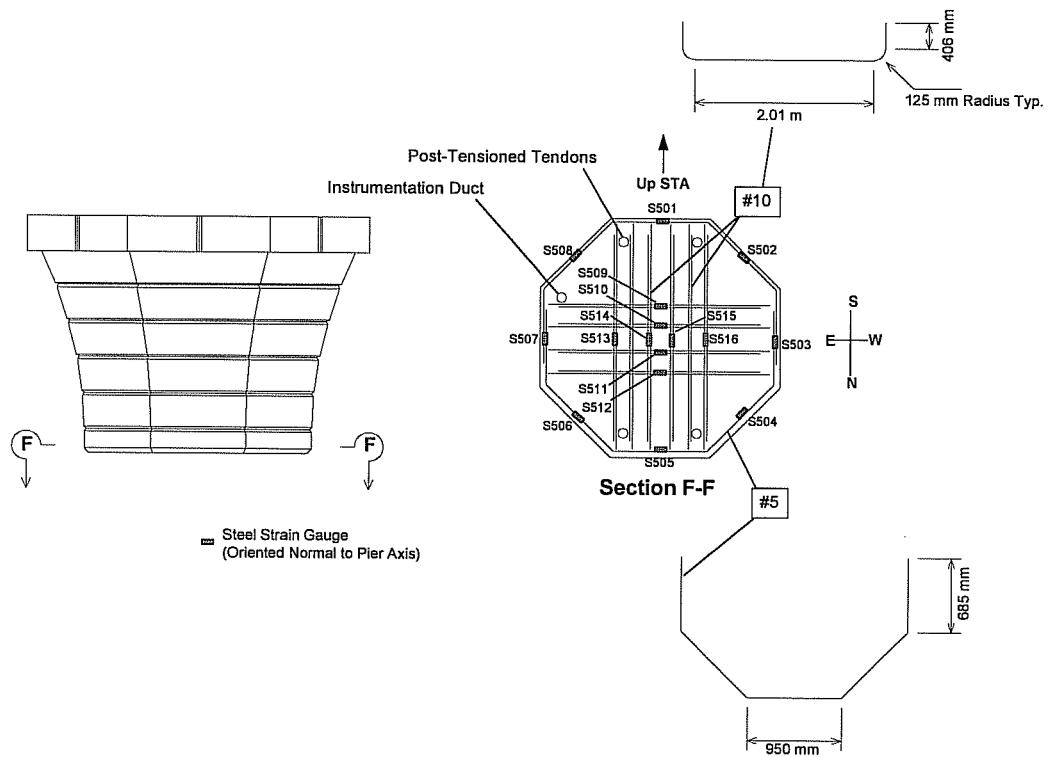


Figure 3.23: Location of steel strain gauges at the bottom face of the capital.

Steel gauges were also installed at tensile tie locations at the top face of the capital. Gauges S541 through S552 were located on the large #11 rebar running the full width of the capital at that section. These gauges would become critical during pier post-tensioning operations because tensile forces would likely develop between the tendon anchorages. Figure 3.24 illustrates the gauge locations.

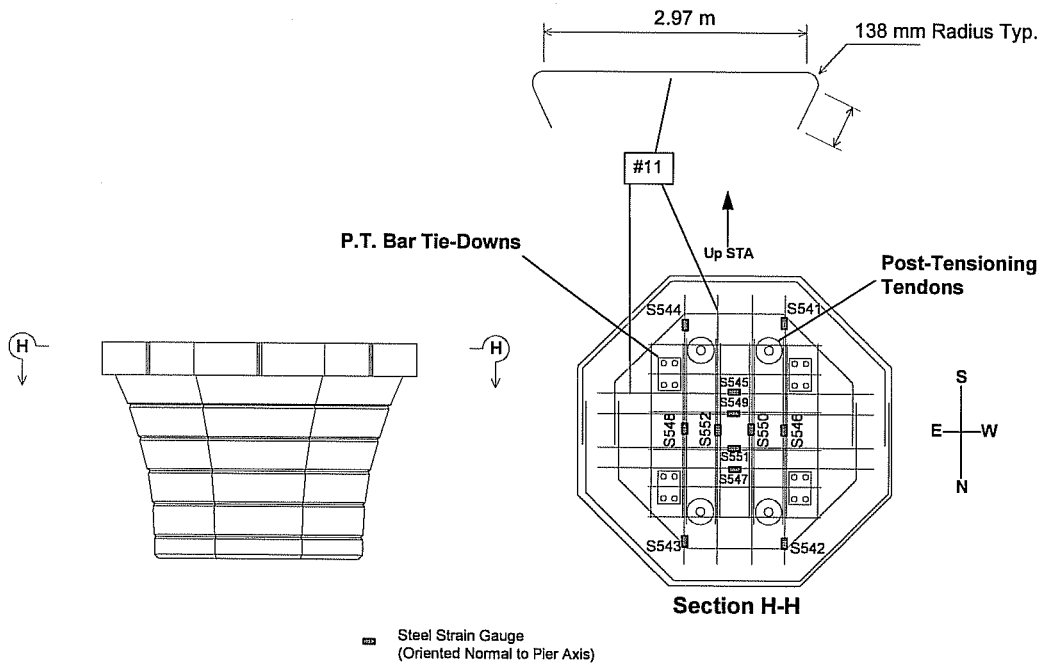


Figure 3.24: Locations of steel strain gauges near the top face of the capital.

Finally, steel strain gauges were installed on the DYWIDAG post-tensioned tied down bars anchored in the capital. Figure 3.25 illustrates the configuration of the bars and gauges. The capital anchors four groups of four bars arranged so as to run from the capital to the top of the ramp superstructure as shown in Figure 3.18. Each of the DYWIDAG bars was instrumented with one gauge to measure the distribution of forces between the bars. In addition, one bar out of each four bar group had two more gauges added. Thus, four of the sixteen bars had three gauges distributed along them in order to measure the distribution of force along the bars and to determine how effectively the bars were anchored in the concrete.

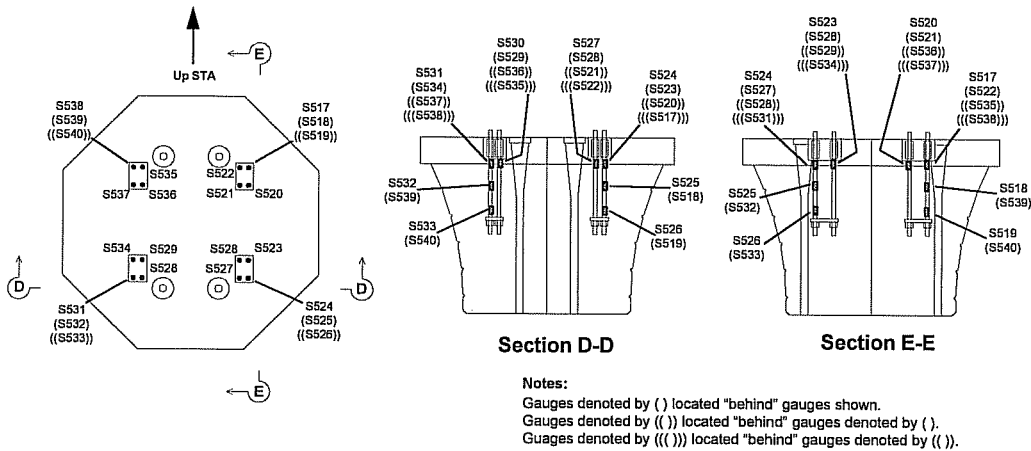


Figure 3.25: Locations of strain gauges attached to DYWIDAG post-tensioned tie-downs.

### 3.8.4 Thermocouples

The locations of thermocouples T501 through T572 were distributed throughout the capital segment. Two layers for measuring temperature gradients in the monolithic segment were located at sections 75 mm and 915 mm from the bottom face (see Figure 3.26). These gauges would measure a temperature gradient shape that would probably differ from that of the hollow cross-section of segment PC16-5.

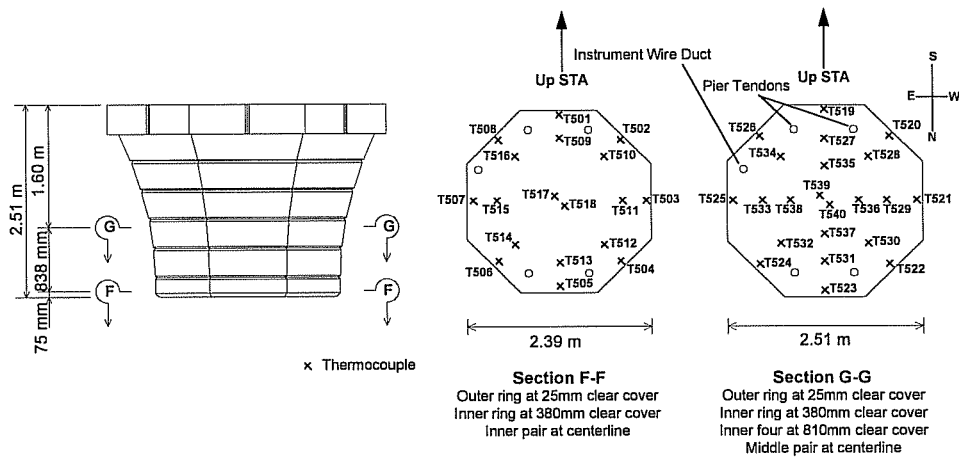


Figure 3.26: Temperature gradient thermocouples located near base of capital segment.

Thermocouples were also installed to measure gradients in two sections near the top face of the capital. Figure 3.27 shows the distribution of gauges in sections 50 mm and 330 mm below the top face. Together these two sections would provide readings for horizontal temperature gradients as well as gradients oriented vertically through the capital. This information on vertical gradients was augmented by the placement of several thermocouples in various locations coinciding with the compression struts discussed in section 3.8.1. Figure 3.28 shows the locations of these gauges.

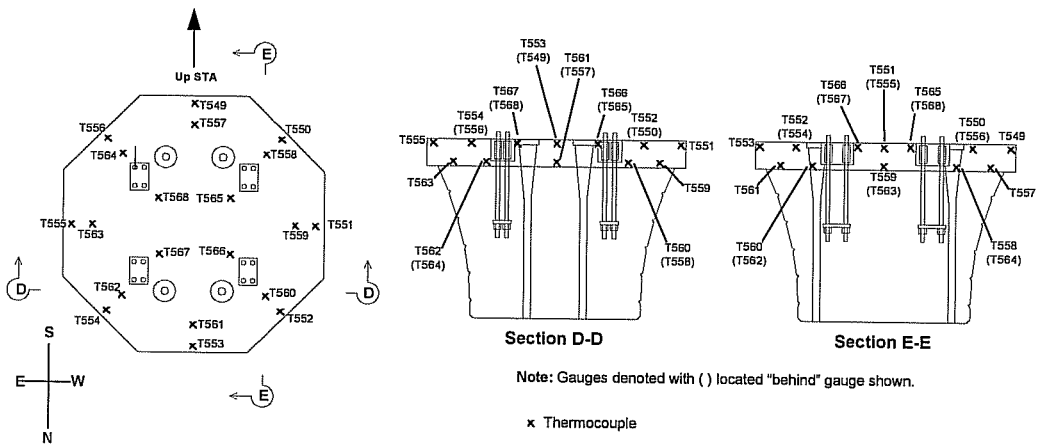


Figure 3.27: Thermocouples located near top face of capital segment.

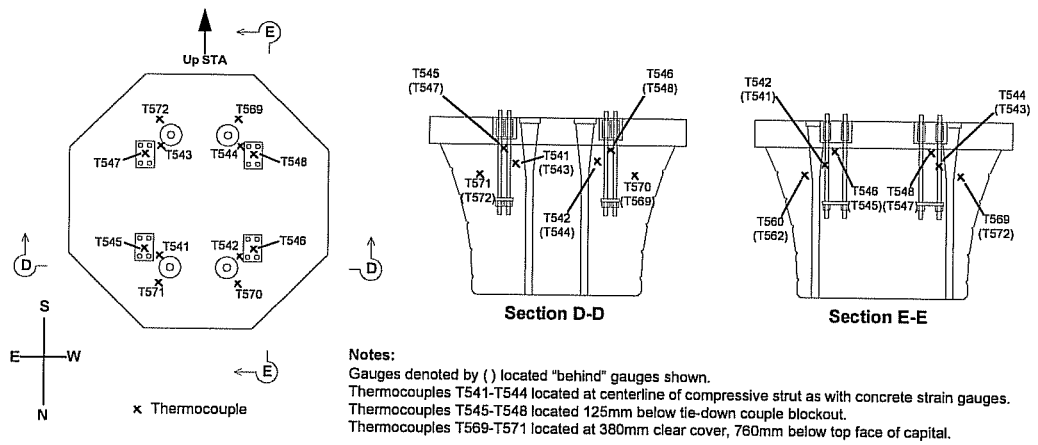


Figure 3.28: Thermocouples placed in compression strut areas.

The distribution of thermocouples throughout the capital segment allowed a comprehensive measurement of thermal distributions during curing. Large, monolithic capitals previously cast during the course of the bridge construction had undergone curing temperature differentials large enough to cause some superficial cracking. In

addition, the thermocouples in the capital would provide more information concerning sunlight-induced temperature gradients on solid concrete elements.

### 3.9 *DATA ACQUISITION SYSTEM*

All gauges in the pier were connected by means of the 100mm diameter instrument wire conduit to an instrument box located at the top of the pier. Positioning the data recorders at the top of the pier facilitated their future installation inside the ramp superstructure.

The data recorders used for the long-term data collection on this project were two Campbell 21X Data Loggers. Connected to each 21X unit were several Campbell AM416 Multiplexers that acted as switchboxes and enabled as many as 256 gauges to be read. Due to the limited temporary memory storage capacity of the Data Logger units, only four multiplexers were connected to unit "E" and five to unit "G". With each multiplexer filled to capacity with 32 gauges, unit "E" read a total of 128 strain gauges and unit "G" recorded 128 thermocouples and 32 strain gauges. The memory capacity of the 21X units reading gauges on the hour required researchers to download data from them to an Intel 386 based laptop computer once every five days.

The Campbell equipment was compact and reliable. With a 12 volt marine battery to supply power, the 21X units could be left to run continuously at the top of the pier. Researchers did not need to access the top of pier P16 to download data: serial cables for data transfer and a power cable for battery charging followed the instrumentation conduit back down to the base of the pier for easy access. All data recording electronics were packed in a steel ammunition box with dehumidifying agents and covered by a painted plywood box for further protection from water and intense sunlight (see Figure 3.29).

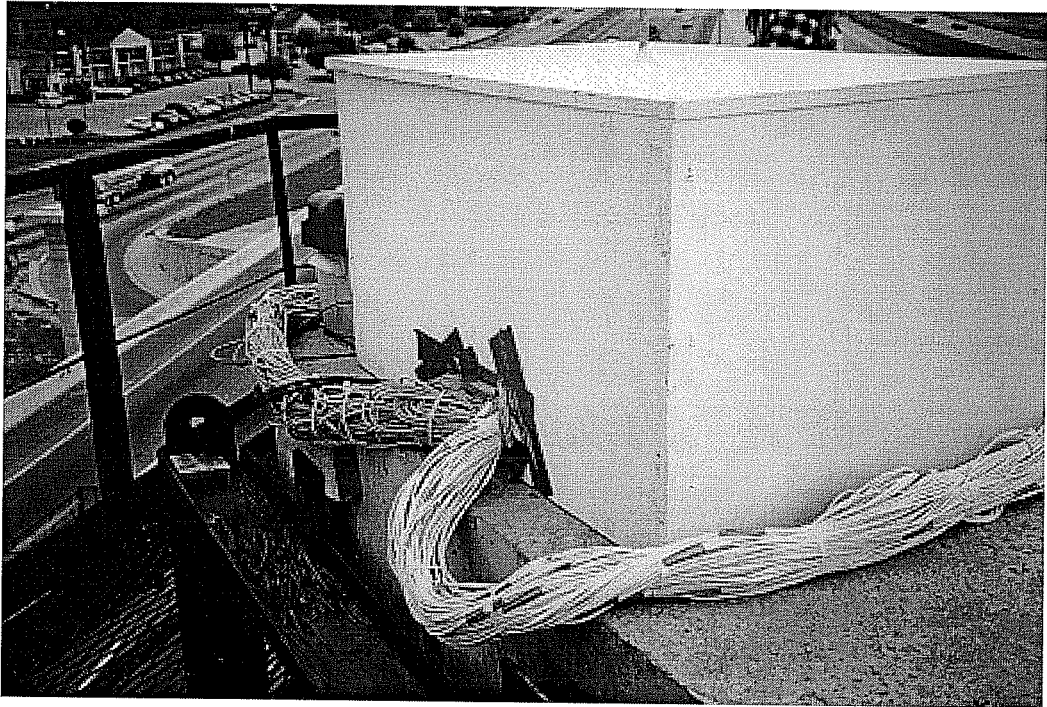


*Figure 3.29: Data recording equipment in place at top of pier.*

## CHAPTER 4

### *PIER AND RAMP SUPERSTRUCTURE CONSTRUCTION SEQUENCE*

#### *4.1 INTRODUCTION*

The casting and erection sequences for pier P16 were similar to those of segmental piers previously constructed in the United States. However, the unique characteristics of the segmental piers located on the U.S. 183 viaduct warrant a detailed examination of the construction methods undertaken. In a concrete segmental bridge the construction loads are often the most important and complex sets of loads that occur during the service life of the structure. An overview of the construction process for pier P16 and the ramp superstructure it supports will further clarify the nature and configuration of the instruments used to monitor its behavior.

#### *4.2 SEGMENTAL PIER CONSTRUCTION*

##### **4.2.1 Segment Casting Operations**

All of the segments for pier P16 were cast during the summer of 1995 at the constructor's precasting yard located in south Austin (see Figure 4.1). After precasting, the segments were placed in storage at the same site until pier erection activities began in March of 1996 (see Figure 4.2).

The U.S. 183 project plans called for 13 segmentally constructed piers of which 12 were located along the flyover ramp P. One segmentally constructed large ramp pier provided the center support for two adjacent straddle-bents supporting the north- and south-bound mainlanes of the viaduct. Large ramp piers along ramp P ranged in height from 8.2 meters to 21.6 meters. The piers were comprised of a total of



fifty-seven 2.44-meter segments, seven 1.22-meter segments, and thirteen capital segments.

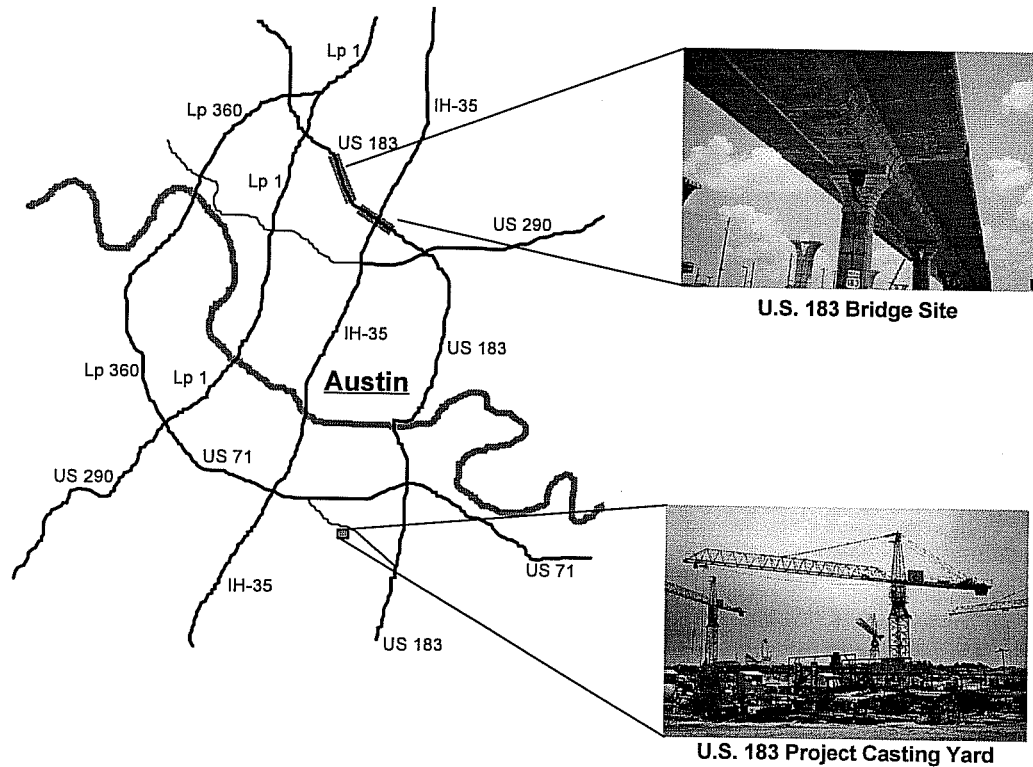


*Figure 4.1: Location of precasting facility and bridge site.*

The contractor chose to cast all 2.44-m segments before beginning any other pier segments. Likewise, all 1.22-m segments were cast before any capitals were constructed. Thus precasting operations for segments PC16-1 through PC16-6 and all 2.44-m segments from other piers were completed first. The casting operations for all 1.22-m segments including PC16-7 and all capitals including PC16-8 then followed. This method eliminated the need to handle more than one form at any given time and relieved congestion in the casting yard.



*Figure 4.2: Completed pier segments in storage at the casting yard.*

Precast pier segments were cast in a specially designed casting bed at the precasting facility. The bed consisted of tandem casting platforms, each with hydraulic jacks to control segment attitude and alignment (see Figures 4.4 and 4.5). Two platforms were utilized to enable constructors to cast one pier segment per day. Figure 4.3 illustrates the typical cycle for casting pier segments.

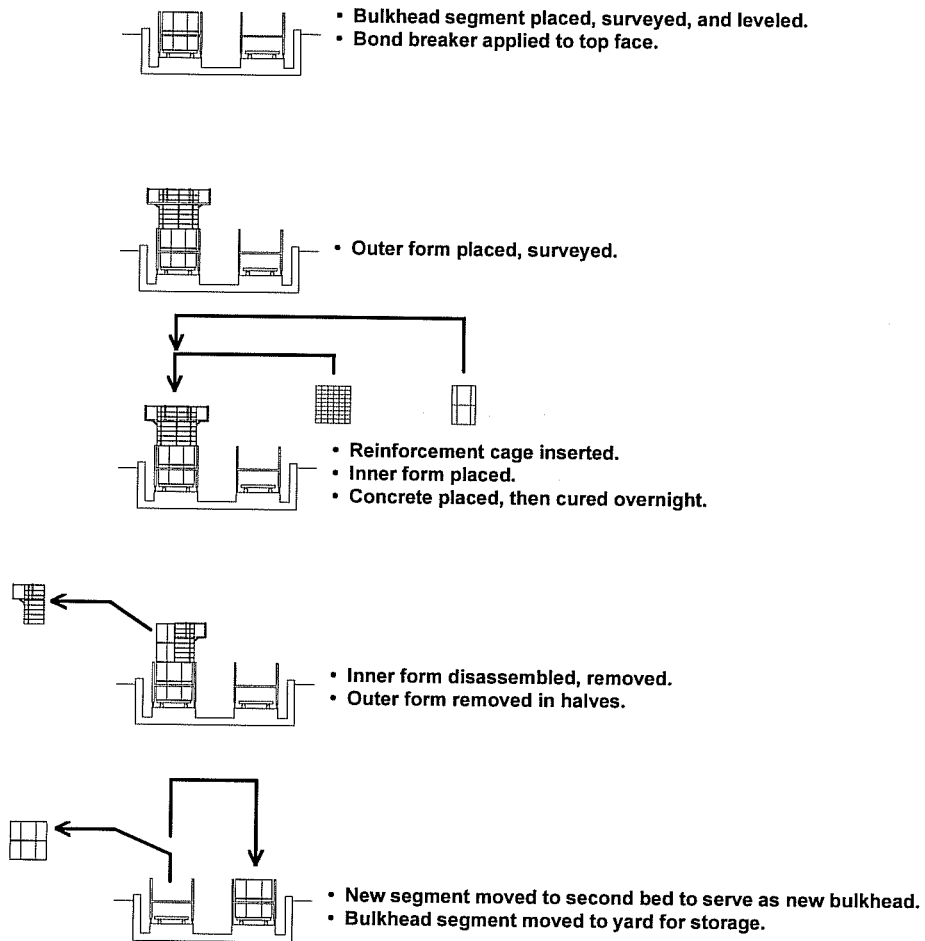


*Figure 4.3: Typical segment-per-day casting sequence.*

The short-line match-cast method of segmental construction was used to cast all pier segments. A typical casting cycle began with the placement of the previous cycle's segment into one of the sides of the tandem casting bed. This segment served as the bottom "bulkhead segment" for the next segment to be cast on top of it. This technique ensures a perfect fit between segments, and reduces or eliminates any systematic alignment errors (see Figure 4.6). The bulkhead segment was then checked by surveyors to ensure that it was plumb and aligned correctly.

When concrete is cast against a cured concrete face, the new concrete often bonds to the cured concrete, creating problems in the separation of the two faces. To prevent inadvertent adhesion during the match-casting process, a bond breaker must be applied to the concrete face used as a bulkhead. During the casting of the segmental pier segments, a relatively inexpensive mixture of Murphy's® oil soap and talc was applied to the face of the bulkhead segment (see Figure 4.7). This ensured an easy and clean separation of the two segments after curing was complete. Removal of the bond breaker from completed segments was simple and non-toxic.

The cycle continued with the placement of the steel outer form onto the top of the bulkhead segment (see Figure 4.8). The form was supported by the segment and a steel support cage with a set of jacks that could be leveled independently of those supporting the bulkhead segment. The reinforcement cage, which had been assembled during the previous day's casting operations, was then lowered into the outer form. To ensure adequate bottom clear cover for the cage, it rested on small 50 mm thick chunks of concrete masonry units which in turn rested on the bulkhead segment. Cover requirements for the outer face of the new segment were also met using small rebar "chairs" placed between the rebar cage and the outer form wall (see Figures 4.9 and 4.10). Steel ductwork for the post-tensioned tendons and temporary post-tensioning bars, PVC drainage piping, and electrical wiring ducts were placed at this point in the cycle. Steel pipe mandrels were inserted into all ducts to ensure good duct alignment between segments.

Constructing the hollow box shape of the pier segments required the use of an inner "core" form, which was placed through the middle of the reinforcement cage and rested on the same steel frame as the outer form. After installation of rebar chairs against the inner core face was complete, blockouts were installed in the top face for temporary post-tensioning bar anchor plates. Lifting hooks were also installed so that

the segment could be carried by the yard's straddle crane. Shear keys were formed into the top segment face with small, hand-held key forms inserted into the fresh concrete.

Concrete was supplied by an on-site batch plant, and placed in the form using a concrete bucket supported by one of four tower cranes continually servicing the yard's ten casting beds. After concrete placement was complete, the new segment was covered with insulating blankets and cured until the following morning (approximately 18 hours.)

After curing was complete, the core form was removed in several pieces. The outer form was removed in halves (see Figure 4.11). The new segment was lifted off of the bulkhead segment by the straddle crane, and immediately placed in the second casting frame. The bulkhead segment was placed in storage in the yard, and work could quickly begin again on the next segment. In this way, the tandem casting bed arrangement minimized the number of heavy lifts in the process.

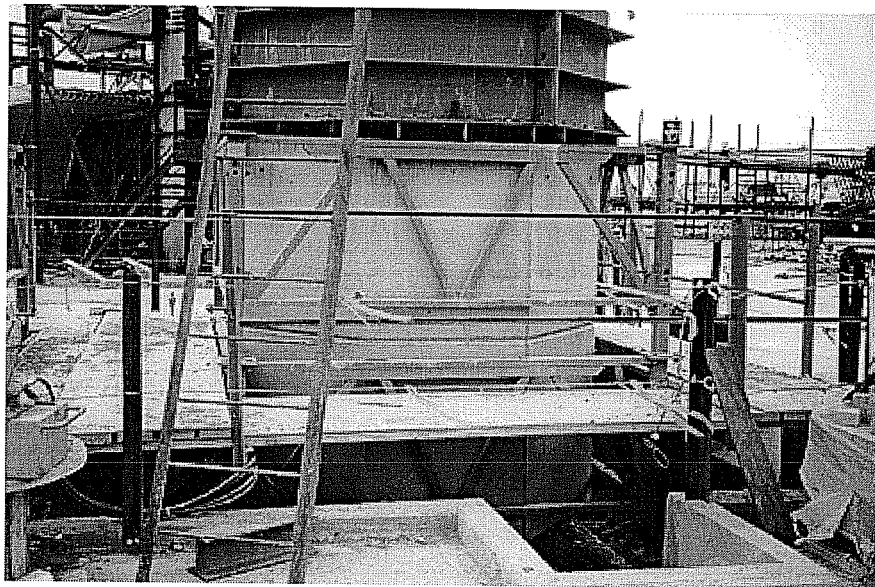


*Figure 4.4: Casting bed with steel support frame for formwork.*

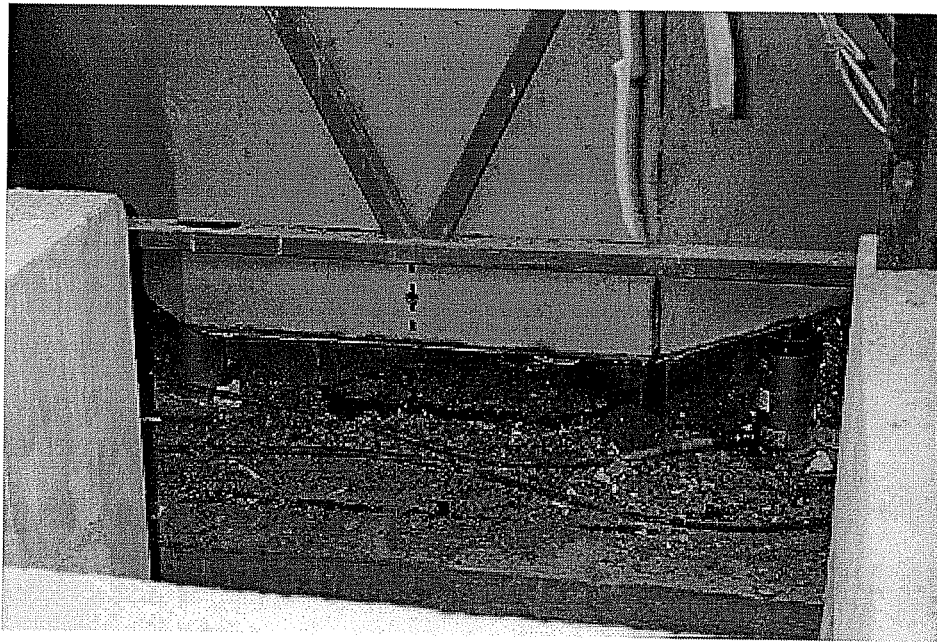


*Figure 4.5: Hydraulic jacks used to align the bulkhead pier segment.*

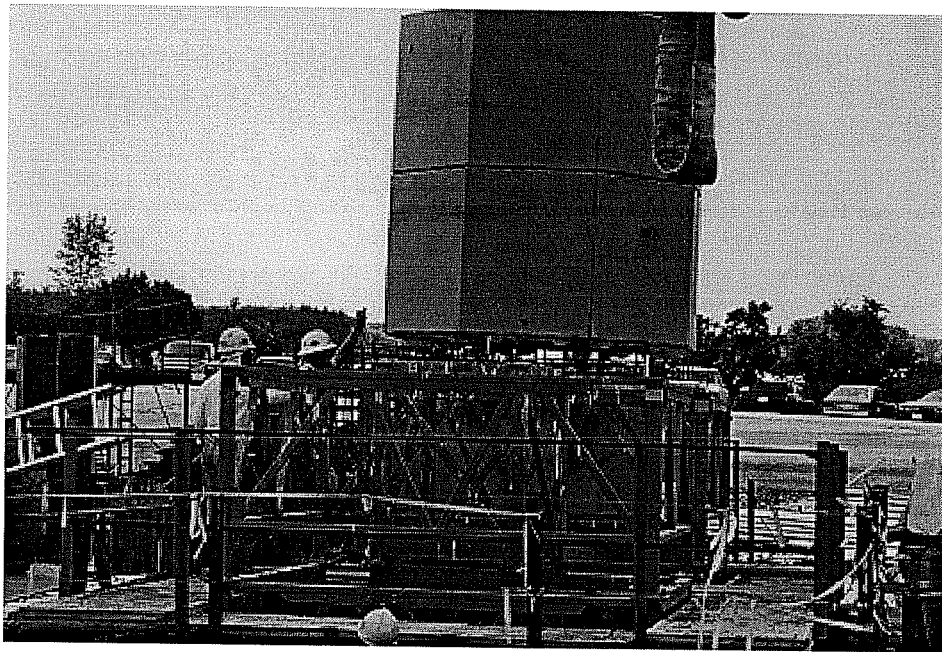


*Figure 4.6: Match cast segments fit together perfectly.*



*Figure 4.7: Application of bond breaker to bulkhead segment top face.*



*Figure 4.8: Pier segment outer form and scaffolding.*



*Figure 4.9: Placement of 50 mm thick cinder blocks under reinforcement cage.*

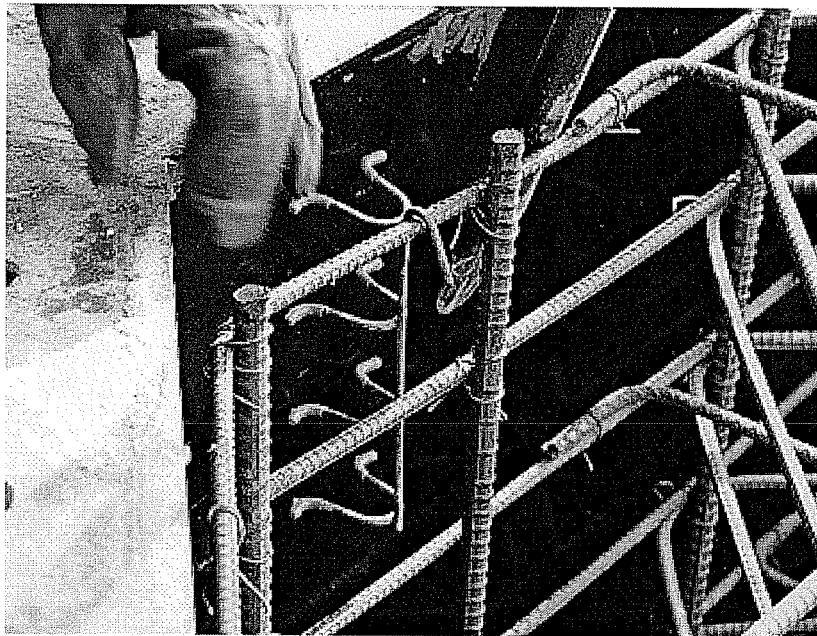


*Figure 4.10: Rebar chair used to ensure adequate clear cover.*



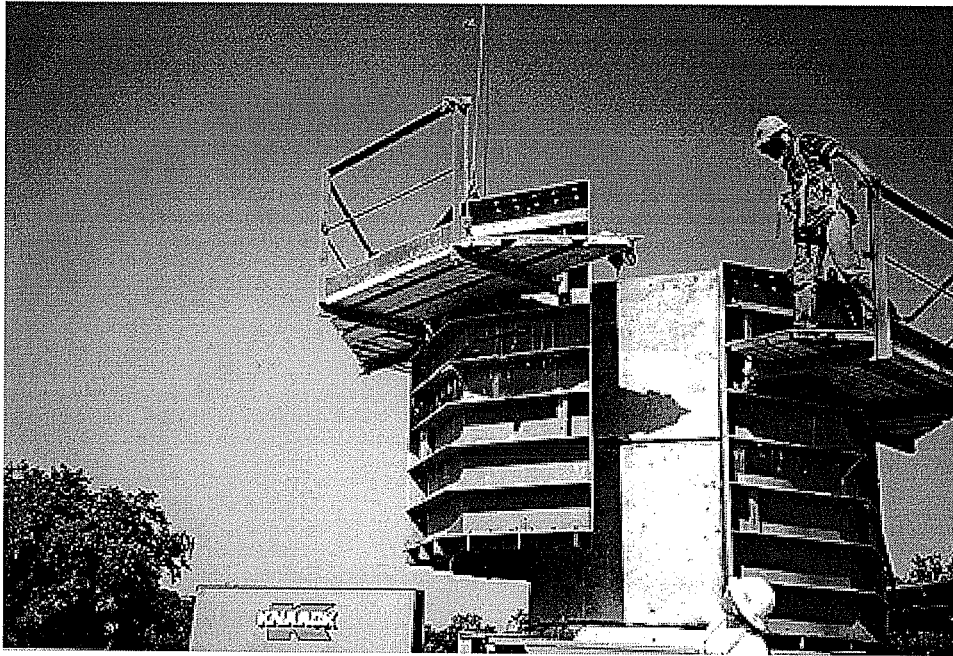


*Figure 4.11: Removal of outer formwork.*

#### **4.2.2 Pier Erection**

The segmental piers on the U.S. 183 project were designed to be post-tensioned from the top of the capital segment. For this reason the post-tensioning ducts were designed with a “U-turn” at the base of the pier. Figure 4.12 shows this duct configuration at the pier’s foundation. It was necessary to cast in place this foundation and ductwork after the construction of the drilled piers supporting the pier were complete. After completion of the cast-in-place foundation, an adjustable steel frame was installed atop the foundation to support the base segment PC16-1 (see Figure 4.13).

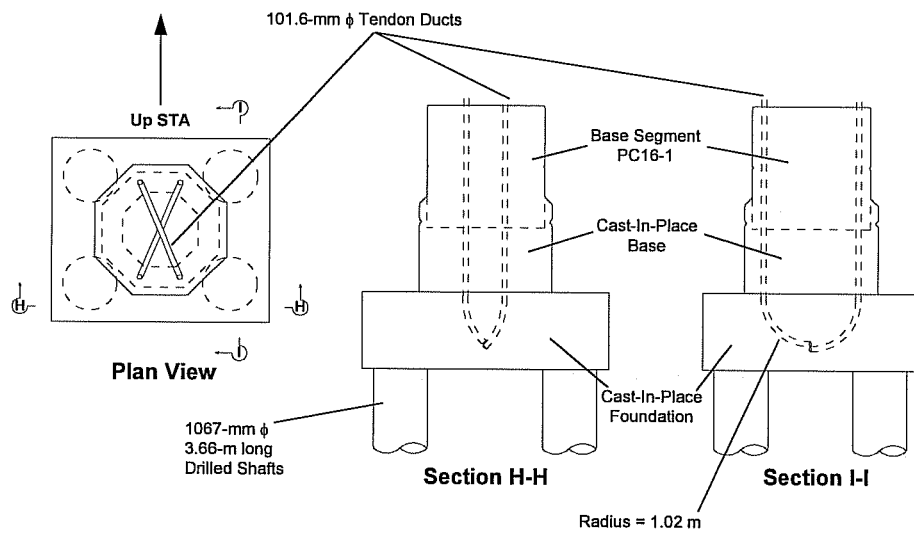


Figure 4.12: "U-turns" in tendon ducts located in pier foundation.



Figure 4.13: Steel support frame for segment prior to cast-in-place base construction.

The steel leveling frame provided only a temporary support for PC16-1. After alignment and leveling of the bottom segment, a concrete base was cast around it. During construction of the cast-in-place base, the concrete was mechanically vibrated and forced to flow up against the bottom face and into the core void of segment PC16-1, ensuring good contact between the base and the bottom segment and solidifying the moment-resisting connection at the column base. A pier of any height could be constructed with standard segments and base sizes in this manner by simply varying the elevation of the top of the cast-in-place base with respect to the bottom precast segment. Figure 4.14 shows the cast-in-place base after completion of the pier.



*Figure 4.14: Cast-in-place base forming a rigid moment connection between base segment PC16-1 and foundation.*

Subsequent segments were placed using a crane situated on the north-bound overpass of Interstate Highway 35. Segments were placed with “wet” joints; two-part bridge epoxy was spread over the adjoining segment faces before the segments were installed permanently. After each segment was placed and epoxied, a portable scaffold was lifted to the top of the new segment. From here, DYWIDAG post-tensioning bars were stressed to ensure complete contact between segments as the epoxy cured. Figure 4.15 shows the hydraulic ram used for post-tensioning the DYWIDAG bars.

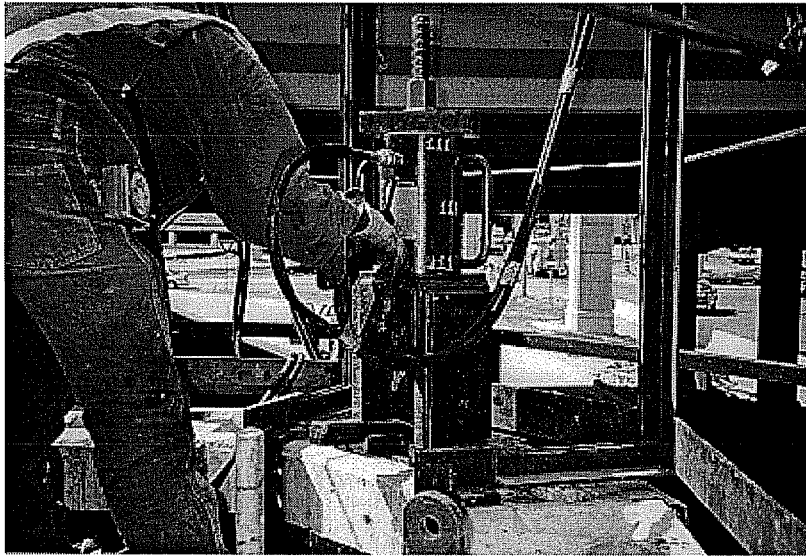


*Figure 4.15: Hydraulic ram stressing temporary post-tensioning bars.*

Post-tensioning of the pier's tendons followed the placement of the capital segment PC16-8. Tendons consisting of 19 ~ 15-mm  $\phi$  strands were cut to an approximate length, lifted by crane to the top of the pier, and inserted into the tendon ducts. The crane was then used to pull the tendons through the full lengths of the ducts. After installation of the post-tensioning anchorage heads and wedges, the tendons were stressed in the order shown in Figure 4.16.

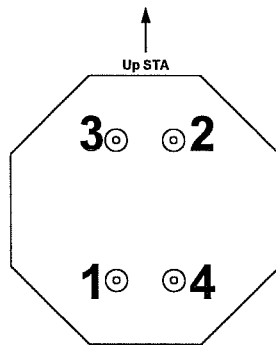


*Figure 4.16: Sequence of final post-tensioning of pier P16 tendons.*

For the first pull the hydraulic jack was placed at the live end position 1 and position 2 served as the dead end. In a frictionless duct, no further stressing from position 2 would be needed, but the 180° angle change at the “U-turn” in the duct at the base of the pier caused about a 50% loss of post-tensioning force due to friction. The calculated frictional coefficient  $\mu$  of the post-tensioning ducts in pier P16 is 0.23, or less than the typical design value of  $\mu = 0.25$ . Friction loss in a post-tensioning duct is found using the following equation:

$$\text{Friction Loss(\%)} = \frac{1}{e^{\mu\alpha}} \times 100\%$$

where:  $\mu$  = frictional coefficient

$\alpha$  = angle change in duct in radians

The alignment of the ducts was quite good, as the accepted value for a duct with no wobble (unintentional angle change) is  $\mu = 0.221$ . However, a pull at position 2 was needed to stress the complete length of the tendons to the specified level. The same procedure then followed for pulls 3 and 4. After tendon post-tensioning was complete, the tendons were grouted and the anchor heads were covered with a grout shell for corrosion protection. Table 4.1 outlines the entire precasting, erection, and instrumentation process for pier P16.

| Date            | Time             | Event   |
|-----------------|------------------|---|
| 24-May-95       | 1:00 PM          | Bottom segment PC16-1 instrumented and cast.              |
| 25-May-95       | 1:00 PM          | Segment PC16-2 cast.                                      |
| 26-May-95       | 1:00 PM          | Segment PC16-3 cast.                                      |
| 31-May-95       | 1:00 PM          | Segment PC16-4 cast.                                      |
| 2-Jun-95        | 1:00 PM          | Segment PC16-5 instrumented and cast.                     |
| 3-Jun-95        | 1:00 PM          | Segment PC16-6 cast.                                      |
| 6-Jul-95        | 1:00 PM          | Top segment PC16-7 instrumented and cast.                 |
| 18-Sep-95       | 10:00 AM         | Capital segment PC16-8 instrumented and cast.             |
| Sep 18 - Sep 25 | hourly           | Collection of capital segment PC16-8 curing temperatures. |
| 15-Mar-96       | 3:00 PM          | Segment PC16-1 placed, cast-in-place base constructed.    |
| 2-Apr-96        | 12:00AM - 5:00AM | PC16-2 through PC16-4 placed.                             |
| 5-Apr-96        | 12:00AM - 5:00AM | PC16-5 through PC16-7 placed.                             |
| 8-Apr-96        | 2:00 AM          | Capital PC16-8 placed.                                    |
| 12 Apr - 30 Apr | hourly           | Collection of pier temperature data.                      |
| Apr 30, May 1   | 10:00PM - 5:00AM | Pier Post-Tensioning Operations                           |
| Apr 30, May 1   | every minute     | Collection of post-tensioning data.                       |
| May 4 - present | hourly           | Permanent collection of temperature and strain data.      |

*Table 4.1: Construction and instrumentation sequence for pier P16.*

### 4.3 BALANCED-CANTILEVER SUPERSTRUCTURE ERECTION

Although a detailed description of the casting process for the balanced-cantilever ramp segments is beyond the scope of this report, an outline of the erection sequence for the superstructure is important for understanding the nature of the loading that the segmental pier will experience over its lifetime. The following is the construction sequence proposed by the Texas Department of Transportation.

#### **4.3.1 Phase I**

Construction of the five-span continuous unit in balanced-cantilever involves the use of both an erection truss and some type of beam and winch assembly attached to the superstructure. A ground-based crane could also be used to place segments. Figure 4.17 shows the possible construction configuration. Phase I begins with the placement of the erection truss at the 38.1-meter Span A from pier P13 to P14. The anchor segment located atop pier P14 would be placed first. Temporary post-tensioned

tie down bars would be stressed, fixing the anchor segment to the capital of the pier. From the anchor segment, segments would be added on each side of P14 in cantilever until they reach about 27 meters from each side of the pier, or half the 55-meter Span B distance to pier P15. After each balanced pair of segments is placed, negative moment-resisting tendons would be stressed to support them. Segments supported by the truss would bridge the remaining distance between piers P13 and P14.

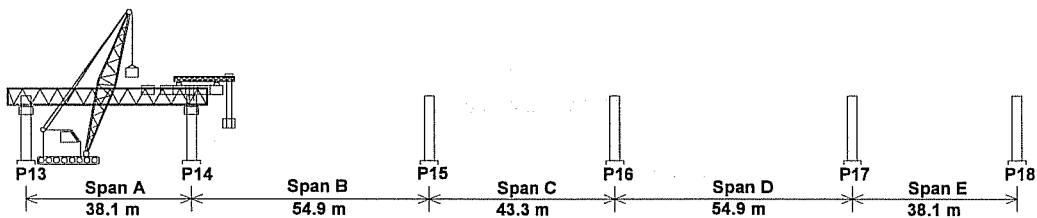


Figure 4.17: Phase I, cantilevering from pier P14.

#### 4.3.2 Phases II and III

After cantilevering from pier P14 is complete, a small 300-mm closure joint between the left-hand cantilever from P14 and the truss supported segments would be cast, and positive-moment tendons would be stressed in Span A. Balanced-cantilever erection would proceed from piers P15 during Phase II and P16 during Phase III as shown in Figure 4.18. During the placement of these segments pier P16 would see some of the largest bending moments applied in its lifetime. The anchor segments at P15 and P16, unlike those at P14 and P17, are permanently fixed to the tops of the piers by post-tensioned tie-down bars.

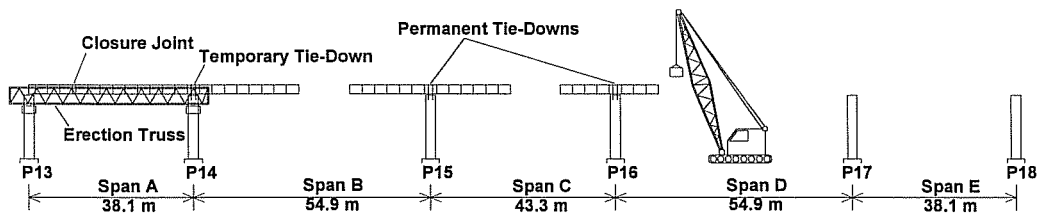
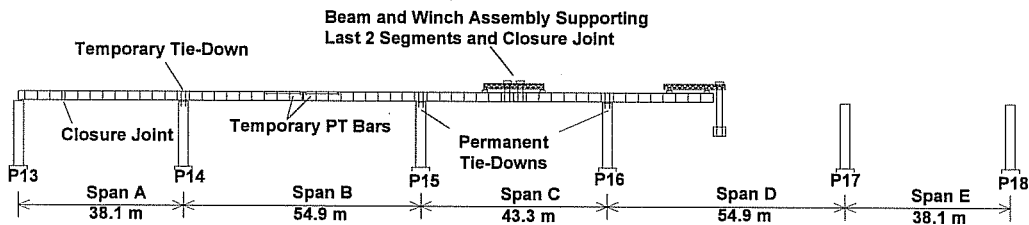


Figure 4.18: Phases II and III, cantilever construction from piers P15 and P16.

### **4.3.3 Phase IV**

During Phase IV, shown in Figure 4.19, the central 43.3-meter Span C would be completed with the use of a beam and winch assembly supporting the last two segments and the formwork for the cast-in-place closure joint located at midspan. After completion of the closure pour and stressing of the positive moment tendons in Span C, P16 becomes part of a frame configuration with pier P15 and Span C. Any induced moments in P16 due to temperature gradient effects become important due to the indeterminate nature of the structure (see Chapter 2 for information on temperature gradient effects on indeterminate structures).



*Figure 4.19: Phase IV, completion of the 43.3-meter central span.*

### **4.3.4 Phases V and VI**

The placement of the temporary truss at Span E occurs during Phase V of construction (see Figure 4.20). The sequence is similar to Phase I except that cantilevering takes place from pier P17. The anchor segment at P17 is temporarily tied down. In Phase VI, the 38.1-meter span is completed with a closure joint and the installation of positive-moment tendons.



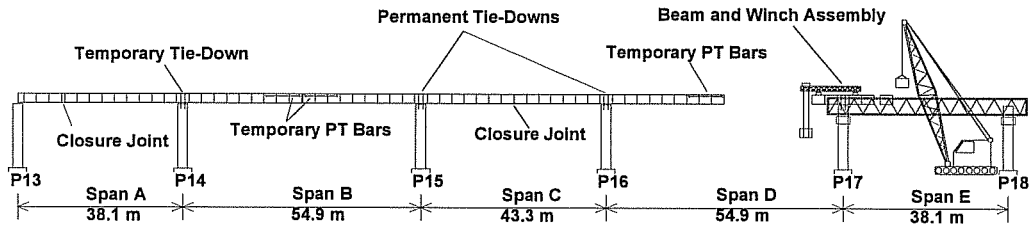


Figure 4.20: Phases V and VI, cantilevering of segments from P17, placement of temporary truss, and erection of 38.1-meter Span E.

#### 4.3.5 Phase VII

Phase VII includes the completion of Span D, the second 54.9-meter span and the installation of positive-moment tendons in this span (see Figure 4.21). After the erection of all the ramp segments is complete, the tied down anchor segments at piers P14 and P17 are released and the superstructure is jacked at these points to allow the placement of permanent bearing pads. Thus, P15 and P16 are fixed connections and P13, P14, P17, and P18 have movable bearing seats. Finally, continuity tendons running from Span A to B and from Span D to E are installed and stressed, as are tendons running from Span B through Span D. These continuity tendons complete the post-tensioning operations and enable the five spans to function as one unit.

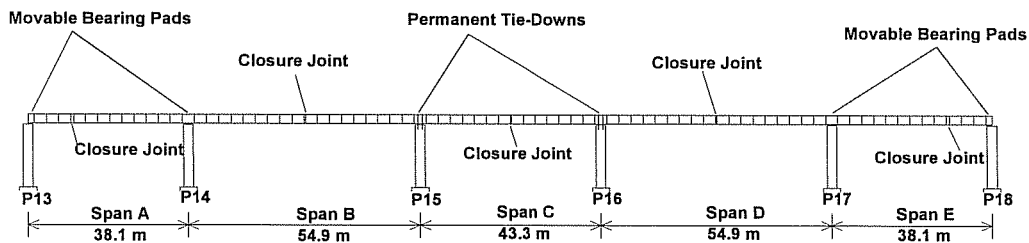


Figure 4.21: Phase VII, completion of Span D and installation of continuity tendons.

## CHAPTER 5

### *DATA PRESENTATION*

#### *5.1 GENERAL TEMPERATURE TRENDS*

Thermocouples measured temperatures in pier P16 beginning on April 12, 1996, and continuing hourly through May 1, 1996. After a brief interruption following pier post-tensioning operations, data were again recorded hourly from May 4, 1996, to August 1, 1996. The thermocouples appear to be extremely reliable and consistent, and from their measurements several general trends in temperature became apparent.

##### **5.1.1 Daily Cycles**

The general assumptions regarding the effects of thermal gradients on members made in Chapter 2 are valid for bridge piers and superstructures. However, predicting the characteristics of temperature gradients in bridge pier sections is more complex due to the pier's physical orientation.

Bridge superstructures, especially winged trapezoidal box girders, will typically experience well-defined gradients during the course of any given day. The sun's path across the sky causes it to directly heat the top slab of the girder, while the webs and bottom flange see virtually no solar heating. The thermal gradients always occur most significantly along the depth of the girder. Therefore the induced stresses also act in a well-defined manner.

However, bridge piers do not undergo a thermal gradient in only one direction over the course of a day. Due to the pier's orientation with respect to the sun's path across the sky, the largest temperature gradients occur at any given time along an axis oriented towards the sun's location (see Figure 5.1). Gradients in other directions will

also be present, but will exhibit smaller temperature differences. Thus the pier's response changes over the course of the day.

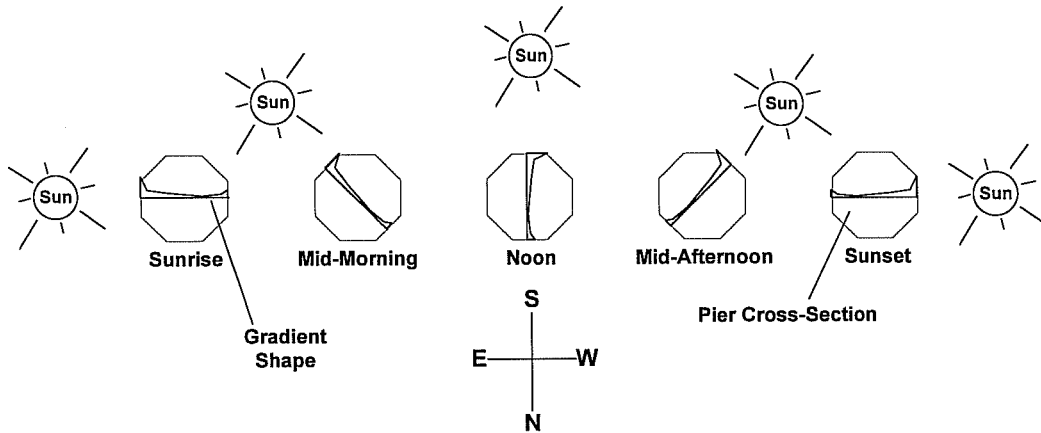


*Figure 5.1: Temperature gradient orientations at different times in the day.*

The thermocouples located in the “gradient” segment PC16-5 were ideally placed to record the daily change in gradient orientation as the sun moved across the sky and heated progressive faces of the pier's surface. Figure 5.2 illustrates this concept with temperatures recorded on June 17, 1996. This date was chosen to represent a typical summer day because it occurred in the middle of several consecutive days that exhibited steady daily cycles of temperature. Each thermocouple is located within 25 mm of the pier's outer surface. After the sun heats each outer face, the corresponding thermocouple records a peak in temperature. The thermocouple then cools slightly while the subsequent face is heated.

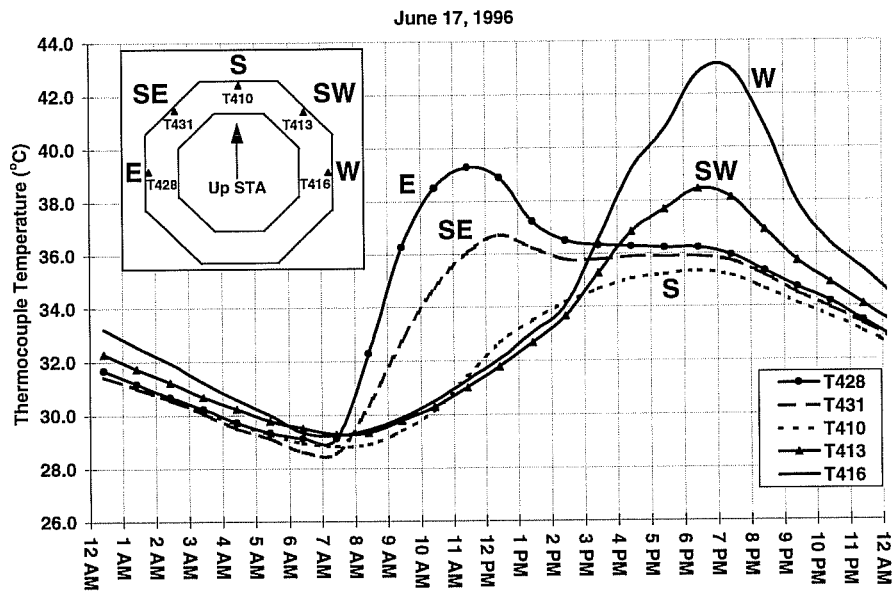


Figure 5.2: Typical daily temperature cycle of selected outside-layer thermocouples in gradient segment PC16-5.

East-facing thermocouple T428 is the first to experience this peak during the daily cycle. After a steady cooling trend throughout the early morning hours, T428 records a sudden rise in temperature just after 7:00 AM. The rapid morning temperature rise at this instrument's location indicates that sunlight almost directly strikes the eastern face of the pier during the first few hours of daylight. T428 reaches its peak temperature around 11:30 AM. The sudden drop in temperature after this time probably indicates that sunlight no longer directly strikes the eastern face of the pier after this time of the day. However, the temperature levels off from about 3:00 PM until 7:00 PM as the ambient air temperature continues to rise in the afternoon. The temperature of T428 does not rise or fall because the eastern face is re-radiating heat at about the same rate that it is being heated by the increasing ambient air temperature. After sunset, T428 begins a steady cooling trend until the next morning.

The thermocouple located in the southeastern face of the pier and designated T431 exhibits a temperature cycle similar to that of T428. The morning rise in temperature is not as steep, however, and the peak temperature is slightly less. The southern facing thermocouple T410 recorded the lowest peak temperature of the group. Its peak occurred much later in the day around 6:30 PM. This may indicate that T410 was placed slightly farther from the outside face of the pier than the other instruments. Also, the south face of the pier is struck by the most indirect sunlight during the day. The sun's vertical angle is large, and sunlight strikes the southern face at a high angle of incidence.

The western facing thermocouple T416 recorded the highest peak temperature among the gauges. This indicates that the temperature of the pier's west face is influenced greatly by direct solar radiation and a high ambient air temperature. T413 at the southwest face recorded a similar set of temperatures, although the peak was much lower than that of T416.

These data indicate that the east- and west-facing sides of the pier undergo the largest daily fluctuations in temperature. It is most likely, therefore, that the largest temperature gradients across the pier's section will occur along an axis running east to west. Gradients occurring along other axes could also be important, though, depending on bridge geometry.

### **5.1.2 Seasonal Characteristics**

As discussed in Chapter 2, environmental effects such as prevailing weather patterns can strongly influence the shape and magnitude of thermal gradients in bridge members. Alternating warm and cold fronts cause wide fluctuations in daily ambient temperatures and can mitigate solar radiation with cloud cover. Conditions that vary in this manner have a greater potential to produce large temperature gradients than more stable and cyclical patterns.

Figures 5.3 through 5.6 illustrate some seasonal characteristics of weather that typically occur in Austin, Texas. In the graphs, the panel temperature recorded by the internal thermometer of the Campbell 21X Datalogger is plotted for three months. The panel temperature is not necessarily an accurate representation of temperature magnitude because of its location on top of the pier, but it is useful for tracking general trends in ambient temperature. Although the temperature records are not complete, it becomes immediately apparent that the month of April is characterized by particularly variable weather patterns. Temperatures fluctuate widely over the period of time plotted in Figure 5.3, with a maximum temperature change in a 24-hour period of about 18° C on April 29. This time of the year is typically the rainy season in Austin and often marked by the arrivals of alternating warm and cold fronts to the area every few days.

In contrast, the month of May exhibits very stable weather patterns (see Figure 5.4). From May 13 through May 27 daily high and low temperatures changed very little. The largest temperature change in 24 hours occurred on May 30 with a drop of about 11° C. The month of June was characterized by slightly more variable weather, but temperatures wavered very little for much of the month (see Figure 5.5). The largest change in temperature was only about 12° C on June 21. July also saw very stable, regular weather patterns (see Figure 5.6).

Thus it appears that large short-term changes in ambient temperature, and possibly large section temperature gradients, will most likely occur during the spring in Austin. The summer months are too hot and humid (humidity prevents rapid cooling at night) to undergo large variations in temperature, and tend to exhibit very regular, stable characteristics. Likewise, the winter months may be too cold to allow significant heating of the pier to produce large gradients. The fall season may again bring weather patterns conducive to producing large daily temperature differentials and the large thermal gradients associated with those variations.

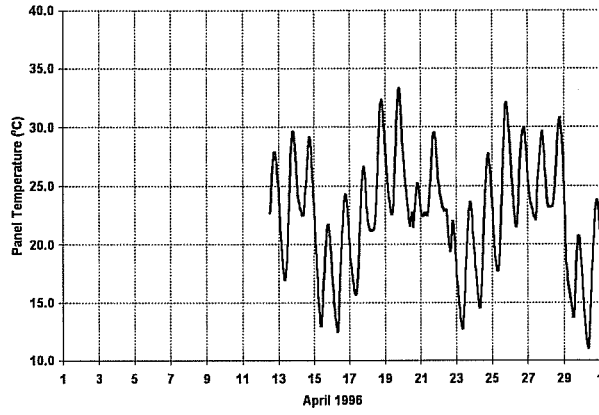


Figure 5.3: Datalogger panel temperatures recorded during April 1996.

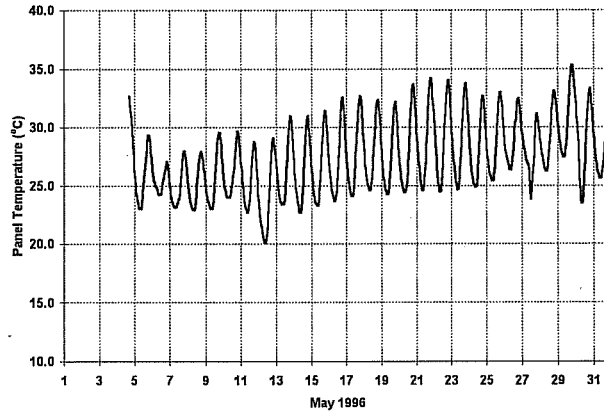


Figure 5.4: Datalogger panel temperatures recorded during May 1996.

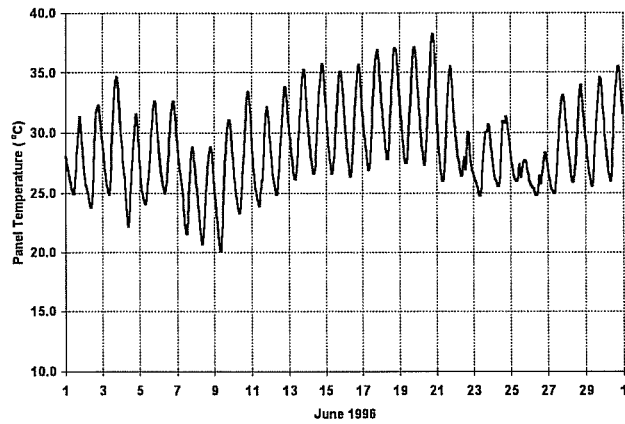
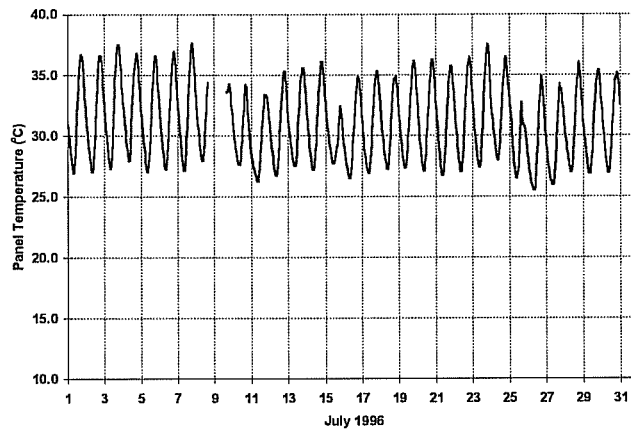


Figure 5.5: Datalogger panel temperatures recorded during June 1996.



*Figure 5.6: Datalogger panel temperatures recorded during July 1996.*

### **5.1.3 Effects of Cover**

The extremely low thermal conductivity of concrete insulates gauges located away from surfaces exposed to sunlight. This effect produces severe temperature gradients as discussed in Chapter 2. The positions of thermocouples in the gradient segment PC16-5 were chosen to track the effects of concrete cover on the temperature distribution. Temperatures recorded by the three instruments located in the west face of segment PC16-5 over the course of a typical summer day (June 17, 1996) are plotted in Figure 5.7. It is readily apparent that the outermost gauge T416 undergoes relatively large fluctuations in temperature on a daily basis. During this particular day, a maximum temperature change of about 14° C occurred at the location of T416.



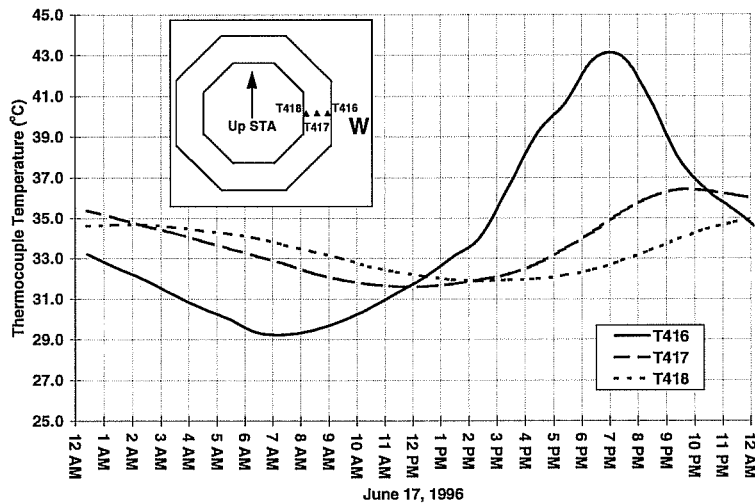


Figure 5.7: Comparison of temperatures recorded through the thickness of the west wall on June 17, 1996.

In contrast, the temperature changes are much smaller at the middle of the thickness of the pier’s west wall (T417). The temperatures here range from about 31.5° C at midday to just over 36° C at 9:00 PM. The temperature change of about 5.5° C is significantly less than that recorded by T416 at the outer face. T418, located at the inner face, experiences even smaller thermal fluctuations.

A comparison of the peak temperatures of the three gauges illustrates the time lag associated with the concrete’s thermal properties. The peak reading of T416 occurred at 7:00 PM. This is also the peak temperature gradient with about 10° C difference between T416 and T428. The temperatures recorded by T417 peaked about 3 hours later at 10:00 PM. Based on the early morning temperatures, one can estimate that the peak for thermocouple T418 occurred about 5 hours after that of T417, and 8 hours after T416. Thus, the occurrence of peak temperatures through the section being heated appear to “decelerate” as heat travels through the pier wall’s thickness. The difference in temperature between T416 and T417 is greater than that between T417 and T418, indicating a nonlinear temperature distribution through the wall.

Curiously, the lowest temperature points for each gauge do not “decelerate” in occurrence but instead “accelerate.” The lowest temperature recorded by T416 at 7:00 AM is followed by the lowest reading at T417 about 5 hours later. Similarly, T418 recorded its lowest temperature at 3:00 PM, about 3 hours after T417 and 8 hours after T416.

#### **5.1.4 Effects of Shading**

Thermocouples were distributed in segment PC16-5 to measure the shapes of temperature gradients occurring there. However, only a minimal number of thermocouples were placed in segments PC16-1 and PC16-7. The arrangements of instruments in these segments are not adequate to directly measure the thermal gradient shapes.

One can approximately deduce the gradient shapes in these segments by comparing thermocouple measurements at corresponding locations in each segment. Figure 5.8 shows temperatures recorded on June 17, 1996, for thermocouples located in similar positions in segments PC16-1, PC16-5, and PC16-7. Included for comparison is one thermocouple located in the capital segment and designated T511. The temperature tracks for segments PC16-5 and PC16-7 are almost identical because the two segments are both fully exposed to sunlight during the day. PC16-1 is continually shaded by the two overpasses of Interstate Highway 35 (see also Figures 3.2 and 3.7). The temperatures it experiences are lower overall and vary less than those of the upper segments exposed to direct sunlight. The capital thermocouple T511 should exhibit a similar curve to those of segments PC16-5 and PC16-7 due to the capital’s full exposure to sunlight. However, T511 is located at a position of slightly more cover, causing it to experience smaller variations in temperature throughout the day. The magnitudes of the temperatures measured by T511 are similar to those occurring in the exposed column segments.

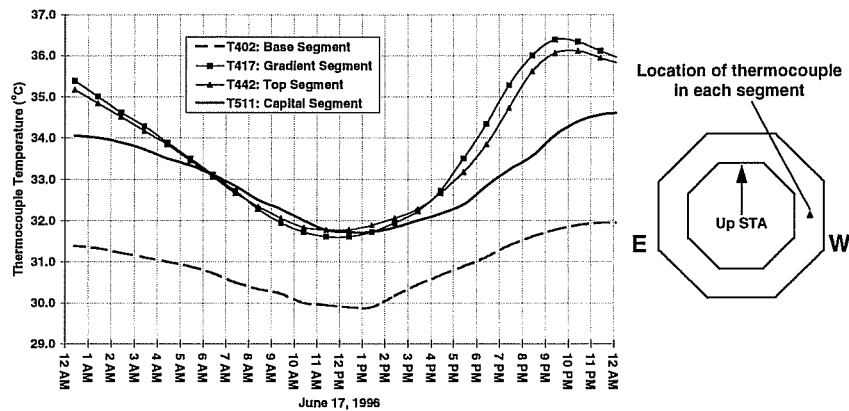


Figure 5.8: Comparison of temperatures at locations along the height of pier P16.

Therefore, it can be assumed that temperature gradients will exhibit similar shapes along the entire sunlit portion of the pier's shaft. The shapes of gradients in the shaded portion of the shaft cannot be determined. The capital will experience somewhat different gradient shapes due to its monolithic cross section.

## 5.2 THERMAL GRADIENTS

### 5.2.1 Pier Shaft Gradients

The shapes of thermal gradients occurring in the hollow, octagonal pier shaft cross-section can be directly obtained from the thermocouple measurements in segment PC16-5. Three thermocouples were placed through the thickness of each wall of the shaft. This distribution allows gradient shapes to be determined along four axes normal to the pier's longitudinal axis.

Figure 5.9 shows thermal gradient shapes plotted along an axis oriented north-south through the pier's cross-section. These temperature distributions were measured over the course of one day on June 17, 1996. As stated earlier, this day represents a typical summer day in Austin with hot, sunny weather and very little cloud cover.

Therefore, the plots in Figure 5.9 represent typical temperature gradients occurring on hot summer days.

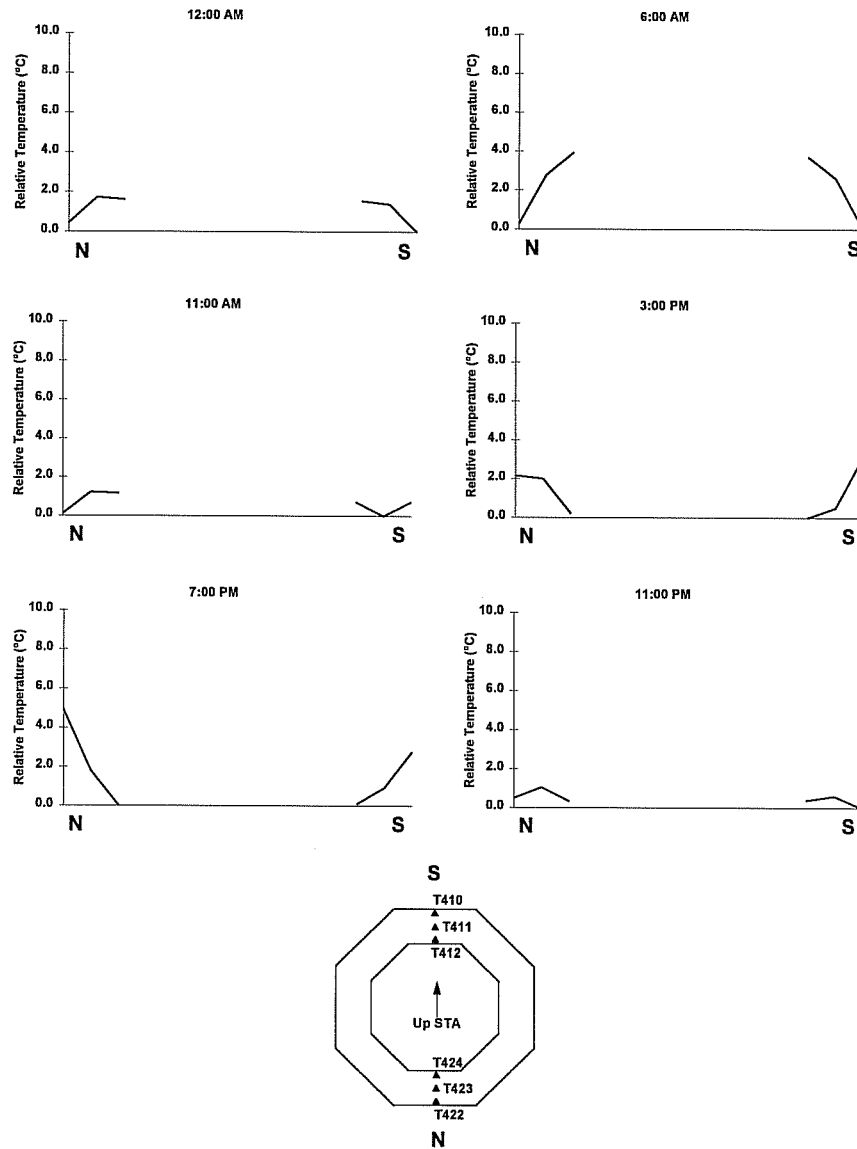


Figure 5.9: One day cycle of thermal gradients along the north-south axis of the pier P16 cross-section on June 17, 1996.

From midnight until early morning the pier's outer surface undergoes cooling as heat from the previous day is re-radiated into the cooler ambient air. The 6:00 AM plot shows that the outer surface is cooler than the inner core. The southern face of the pier does not begin to heat up until about 11:00 AM. At this time the section's thermal gradient appears relatively flat because the warming ambient air has caused temperatures to rise on the northern and southern faces to nearly those in the interior of the pier. By 3:00 PM even the shaded north face has warmed above the level of the interior. Temperatures continue to rise on the outer faces until the ambient air temperature begins to drop later in the evening. By 11:00 PM the outer faces have cooled to levels below those of the inner core. It is apparent from these plots that the north-south axis does not undergo significant *differential* thermal gradients during the course of a typical summer day. Nevertheless, the outer faces undergo significant thermal changes compared to the interior of the pier's section.

Similar to the previous plot, Figure 5.10 shows the distribution of temperatures along an axis oriented northeast-southwest that occurred on June 17, 1996. As in the previous plots, the outer faces cool significantly during the early morning hours. However, by 11:00 AM the northeast face has undergone heating due to indirect sunlight during the first few hours after sunrise. Heating of the outer surfaces continues throughout the day, and by 7:00 PM the southwest face exhibits higher temperatures than the rest of the axis. After sunset cooling takes place due to cooler ambient air temperatures and re-radiation from the pier's surface.

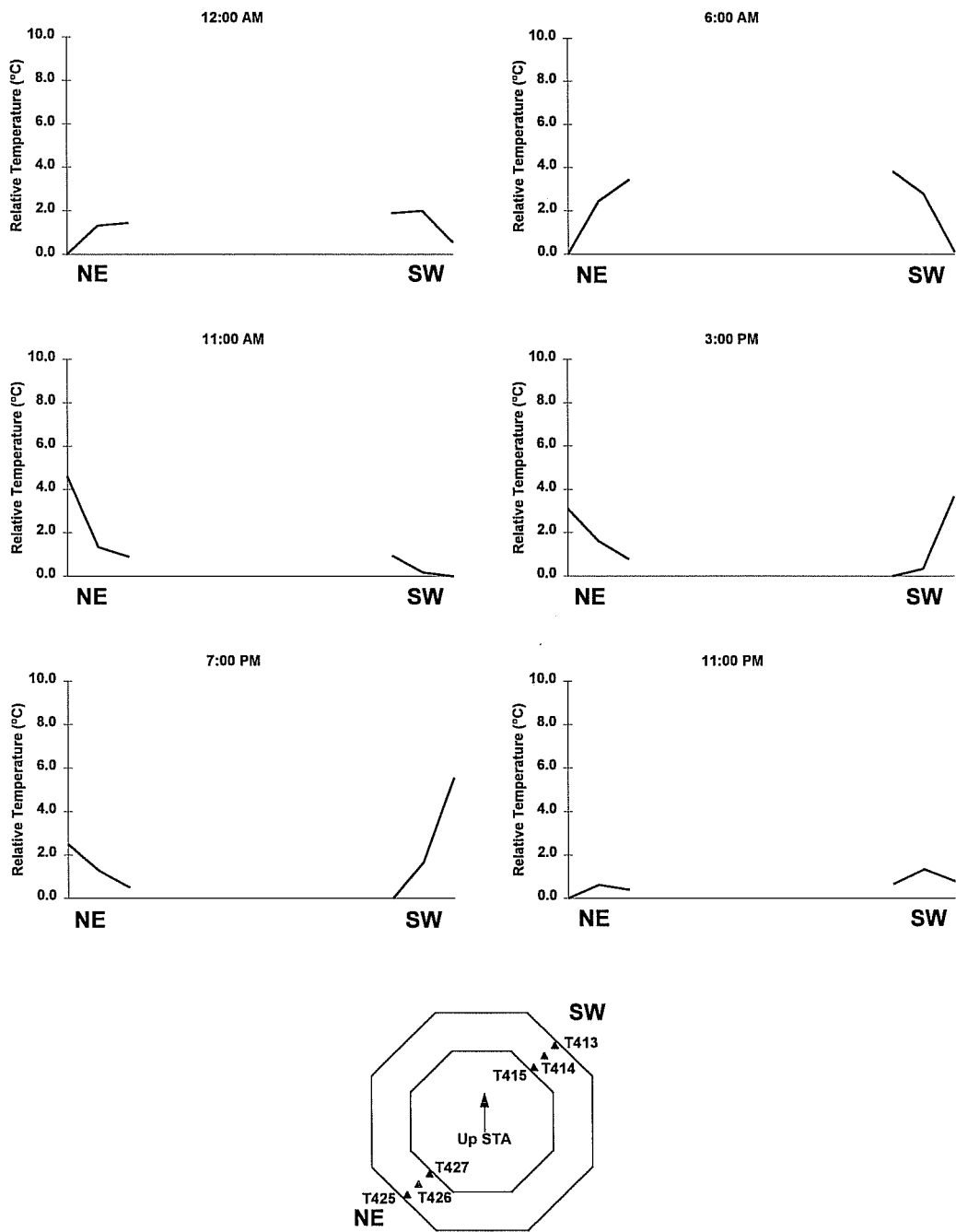


Figure 5.10: One day cycle of thermal gradients along the northeast-southwest axis of the cross-section: June 17, 1996.

The east-west axis of the pier's cross-section almost always undergoes the largest variations in temperature over the course of a day (see Figure 5.11). At 6:00 AM the outer surfaces of the pier are several degrees cooler than the interior. Throughout the morning the eastern face undergoes rapid heating as radiation from the rising sun strikes it directly. By mid-afternoon the east and west face temperatures have equalized, but the outer surfaces are much warmer than the pier's interior. The largest differential gradient occurs around 7:00 PM, when the west face is 10° C warmer than the interior, and 7° C warmer than the eastern face. High afternoon air temperatures and direct sunlight combine to heat the western face to a much higher level than along the rest of the axis. Note that the shape of this gradient is very similar to that of the AASHTO Code design gradient discussed in Chapter 2.

As shown in Figure 5.12, the northwest-southeast axis undergoes heating and cooling in a similar fashion to that of the east-west axis. However, the gradients' differential magnitudes are slightly less. The northwest face heats up significantly during the afternoon, reaching relative levels close to that of the western face.

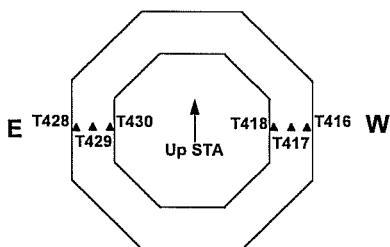
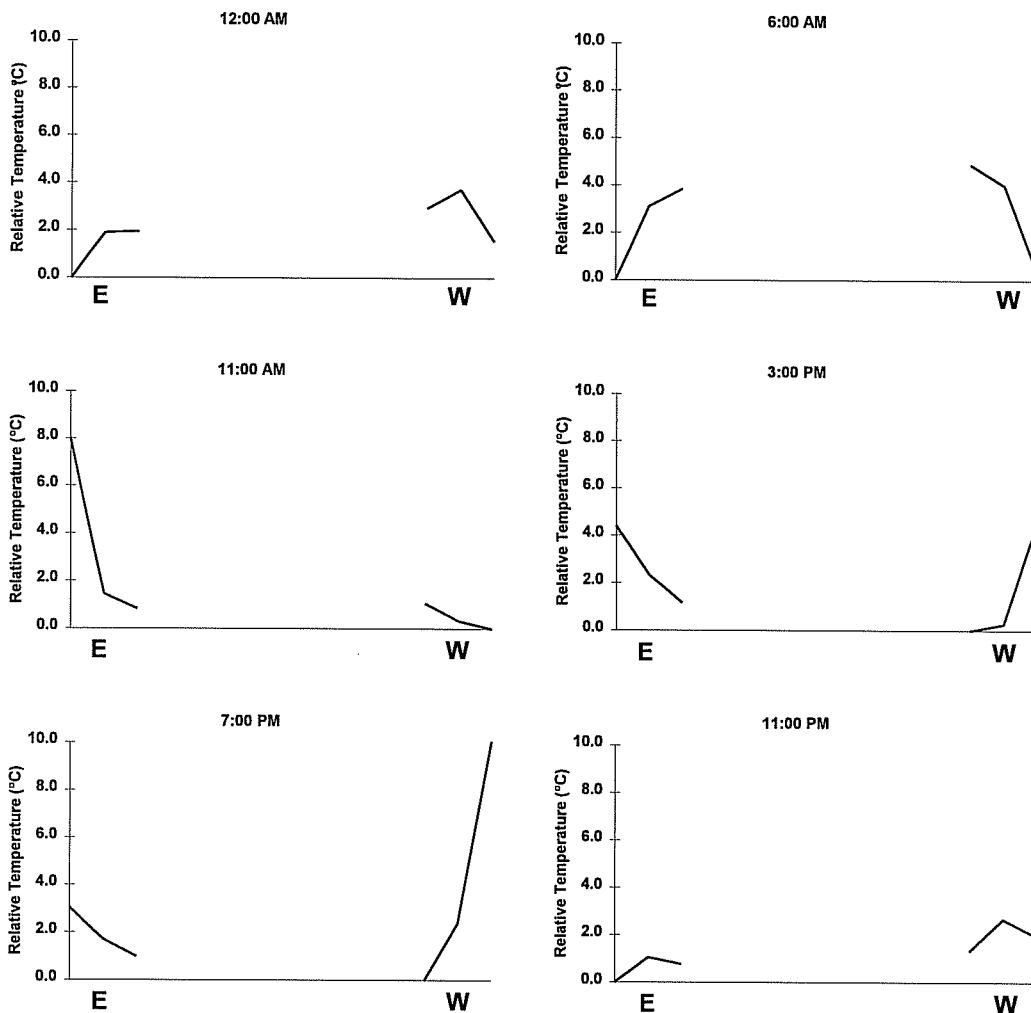


Figure 5.11: One day cycle of thermal gradients along the east-west axis of the cross-section, June 17, 1996.



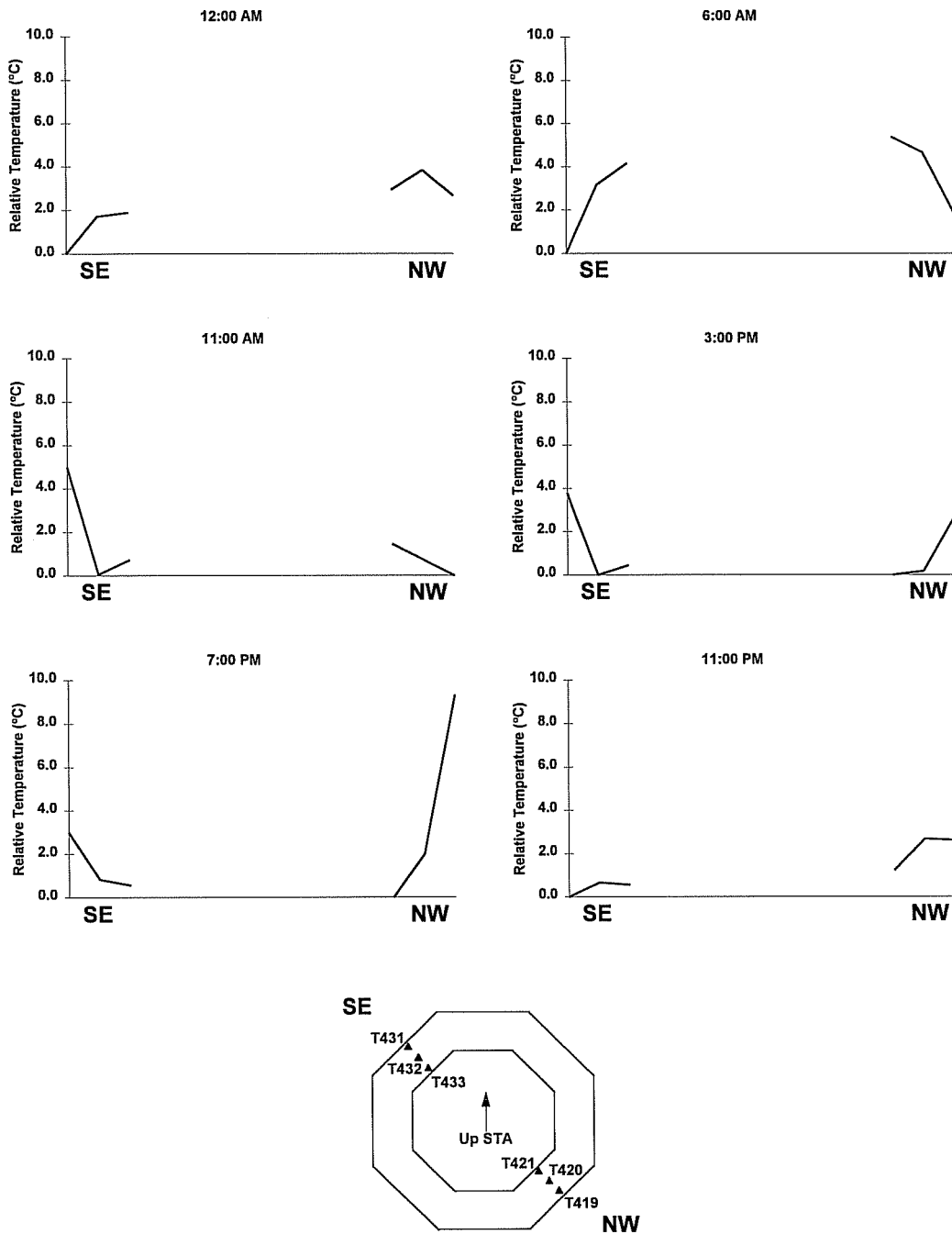


Figure 5.12: One day cycle of thermal gradients along the northwest-southeast axis of the pier's cross-section, June 17, 1996.

### **5.2.2 Capital Gradients**

Thermocouples were also installed to determine thermal gradients in the monolithic capital segment PC16-8 (see Chapter 3 for a detailed discussion of gauge locations in the capital). Figures 5.13 through 5.16 show plots of thermal gradients measured by the bottom layer of thermocouples located about 75 mm from the bottom face of the capital segment. As discussed previously, temperatures were measured along four axes oriented normal to the pier's longitudinal axis.

Gradient shapes occurring along the north-south axis of the section over the course of June 17, 1996, can be found in Figure 5.13. Temperatures were plotted for the same day for both the shaft and capital segments for comparison purposes. Note the similarities between the shapes and magnitudes of thermal gradients from the capital and from the pier segment PC16-5 (see Figure 5.9). Temperatures at the outside faces of the capital tend to rise and fall with respect to the inner core throughout the day.

Figure 5.14 illustrates gradient shapes along the northeast-southwest axis of the capital's cross-section. Again, both the shapes and magnitudes of these temperature distributions are similar to those found in the hollow shaft section discussed earlier and plotted in Figure 5.10. Gradients oriented along the east-west and northwest-southeast axes also exhibit characteristics similar to their counterparts in segment PC16-5 (see Figures 5.15 and 5.16). The maximum relative temperature recorded along the east-west axis is approximately 11° C, slightly larger than that found in the hollow shaft. This is most likely due to the well-insulated location of T517 deep within the concrete at the centerline of the capital's cross-section.

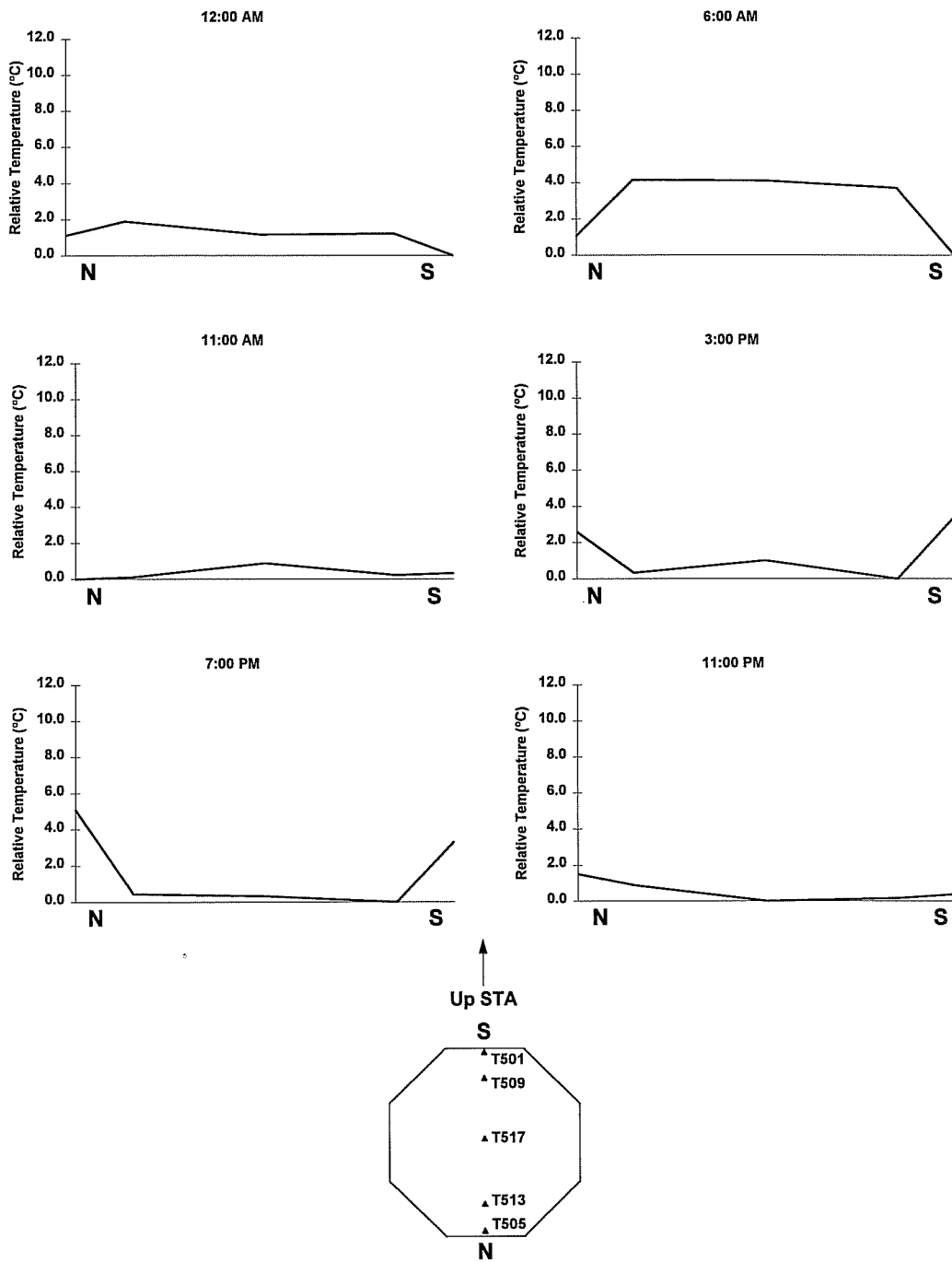


Figure 5.13: One day cycle of thermal gradients occurring along the north-south axis of the capital segment cross-section on June 17, 1996.

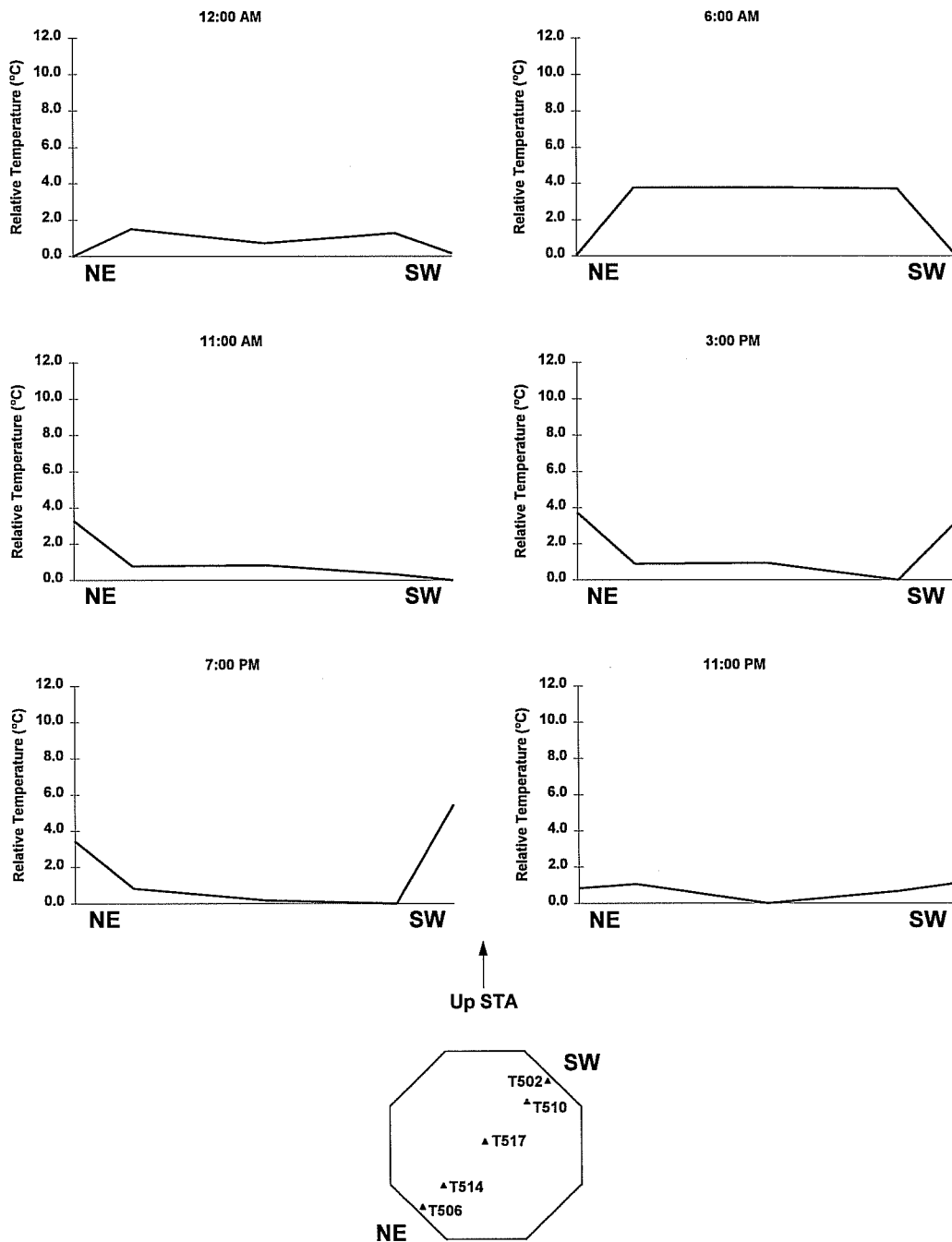


Figure 5.14: One day cycle of thermal gradients along the northeast-southwest axis, capital segment PC16-7, June 17, 1996.

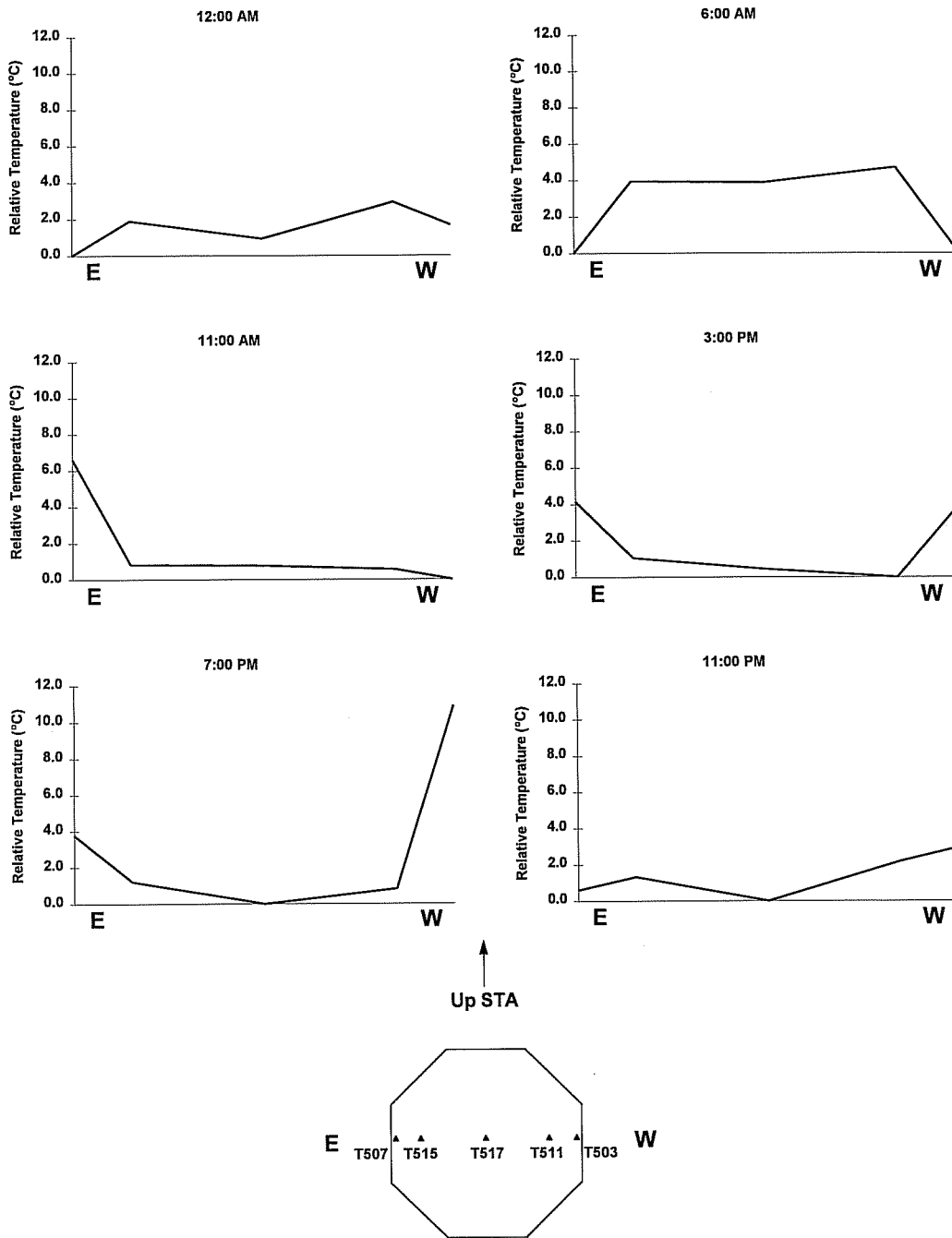


Figure 5.15: One day cycle of thermal gradients along the east-west axis, capital segment PC16-8, June 17, 1996.

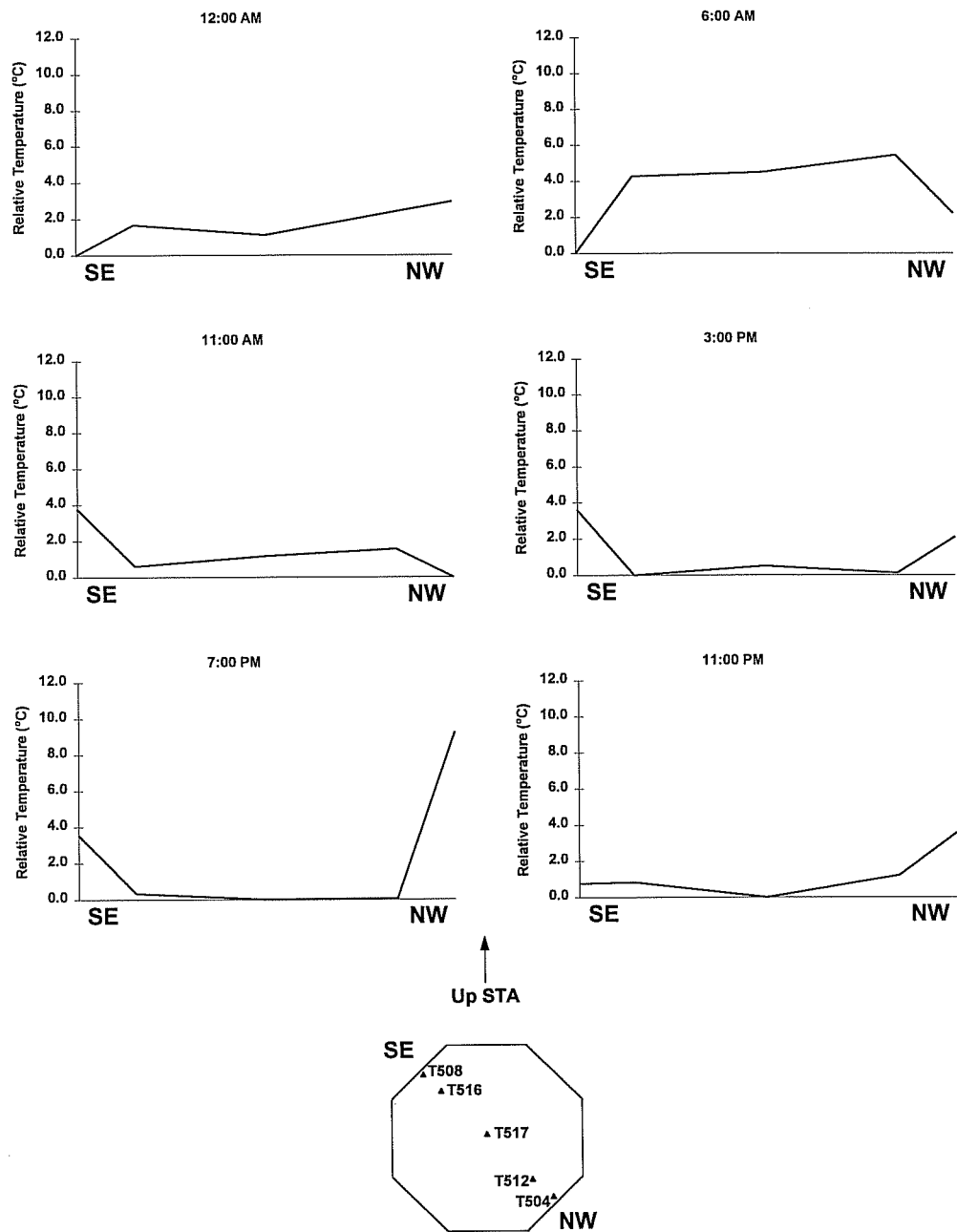
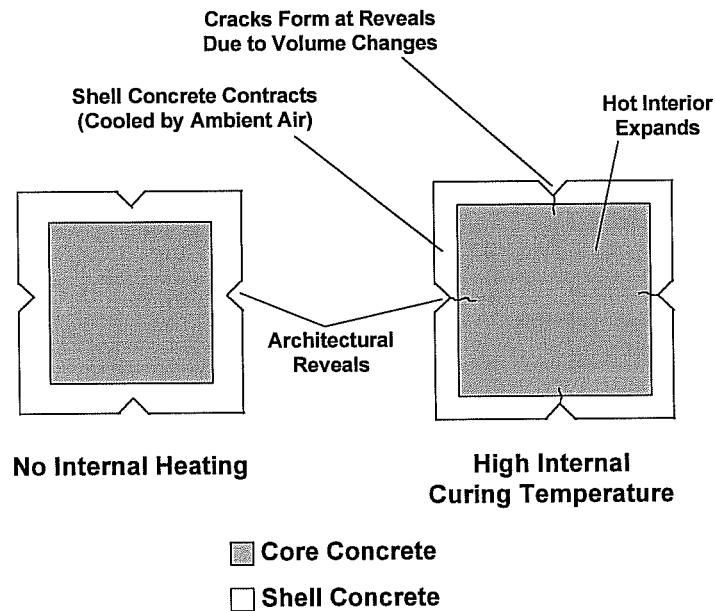


Figure 5.16: One day cycle of thermal gradients along the northwest-southeast axis, capital segment PC16-8, June 17, 1996.

### 5.2.3 Capital Curing Gradients

Large thermal gradients can be induced during the construction of large monolithic concrete members. One of the byproducts of the concrete curing process is waste heat. Because of concrete's poor thermal conductivity, waste heat generated in the middle of a large monolithic member is trapped in the interior by the surrounding concrete, producing large thermal differences between the hot inner core and the cooler outer surface. During production of the capital segments, the contractor noticed small cracks along locations of reentrant corners such as reveals and blockouts. These fractures were already present when the forms were removed, indicating that they were not induced by shrinkage. Also, the cracks tended to close after several days when the capitals reached an equilibrium temperature with the ambient air. Therefore it was postulated that the cracking was due to large thermal differences between the inner core and outer surface of the capitals during curing (see Figure 5.17).



*Figure 5.17: Mechanism for cracking of large monolithic members during curing.*

Temperatures in the capital segment PC16-8 were monitored during and after casting to determine the thermal gradients present during the curing process. As shown in Figure 5.18, the inner core temperature (as measured by thermocouple T539) increased quickly after the placement of concrete was complete. The core temperature peaked about 26 hours after concrete placement and steadily declined over a period of 7 days. Meanwhile, the ambient air temperature rose and fell over the course of several daily cycles. The maximum difference between the core and ambient temperatures occurred around 11:00 PM on September 19. At this point, the temperature difference reached almost 55° C. However, this figure does not necessarily indicate when the largest temperature gradient in the concrete occurs due to the concrete's ability to store heat and dissipate it slowly (at that time the concrete's surface might still have been quite warm from the heating during the previous day.)

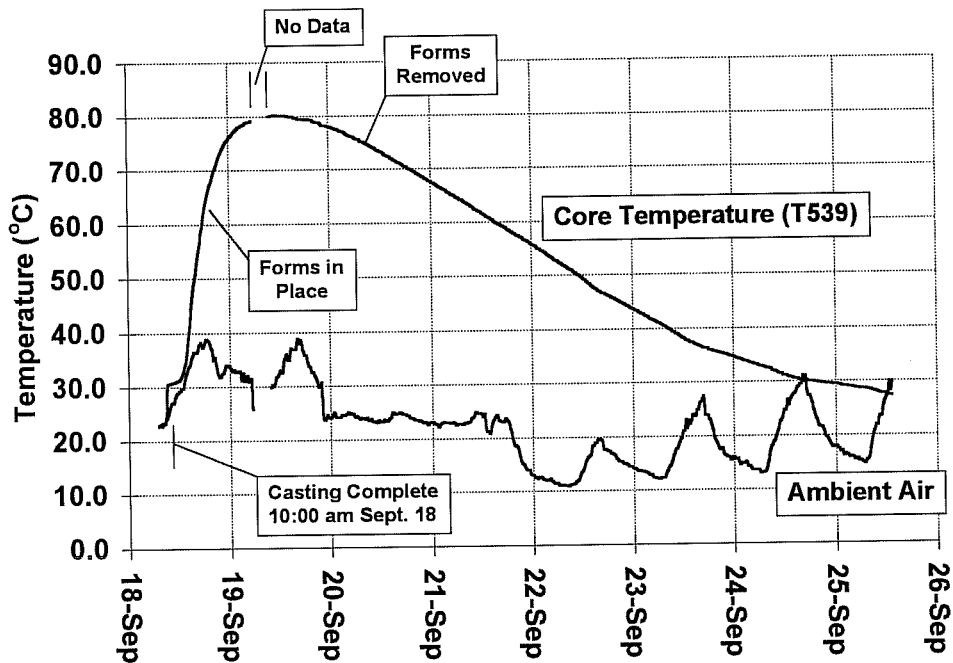


Figure 5.18: Comparison of internal curing temperature to ambient air temperature, capital segment PC16-8.



The maximum temperature gradient in the concrete occurred at noon on September 20. The gradient shape produced by the high internal curing temperatures was similar to those typically found during the early morning hours in the pier after erection. It is distinguished by a high internal core temperature with relatively cool outer surfaces (see Figure 5.19). Note, however, that the temperature difference during curing of almost 36° C is much greater than the typical differentials measured after erection (see Figures 5.13 through 5.16).

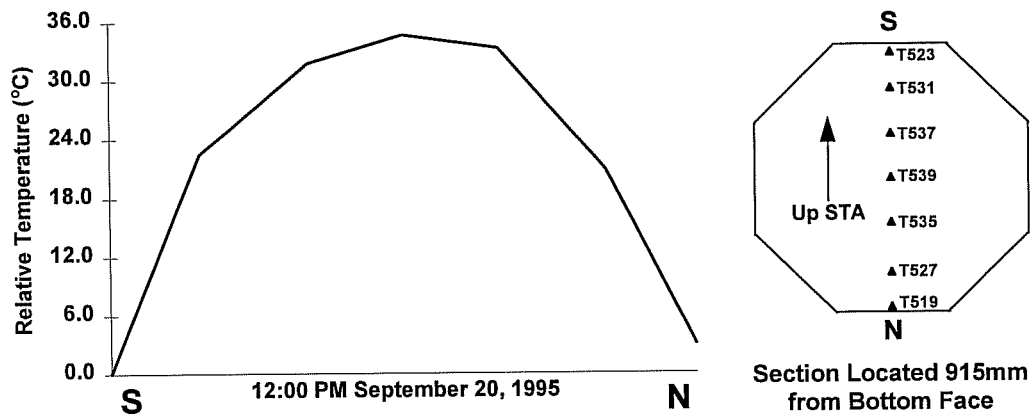


Figure 5.19: Maximum gradient shape during curing of capital.

Temperature differentials like those measured during curing of the capital can cause superficial cracking by the mechanism shown previously in Figure 5.17. To gauge the effects of the high temperatures measured in the capital segment during the curing process, the capital was inspected for cracks 24 hours after casting was completed. This was also very close to the time when the maximum difference between the inner core and ambient air temperature was observed. The cracks found during the inspection tended to follow architectural reveals, corners, and other surface irregularities as these were areas of stress concentrations (see Figure 5.20).

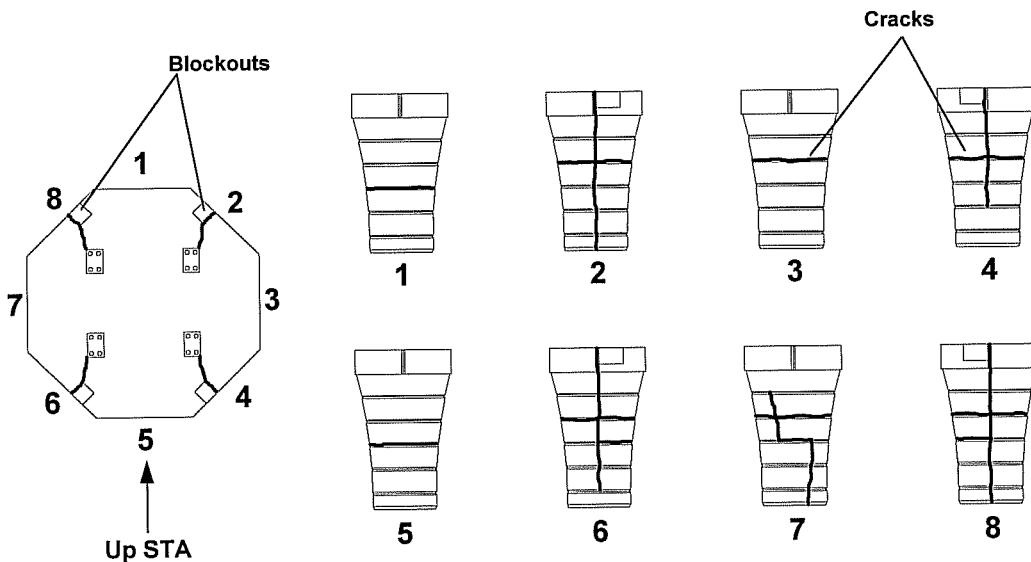


Figure 5.20: Map of cracks found during curing of capital segment PC16-8.

To prevent surface cracking of large monolithic members, the effects of temperature differences between the inner core and outside surfaces must be mitigated. This can be accomplished in three ways: the internal core temperature can be reduced, the outer surface temperature can be raised, or a combination of the two can be applied. High internal temperatures can be reduced by providing ventilation through ducts running through the interior of the member. This provides a mechanism for the escape of heat into the surrounding air. In large concrete dams, water in pipes imbedded in the concrete provide cooling. A simpler solution could be achieved by carefully insulating the outside of the member. This not only would prevent the ambient air from severely cooling the outer concrete, but would serve to hold the interior heat in the concrete, thus providing a more uniform temperature throughout the cross-section. However, merely insulating the member may be inadequate due to the extremely high internal temperatures. A combination of the two methods would produce the best results.

### 5.3 *CONCRETE STRAIN GAUGE MEASUREMENTS*

#### **5.3.1 Axial Strains**

Concrete strain gauges located in the hollow column of pier P16 were oriented to measure strains parallel with as well as normal to the longitudinal axis of the pier. Axially oriented strain gauges were placed to measure strains from thermal effects and bending strains from externally applied loads about each of the four axes normal to the pier's length (similar to the placement of thermocouples as discussed previously in this chapter). For more detailed information on the placement of gauges in the pier see Chapter 3.

Figure 5.21 shows a plot of temperature and strain changes throughout the day on June 17, 1996. The measurements were taken by instruments located along the north-south axis of the pier's cross section in segment PC16-5. Both the strain gauges and thermocouples were located near the outside of the north and south faces of the section. It should be noted that the electronic strain gauges automatically remove any strain effects due to temperature change in the concrete. The thermal strains from concrete expansion or contraction are removed internally: all strain measurements reflect strains due to stresses only. From the graph, it is apparent that strain changes occur simultaneously with the changing temperatures at the same locations. The strain gauges indicate compressive strains as the temperature increases, while tensile strains occur as the temperature drops. The theory discussed by Andres [1] (see Chapter 2) which predicts that compressive strains occur during a rise in temperature seems to match the measured strains at the locations in Figure 5.21 quite well.

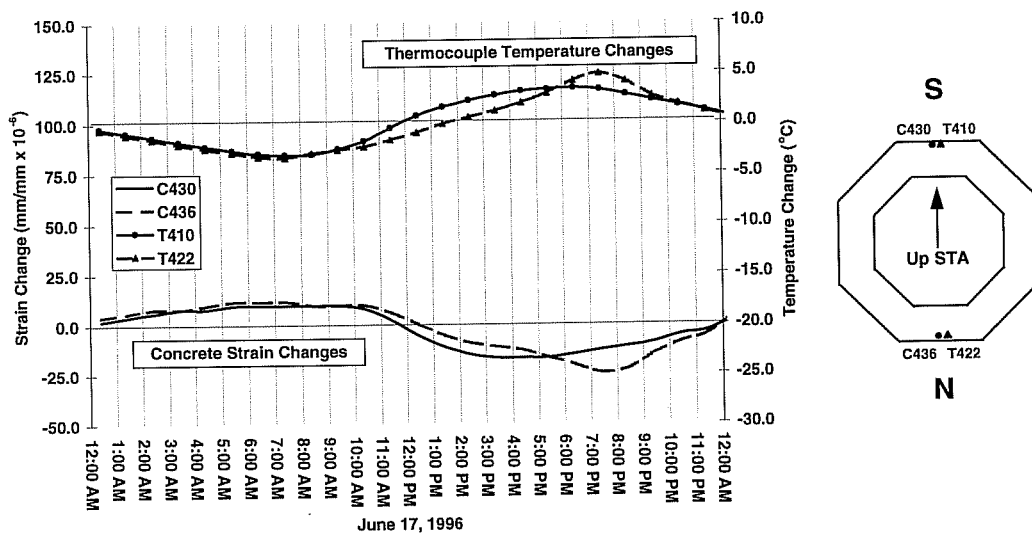


Figure 5.21: Temperature and strain changes on June 17, 1996: outer gauge locations, north-south sectional axis.

Figure 5.22 stands in marked contrast to the previous illustration. The internally balanced stresses are larger along the east-west axis than for the north-south axis shown previously. Maximum strains measured here are quite low: about 5% of the approximate maximum linear strains in the concrete. However, the longitudinal strain gauge C439 exhibits strange behavior during the cycle of changing temperatures. Instead of recording compressive strain changes as predicted by theory, C439 recorded a sharp tensile change that coincided with the rapid increase in temperature at the eastern face of the pier after sunrise. In contrast, gauge C433 undergoes compressive strain changes as the temperature at its location rises during the late afternoon (see Figure 5.22).

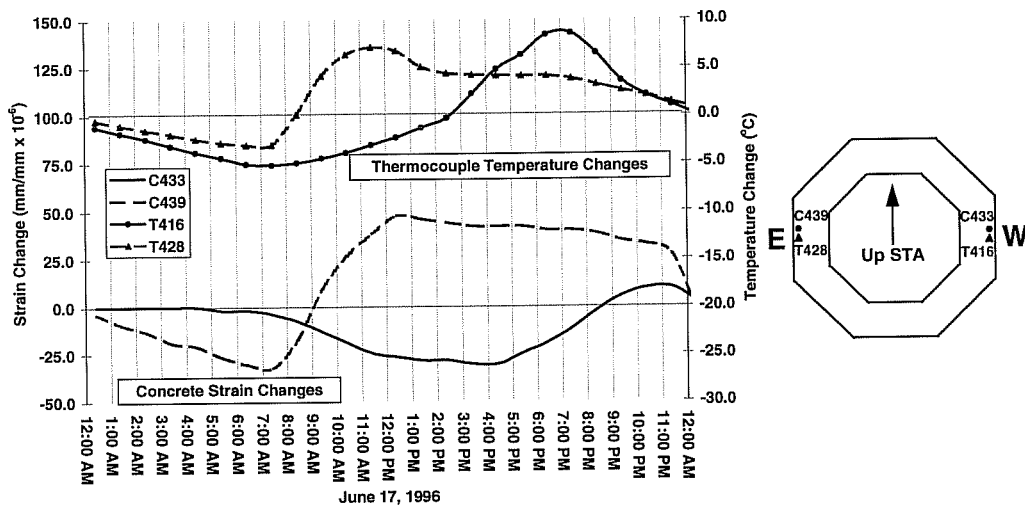


Figure 5.22: Temperature and strain changes on June 17, 1996: outer gauge locations, east-west sectional axis.

To confirm the unusual behavior of gauge C439, longitudinal strain gauges also located at the east faces of their respective segments were analyzed. Figure 5.23 shows a comparison of the behavior between the three longitudinal strain gauges located in the east faces of segments PC16-1, PC16-5, and PC16-7. It is apparent that gauge C439 exhibits anomalous behavior, as it is the only gauge in the group to record tensile strain changes during heating. The strain changes in the base segment PC16-1 are relatively small in magnitude due to the smaller rise in temperature at that shaded location. Gauge C465, located in the fully exposed eastern face of segment PC16-7, recorded much larger compressive strain changes. From Figure 5.23, it appears that the data recorded by gauge C439 is unreliable.

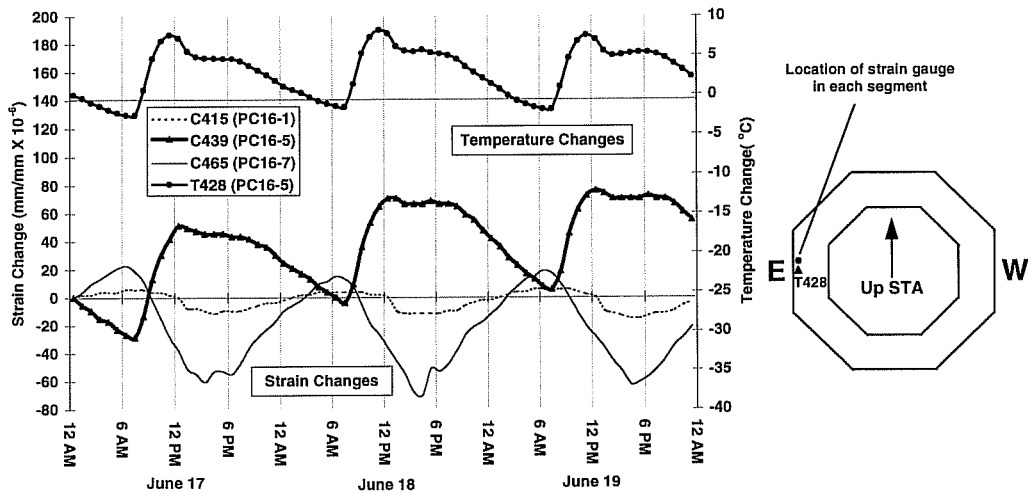


Figure 5.23: Comparison of longitudinal strains on June 17, 1996: eastern face gauge locations in segments PC16-1, PC16-5, and PC16-7.

It is also interesting to note the strain distribution through the thickness of each wall of the pier's shaft. Figures 5.24 and 5.25 show that differences in strain exist between the inner and outer strain gauges in the north and west walls of the pier, respectively. As before, the strain changes match the temperature changes throughout the day.

The strain changes in the north wall of the pier exhibit well defined opposing changes (see Figure 5.24). Again, a mechanism like that described by Andres [1] (see Chapter 2) may cause the measured strains. As the outside of the pier heats up, the outer strain gauge records a compressive change while the inner gauge undergoes tension. This reflects the hypothesis presented by Andres [1] that the core concrete is pulled in tension by the heated and expanding outer concrete shell. The shell, in turn, undergoes compressive strains caused by the restraint imposed by the cooler core concrete.

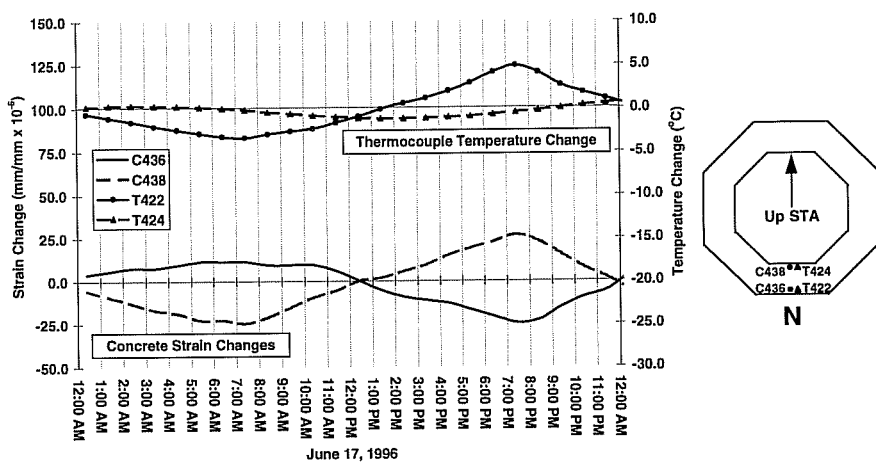


Figure 5.24: Temperature and strain changes on June 17, 1996: outer and inner gauges, north wall of pier P16.

The west face of the pier (see Figure 5.25) does not exhibit such well defined patterns through the course of the day. The strain and temperature changes do not coincide directly like those in the north wall. In general, though, the strain gauges exhibit compressive strain changes during periods of heating. Gauge C433 recorded a tensile strain change corresponding to a drop in temperature at its location after sunset.

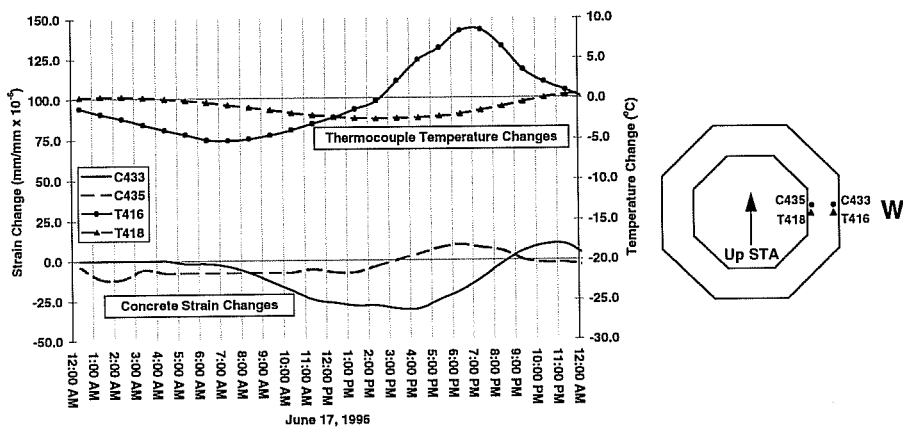


Figure 5.25: Temperature and strain changes on June 17, 1996: outer and inner gauges, west wall of pier P16.

The largest longitudinal strain changes occurred along the east-west cross-sectional axis of the pier. This behavior corresponds to the axis along which the maximum differential temperatures were observed. The observations made concerning strains using data from segment PC16-5 also correlate with the measurements of gauges located in segment PC16-1 and PC16-7. Thus, the state of strain in the entire pier appears to be influenced by temperature distributions changing within it throughout the day. However, because the pier is not restrained, all induced stresses are internally balanced.

### **5.3.2 Transverse Strains**

Strain gauges oriented normal to the pier's longitudinal axis also exhibit large changes in strain due to temperature changes. However, the daily patterns in the strains recorded by these instruments are not clearly defined.

Figure 5.26 illustrates the daily cycle of strain changes for gauges C431 and C437. These instruments are located near the outsides of the south and north faces, respectively. C431 exhibits strain characteristics similar to those shown in Figure 5.24. As the outside of the pier heats up (recorded by gauge T410) compressive strains occur due to restraint imposed by the cooler core concrete. This behavior matches that of concrete strain gauge C436 in Figure 5.24.

Unfortunately, the measurements from gauge C437 do not seem to follow the same pattern coinciding with the temperature changes at the location of the gauge. As the concrete is heated, C437 undergoes tensile strains instead of the expected compressive strains (see Figure 5.26).



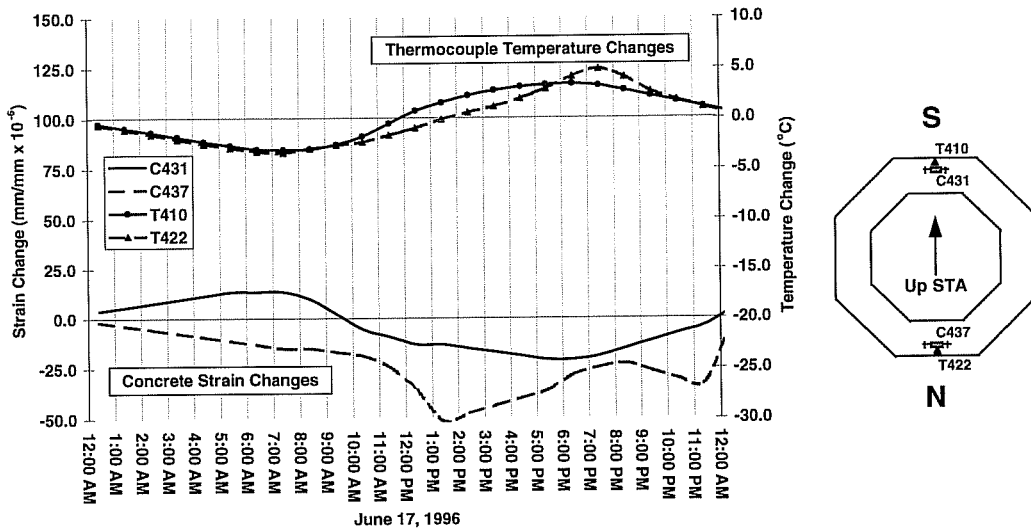


Figure 5.26: Temperature and strain changes on June 17, 1996: north and south faces, horizontal gauges.

A closer examination of the readings from gauge C437 reveals more problems. Figure 5.27 shows a graph of strain changes plotted over the course of several days. For comparison, data from gauges in similar positions in all three column segments are plotted together. The gauges located in the base and top segments (C411 and C461) appear to behave as theory would predict. They exhibit compressive strain changes during heating of the northern face of the pier, and tensile changes at night during cooling. Both gauges recorded daily patterns consistent with the regular cycle of temperatures recorded during the typical summer days represented. In contrast, gauge C437 recorded an erratic set of strain changes which did not vary in a regular, daily pattern. The shape of the plot of data from C437 indicates a malfunction in the gauge. The electronic strain gauge may have partially debonded from the steel rod, producing anomalous readings (see Figure 5.27).

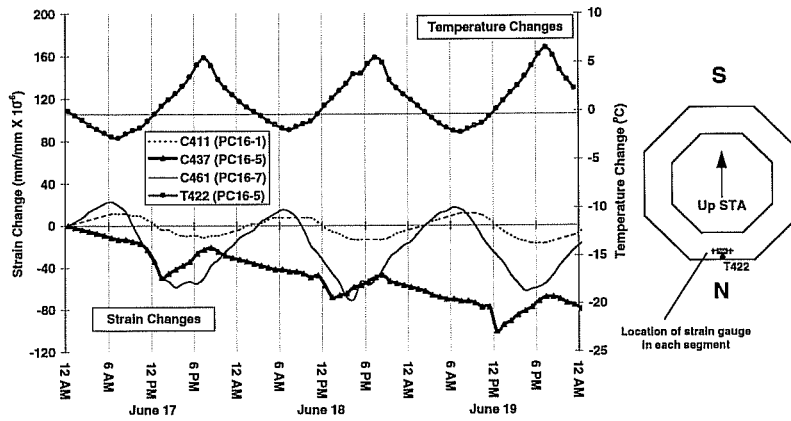


Figure 5.27: Comparison of transverse strains near the north face of the pier, segments PC16-1, PC16-5, and PC16-7.

Horizontally oriented strain gauges in the east and west faces of the pier follow recognizable patterns through the course of the day (see Figure 5.28). Concrete strain gauge C440, located on the east face, appears to exhibit strains coinciding well with the temperatures recorded at that location. Similarly, C434 undergoes compressive strain changes as the temperature at the west face of the pier rises in the afternoon. Both gauges produce data that are consistent with theoretical expectations.

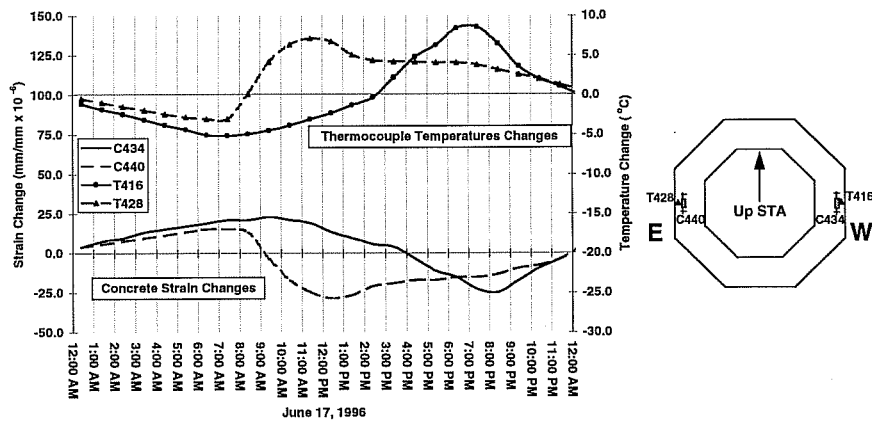


Figure 5.28: Temperature and strain changes on June 17, 1996: horizontally oriented gauges, east and west faces.

## 5.4 PIER POST-TENSIONING STRAINS

### 5.4.1 General

Pier P16 was erected during the month of April 1996, and was post-tensioned during the early morning hours of May 1, 1996 (see Chapter 4 for more information concerning the construction sequence.) Temperature and strain data were recorded once every minute during the post-tensioning process. In addition, a pressure transducer was attached to the hydraulic ram to measure jacking forces at four locations. Pier P16 was post-tensioned with four tendons each with 19 strands of 13 mm diameter running from the pier capital through a 180° bend in the footing and ending at an adjacent anchorage (see Figure 4.12). The tendons were initially stressed to 80% of the strands' guaranteed ultimate tensile strength of 1860 MPa.

Figure 5.29 shows a plot of the readings taken by the pressure transducer over the course of the post-tensioning process. The tendons were stressed in the order indicated. Note that the plots for pulls 2 and 4 show a sharp increase in pressure to about 50% of the highest measurement. This reflects the fact that pulls 2 and 4 were already partially stressed by pulls 1 and 3. Chapter 4 provides an in-depth discussion pertaining to the stressing sequence.

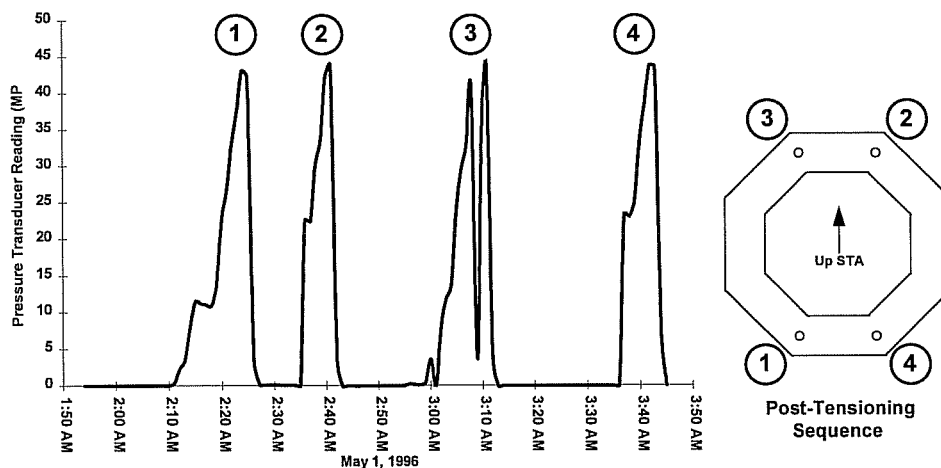


Figure 5.29: Pressure transducer readings during pier post-tensioning.

### 5.4.2 Axial Strains

Strains were measured in the hollow shaft of the pier along the longitudinal axis. Figures 5.30 and 5.31 show the measurements of strain gauges oriented along the vertical axis of the pier in segment PC16-1.

As shown in Figure 5.30, gauges located along an axis running north-south through the pier's cross-section show several well-defined trends during post-tensioning. After stressing takes place at position 1, the formerly uniform strains exhibit large differences between the north and south side of the pier. This differential strain is caused by a large load (i.e., the jacking force at position 1) eccentrically located with respect to the section's centroidal axis. Because position 1 is eccentric primarily with respect to the east-west centroidal axis, large differential strains occur in the north and south faces.

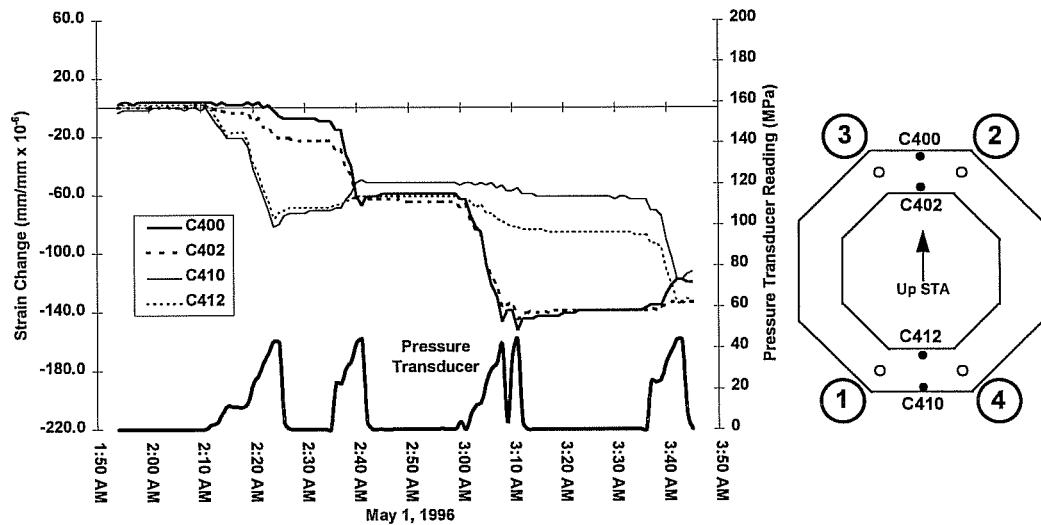


Figure 5.30: Selected axial strains in segment PC16-1 during pier post-tensioning, north-south axis locations.

Conversely, after stressing at position 2 is complete, the post-tensioning loads experienced by the pier are symmetric about the east-west axis. This is reflected in the

plots of strains after stressing at position 2: the strain levels are almost uniform in magnitude.

The loads become unbalanced again after stressing at position 3. The gauges located directly under anchor position 3 experience large compressive strains, while the gauges located on the opposite side of the section (the north wall) undergo comparatively lower compressive strain changes. Gauge C410, located near the outside surface of the north wall, experienced only slight compressive strains during the stressing operations at position 3.

Unfortunately, strain data was not recorded immediately after post-tensioning operations were completed. The data recording system was temporarily shut down for reconfiguration at this time. It is expected, however, that strains occurring immediately after post-tensioning was complete would be uniform in magnitude similar to other times during the stressing operations.

Strains plotted in Figure 5.31 show similar trends to those in Figure 5.30. In this illustration, strains are plotted from instruments located along the east-west axis of the pier's cross-section. As before, the gauges located more directly underneath the anchorage being stressed exhibit much larger strain changes than gauges in the opposing positions. C415 and C417 undergo large compressive strain changes during stressing at positions 1 and 3. Gauge C407 recorded only small strain changes even during post-tensioning at positions 2 and 4. This may indicate that the strain gauge is partially debonded from its steel rod or the presence of a void in the concrete surrounding the gauge is affecting the measurements. Unfortunately, the outer face gauge on the west side did not survive the casting process, so no correlative data are available for this face in segment PC16-1.

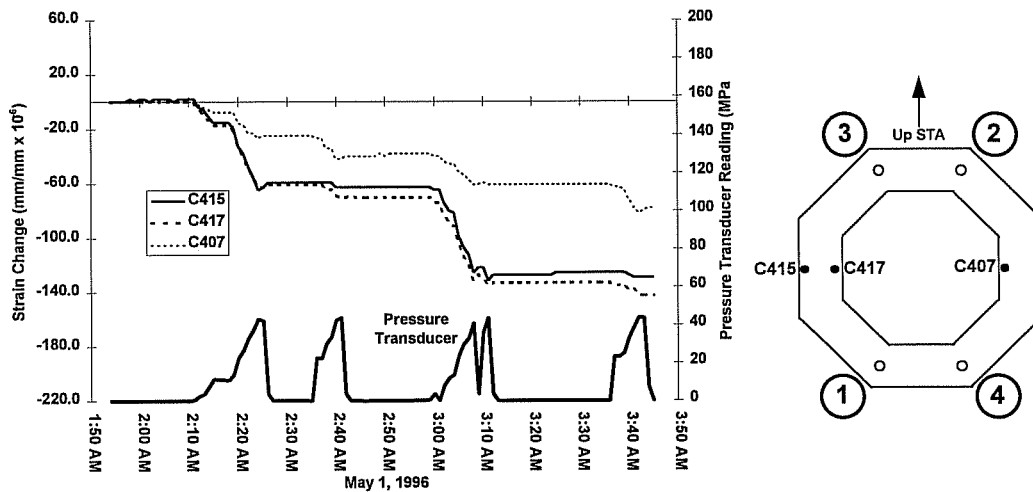


Figure 5.31: Selected axial strains in segment PC16-1 during pier post-tensioning, east-west axis locations.

However, a good estimate of the strains at the west face of segment PC16-1 can be determined from the measurements of gauges in other segments. Figure 5.32 shows a comparison between strains at the south face for the three instrumented shaft segments. Throughout the post-tensioning process, strains along the length of the pier at the south face are nearly equal in magnitude. They change in unison, reflecting the activities taking place at the top of the pier. Due to the gauges' locations at the south face, larger compressive strain changes are recorded during stressing at positions 2 and 3. The outer face of the pier even undergoes small tensile strains during post-tensioning at position 4. Thus, the strains measured in other segments can be used to estimate those in segments where gauges have failed in certain areas.

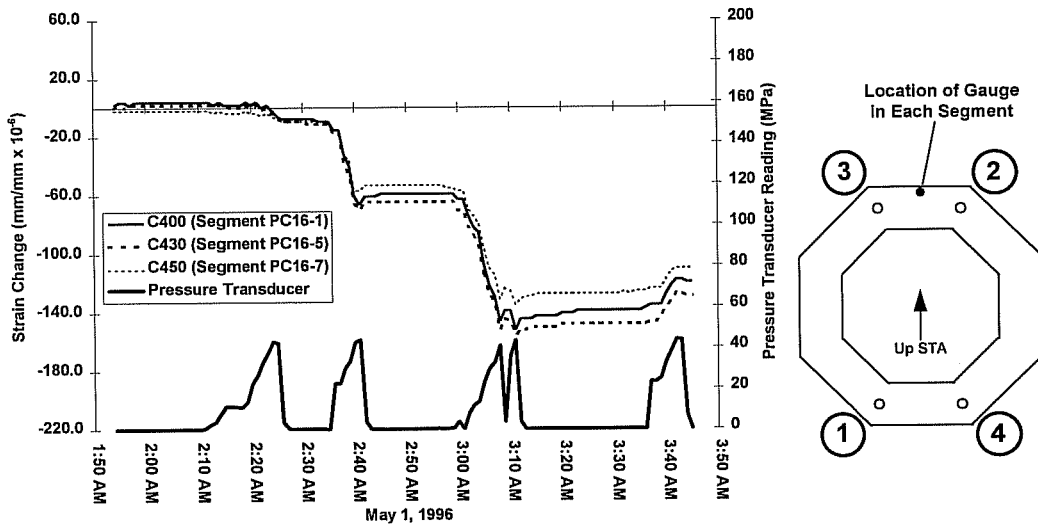


Figure 5.32: Comparison of strains along length of pier during post-tensioning.

### 5.4.3: Transverse Strains

As stated earlier, gauges were also positioned to measure strains occurring normal to the pier's longitudinal axis. In some cases, longitudinal and horizontal gauges are located in the same area, allowing a determination of the ratio of axial to transverse strains at a given point (i.e., Poisson's ratio). The graph in Figure 5.33 illustrates this relationship for gauges located on the north-south cross-sectional axis. As expected, tensile strain changes occur in the horizontal direction (gauges C401 and C411) as the pier is loaded axially. The magnitudes of transverse strains are much less than the corresponding axial strains, reflecting the Poisson effect. Similar behavior is evident in gauges located along the east-west cross-sectional axis as shown in Figure 5.34.

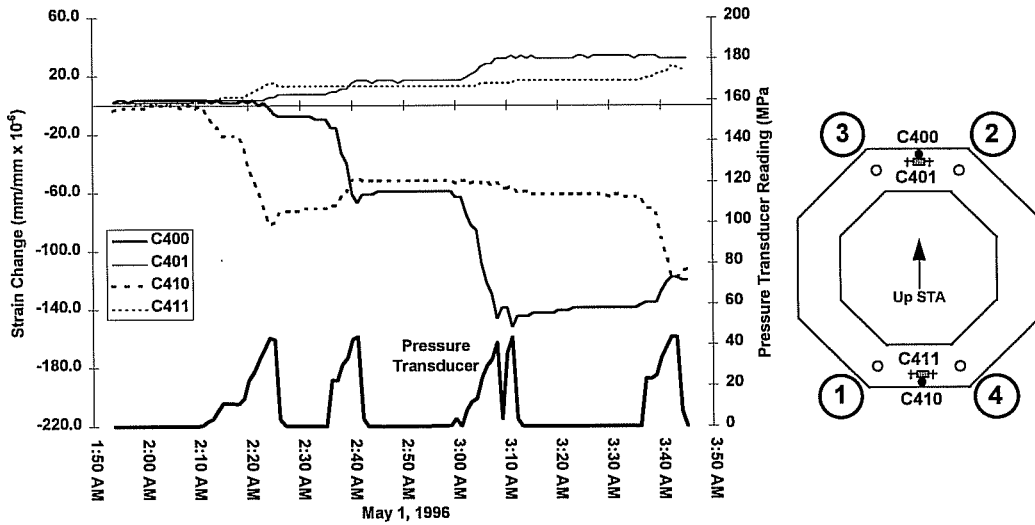


Figure 5.33: Comparison of axial and transverse strains during post-tensioning, north-south axis locations.

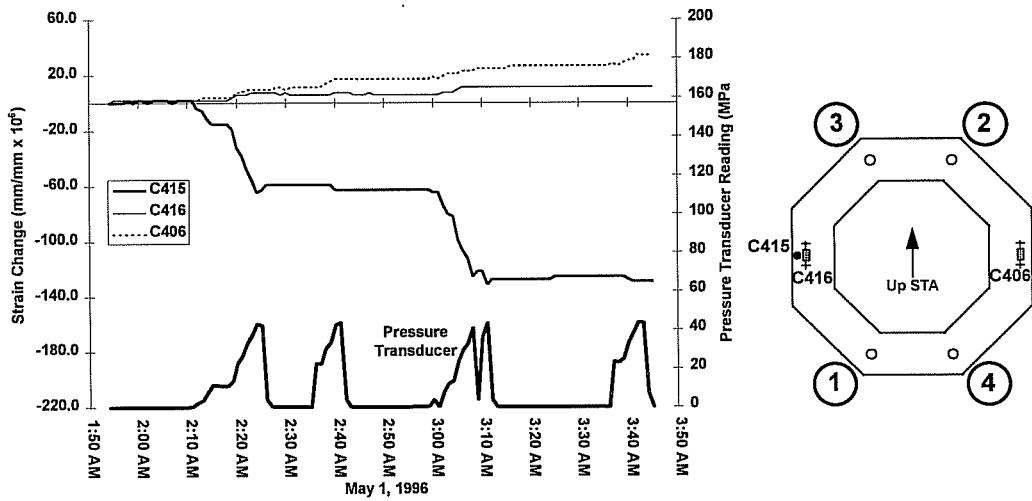


Figure 5.34: Comparison of axial and transverse strains during post-tensioning, east-west axis locations.



A comparison of transverse strains in different segments yields inconsistent results. Figure 5.35 shows strains recorded by horizontally oriented gauges located near the south face in each of the three instrumented shaft segments. While the strains in segments PC16-1 and PC16-5 are comparable, the transverse strains recorded in the segment located directly beneath the capital are significantly less. All three measurements should be very close in magnitude, especially when one considers the results from the axially oriented gauges in each segment plotted in Figure 5.32.

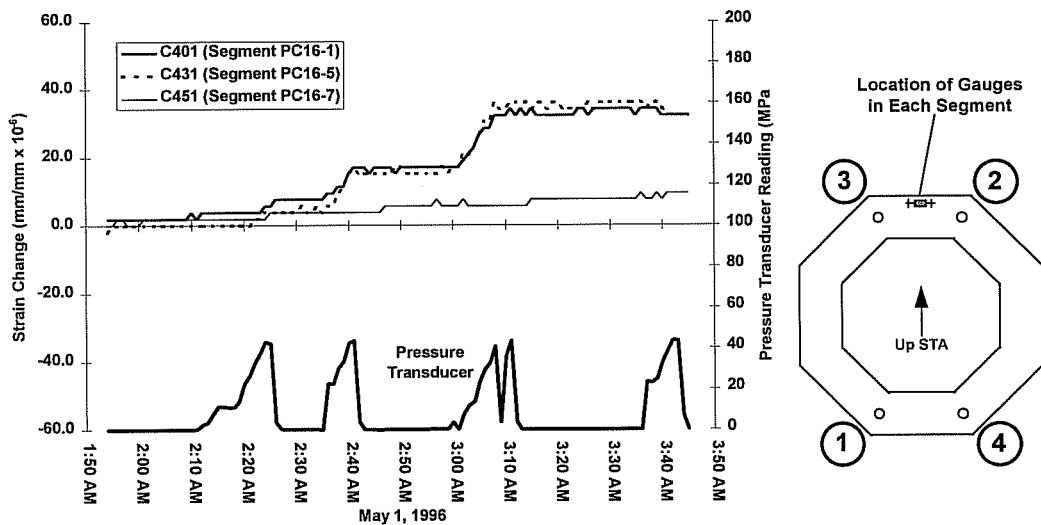


Figure 5.35: Comparison of transverse strains near the south face of each segment.

Similar inconsistencies become apparent in Figures 5.36 and 5.37. Horizontally oriented strains in both the north and east faces do not exhibit uniform behaviors or magnitudes. Thus it would appear that the transverse strains are much more difficult to predict due to their erratic behavior. The plot of data from gauge C437 in Figure 5.36 provides confirmation that the gauge is probably partially debonded from its steel rod. C437 also produced inconsistent readings under temperature loading as discussed earlier.

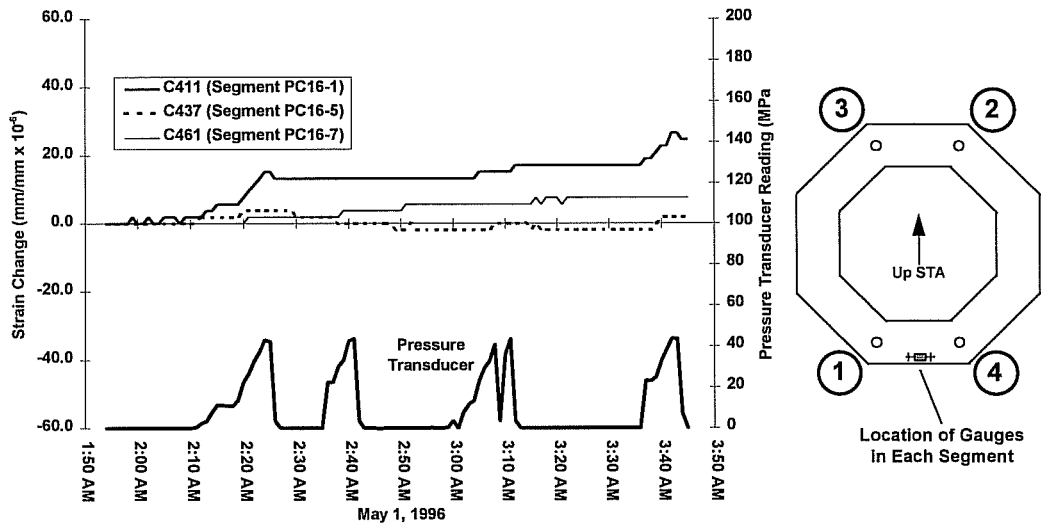


Figure 5.36: Comparison of transverse strains near the north face of each segment.

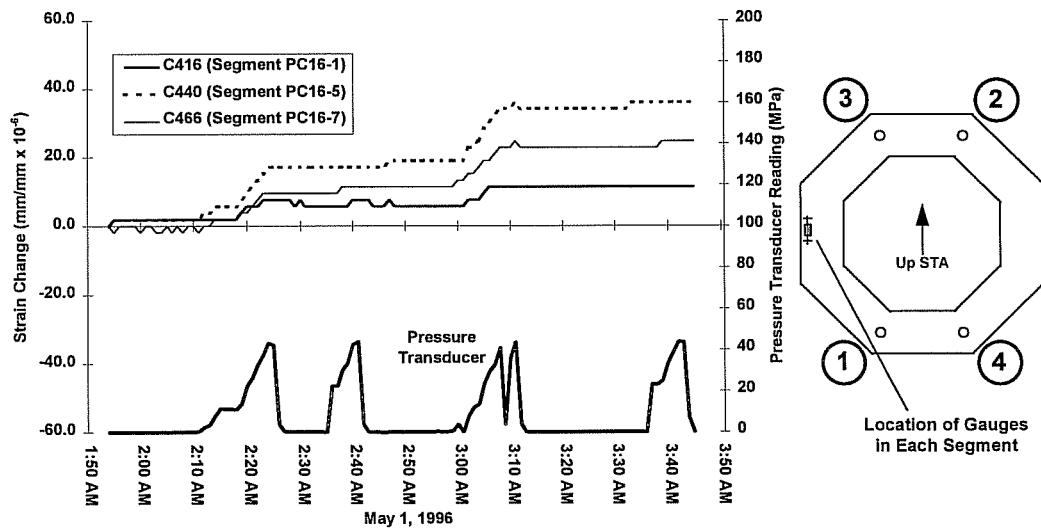


Figure 5.37: Comparison of transverse strains near the east face of each segment.

The transverse strains near the west face of the pier show the most consistent behavior (see Figure 5.38). Because of the apparent uniformity of axial strains in the same areas as the measured transverse strains (as in Figure 5.32), one would expect all of the transverse strain comparisons illustrated here to behave like those of the gauges plotted in Figure 5.38. However, this is not the case. Strains in the horizontal direction in segment PC16-7 may be partly restrained by the nearby capital segment.

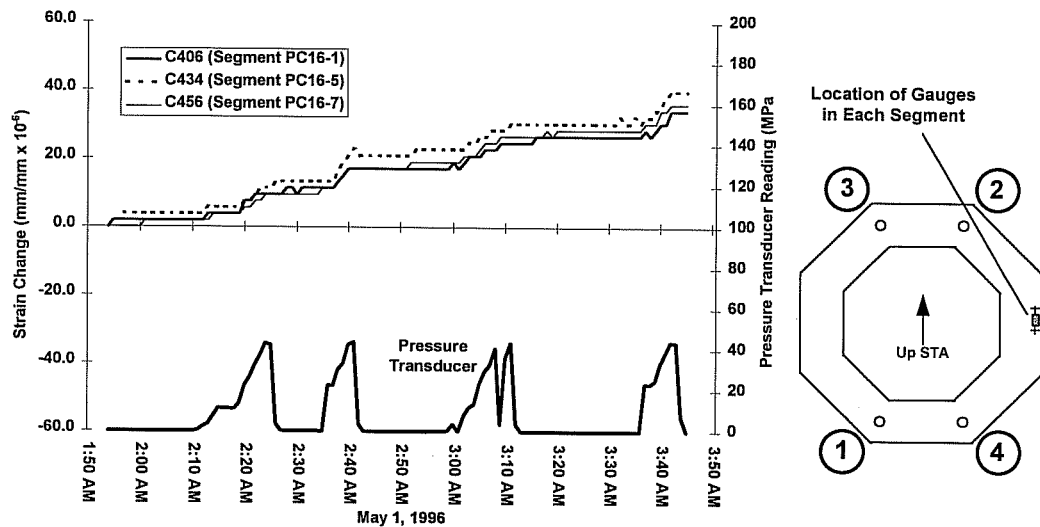


Figure 5.38: Comparison of transverse strains near the west face of each segment.

## CHAPTER 6

### *TEMPERATURE STRESS ANALYSIS*

#### *6.1 MAXIMUM OBSERVED TEMPERATURE GRADIENTS*

##### **6.1.1 Maximum Gradient Selection Process**

As discussed in previous chapters, maximum temperature gradients in bridge superstructures are associated with certain types of weather and climatic conditions. Maximum temperature effects in piers are less predictable than those in bridge superstructures due in part to their orientation with respect to the sun. Varying ambient temperatures, changing weather patterns, and the sun's daily path across the sky all contribute to an extremely complex and variable distribution of temperatures in the segmental pier's cross section.

##### ***6.1.1.1 Maximum Positive Gradient Determination***

It was determined in Chapter 5 that the highest temperatures on the pier's outer surface occurred during the late afternoon and early evening hours on the west and north-west faces. Relatively lower temperatures were present at the opposite face of the pier during these times and temperatures in the interior of the cross-section were significantly lower. Thus, the maximum non-linearity of the thermal distribution in the pier tended to occur after an entire day of solar radiation and ambient temperature heating. However, the maximum gradient acting on the pier is not simply the temperature distribution present at a given time. The maximum effective temperature gradient is the set of temperature *differences* between the most uniform set of temperatures and the set exhibiting the largest differential temperatures across the section during the course of a day. Thus, the associated strains are actually *changes* in strain induced by the changing pier temperatures.

A data analysis spreadsheet was created to determine the maximum gradients occurring in the pier over the course of four months monitored by this portion of the project. Temperatures measured by the thermocouples in segment PC16-5 were used to determine gradient magnitudes and shapes.

Two methods were used to determine the most uniform set of temperatures in the pier on any given day. First, the standard deviation of the temperatures present at each measurement time were calculated. The lowest standard deviation would indicate the time of day with the most uniform temperature distribution. Second, it was noted from the temperature distributions presented in Chapter 5 that the most uniform temperature state typically occurred during the time when the pier temperatures were lowest. Thus, the average temperature in the pier's cross-section was determined for each measurement time, and the lowest daily average was recorded as a second indicator of uniform temperature.

The time of day when the maximum non-linearity of the gradient occurred typically corresponded with the maximum difference in temperatures between opposite outside faces. For each day during the months studied, the difference in temperature between each of four sets of opposite faces was recorded. The time of the maximum occurrence was determined. Typically, there was a small peak in the temperature difference between opposing faces during the first few hours after sunrise. This was followed by a larger peak difference when the western side of the pier rose significantly in temperature around late afternoon. The largest differences in temperature between opposing faces almost always occurred along the east-west cross-sectional axis of the pier. The north and south faces were more uniform in temperature.

For each of the four months, the three days corresponding to the three largest differences in opposing-face temperatures were selected for closer examination. For each selected day, two possible gradients were identified. The first gradient was calculated using the temperatures with the lowest standard deviation. The second gradient used the temperature set with the lowest average temperature for the day. In

this way, the determination of the largest positive temperature gradient shape corresponding to daily temperature changes could be calculated for each month. These four data sets were used to analytically determine the strains and stresses on the pier caused by positive temperature gradients. They were also used as input for the finite element analysis presented in Chapter 7.

#### ***6.1.1.2 Maximum Negative Gradient Determination***

Negative gradients typically occurred in the pier during the early morning hours of each day. The outside faces of the pier were cool compared to the still-warm inner core. To determine the time of day when the pier temperatures were most uniform, the standard deviation of all of the thermocouple readings was calculated for each data set. The difference between the inner and outer face temperatures was calculated for each wall of the pier at each reading. The average of the temperature differences was then calculated for each set. The minimum of these averages indicated what time the pier temperatures were lowest on the outside of the pier relative to the inside.

Three days were selected from each month that exhibited the largest inner-to-outer average temperature differences. Temperature differences were calculated as before, and the times with the greatest differences for each month were selected as the maximum monthly negative gradients. These four data sets were also used for calculated determinations of stress and strain and as input data for the finite element analysis.

#### **6.1.2 Octagonal Shell Projection Method**

The calculation method used by Imbsen, et al [5] and Roberts [7] for determination of the longitudinal self-equilibrating stresses acting on a section was presented in Chapter 2. This method assumes that temperature varies primarily through the depth of the section. Thus, the average of all measured temperatures across the thickness of the section can be plotted at points along an axis through the depth of the

section, producing an accurate estimate of the gradient shape. This method works well for bridge superstructures heated only at the deck surface. In contrast, an octagonal pier's orientation to the solar radiation striking it causes high temperatures to occur at more than one side of the pier simultaneously. Plotting average temperatures along one axis through the depth of the pier's cross-section produces a gradient shape that is influenced heavily by high outside face temperatures (see Figure 6.1).

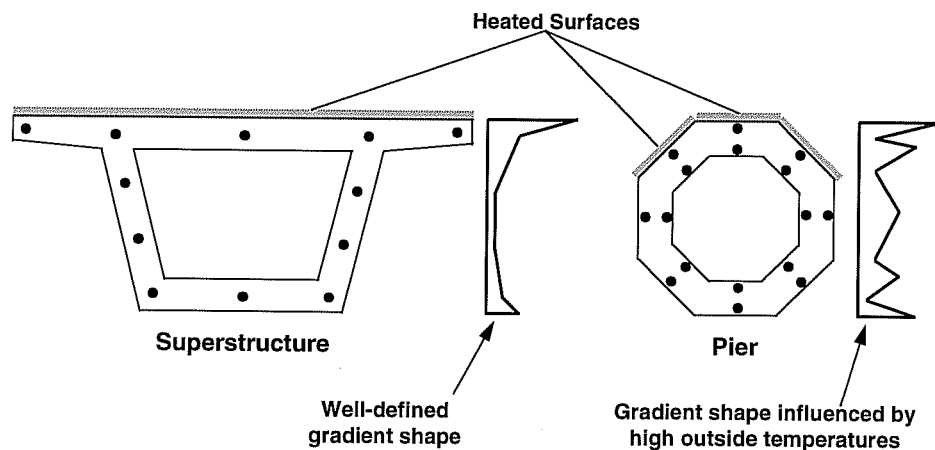


*Figure 6.1: Gradient shapes plotted using average temperatures at each depth.*

The following alternate method of determining temperature at a given depth is more appropriate for members heated on more than one side. Solving for temperature distributions with only measurements from the thermocouples present in segment PC16-5 produces gradient shapes like the one shown for the pier in Figure 6.1. A smoother gradient shape would take into account the larger interior areas of the pier's cross-section where temperatures are much cooler.

An interpolation method must be used to determine temperatures at locations away from the measured temperatures in the section. Linear interpolation through the thickness of the pier walls is not sufficient, as the temperature variation with depth is highly non-linear due to the poor thermal conductivity of the concrete. As assumed by

Imbsen, et al [5] and Roberts [7], temperatures can be interpolated across any given depth from the heated surface. Thus, the pier's cross-section can be visualized as three octagonal "shells" which do not exchange heat with each other. Temperatures can then be linearly interpolated around the perimeter of these shells with a good degree of accuracy (see Figure 6.2).

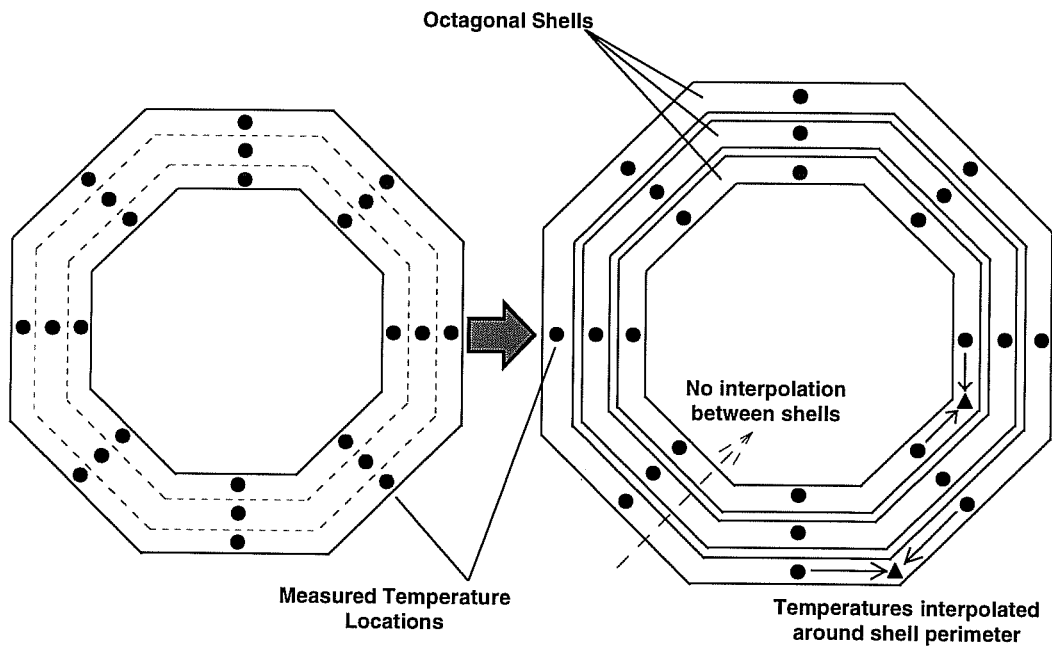


Figure 6.2: Independent octagonal "shells".

After calculation of additional temperatures at points around the perimeters of the shells, the gradient shape can be plotted as shown in Figure 6.3. The average temperature is calculated at each position along an axis of the pier's cross-section, and the results are projected onto a single axis running through the pier.



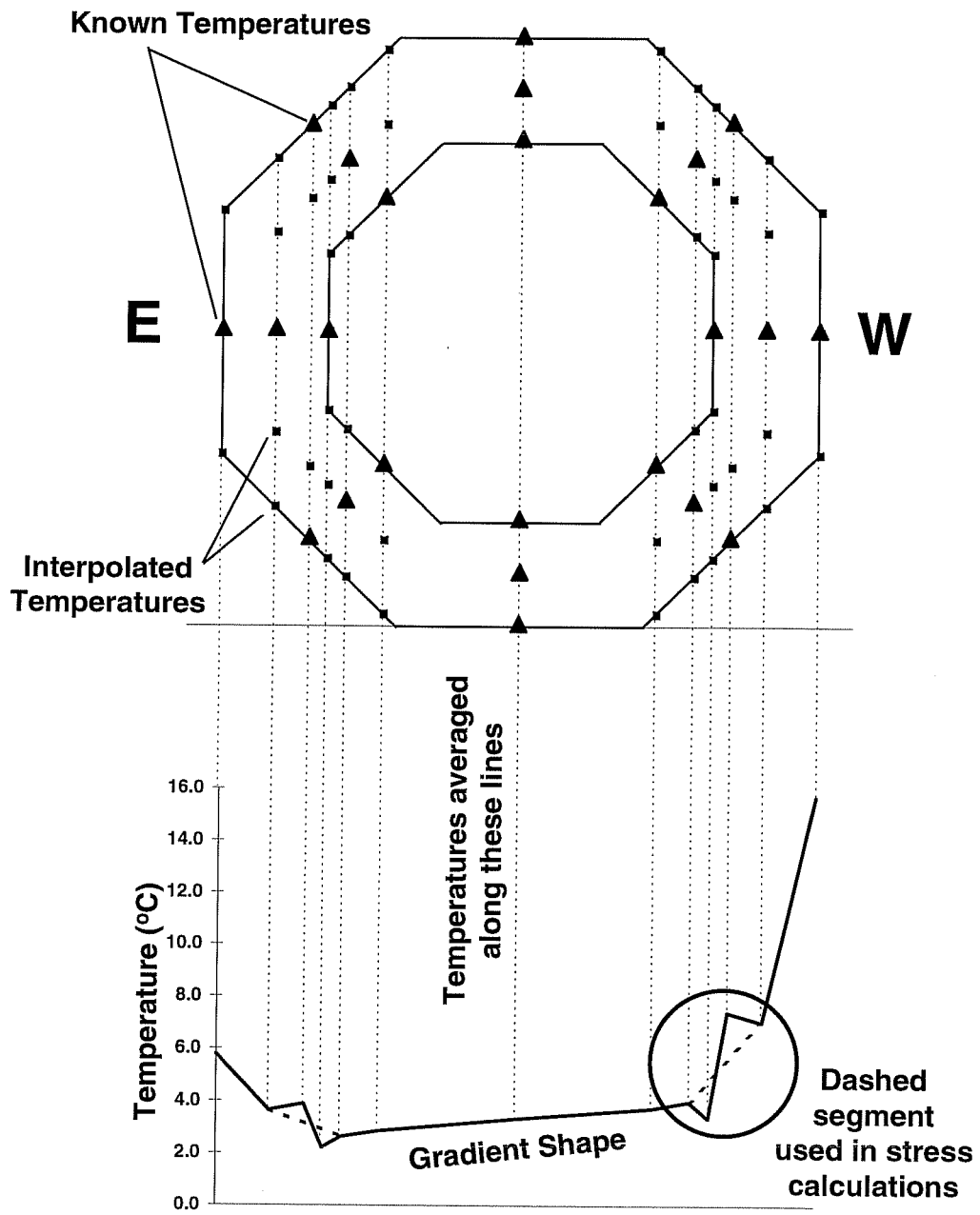


Figure 6.3: Projection of temperature gradient shape onto a single axis.

### 6.1.3 Maximum Temperature Gradients

#### *6.1.3.1 Maximum Positive Gradients*

The sets of temperature changes corresponding to the maximum positive temperature gradients measured for each month were input into a spreadsheet to calculate the projected gradient shapes using the octagonal shell method. Figure 6.4 illustrates the monthly maximum positive gradients as measured from thermocouples located in segment PC16-5. All maximum positive gradients occurred along the east-west cross-sectional axis of the pier.

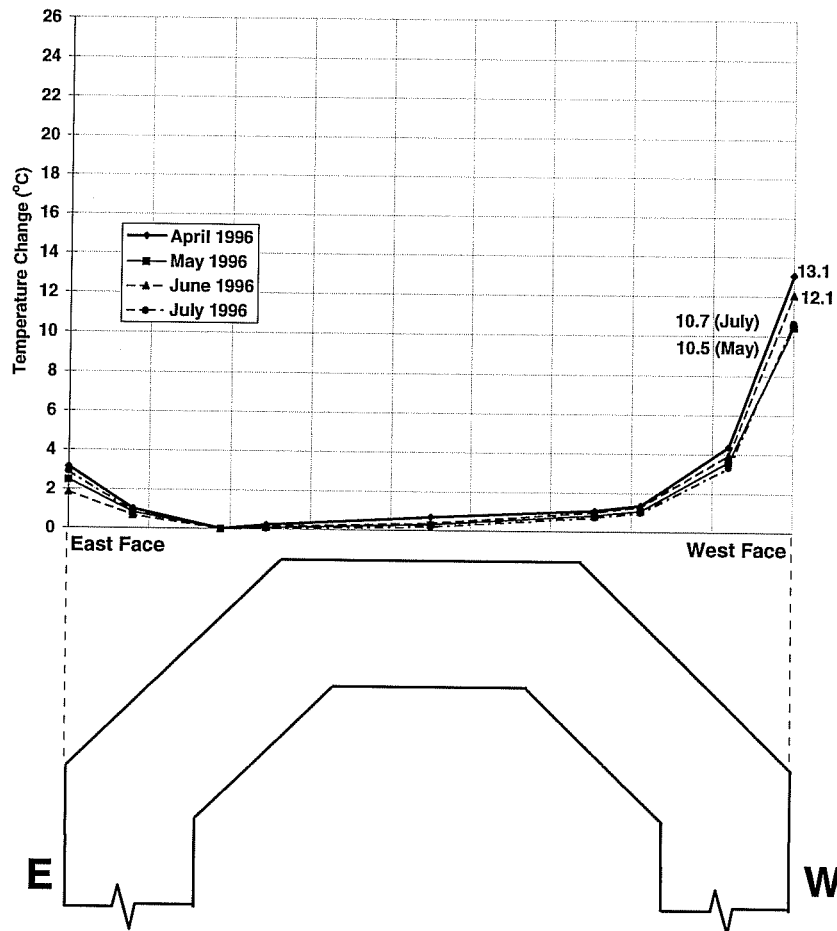


Figure 6.4: Maximum measured monthly positive temperature gradients.

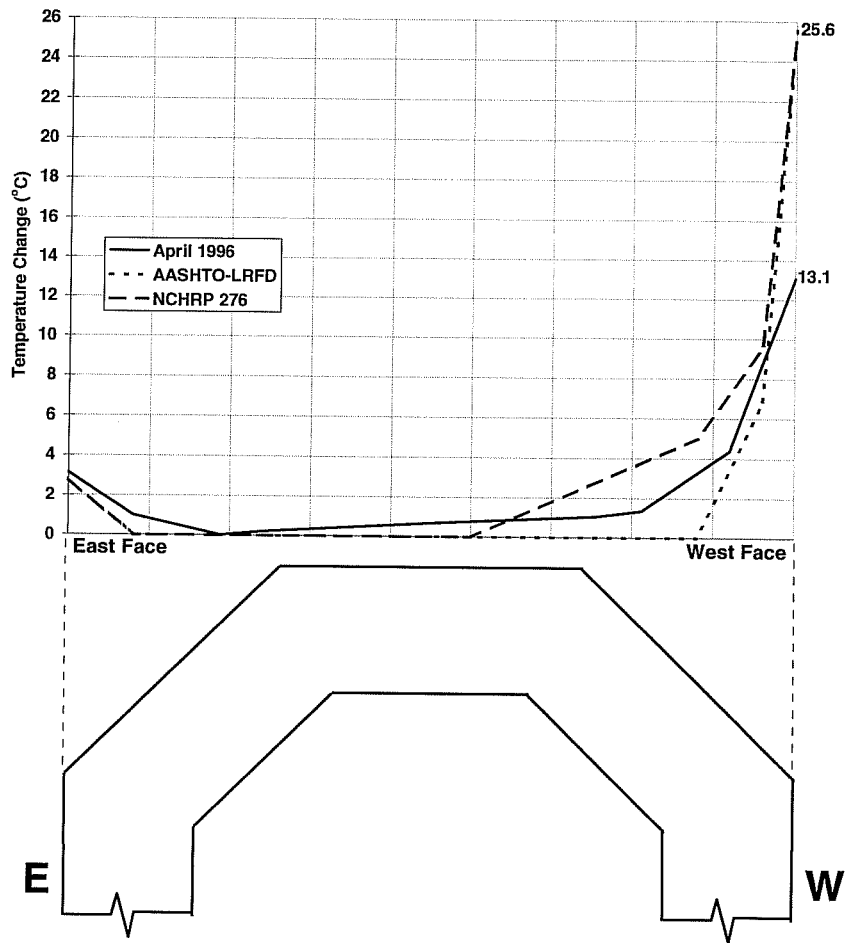


Figure 6.5: Design code positive temperature gradients.

Maximum positive temperature gradients calculated by the octagonal shell projection method were similar both in shape and magnitude for the four months monitored. The largest temperature changes occurred during April. Outer fiber temperatures on the west face were as much as 13.1°C greater than the average interior temperatures. On the east face, temperatures were only a few degrees above those in the interior (see Figure 6.4).

For the purposes of comparison, the design gradient shapes from the *AASHTO LRFD Bridge Design Specifications* [11] and NCHRP Report 276 [5] are presented in Figure 6.5, along with the measured maximum value in the pier. Design code temperature values are plotted for the pier's location in Zone 2, Austin, Texas. The design code gradients plotted in Figure 6.5 were significantly larger than even the largest measured gradient. The maximum measured positive gradient's highest temperature change was only 51% of the maximum temperature specified by both the AASHTO LRFD Code [11] and NCHRP Report 276 [5]. The LRFD Code gradient also has a sharp temperature difference between the outside fibers and the area a few centimeters from the surface. The NCHRP gradient's shape more closely follows that of the observed temperature gradient. Both design gradients, however, are larger in magnitude and more severe in shape.

#### ***6.1.3.2 Maximum Negative Gradients***

Figure 6.6 shows the gradient shapes for the maximum monthly negative temperature gradients. Results plotted are from thermocouples located in segment PC16-5. All maximum gradients occurred along the east-west cross-sectional axis of the pier. Figure 6.7 shows the design negative gradients for comparison. Design code temperature values are plotted for the pier's location in Zone 2, Austin, Texas.

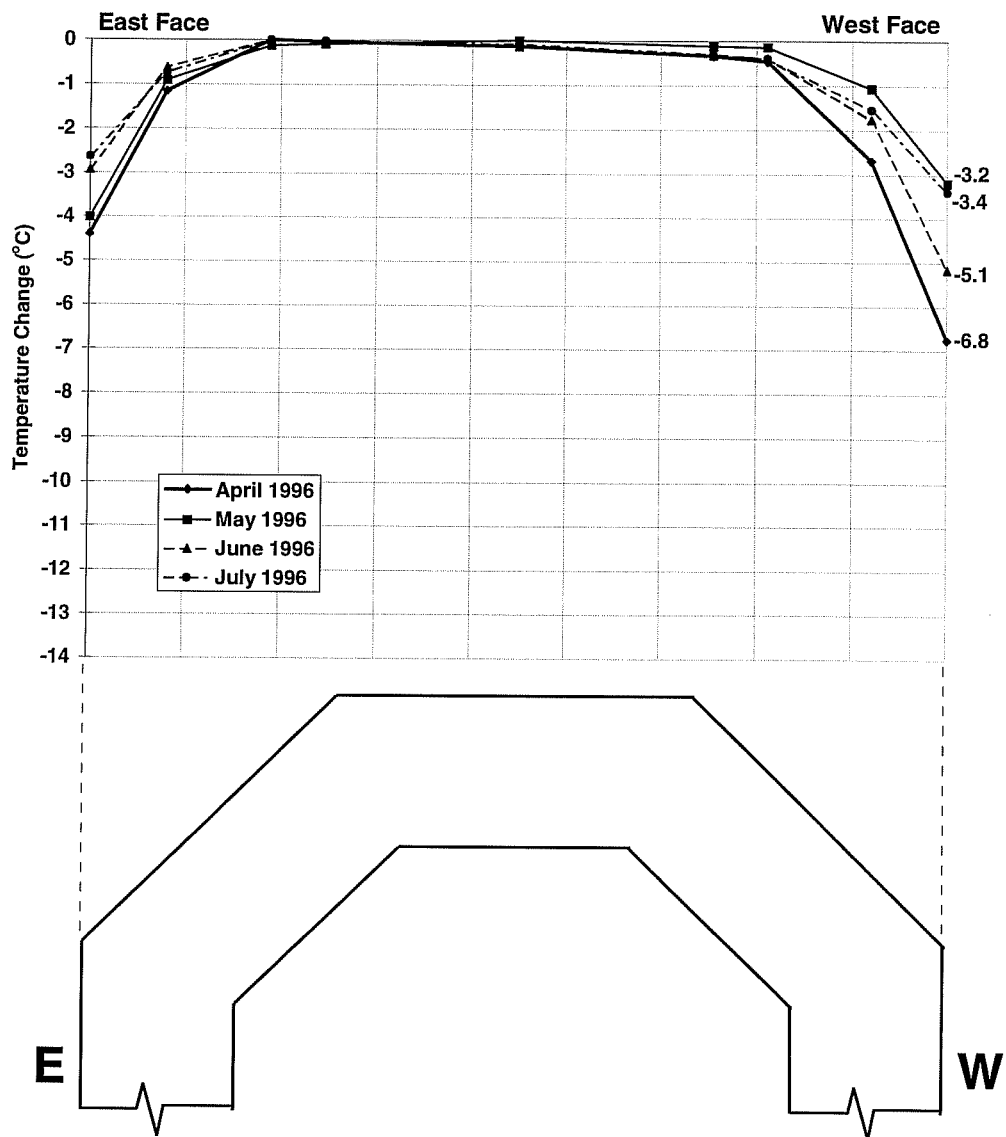


Figure 6.6: Maximum measured monthly negative temperature gradients.

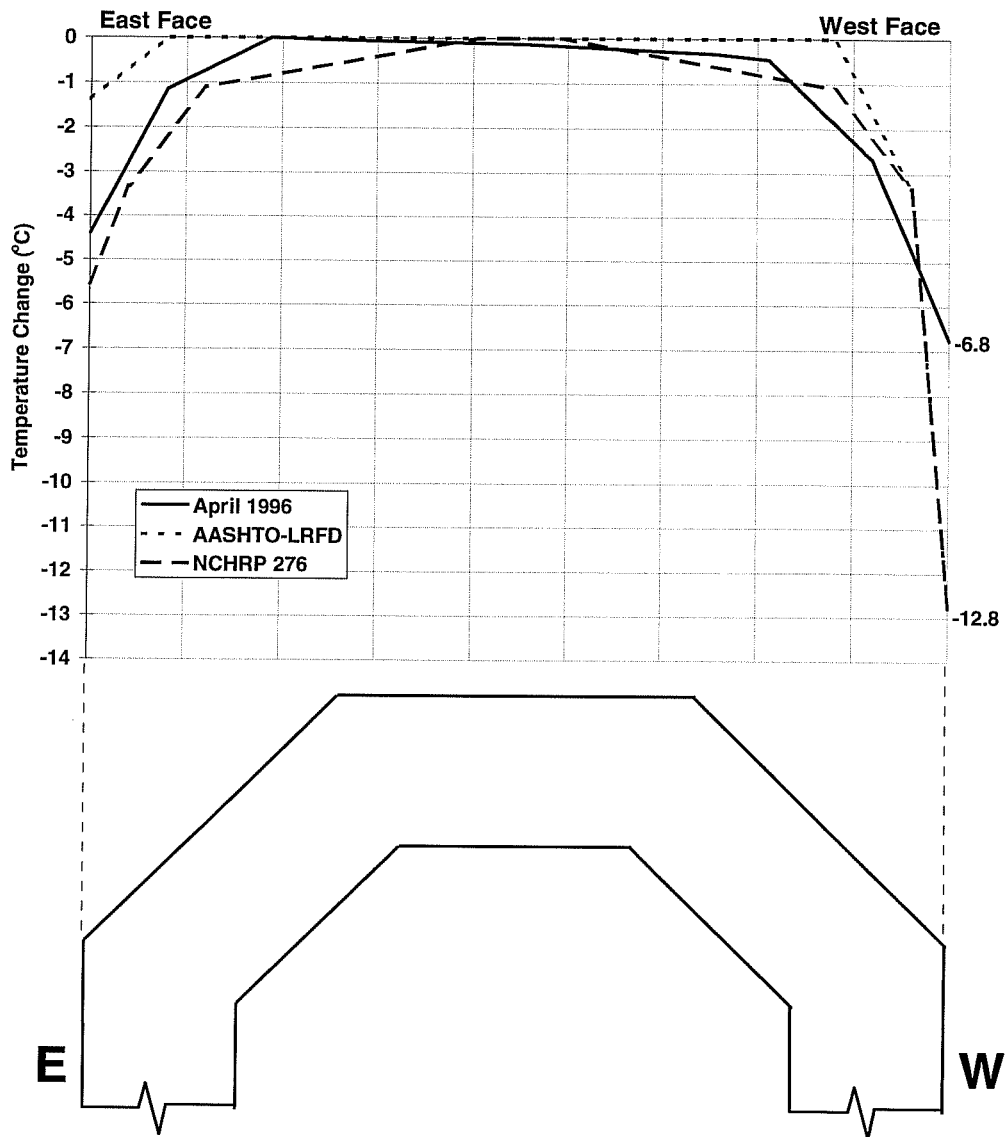


Figure 6.7: Design code negative temperature gradients.

The maximum monthly negative temperature gradients plotted using the octagonal shell method showed more variation than the positive gradients. This is probably due to two factors.

First, weather patterns differed greatly between the months monitored (see Chapter 5). April's weather was extremely variable, with large rises and drops in ambient temperature on a day-to-day basis. Relatively large drops in nighttime ambient air temperatures cooled the outer fibers of the pier to a greater extent than in subsequent months.

Second, gradient shapes plotted along the east-west axis of the pier's cross-section may underestimate the maximum outer fiber temperature changes if the largest changes occurred at faces other than the east or west faces of the pier. The temperature changes plotted at the east and west faces in those cases would be averages calculated from temperature changes that did not reflect the maximum changes during that particular time period. If the projection was plotted along a different axis, the maximum outer fiber temperature changes might be larger in magnitude. However, the similarities in the gradient shapes at the locations of the interior fibers makes this second possibility less likely.

No measured temperature gradient matched the magnitudes of the design gradients. The largest temperature change recorded during the April maximum temperature change, located on the west face of the pier, was only 53% of the maximum temperature specified by both the AASHTO LRFD Code [11] and the NCHRP report 276 [5]. The design gradient shapes sloped more severely than the measured gradients near the west face. The NCHRP design gradient matched the measured temperatures well at the eastern side of the pier.

## 6.2 *STRESS/STRAIN ANALYSES - HAND CALCULATION METHODS*

### **6.2.1 Classical Method**

The calculation methods outlined in Chapter 2 used by Imbsen, et al [5] and Roberts [7] were also employed here to determine the longitudinal stress and strain

distributions along the depth of the pier induced by the non-linear temperature gradients measured in the field and presented earlier in this chapter. This method is commonly used during superstructure design to locate potential areas of tensile stress. Example calculations for the segmental pier's cross-section can be found in the Appendix.

#### ***6.2.1.1 Positive Gradients***

Figure 6.8 shows the temperature and stress distributions calculated for the maximum positive gradient for the month of April, 1996. As discussed in Chapter 2, the pier is initially assumed to be fully restrained. The stress distribution in this state is computed from the temperature distribution measured in the pier. Using the methods outlined in Chapter 2, the restraining axial force and moment are then calculated. To find the self-equilibrating stress distribution in the statically-determinate pier, the restraining forces are released and the axial and bending stresses are subtracted from the fully restrained stress distribution (see Figure 6.8).



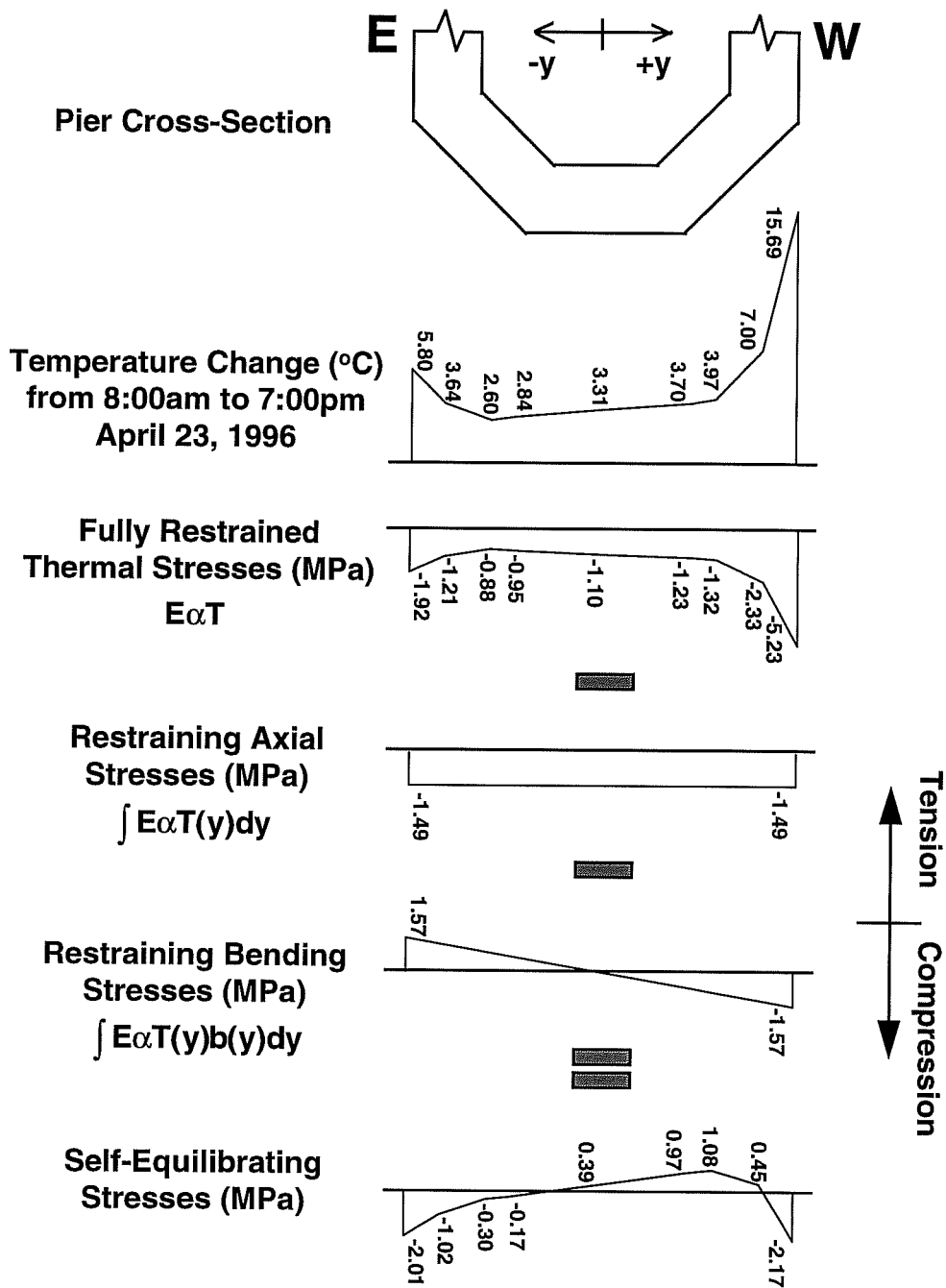


Figure 6.8: Calculation of self-equilibrating stresses induced by the maximum positive temperature gradient, April 1996.

For the sake of comparison with measured strains and the finite element model presented in Chapter 7, the longitudinal stresses calculated using this method are expressed as strains in the following figures. The calculation method illustrated in Figure 6.8 assumes that the longitudinal and transverse stress components due to temperature distributions are separable. The stresses calculated above do not include effects due to transverse stresses, which will be calculated later in this chapter. Thus, the strains plotted in the following figures are calculated using Hooke's law:

$$\epsilon_{\text{longitudinal}} = \frac{\sigma_{\text{longitudinal}}}{E} \quad (6.1)$$

The method shown in Figure 6.8 was used to calculate the strain distributions induced by the monthly maximum positive temperature gradients (see Figure 6.9). All strain distributions are plotted on the east-west cross-sectional axis as they coincide with the temperature distributions shown earlier in this chapter. Regions of high temperature in the pier's cross-section are marked by compressive self-equilibrating stresses. For positive gradients, the interior areas undergo tensile stresses associated with the relatively low temperatures there. This behavior is consistent with the theory presented by Andres [1] and discussed in Chapter 2. Figure 6.10 shows the longitudinal strains calculated from the application of the design positive gradients on the pier's cross-section.

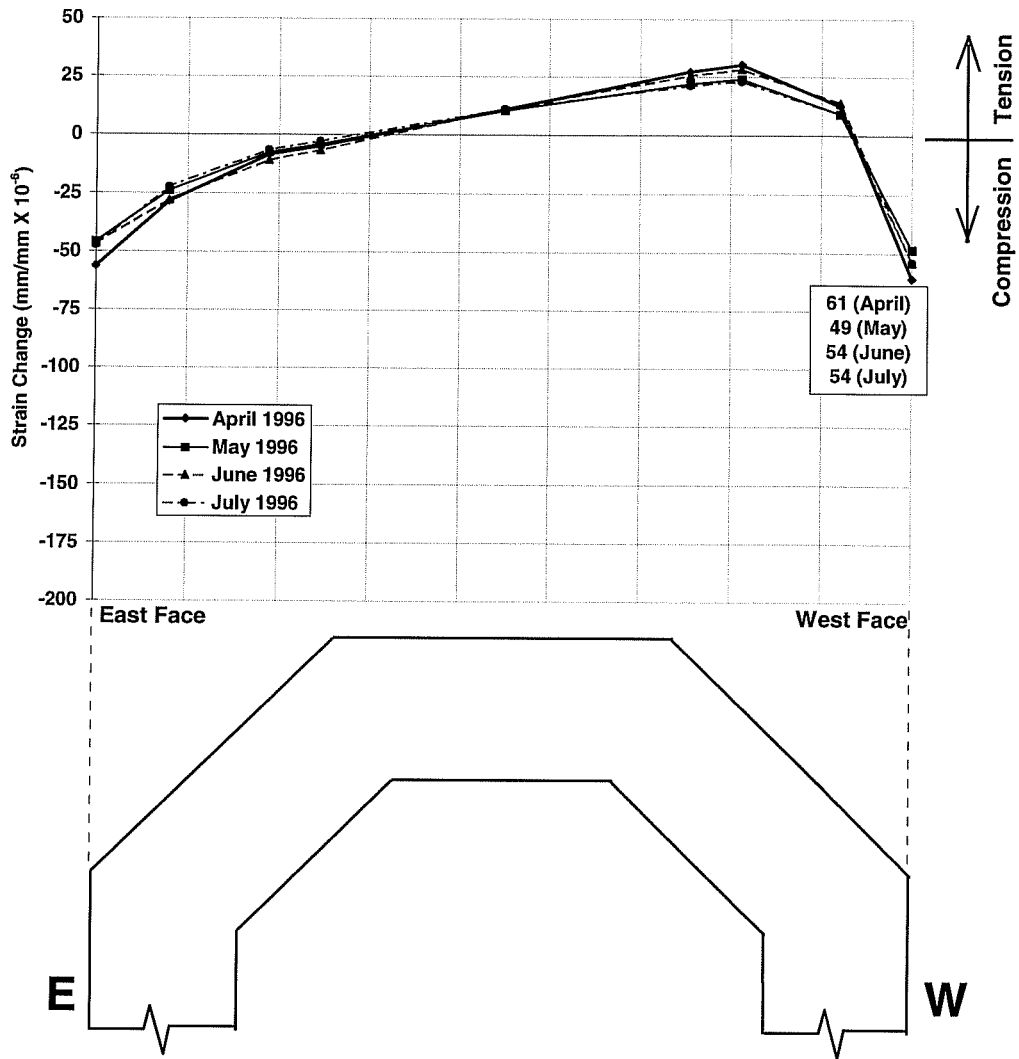


Figure 6.9: Longitudinal strains due to self-equilibrating stresses induced by monthly maximum positive gradients, plotted on the east-west cross-sectional axis.

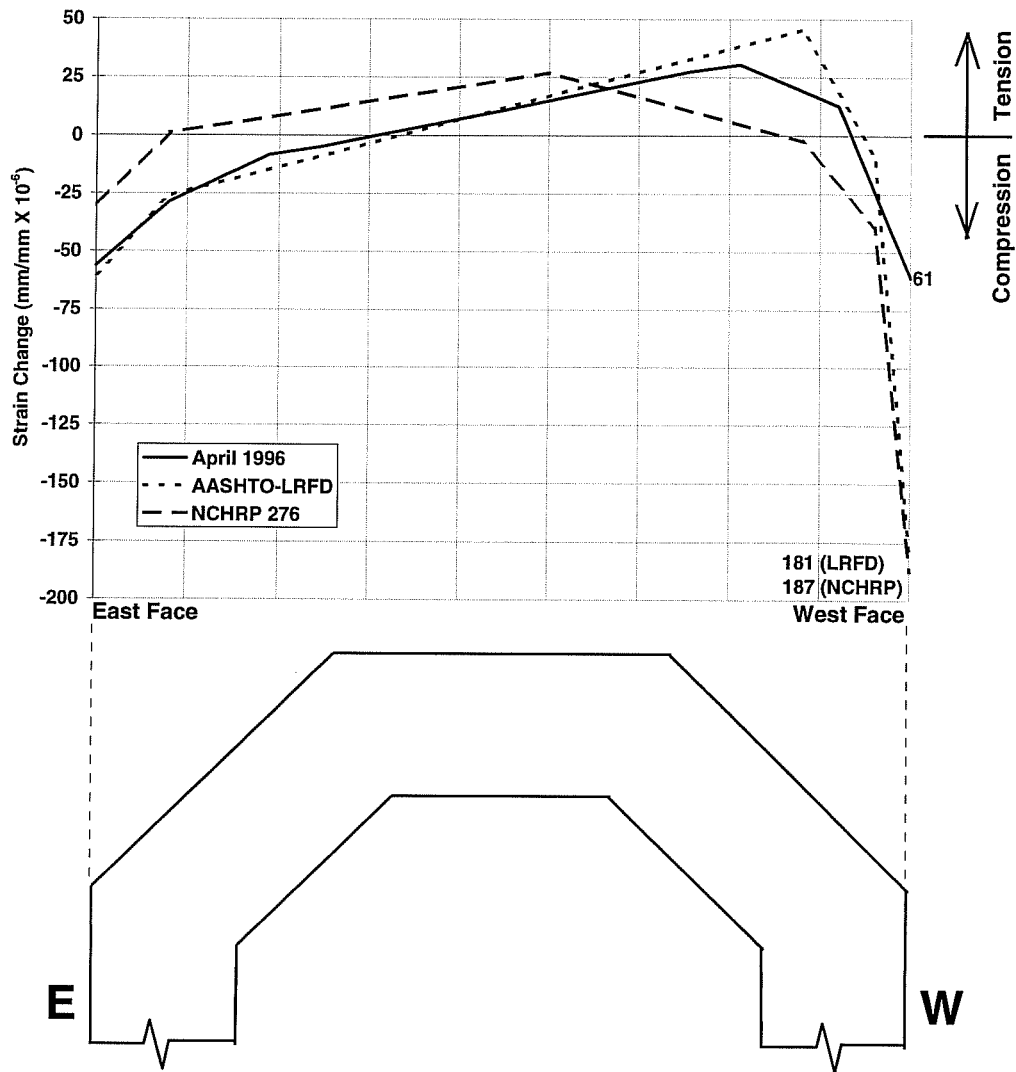


Figure 6.10: Longitudinal strains due to self-equilibrating stresses induced by design positive gradients, plotted on the east-west cross-sectional axis.

The distributions of self-equilibrating longitudinal strains calculated from the maximum monthly positive temperature changes were virtually identical for all four months. The April maximum positive temperature gradient produced the largest compressive strains at the west face of the pier. It also induced the greatest amount of

tensile strain change in the interior fibers. This is consistent with the fact that the largest temperature gradient occurred in April.

The self-equilibrating strains calculated from the design code positive gradients were larger in magnitude than those calculated from observed temperature changes. The highest compressive strain change on the pier's west face from the April maximum gradient was only 34% of the strain due to the AASHTO LRFD Code gradient, and 33% of the NCHRP design gradient. Relatively large tensile strains in the interior fibers were calculated using the AASHTO-LRFD gradient. Tensile strains in that location induced by the April maximum gradient and the NCHRP gradient were approximately the same magnitude.

#### ***6.2.1.2 Negative Gradients***

The same longitudinal strain calculation method was used to determine the sectional strains occurring due to the largest negative gradients. Negative temperature gradients, where the outer surfaces are cool compared with the interior, cause tensile strains to develop at the outer faces of the pier. Figure 6.11 shows the stress calculation method for the maximum monthly negative gradient for April, 1996. The longitudinal stress component is then converted to strain using Hooke's law as before. The monthly maximum self-equilibrating strain distributions are shown in Figure 6.12. All maximum negative gradients are plotted along the east west cross-sectional axis for comparison purposes. Figure 6.13 illustrates the strain distributions calculated from the application of the design negative temperature gradients to the pier cross-section.

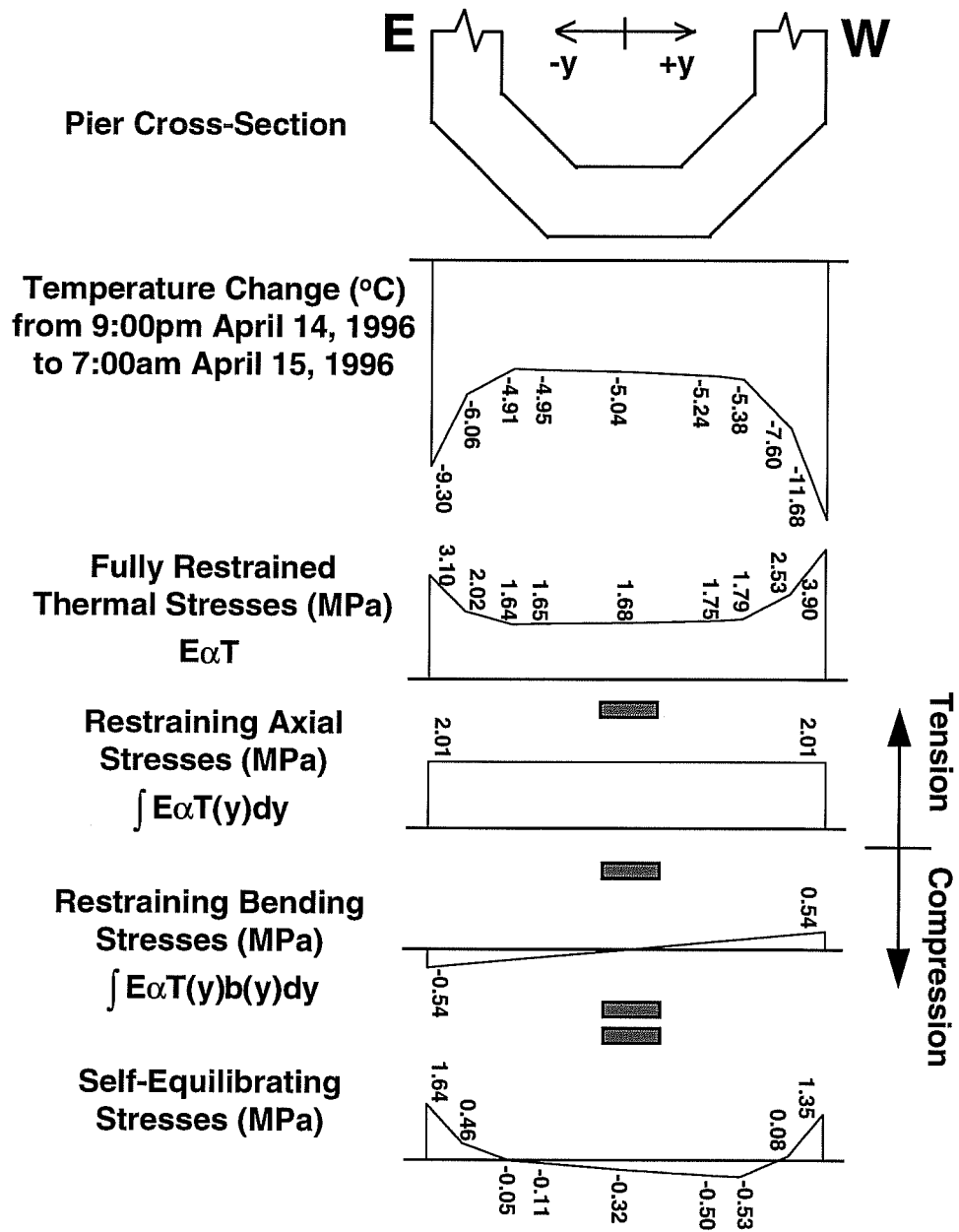


Figure 6.11: Calculation of self-equilibrating stresses induced by the maximum negative temperature gradient, April 1996.

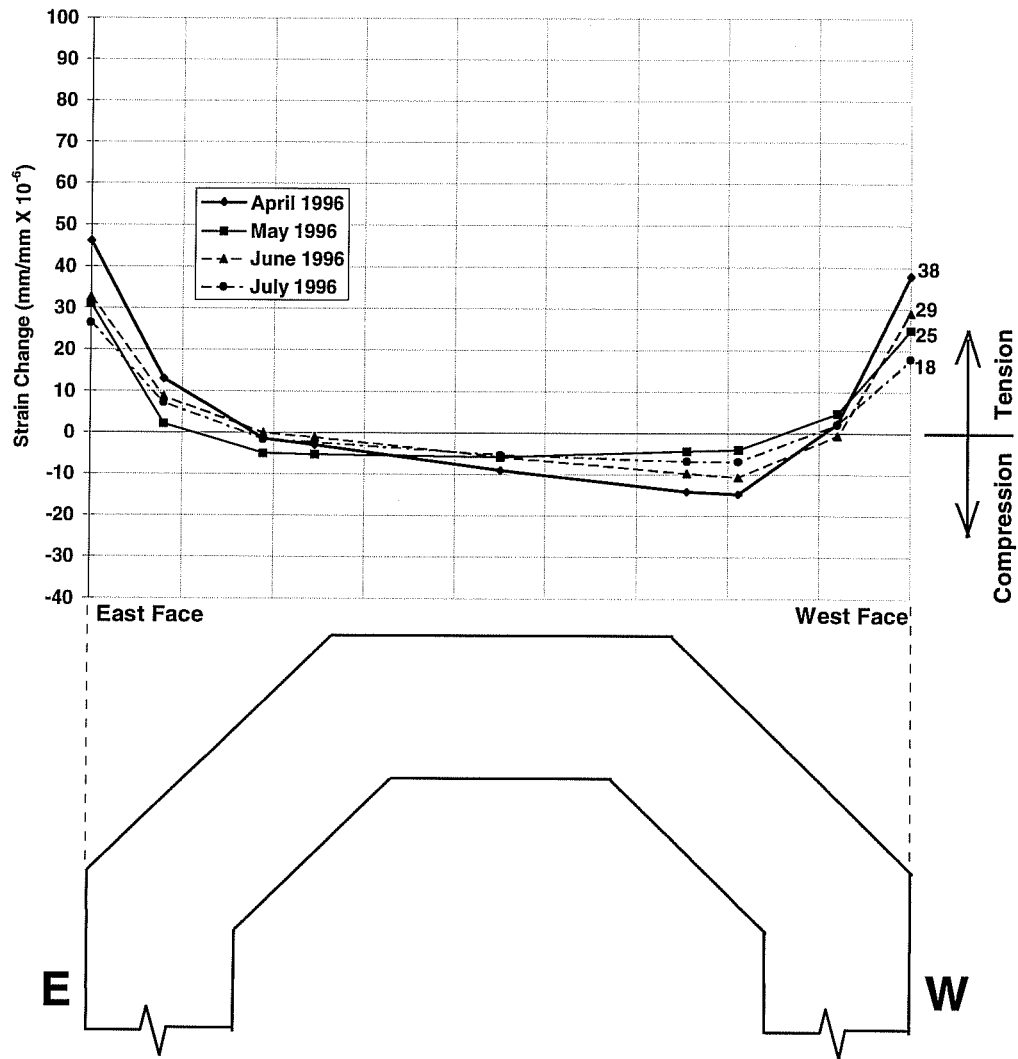


Figure 6.12: Longitudinal strains due to self-equilibrating stresses induced by monthly maximum negative gradients, plotted on the east-west cross-sectional axis.

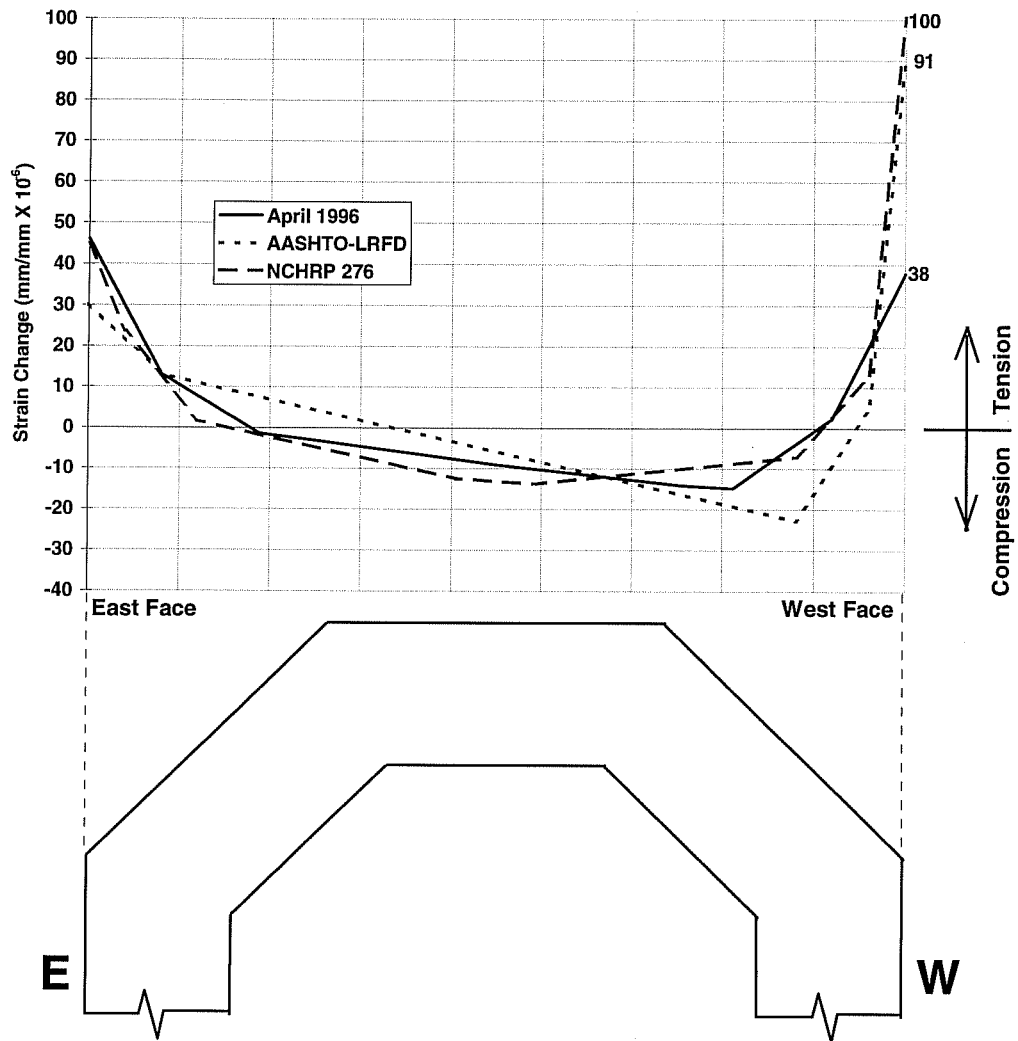


Figure 6.13: Longitudinal strains due to self-equilibrating stresses induced by design negative gradients, plotted on the east-west cross-sectional axis.

The maximum tensile strain changes due to the measured negative gradients occurred at the east face of the pier for each of the four months monitored. However, the tensile strains at the east and west faces of the pier were very close in magnitude, indicating almost symmetrical temperature loading. The April maximum negative



gradient produced the largest tensile and compressive strain changes in the pier's cross-section.

The design code negative temperature gradients produced large tensile strain changes at the west face of the pier. The maximum tensile strain change calculated from the April observed negative gradient was only 42% of the tensile strains induced by the AASHTO-LRFD Code negative gradient, and 38% of those from the NCHRP negative design gradient.

### **6.2.2 Primary Bending Axis Method**

The classical method described in the previous section works well for estimating the longitudinal self-equilibrating stresses at any depth in a bridge member. The method is useful only for a one-dimensional distribution of temperatures through the section, as it does not account for any temperature distributions in the transverse direction across the section. Bridge piers, as stated earlier, pose a slightly more complicated problem because they are not heated from a single direction. Thus, the self-equilibrating stresses induced by temperature changes will vary along both the depth and width of the pier's section.

A more general approach to the determination of temperature-induced stresses in a member involves a process similar to that of the classical method used previously. In this general method, temperatures are assumed to be constant over discrete *areas* of the cross-section, rather than at discrete *depths*. Thus, the member is loaded with a set of temperatures that can be visualized as a three-dimensional surface bounded by the geometry of the cross-section.

The assumption that plane sections remain plane requires the addition of an intermediate step in the process. The orientation of the axis about which bending occurs (i.e. the neutral axis) is assumed to be known in the classical method used previously in this chapter. However, the two-dimensional temperature loading applied to the pier causes it to bend about an axis that does not necessarily coincide with the

neutral axis (see Figure 6.14). The bending axis, which is dependent on the temperature distribution, must be determined before a calculation of the restrained axial and bending stresses can be performed.

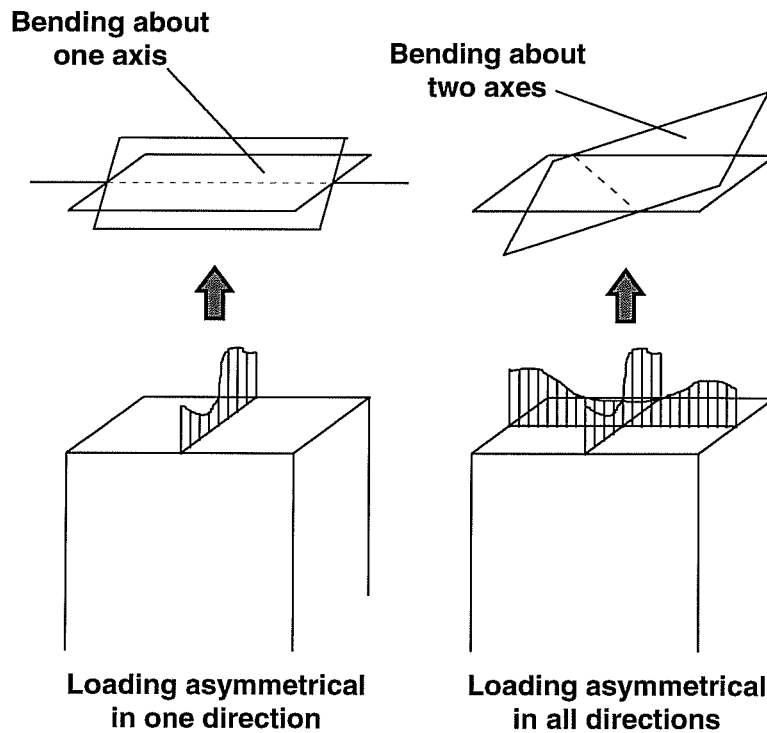


*Figure 6.14: Final planar section orientation is dependent on temperature loading.*

To determine the bending axis orientation, the cross-section is divided into areas of constant temperature. For the purposes of the following calculations, areas defined by the measured temperatures in the pier's cross-section will be used (see Figure 6.15). A distribution of smaller areas of constant temperature would produce more refined results, but temperatures are only known at the points indicated.

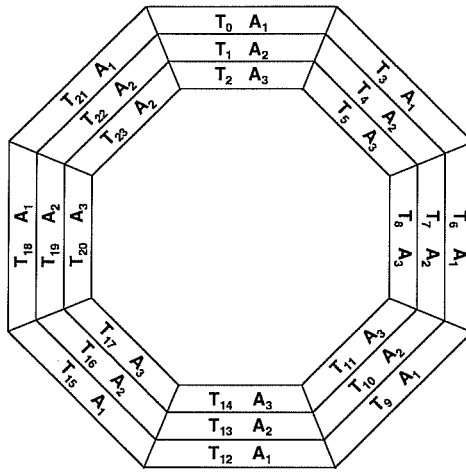


Figure 6.15: Areas and assigned temperatures used for stress calculations.

In a plan view of the pier's cross-section, the axis located normal to the bending axis possesses a unique characteristic: the volumes in space defined by the cross-sectional geometry and the temperature loading "surface" are equal on each side of this axis. Thus, no bending occurs about this axis because the loading (in this case, temperature) is symmetrical about it (see Figure 6.16a). The angle  $\phi$  can be found by equating the volumes located on each side of the axis as shown in Figure 6.16b.

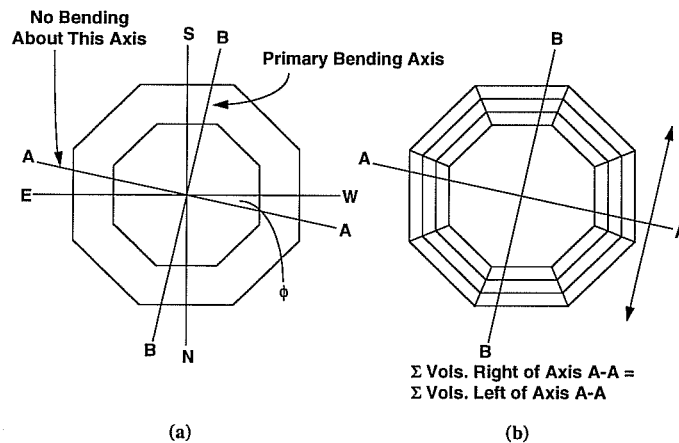


Figure 6.16: (a) Primary bending axes through the pier cross-section. (b) Summation of volumes to determine  $\phi$  angle.

After the location of the primary bending axis has been found, the solution proceeds in a manner similar to that of the classical method discussed earlier in this chapter. The pier is artificially restrained, and the fully restrained stress at any subdivided area on the cross-section is found with the relation:

$$\sigma_{i,\text{restrained}} = E\alpha T_i \quad (6.2)$$

where  $T_i$  is the temperature assigned to the  $i^{\text{th}}$  area of the pier's cross-section. Similarly, the restraining axial force on the pier is defined as:

$$\sigma_{i,\text{axial}} = \frac{\sum E\alpha T_i A_i}{\sum A_i} \quad (6.3)$$

Equation 6.3 describes the average axial stress induced by the pier's artificially-restrained expansion due to temperature change.

To determine the magnitude of the restraining moment and its affects on the pier, the distance to the primary bending axis must be described for each subdivision of the cross-section (see Figure 6.17). The quantity  $y_i$  defines the "moment arm" for each area of constant temperature.

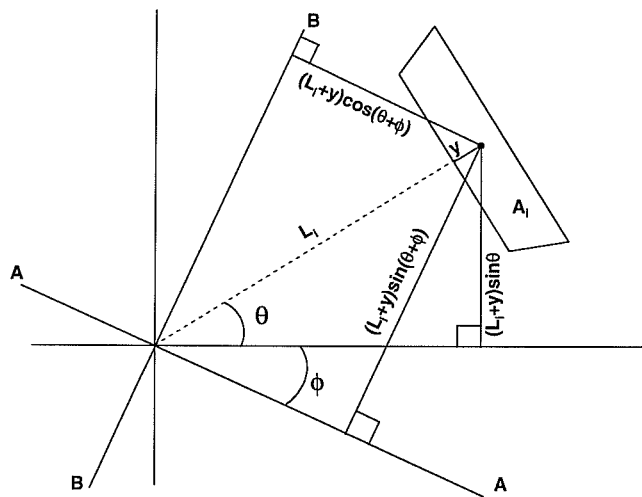


Figure 6.17: Distance of each subdivided area's centroid to the bending axis B-B.

The artificial restraining moment acting on the pier is found using the equation:

$$M_{\text{restraining}} = \sum E\alpha T_i A_i y_i \quad (6.4)$$

where  $y_i$  is the distance from the centroid of each subdivided area to the primary bending axis. The bending stress at any area of the cross-section can be described as:

$$\sigma_{i,\text{bending}} = \frac{(\sum E\alpha T_i A_i y_i) y_i}{I_{\text{section}}} = \frac{(M_{\text{restraining}}) y_i}{I_{\text{section}}} \quad (6.5)$$

Similar to the classical method, after the artificial restraining forces and their associated stresses have been determined, the restraint is removed. The artificial stresses are subtracted from the fully-restrained stress distribution to determine the remaining self-equilibrating stresses at any subdivision in the cross-section:

$$\sigma_{i,\text{self-equilibrating}} = \sigma_{i,\text{restrained}} - \sigma_{i,\text{axial}} - \sigma_{i,\text{bending}} \quad (6.6)$$

For the purposes of illustration, the stresses found in each subdivision can be projected onto an axis using the octagonal shell projection method described at the beginning of this chapter. The following sections contain these stress distributions.

The primary bending axis method for calculating the self-equilibrating stress at a given point on the cross-section of the pier is analogous to methods used to determine the principal stresses at a point under a set of applied normal and shear stresses. In this case, however, the primary bending axis orientation is determined by the temperature distribution across the section.

#### **6.2.2.1 Positive Gradients**

The stress distributions found using the primary bending axis method are expressed in terms of longitudinal strain for comparison purposes. The self-equilibrating strain distributions found from the primary bending axis method for each monthly maximum positive temperature gradient are illustrated in Figures 6.18. The

orientation of the primary bending axis for each set of temperatures is shown in Figure 6.19. Note that the primary bending axis is located very close to the east-west cross-sectional axis, and that the strain distributions are plotted along the east-west axis for comparison to other distributions discussed earlier in this chapter.

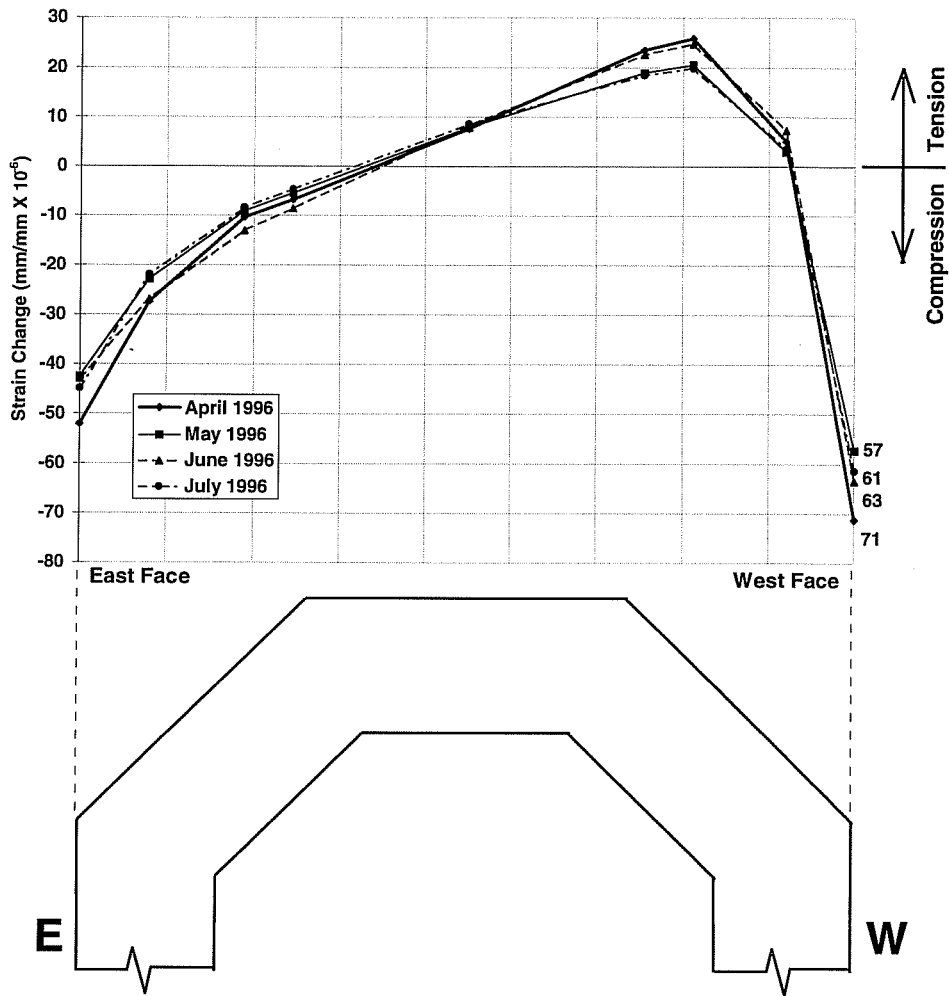
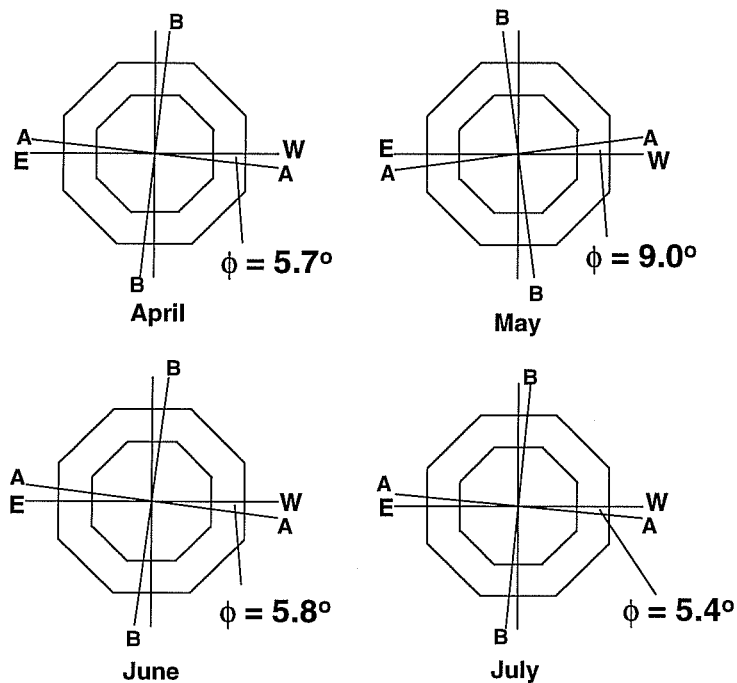


Figure 6.18: Longitudinal strains due to self-equilibrating stresses induced by monthly maximum positive gradients, calculated by the primary bending axis method and plotted on the east-west cross-sectional axis.



*Figure 6.19: Orientation of primary bending axis B-B calculated for each monthly maximum positive gradient load case.*

The longitudinal strain distributions produced by the primary bending axis method are consistent with those produced by the classical method of self-equilibrating strain calculation. The plots for all four months are virtually identical, with only small variations in the magnitudes of strain changes (see Figure 6.18). As calculated previously, the maximum positive gradient during April induced the largest self-equilibrating strains.

The orientation of the bending axis B-B is quite similar for all four load cases (see Figure 6.19). This seems to confirm the observations made previously that the largest temperature differences primarily occur along the east-west axis of the pier's cross-section. For the positive gradient temperature distributions, the bending axis B-B almost directly corresponds with the north-south cross-sectional axis.

### 6.2.2.2 Negative Gradients

The longitudinal strain distributions found by the primary bending axis method corresponding to the maximum monthly negative temperature gradients are shown in Figure 6.20. All distributions are projected along the east-west cross-sectional axis using the octagonal shell projection method for comparison with previously calculated self-equilibrating strains.

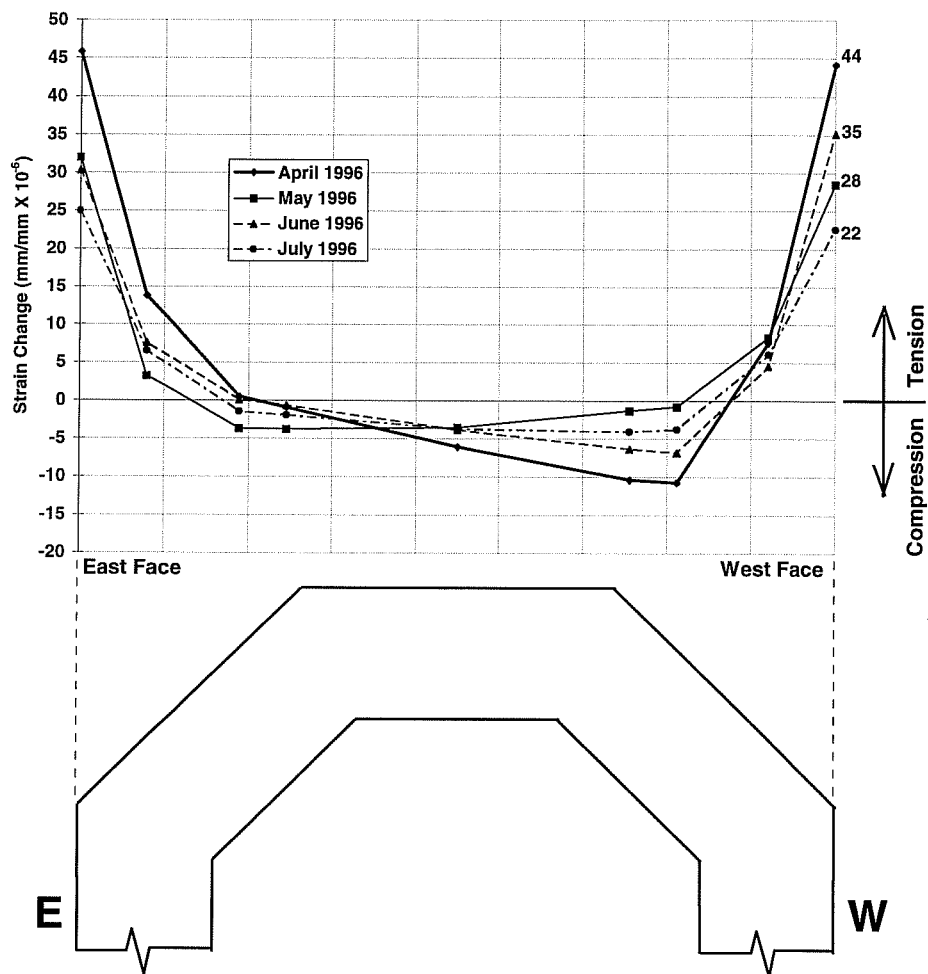


Figure 6.20: Longitudinal strains due to self-equilibrating stresses induced by monthly maximum negative gradients, calculated by the primary bending axis method and plotted on the east-west cross-sectional axis.



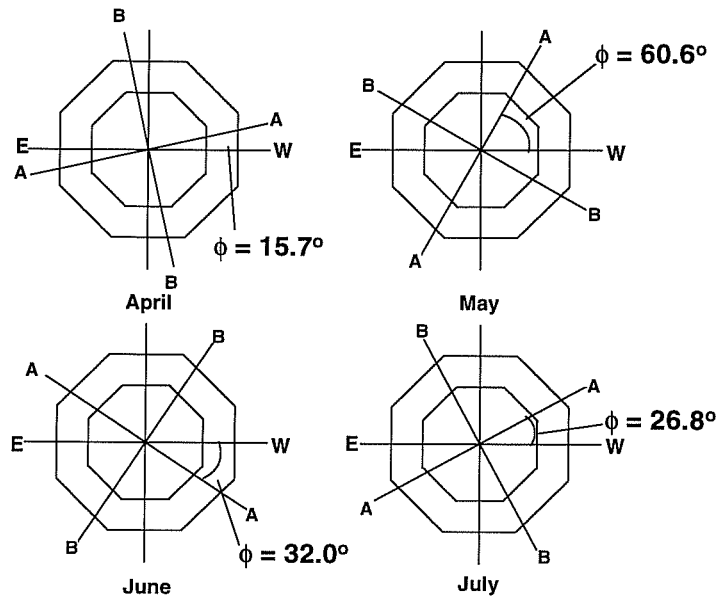


Figure 6.21: Orientation of primary bending axis B-B calculated for each monthly maximum negative gradient load case.

The strain distributions calculated by the primary bending axis method produced consistent results between all four monthly temperature load cases. The maximum negative gradient from April produced the largest outer fiber tensile strain changes, and the maximum tensile strain change occurred at the east face of the pier.

The orientations of the bending axes B-B for the maximum monthly negative gradients varied greatly (see Figure 6.21). This indicates that the locations of the maximum temperature changes occurring during a negative temperature gradient are extremely difficult to predict.

### 6.2.3 Transverse Stresses

The longitudinal stresses calculated previously in this chapter do not describe the complete state of stress induced in the pier during temperature changes. Transverse stresses are also present due to the local effects of non-linear temperature gradients through the pier walls. During the analysis of most superstructures, local gradients

across the thickness of flanges and webs are assumed to be linear. However, for walls with thickness greater than about 28 mm, the linear temperature gradient assumption no longer adequately describes the temperature distribution through the wall [5].

For the purposes of this project, the transverse stresses induced in the pier's walls can be analyzed with a method suggested by Imbsen, et al [5] (see the appendix for an example transverse stress calculation). First, the walls of the cross-section are treated separately. Each wall is artificially restrained, and the corresponding non-linear temperature gradient through the thickness is applied (see Figure 6.22).

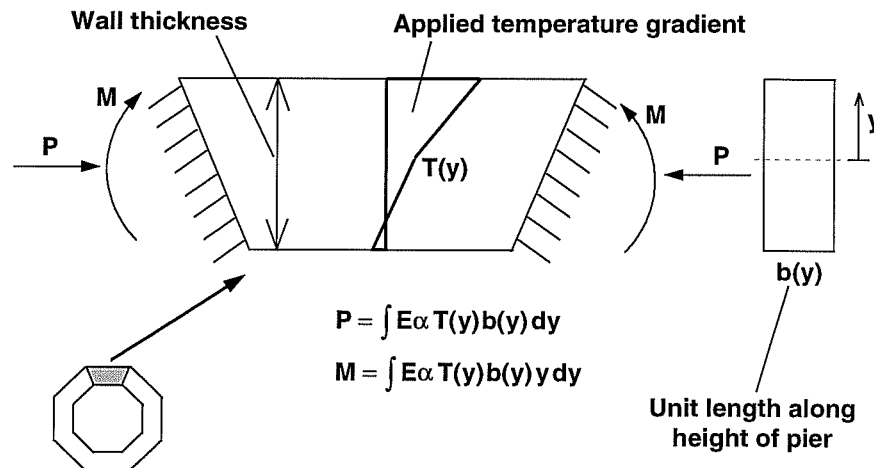


Figure 6.22: Application of non-linear thermal gradient to individual pier walls.

The fully-restrained stress distributions as well as the restraining axial forces and moments are found by the method used earlier in this chapter. The axial force is expressed as:

$$\int E\alpha T(y) b(y) dy \quad (6.7)$$

where  $b(y)$  can be assumed to be a unit width of pier wall. Similarly, the restraining moment per unit width of wall along the pier's length is:

$$\int E \alpha T(y) y dy \quad (6.8)$$

The unit width term  $b(y)$  is dropped from the calculation. The geometry of the section is idealized as a frame and the *opposites* of all the axial forces and moments found above are applied as loads in a frame analysis computer program (see Figure 6.23). The program then redistributes the applied forces around the cross-section. Finally, the stresses associated with the redistributed forces found by the computer solution are *added* to the fully-restrained stress distributions in each wall found earlier (essentially the same as subtracting the restraining stresses as done previously for the longitudinal analyses). See the appendix for example calculations.

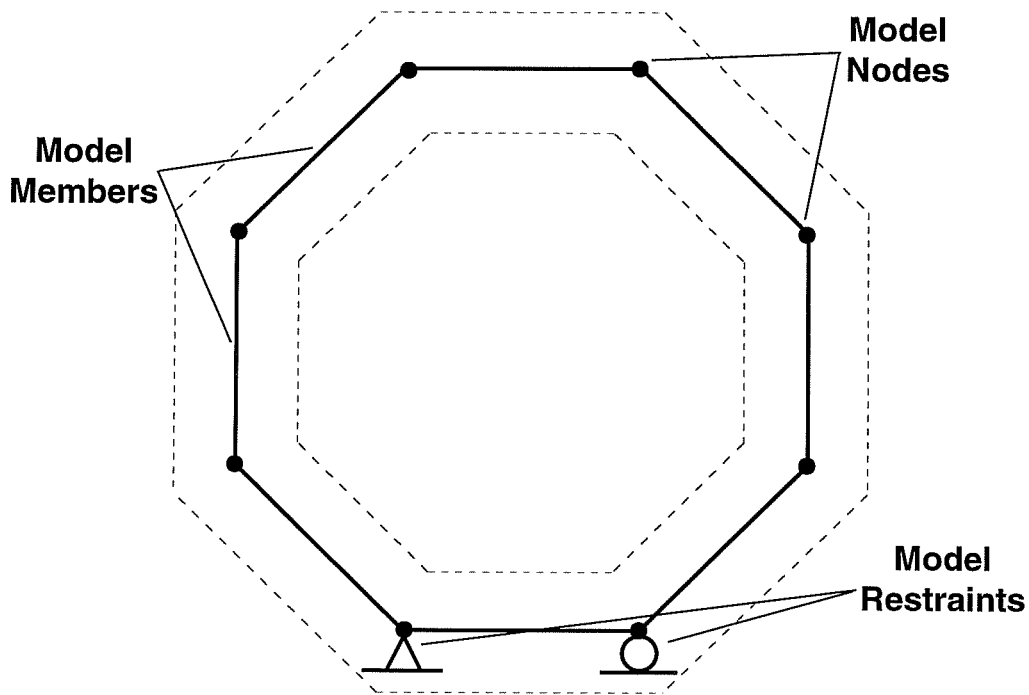
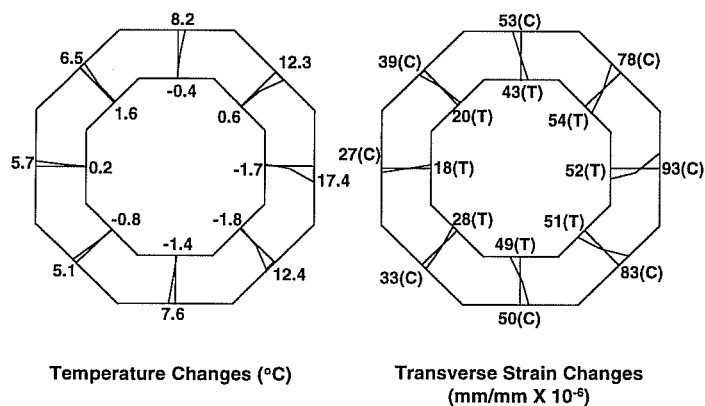


Figure 6.23: Frame model of pier cross-section used for redistribution of forces by computer frame analysis program.

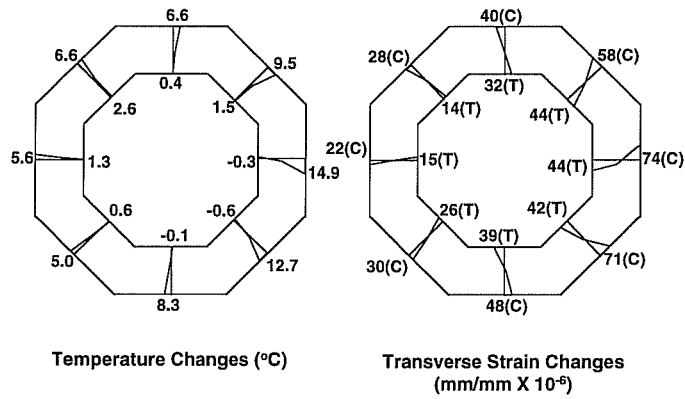
### 6.2.3.1 Positive Gradients

Transverse stresses and their associated strains were found at mid-length of each wall of the pier. The temperatures measured by the thermocouples located in segment PC16-5 (see Chapter 3) were used to determine the non-linear temperature gradients occurring through each wall of the pier for the monthly maximum temperature gradient load cases. Figures 6.24a through 6.24d illustrate the applied temperature distributions and their associated self-equilibrating transverse stresses for each month's maximum positive gradient. Note that for all load cases, relatively warm outside temperatures induced transverse compressive strains at the walls' outer faces.

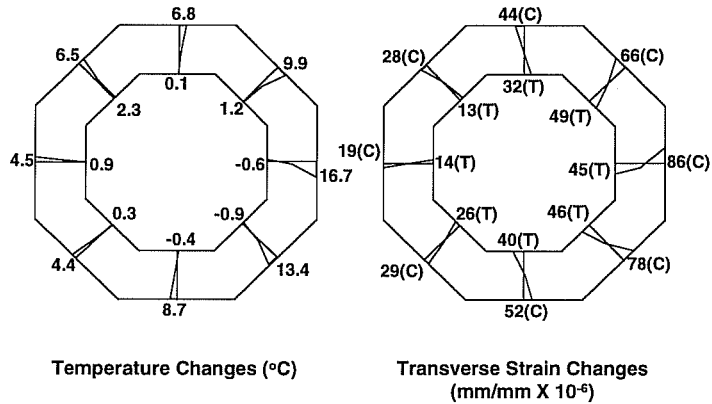
The largest transverse strain changes occurred during the April maximum positive gradient. At the west face, the transverse compressive strain change was larger than the longitudinal strain change calculated earlier in this chapter. The transverse tensile strain changes located near the interior faces of the pier's walls were also larger than the longitudinal strains calculated there. The largest differences in temperature across the wall thickness produced the largest transverse self-equilibrating strains. This is consistent with the observations made concerning the longitudinal strain changes earlier in this chapter.



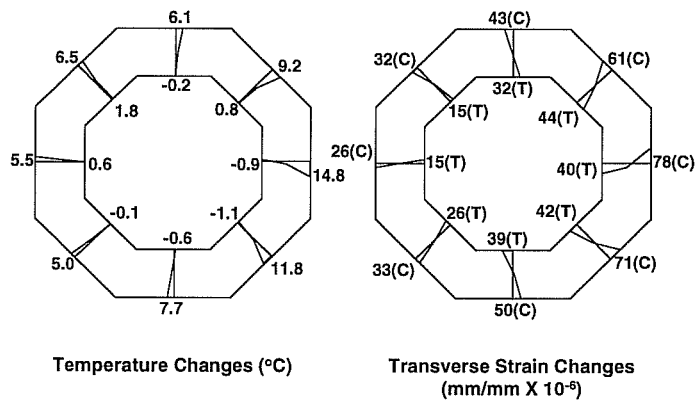
(a) April 1996 Positive Gradient



(b) May 1996 Positive Gradient



(c) June 1996 Positive Gradient



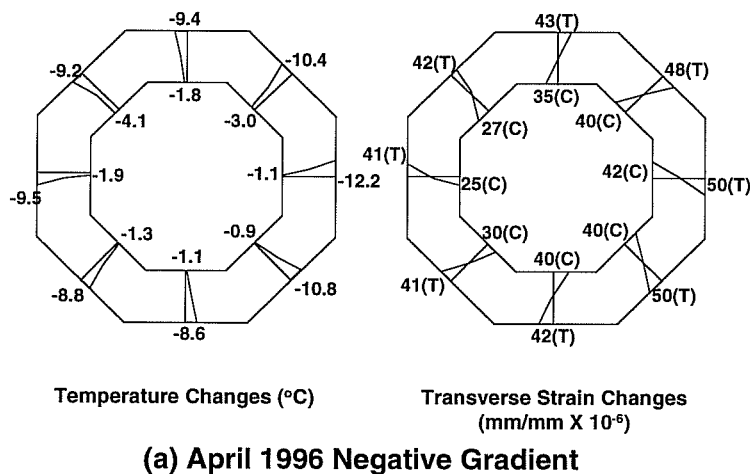
(d) July 1996 Positive Gradient

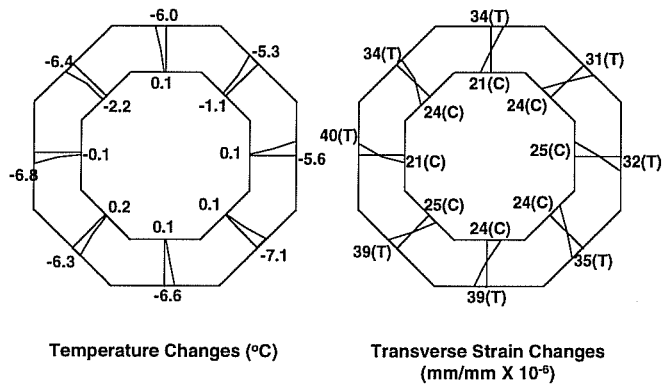
Figure 6.24: Temperature distributions and self-equilibrating transverse strains caused by positive temperature gradients for (a) April, (b) May, (c) June, (d) July.

### 6.2.3.2 Negative Gradients

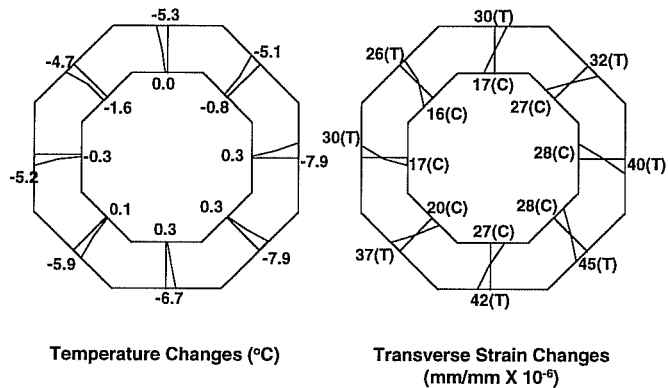
Figures 6.25a through 6.25d show the temperature and transverse stress distributions through the pier walls for each monthly maximum negative gradient. The cooler outside temperatures cause tensile stresses to develop at the outer faces of the pier walls, consistent with the stresses induced in the longitudinal direction under such loading.

Transverse strains induced by the negative thermal gradients through the wall thickness produced tensile strain changes at the outer faces of the pier that were larger than those previously calculated in the longitudinal direction. The April maximum negative temperature gradient loading produced the highest tensile strain changes which occurred at the west face of the pier. However, the largest strain changes did not always occur at the west face for the four months monitored, and did not always coincide with the largest temperature gradients present in the walls. This is due to the pier's redistribution of stresses to maintain equilibrium. Thus, the location of the maximum transverse tensile strain for a given temperature loading cannot be assumed to coincide with the largest temperature changes. The maximum strain location is a function of both the geometry of the member cross-section and the distribution of temperatures across the section.

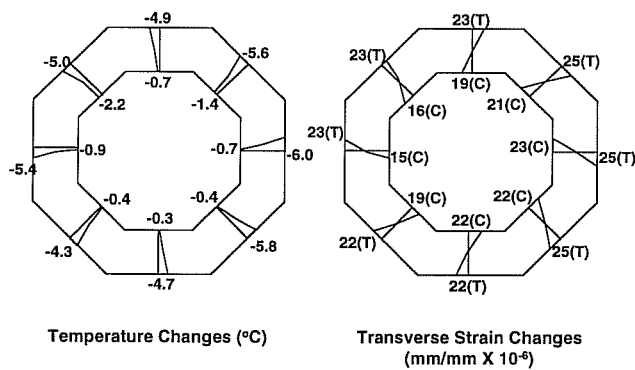




**(b) May 1996 Negative Gradient**



**(c) June 1996 Negative Gradient**



**(d) July 1996 Negative Gradient**

Figure 6.25: Temperature distributions and self-equilibrating transverse strains caused by negative temperature gradients for (a) April, (b) May, (c) June, (d) July.

## CHAPTER 7

### *FINITE ELEMENT ANALYSIS*

#### *7.1 GENERAL*

Finite element modeling can be extremely useful for analyzing a wide variety of complex structures. Most commercial finite element packages available today are capable of handling many types of loads on a structure; response due to temperature loading is a common application. Overviews of the theory behind finite element modeling have been presented elsewhere [32,33] and are beyond the scope of this project.

During the course of this project, a finite element model of the large ramp pier P16 was constructed using the commercial finite element program ANSYS 5.0a. This model was used with input data consisting of measured temperatures. The objective of the analysis was to provide a comparison with measured strains and with stresses and strains determined from generally accepted hand calculation methods (see Chapter 6). Analysis of and comparison with the field data was limited due to the number and location of gauges installed in the pier. Longitudinal strains were well represented, but a lack of transverse strain measurements made the determination of stresses more difficult. Generally accepted hand calculation methods consisted of separate analyses of the longitudinal and transverse stresses. The finite element model provided a means to analyze three-dimensional temperature response with fewer simplifying assumptions.

Many commercial finite element computer programs are capable of providing extremely accurate results but lack an easy to use graphical interface for model preparation. The Phil M. Ferguson Structural Engineering Laboratory currently employs ANSYS 5.0a for most finite element analyses. ANSYS provides a simple, menu-driven graphical user interface and can be used for a wide range of analysis



types. Its batch capabilities were useful for this project due to the number of different temperature load cases required for analysis. Temperature loads could be input at node locations in the ANSYS model. This is a convenience due to the nature of the temperature data.

## 7.2 MODEL INPUT

### **7.2.1 Pier Geometry**

As discussed in Chapter 1, pier P16 consists of a hollow, octagonal cross-sectional column with a solid capital segment. The pier is post-tensioned with tendons running through the pier's height and anchoring the column segments firmly to the foundation. Some assumptions concerning pier geometry were made to reduce the complexity of the computer model and decrease the solution time.

The computer model was constructed under the assumption that the completed, post-tensioned pier would act as a monolithic member. It has been shown that segmentally constructed, post-tensioned members behave monolithically [34]. The pier's post-tensioning and epoxied joints provide excellent continuity across segment interfaces, particularly at the low service limit state stresses induced by the temperature distributions.

For comparison with the hand calculations performed in Chapter 6, only strain and stress *changes* due to temperature load *changes* were required. The field measurements of strains induced by temperature gradients did not include strains due to gravity loading or post-tensioning operations. Thus, the finite element model ignored the self-weight of the structure and post-tensioning loads. The post-tensioning forces will change slowly over time due to creep, shrinkage, and tendon relaxation, but this loading should not change significantly over the short time period of daily temperature fluctuations.

The strains stresses induced by temperature gradients across the hollow cross-section were the primary concern of this computer analysis. Thus, the monolithic capital segment was not included in the finite element model. This served to greatly simplify the model, as the capital segment has complex geometrical features of little importance to the structure's response.

Figures 7.1a through 7.1e show a comparison between the actual pier geometry and the finite element model geometry. As shown in Figures 7.1d and 7.1e, the hollow cross-sectional shape and size was reproduced closely in the computer model. For simplicity, the pier's base was assumed to be rigidly fixed and the top was allowed to freely deflect and rotate. Only the pier height consisting of the octagonal cross-section was modeled (see Figure 7.1b). Thus, the computer model was approximately 15.6 meters in length, while the actual pier height of 20.7 meters included part of the cast-in-place base and the monolithic capital segment (see Chapter 1 for detailed information concerning the actual pier geometry).

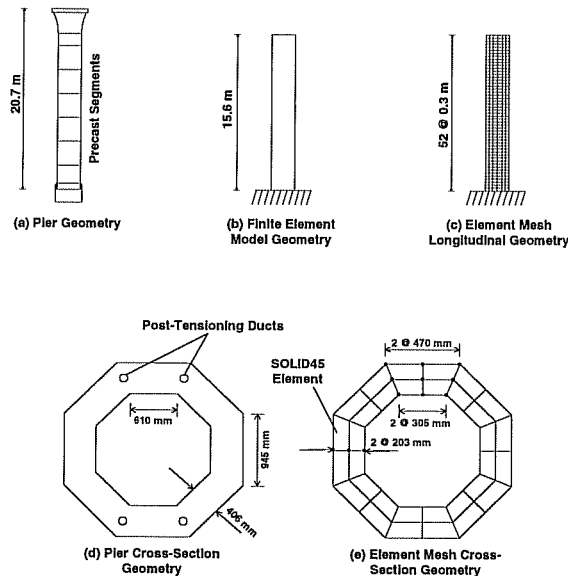


Figure 7.1: (a) Actual pier geometry, (b) finite element model geometry, (c) element mesh longitudinal geometry, (d) actual cross-section geometry, and (e) element mesh cross-section geometry.

### **7.2.2 Material Properties**

ANSYS required certain material property information to accurately model structural response to temperature loading. Both the modulus of elasticity and the coefficient of thermal expansion were determined in laboratory tests of concrete prism specimens cast simultaneously with the pier segments. From these tests, the modulus of elasticity was determined to be approximately 38.7 GPa. This relatively high number reflected the high compressive strength of the concrete used to construct the pier segments. The coefficient of thermal expansion found in temperature variation tests was approximately  $9.36 \times 10^{-6}/^{\circ}\text{C}$ . Typical values for concrete with limestone aggregate range from  $7.0 \times 10^{-6}/^{\circ}\text{C}$  to  $10.0 \times 10^{-6}/^{\circ}\text{C}$  [35].

Poisson's ratio was determined by comparing the longitudinal and transverse strain changes measured during post-tensioning operations. The average ratio was calculated from measurements at several points in the pier's shaft. A value of  $\nu=0.21$  was used for the ANSYS computer model. A shear modulus of  $G = 14.8$  GPa was calculated from the relation [36]:

$$\frac{E}{2G} = 1 + \nu \quad (7.1)$$

### **7.2.3 Temperature Loading**

#### ***7.2.2.1 General***

Temperature changes were referenced to initial temperatures at a given time. Thus what are referred to as "temperatures" here are really temperature changes from the referenced temperature state. As discussed in Chapter 3, temperatures were measured at 24 locations across the cross-section of segment PC16-5. These locations were an important consideration during selection of structural elements to be used for analysis; ANSYS requires temperatures to be assigned to node points corresponding to the corners of solid elements. The simplest element mesh that most closely represented the actual temperatures measured is shown in Figure 7.1e.

Element corners were set so that wall midpoints coincided with thermocouple locations in each of the eight walls of the pier's cross-section. However, temperatures at element corners at the interfaces between walls were not directly measured. To provide a more complete set of input data, temperature changes at these locations were linearly interpolated between measured temperature changes around the perimeter of each of three "octagonal shells" (see Figure 7.2). This method provided a more realistic estimation than if temperatures were to be interpolated *through* the wall thickness: temperature distributions through concrete are highly non-linear due to the material's poor thermal conductivity.

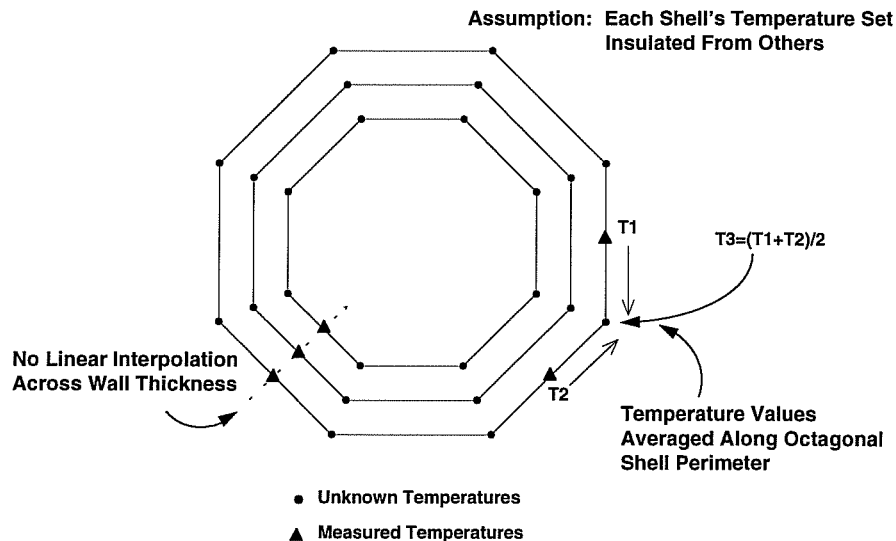


Figure 7.2: "Octagonal shell" method of temperature estimation.

With the element corners set as in Figure 7.1e, element distribution along the length of the pier was chosen to satisfy two requirements. Most finite elements produce more accurate results when the aspect ratio (ratio of height to width) of the element is less than about 2:1 and ideally is 1:1. For three dimensional solids, a ratio of 1:1:1 is ideal. Also, element strain and stress output was required at locations matching those of actual gauges in the pier. Element heights were chosen to produce an aspect ratio of

about 1.3:1.5:1.0. Thus, the element shapes were adequate to obtain reliable results, and produced stresses and strains coinciding with gauge locations.

### 7.2.2.2 Maximum Observed Gradients

Temperature load cases were set up to correspond with the maximum daily temperature changes as discussed in Chapter 6. For the months of April, May, June and July the maximum daily positive and negative temperature gradients served as loading input. Actual measured temperature changes and interpolated values located at element node points for each case were used to analyze pier response. An example load case with assigned temperature changes is shown in Figure 7.3.

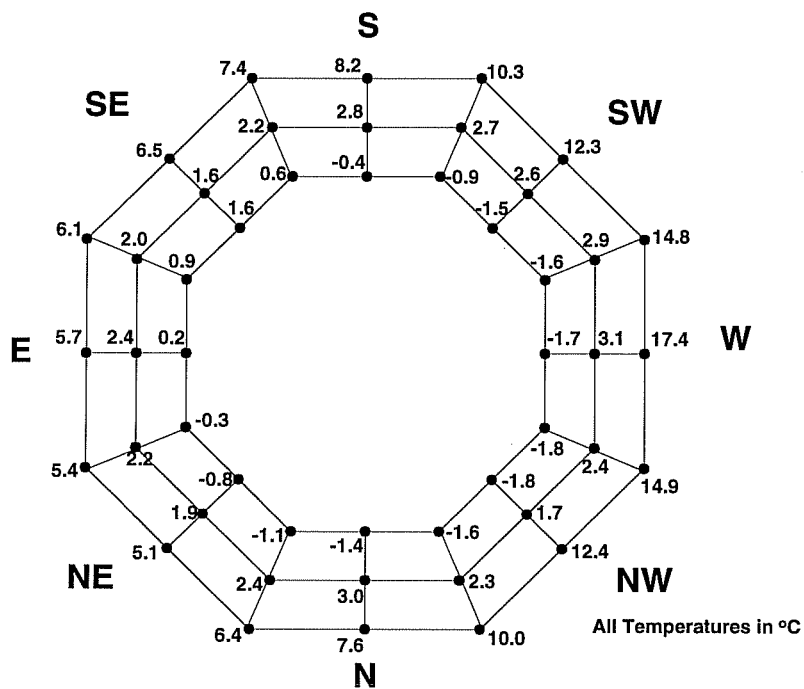


Figure 7.3: Maximum positive gradient load case: April 23, 1996.

### 7.2.2.3 Design Temperature Gradients

Positive and negative design gradients from both the *AASHTO LRFD Bridge Design Specifications* [11] and NCHRP Report 276 [5] were also input as load cases for comparison with measured temperature distributions. However, a two-dimensional temperature distribution had to be extrapolated from the one-dimensional design temperature gradients. Temperatures were assigned to model nodes as shown in the example in Figure 7.4. The temperature at each node location was interpolated from the design gradient and all temperatures at a particular cross-sectional width were assumed to be identical.

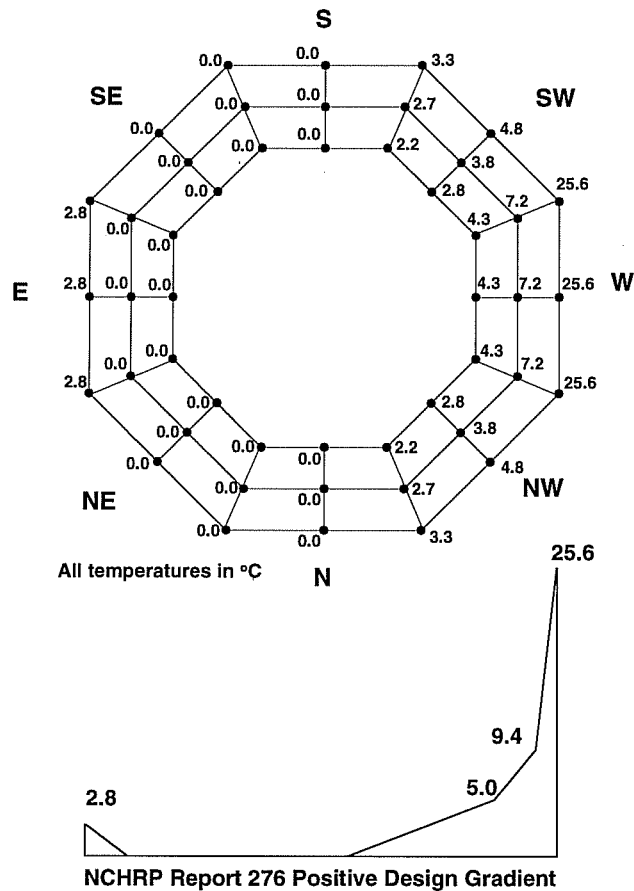


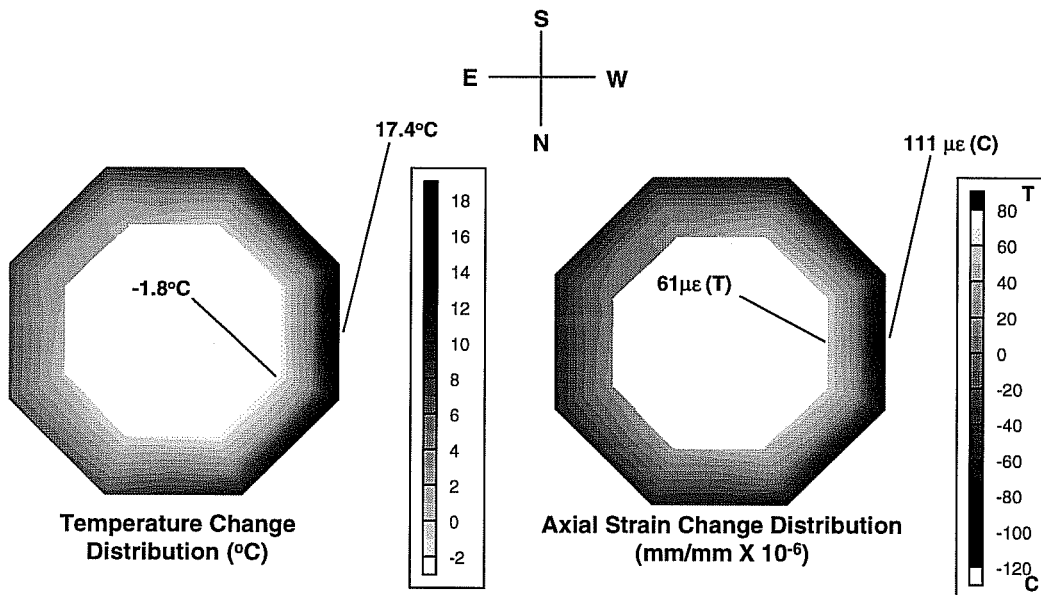
Figure 7.4: Nodal temperature change assignments: NCHRP 276 [5] positive design gradient.

### 7.3 ANALYSIS RESULTS

#### 7.3.1 Longitudinal Strains

##### 7.3.1.1 Positive Gradients

In general, longitudinal strains exhibited well defined characteristics. The higher outer face temperature changes induced large compressive strains at nodes located along the outer perimeter of the section. This behavior is consistent with the strain distributions calculated in Chapter 6 using hand methods. The areas of highest compressive strains matched the locations of high temperatures almost perfectly. Relatively low temperatures produced local regions of tensile strains. Figure 7.5 shows contour plots of temperature and strain produced by the maximum positive gradient for the month of April, 1996.



April Maximum Positive Gradient  
(April 23, 1996)

Figure 7.5: Contour plots of temperature and longitudinal strain, April maximum positive gradient load case.

Projections of the longitudinal strain distributions onto a two-dimensional graph were performed in a similar fashion to those in Chapter 6 using the octagonal shell approach. Figure 7.6 shows these strain projections on the east-west axis of the pier for the maximum monthly positive gradients. Figure 7.7 shows a comparison of the strain distributions from the largest measured temperature gradient load case and the design code gradient load cases. A summary of the maximum longitudinal strains for all positive gradient load cases can be found in Table 7.1.

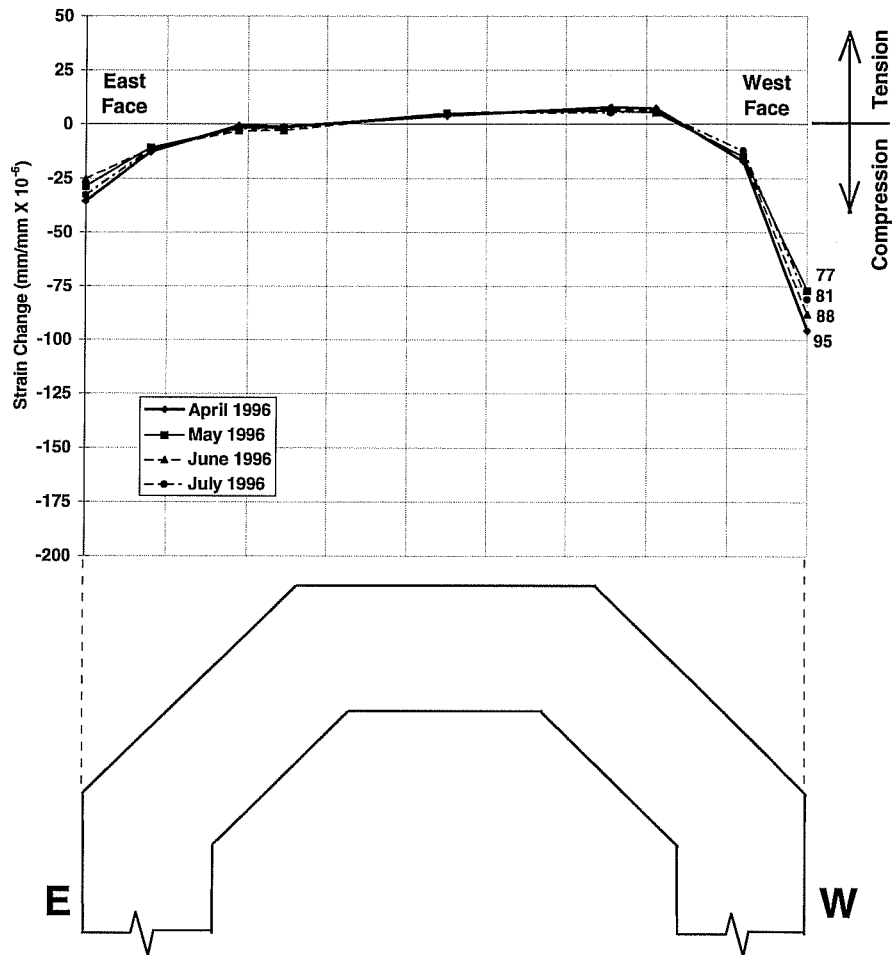


Figure 7.6: Finite element analyses strain projection plots on east-west cross-sectional axis from maximum monthly positive temperature gradients.



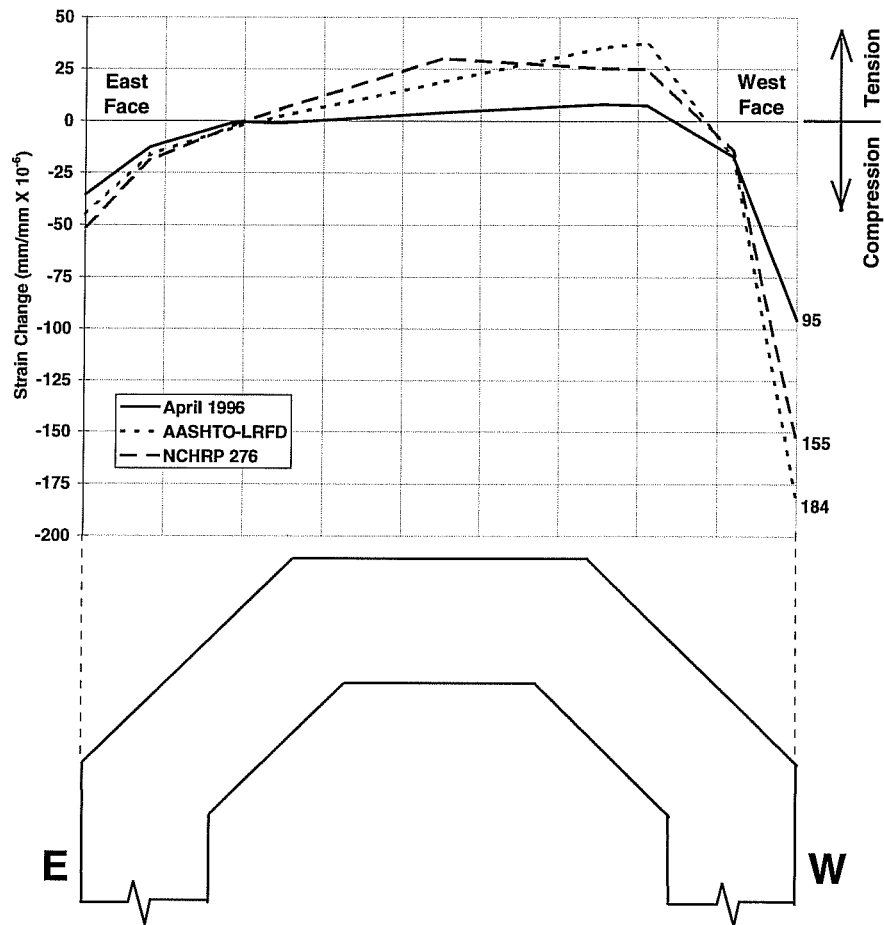


Figure 7.7: Finite element analyses strain projection plots on east-west cross-sectional axis from positive design temperature gradients.

| Positive Gradient Load Case Strain Summary |                                       |   |
|--|---------------------------------------|---|
| Load Case Description                      | Max. Tensile Strain ( $\mu\epsilon$ ) | Max. Compressive Strain ( $\mu\epsilon$ ) |
| April Max. Positive                        | 61                                    | 111                                       |
| May Max. Positive                          | 51                                    | 89  |
| June Max. Positive                         | 54                                    | 104                                       |
| July Max. Positive                         | 50                                    | 94  |
| AASHTO-LRFD Positive                       | 43                                    | 184                                       |
| NCHRP 276 Positive                         | 30                                    | 155                                       |

Table 7.1: Maximum tensile and compressive strains by load case: positive gradients.

The maximum strain changes listed in Table 7.1 are slightly different than the values shown in Figures 7.6 and 7.7. The projection method used to plot the two-dimensional strain distribution on the one-dimensional east-west axis reduces the strain change magnitudes slightly because the maximum strain changes are averaged with other, slightly smaller, strain changes at the same depth in the section.

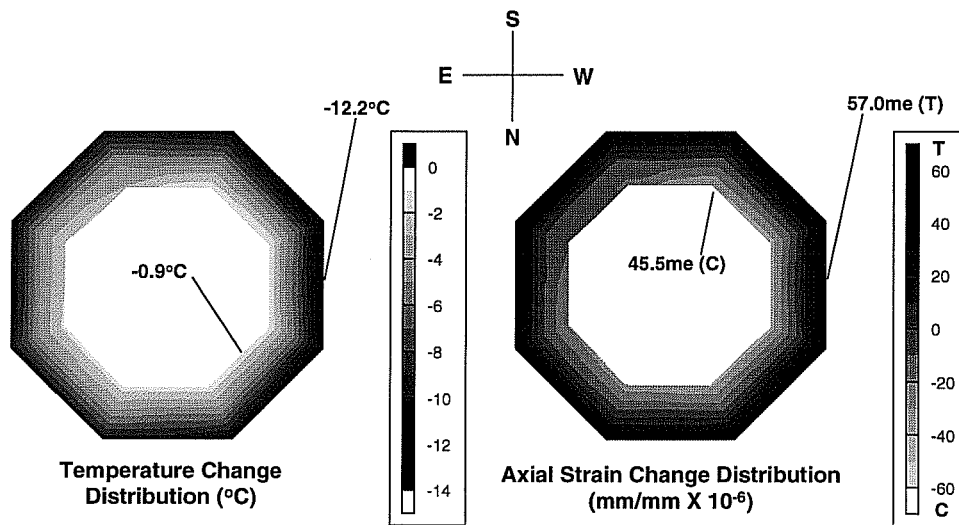
The four maximum monthly strain distributions shown in Figure 7.6 are almost identical in shape and magnitude. The strain changes from the April load case have the largest magnitude, and correspond to the largest observed monthly temperature gradient magnitudes (see Chapter 6). The April load case also exhibits the largest strain change magnitudes at any point in the cross-section for the observed load cases as listed in Table 7.1. The maximum tensile strain change of  $61 \times 10^{-6}$  mm/mm occurred at a point along the inner face of the west wall of the section. The maximum compressive strain change occurred at the outer face of the west wall.

It is apparent from Figure 7.7 that both design code temperature gradients produce resultant strain changes of much larger magnitude than even the largest strain changes due to observed temperature distributions. The maximum compressive strain change at the west face of the section due to the April positive temperature gradient load case is only 60% of the maximum compressive strain due to the AASHTO-LRFD design gradient, and 72% of the maximum compressive strain due to the NCHRP 276 positive gradient. Tensile strains from the design gradients are also larger in magnitude. In general, though, the projected strain distributions have similar shapes.

#### **7.3.1.2 Negative Gradients**

For the negative gradient load cases, the low outer face temperatures induced large tensile strains at nodes located along the outer perimeter of the section. Similar to the previous section, the areas of highest tensile strains matched the locations of the

lowest temperatures almost perfectly. Figure 7.8 shows contour plots of temperature and strain produced by the maximum negative gradient for the month of April, 1996.



**April Maximum Negative Gradient  
(April 15, 1996)**

*Figure 7.8: Contour plots of temperature and longitudinal strain, April maximum negative gradient load case.*

Octagonal shell projections like those performed in Chapter 6 are plotted in Figure 7.9. For comparison with previously calculated stress distributions, all projections were made along the east-west cross-sectional axis. A summary of the maximum longitudinal strains for all negative gradient load cases can be found in Table 7.2.

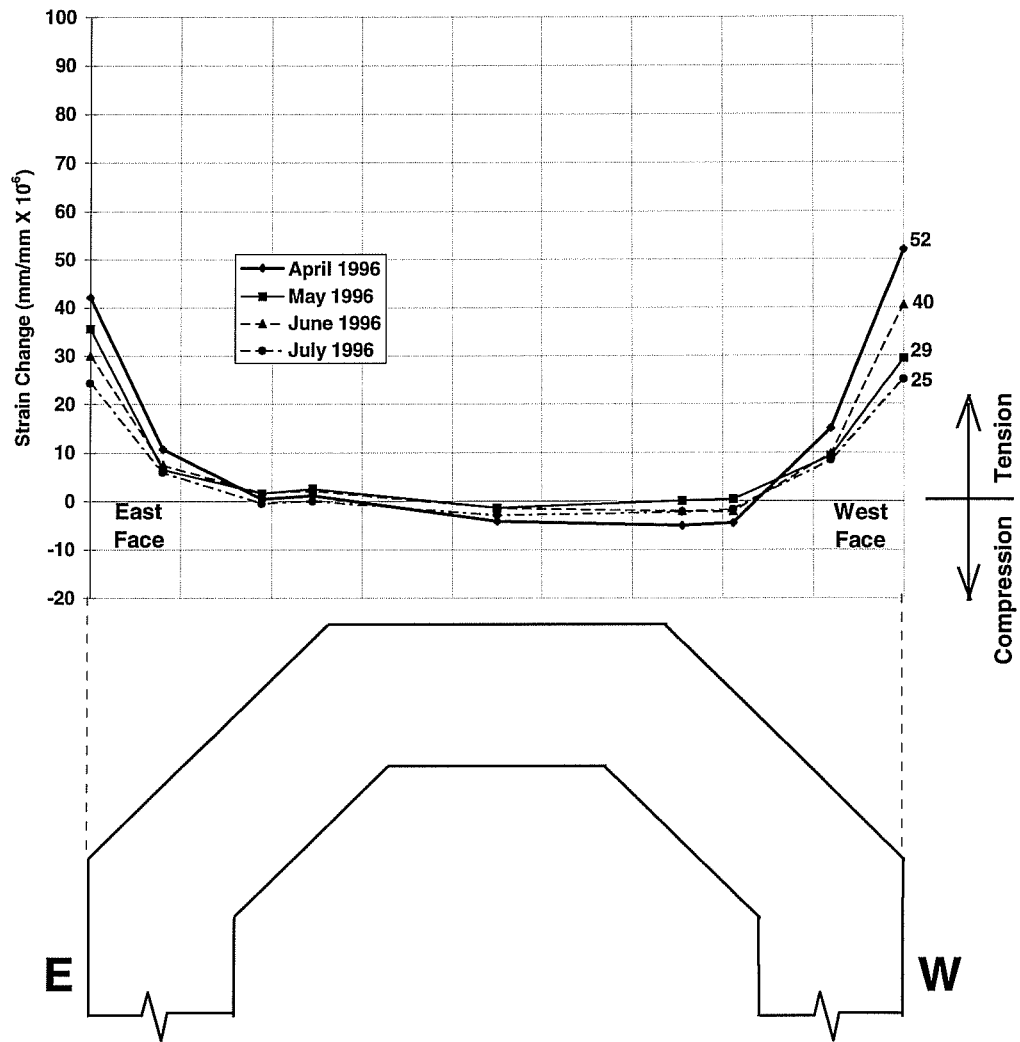


Figure 7.9: Finite element analyses strain projection plots on east-west cross-sectional axis from maximum monthly negative temperature gradients.

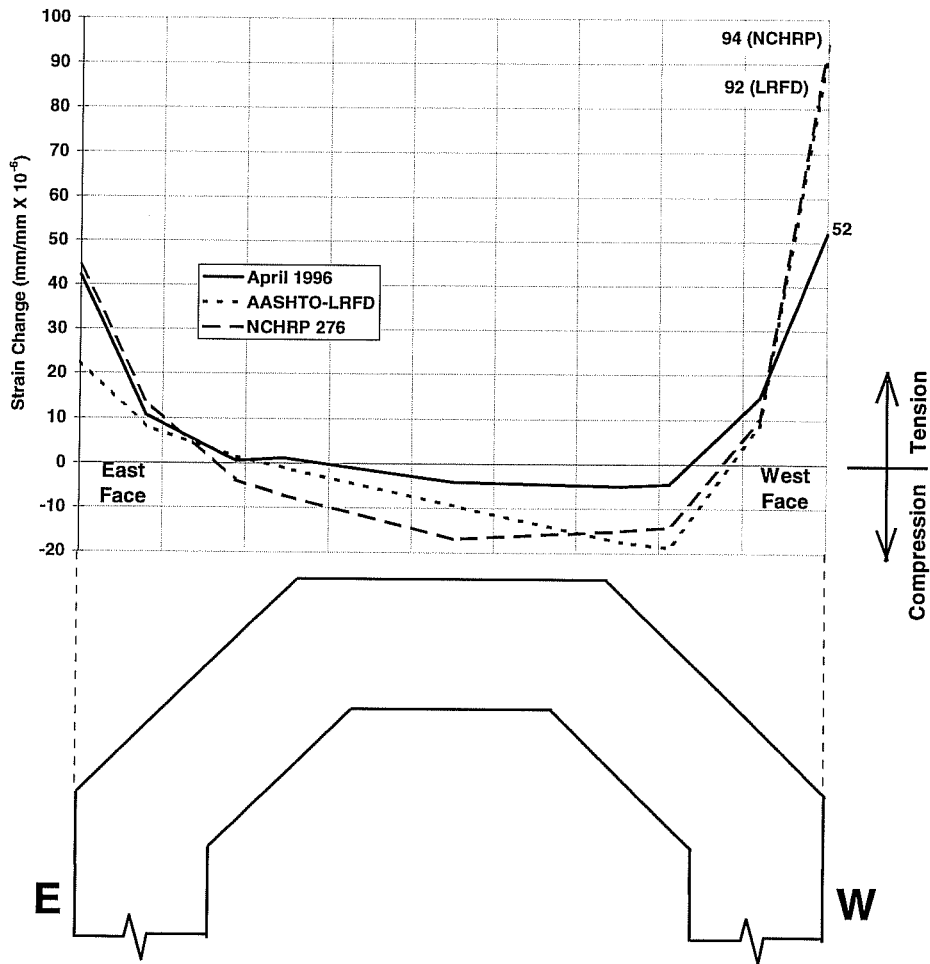


Figure 7.10: Finite element analyses strain projection plots on east-west cross-sectional axis from negative design temperature gradients.

| Negative Gradient Load Case Strain Summary |                          |                          |
|--|--------------------------|--------------------------|
| Load Case                                  | Max. Tensile             | Max. Compressive         |
| Description                                | Strain ( $\mu\epsilon$ ) | Strain ( $\mu\epsilon$ ) |
| April Max. Negative                        | 57                       | 45                       |
| May Max. Negative                          | 41                       | 28                       |
| June Max. Negative                         | 45                       | 31                       |
| July Max. Negative                         | 27                       | 24                       |
| AASHTO-LRFD Negative                       | 92                       | 21                       |
| NCHRP 276 Negative                         | 94                       | 17                       |

Table 7.2: Maximum tensile and compressive strains by load case: negative gradients.

As before, the maximum strain changes shown in the strain distribution projection plots are slightly affected by the projection method (see Figure 7.9). They coincide with the values listed in Table 7.2. Note that the maximum tensile strain change for the May load case occurs on the east face of the pier, while the other observed temperature load cases undergo the largest tensile strain changes on the west face. The April load case produced the largest strain change magnitudes among the observed load cases.

The largest tensile strain changes for the observed temperature load cases are slightly less than those found in the positive temperature gradient analyses (see Table 7.1). However, the locations of the tensile strains at the outer fibers of the section during negative gradient loading are critical for segmentally constructed members. Tensile strain changes during negative gradient loading could violate the design code requirement of zero tensile strain on the outside fibers of the section.

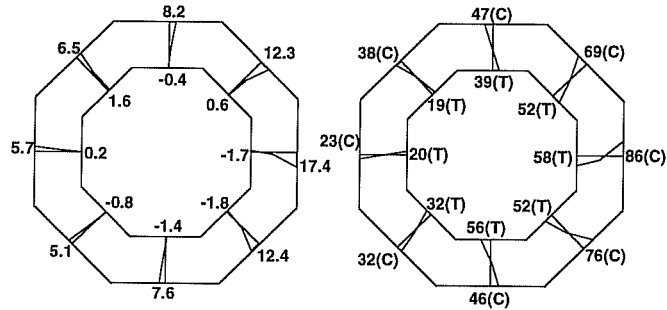
The design code temperature gradient load cases again produced strain changes much greater in magnitude than any observed gradient load cases (see Figure 7.10). The maximum observed load case tensile strain changes (from April 1996) were only 62% of the AASHTO-LRFD load case tensile strains, and 61% of the tensile strains due to the NCHRP 276 design negative gradient load case. The compressive strain changes from the observed temperature load cases were also much smaller than those produced by the design temperature gradients.

### **7.3.2 Transverse Strains**

#### ***7.3.2.1 Positive Gradients***

The distribution of transverse strains induced by temperature changes matched those predicted by theory quite well (see Chapter 6). For positive gradient load cases, where the outer faces of the pier are much warmer than the interior, compressive strains occurred consistently along the outer face, while tensile strains were located on the interior faces where temperatures were relatively low. Figures 7.11a through 7.11d

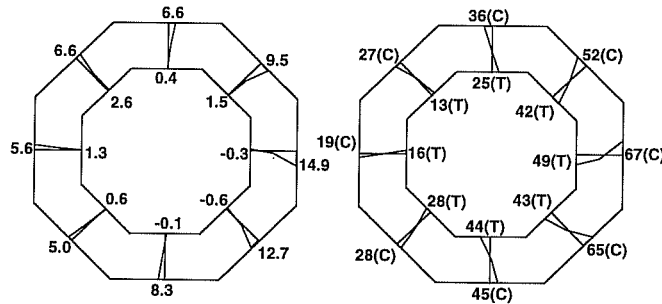
illustrate the temperature and transverse strain distributions for the maximum monthly positive temperature gradient load cases.



Temperature Changes (°C)

Transverse Strain Changes (mm/mm X 10<sup>-6</sup>)

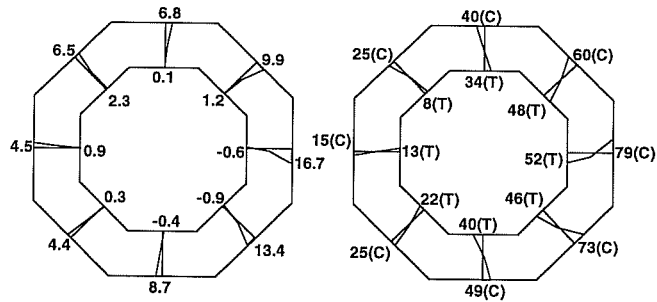
(a) April 1996 Positive Gradient



Temperature Changes (°C)

Transverse Strain Changes (mm/mm X 10<sup>-6</sup>)

(b) May 1996 Positive Gradient



Temperature Changes (°C)

Transverse Strain Changes (mm/mm X 10<sup>-6</sup>)

(c) June 1996 Positive Gradient

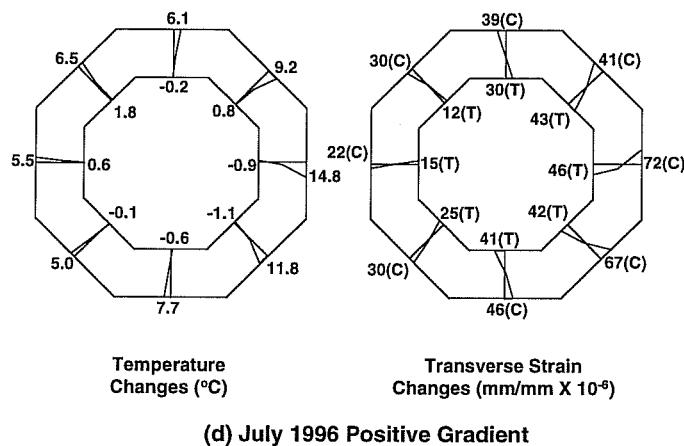


Figure 7.11: Temperature loading and transverse strain from finite element analysis of maximum monthly positive gradients during (a) April, (b) May, (c) June, (d) July.

The maximum positive gradient load case from April 1996 produced the largest transverse strain changes (see Figure 7.11a). Compressive strain changes coincided with temperature increases similar to the longitudinal strains discussed earlier. For the April load case, the maximum compressive strain change of  $86 \times 10^{-6}$  mm/mm occurred at the west face of the pier. The largest tensile strain change occurred at the interior of the west wall.

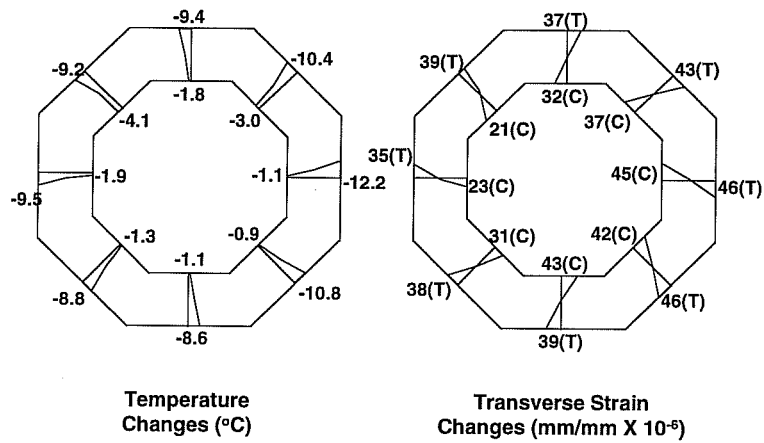
The distributions of transverse strain changes were similar for subsequent months' load cases, but the strain change magnitudes were somewhat smaller. The maximum compressive and tensile strain changes occurred in the same locations for every observed load case. This follows directly from the observation that the largest temperature change for all the load cases occurred in the same location on the west face of the pier.

### 7.3.2.2 Negative Gradients

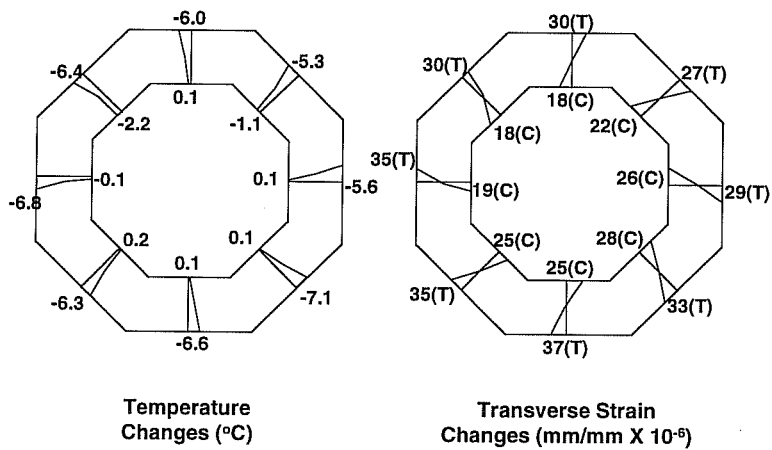
Transverse strains induced by the negative gradient load cases also matched those predicted by theory. Transverse tensile strains occurred along the outer faces of the pier where temperatures were at their lowest. Similarly, compressive strains were



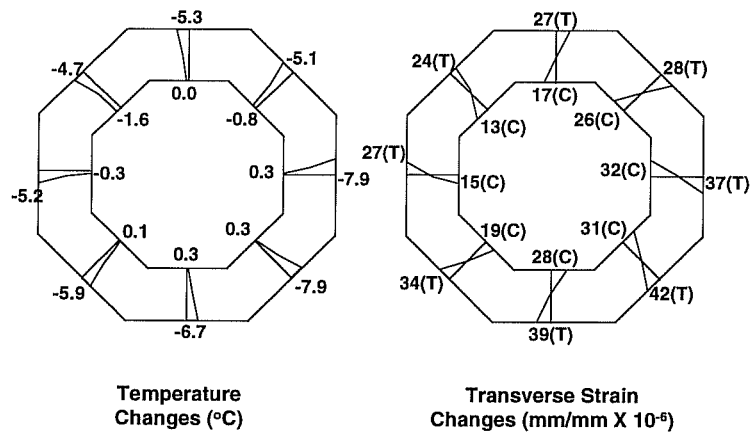
located at the interior of the pier. This indicates that the interior is pulled into compression by the restraint provided by the cooler outer surface concrete, similar to the longitudinal stress distributions discussed earlier. Figures 7.12a through 7.12d show the distributions of temperature and transverse stresses through each wall of the pier under the maximum monthly negative temperature gradient load cases.



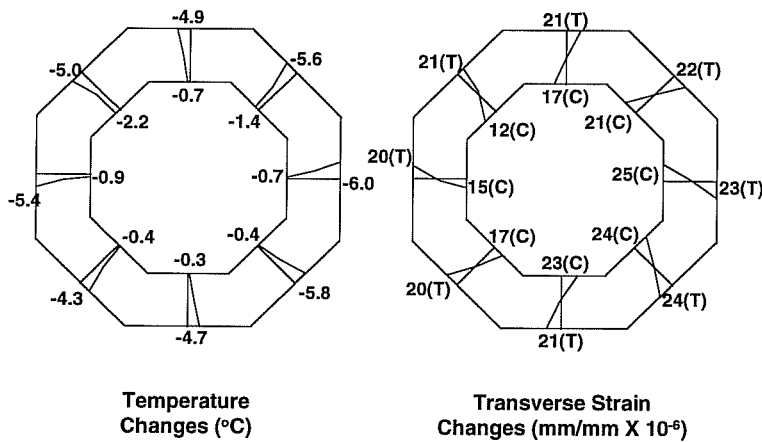
(a) April 1996 Negative Gradient



(b) May 1996 Negative Gradient



(c) June 1996 Negative Gradient



(d) July 1996 Negative Gradient

Figure 7.12: Temperature loading and transverse strain from finite element analysis of maximum monthly negative gradients during (a) April, (b) May, (c) June, (d) July.

Unlike the transverse strain changes produced by the positive gradient load cases, the maximum strain changes due to the negative gradient load cases do not necessarily occur in the same locations for each case. The locations of the maximum tensile strain changes did not always correspond to the largest negative temperature changes. The same holds true for the transverse compressive strain changes.

The unpredictability in the locations of the maximum strain changes is due to the distributions of temperature changes around the perimeter of the section for the negative gradient load cases. The entire outside perimeter of the pier typically undergoes almost uniform decreases in temperature (see Figures 7.12a through 7.12d). Thus the effects due to temperature changes in any one face of the pier do not greatly change those in adjacent faces. There is less redistribution of transverse stresses around the section because the temperature loads are more uniform than that of a typical positive gradient. Positive temperature gradients are characterized by large differences in the perimeter temperature changes in the section (see Figures 7.11a through 7.11d). More redistribution of transverse stress occurs during those temperature changes due to the highly uneven temperature loading.

### **7.3.3 Comments**

In general, the strain results from the finite element analyses of both observed and code-specified temperature gradient load cases matched well the behavior predicted by the calculations performed in Chapter 6. However, it is important to note that the finite element analyses requires modeling assumptions similar to those made during manual calculations. Both methods assumed the same modulus of elasticity, Poisson's ratio, and concrete coefficient of thermal expansion. Similarly, the manual calculations and the finite element analysis assumed linear elastic behavior throughout the pier. The pier was modeled with a constant cross-section for both methods (i.e. the capital and base were ignored). Finally, the contributions to both heat flow and the stress field present in the pier from post-tensioning tendons and imbedded rebar were ignored.

## CHAPTER 8

### *COMPARISON OF RESULTS*

#### *8.1 LONGITUDINAL STRAINS*

##### **8.1.1 Strain Projection Plots**

As discussed previously, the strain gauges used during the instrumentation of pier P16 were temperature compensated so that direct linear expansions or contractions due to temperature were not measured. The strains displayed are the differential strains caused by the temperature gradients and physical member restraints which produce stresses in the members. These are referred to as self-equilibrating strains.

The octagonal shell projection method, discussed in Chapter 6, was used to display two-dimensional distributions of temperature and longitudinal self-equilibrating strains on a one-dimensional axis for comparison purposes. Temperatures and strains plotted in this manner are easier to visualize, as are their effects on the member in a global sense. Comparisons between results from several strain calculation methods can be more easily made.

It should be noted that the strain projection plots presented in this section only provide a general idea of the state of self-equilibrating longitudinal strains present due to the temperature distributions throughout the pier's cross-section. Strains occurring at the outermost east and west fibers of the pier are most accurately represented. The values of strain projected onto the one-dimensional plot at these points are the averages of several strains located at the outermost edges which have similar values. Strains plotted from the interior of the cross-section are the averages of strains located at both the outer faces and the interior, which may differ in magnitude and in direction. For this reason, strains plotted away from the outer edges on the one-dimensional graphs are generally smaller in magnitude than those actually present.

In order to gauge the relative accuracy of the three analytical methods used in Chapters 6 and 7, strain distributions from each were compared on a one-dimensional strain projection plot. This was necessary in part because the strain results from the classical method presented by Imbsen, et al [5] and discussed in Chapter 6 were calculated from the measured temperature distribution projected onto a one-dimensional axis. Thus, the strains due to the one-dimensional temperature loading could not be extrapolated to a two-dimensional distribution (see the appendix for an example calculation).

Strain distributions presented herein were calculated for the maximum positive and negative temperature distributions for the months of April and June. The temperature gradients measured during April were largest in magnitude, as were the calculated self-equilibrating strains. However, no strains were measured in the pier during April due to scheduling constraints. Therefore, results from the month of June are also included here because they represent the largest temperatures and strains that occurred while field measurements of strains were being performed (see Chapter 4 for a timeline of events in the construction and instrumentation of the pier). Only strains calculated from the measured temperatures are presented in this section. Too few points of longitudinal strain were measured in the cross-section to produce a comparable strain distribution projection. Comparisons of measured and calculated strain changes are presented in subsequent sections.

#### ***8.1.1.1 Positive Gradients***

Figure 8.1 shows a comparison between three analytical methods for the calculation of strain induced by the maximum positive temperature gradient for April. The strain distribution is plotted along the east-west axis of the pier's cross-section because the largest strains occurred on the east and west faces. Results from the finite element analysis (see Chapter 7) are compared with two hand calculation methods. The classical method assumes that temperatures vary only along one axis through the cross-section, while the primary bending axis method accounts for the actual two-

dimensional distribution of temperatures (see Chapter 6 for a description of both hand calculation methods).

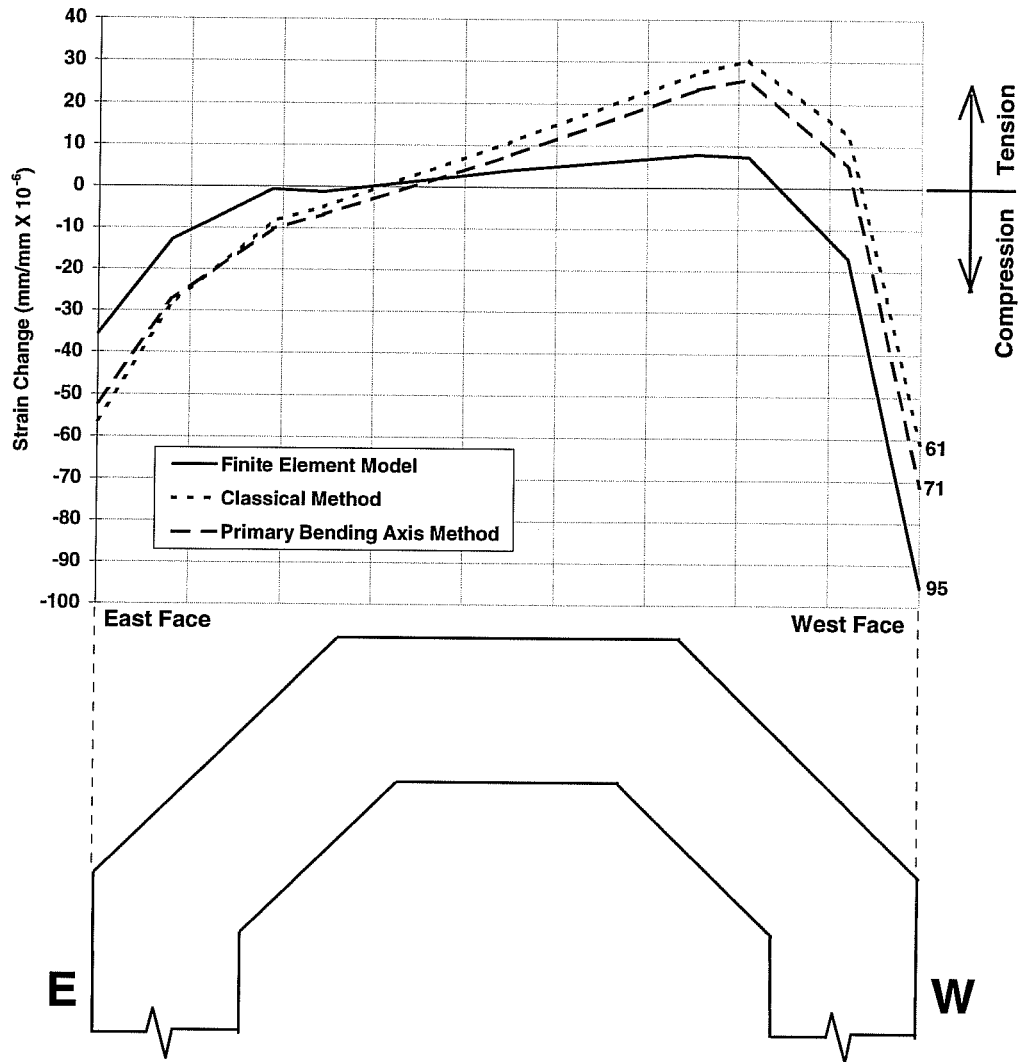


Figure 8.1: Comparison of calculated strains projected on the east-west axis for the April 1996 maximum positive temperature distribution.

From Figure 8.1 it can be seen that strains found by the finite element analysis differed somewhat from the hand calculations. The two hand calculation methods

produce very similar results. Given that all three analyses used the same material properties and cross-section geometry, the finite element model probably produced the most refined computational results. The classical method differed the most from the finite element solution because it required the most significant simplifying assumptions. The two-dimensional temperature distribution across the pier's cross section used for the primary bending axis method might produce results approaching those from the finite element analysis if the areas of constant temperature (i.e. the area "mesh") were made smaller. The ideal solution in this case would consist of infinitely small areas of constant temperature. The areas used in this particular analysis were large to simplify the calculations (see Figure 6.15).

For comparison purposes, the strain distributions calculated from the maximum positive temperature distribution for June are shown in Figure 8.2. As in April, the maximum temperature effects occurred along the east-west cross-sectional axis.

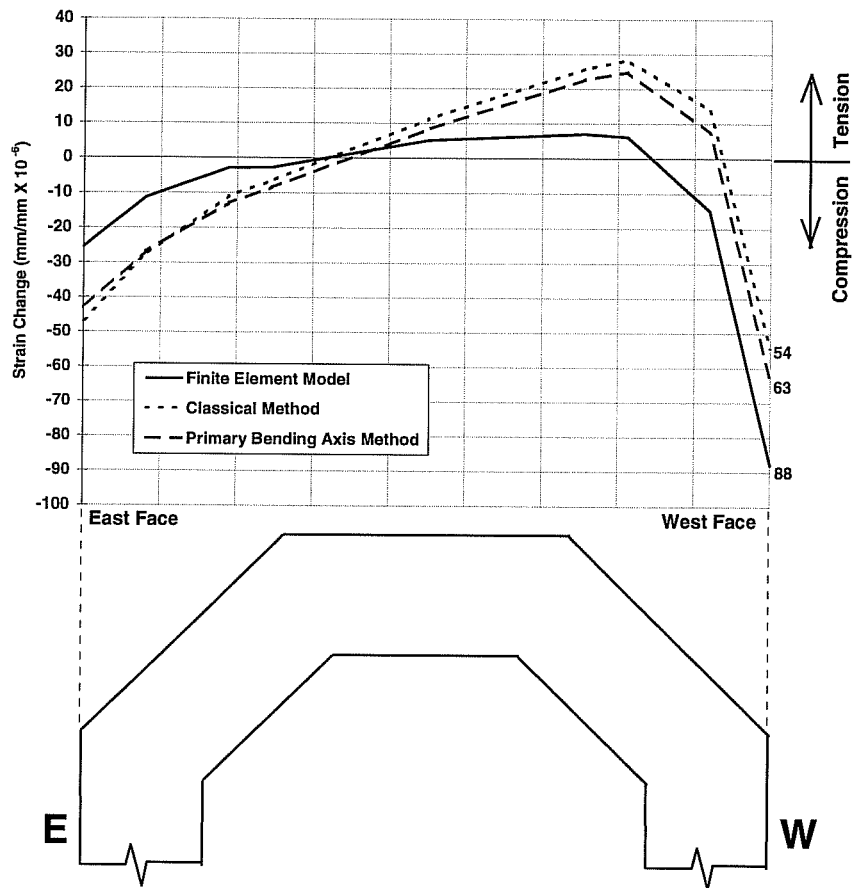


Figure 8.2: Comparison of calculated strains projected on the east-west axis for the June 1996 maximum positive temperature distribution.

The strain distributions plotted in Figure 8.2 are similar in shape to those calculated for the April positive gradient and shown in Figure 8.1. This is to be expected, as the temperature distributions for both months' gradients were similar. As before, the hand calculation methods produced similar distributions, and the primary bending axis method seems to more closely approach the results from the finite element analysis. Note that the magnitudes of strains produced by the June gradient are slightly less than those from April because the temperature changes in June were not as great.



### 8.1.1.2 Negative Gradients

The strain distributions calculated from the maximum negative gradient occurring during April are plotted in Figure 8.3. Note that the cooler temperatures present on the outer faces of the pier during a negative gradient cycle produce substantial tensile strains at those locations. Much smaller compressive strains occur in the interior of the pier where the temperatures are relatively warm. For consistency, the longitudinal strain distributions are plotted along the east-west axis. The negative gradient load case for April did produce the maximum strain effects along the east-west axis.

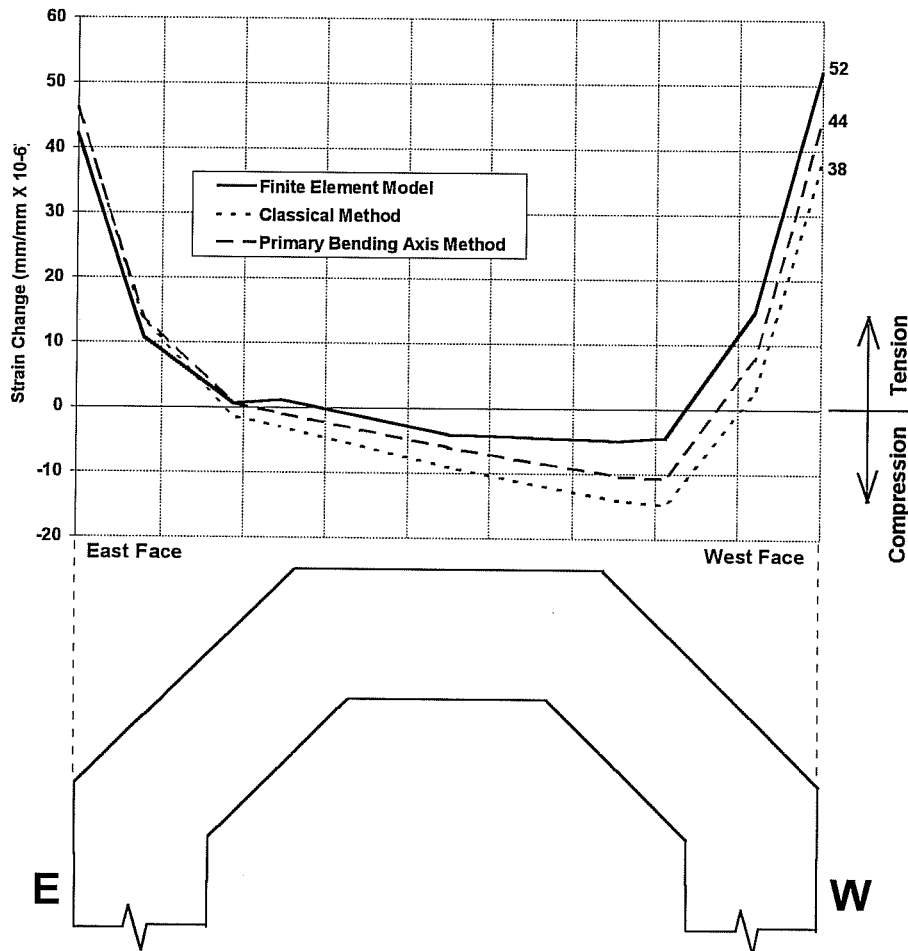


Figure 8.3: Comparison of calculated strains projected on the east-west axis for the April 1996 maximum negative temperature distribution.

General observations concerning the strain distributions plotted in Figure 8.3 are similar to those for the positive gradient discussed earlier. In this case, the differences in calculated tensile strains at the outer faces are smaller than that of the compressive strains at the same locations induced by the positive gradient as shown in Figure 8.1. The percent difference between the tensile strains on the outer west faces from the finite element analysis and the primary bending axis are about 17%, compared with a 25% difference for the compressive strains on the west face from the April positive gradient.

The primary bending axis method again seems to produce results more closely associated with those from the finite element model because both analyses accounted for the two-dimensional temperature distribution. The classical method's assumption that the temperature varies only along one axis through the cross-section produces results that further underestimate the maximum strains occurring in the outer fibers of the pier's cross-section.

Figure 8.4 shows the strain distributions induced by the maximum negative temperature gradient that occurred during June. Calculated tensile strains located at the outer fibers of the section are smaller in magnitude than those from the April 1996 negative gradient. The shapes of the negative gradient strain distribution for the two months are virtually identical, however, as are the relative magnitudes between calculation methods. It appears that the primary bending axis method for calculating self-equilibrating strains consistently gives results more closely matched with those from the finite element analysis.

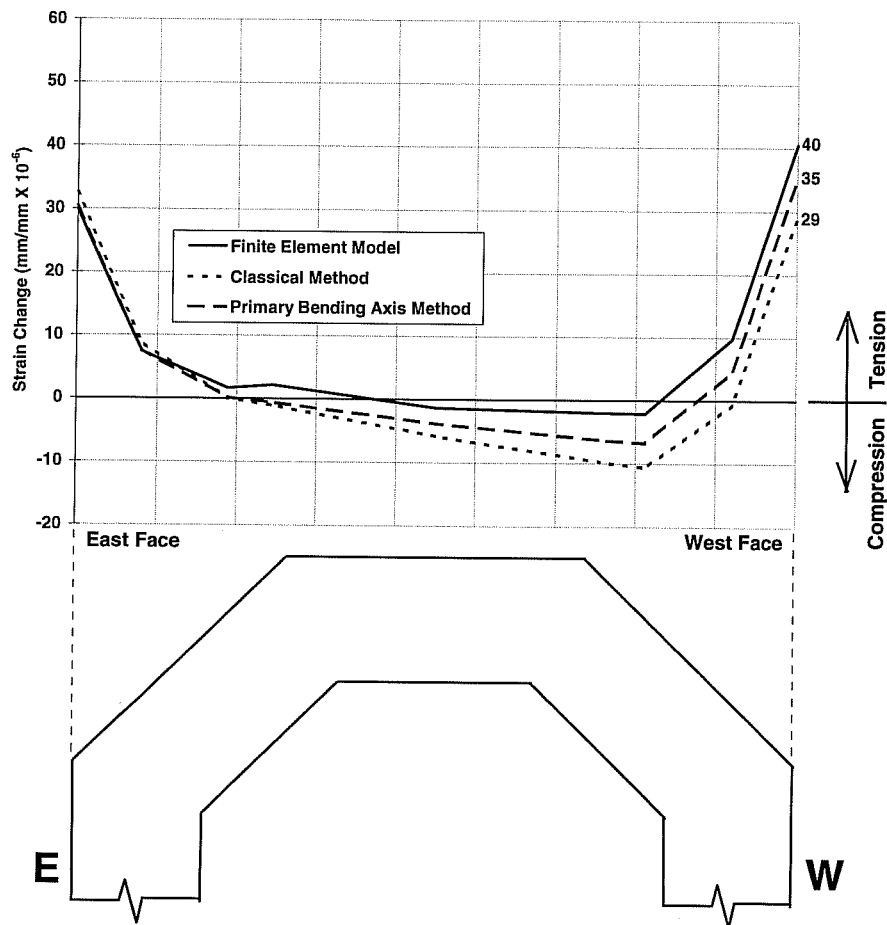


Figure 8.4: Comparison of calculated strains projected on the east-west axis for the June 1996 maximum negative temperature distribution.

### 8.1.2 Measured Strain Comparisons

Longitudinal strains were directly measured by concrete strain gauges located in three column segments and the capital (see Chapter 3 for a full discussion of instrumentation locations). Strains were measured to confirm the validity of the calculation methods used to estimate the self-equilibrating strain distribution at various locations in the pier's height and cross-section.

Strains recorded by the concrete strain gauges installed in the pier and discussed in this chapter are purely due to self-equilibrating stresses induced in the pier by non-linear temperature gradients. The electronic strain gauges used to instrument the pier are specially designed to compensate for any strains occurring due to temperature changes. No elongation or shortening of the strain gauge, steel rod, or concrete matrix surrounding it due to direct temperature *changes* are recorded by the gauge. Therefore, for the non-linear temperature gradient loads applied on the pier, only self-equilibrating strains were recorded by the electronic strain gauges.

Strain projection plots like those discussed earlier in this chapter are not useful for determining the self-equilibrating strains present at a given *point* in the pier's cross-section. The averaging process used to produce the projections "erases" any information concerning the actual strain at a point. This effect varies along the length of the axis of the projection. Strains calculated near the outer fibers of the section are the most accurate, for reasons described earlier in this chapter. The following comparisons of strain were performed at individual points in the cross-section corresponding to the locations of longitudinal strain gauges installed in the concrete. Too few strain gauges were present in any given section of the pier to provide complete verification of the strain projection across the section such as those shown in Figures 8.1 through 8.4.

The results from the two hand-calculation methods discussed in Chapter 6 and the finite element analysis discussed in Chapter 7 were adjusted for more direct comparison with the individual points of strain recorded by the gauges imbedded in the concrete of the pier. In the finite element analysis, strains were calculated at node points (see Chapter 7 for a discussion of node locations). This limited the number of calculated strain points at mid-length of each wall of the pier. Similarly, the strain results from the primary bending axis method were assumed to be located at the same positions as the measured temperatures in each pier wall. Discrete areas of constant temperature used to calculate strains by this method were assumed to coincide with the

measured temperature locations in segment PC16-5 (see Chapter 6 for a discussion of the primary bending axis method). Although only an estimate of the strains at any depth in the pier's cross-section, the classical method of strain determination was also included during comparisons with measured strains.

A full discussion and display of all monthly maximum temperature gradients and their associated strains would be tedious and unnecessary: As discussed in Chapter 6, the temperature distributions of each month's maximum gradients vary only slightly in magnitude and are similar in shape. Ideally, strain comparisons would be made here using the largest measured gradients. However, these gradients occurred during April, and the concrete strain gauges were not operational at that time. As such, comparisons with measured strains in this chapter will be made with strains recorded and calculated for the maximum positive and negative gradients that occurred during the month of June. These temperature distributions represent the most severe which were measured while the concrete strain gauges were operational.

#### **8.2.1.1 Positive Gradient**

The temperature gradients used for calculations are not the static temperature distributions present in the pier at any given time. Instead, the *difference* in temperatures between the coolest, most uniform distribution and the set of temperatures showing the largest changes during the day is used to calculate the temperature gradient present in the pier (see Chapter 6 for a discussion of this process). All discussions of temperature gradients made here actually refer to the largest *changes* in temperature over the course of any given day (and their associated strain changes over the same time period).

The maximum positive temperature gradient for the month of June occurred on June 20, 1996 and consisted of the difference in temperatures between 8:25 AM and 7:25 PM. The coolest and most uniform temperatures typically occur around sunrise. The temperature set exhibiting the highest temperatures with the largest differences

typically occurs just after sundown. As with all of the monthly maximum positive temperature gradients measured in pier P16, the June positive gradient's highest temperatures occurred at the west face of the cross-section. Most of the associated bending of the pier due to differential heating also occurred along the east-west cross-sectional axis.

Longitudinally-oriented concrete strain gauges were positioned along the east-west and north-south axes of the pier's cross-section in all three instrumented column segments. Figure 8.5 shows the temperature changes during the maximum positive gradient for June that were recorded by thermocouples located in segment PC16-5 near mid-height of the pier. Temperatures are plotted for the six thermocouples aligned along the east-west cross-sectional axis. Figure 8.6 illustrates the strain changes recorded by individual strain gauges located along the same axis in the base segment PC16-1. Since a full set of temperature measurements was not available for segment PC16-1, the thermal values from segment PC16-5 were used as input for the strain calculations.

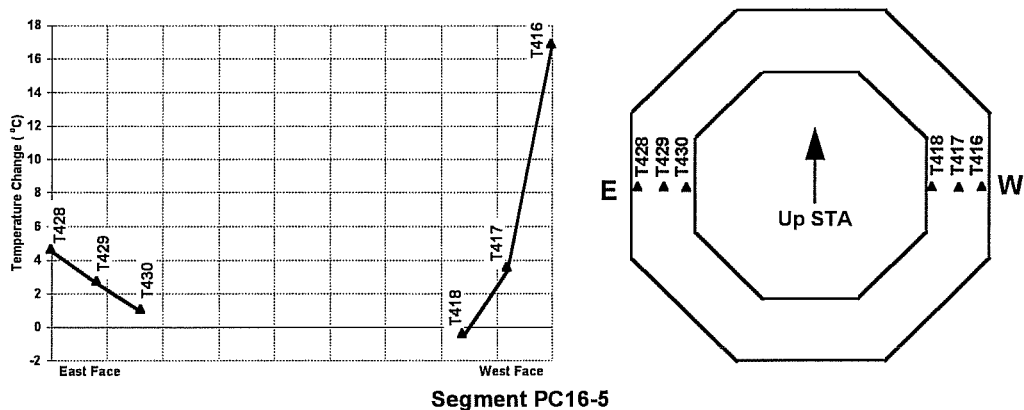


Figure 8.5: Temperature changes along the east-west cross-sectional axis recorded by thermocouples in segment PC16-5.

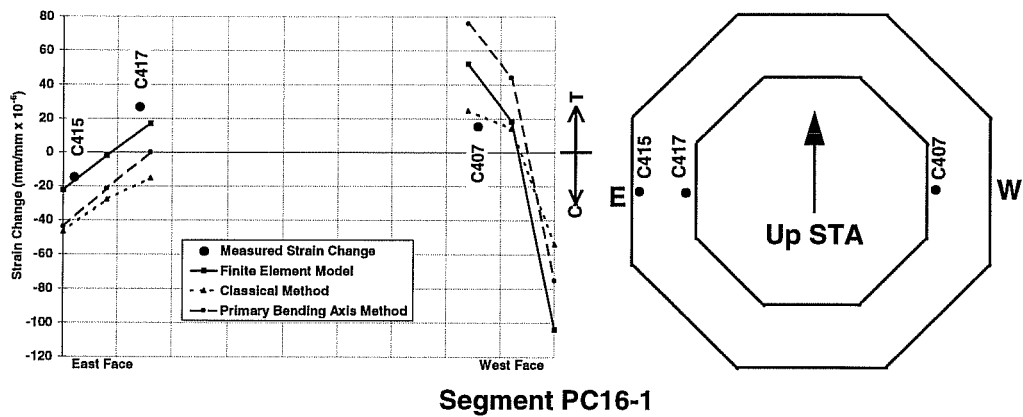


Figure 8.6: Calculated strain changes and strain changes recorded by concrete strain gauges in segment PC16-1, east-west cross-sectional axis.

In general, the shape of the strain changes calculated by various methods seem to be verified by the measured strains with the finite element model giving closest numerical agreement on the east face and the classical method closest agreement on the west face. It is important to note that the methods used for calculation of strain changes presented here assumed that the temperature distribution in Figure 8.5 was present along the entire height of the pier. Segment PC16-1 is located between two overpasses of Interstate Highway 35 and is shaded for the entire day. Thus, the temperatures occurring in the base segment should be somewhat different in magnitude. However, it was shown in Chapter 5 that temperatures in segment PC16-1 tend to follow the same general daily patterns of those in the sunlit portions of the pier. Because of this, one should expect strain changes similar in distribution and slightly differing in magnitude between the two locations. The strain changes recorded in the base segment appear to follow the general distribution of those expected from the sunlit portion of the pier, but are slightly different in magnitude.

Measured strains show the same characteristics along the north-south axis. Figure 8.7 shows temperature changes recorded along the north-south cross-sectional axis in segment PC16-5. Note that the temperature changes are less than those

occurring along the east-west axis. The strain gauges located along the same axis in segment PC16-1 are shown in Figure 8.8. Again they confirm the shape of the strain gradient and the finite element analysis results are in the best agreement overall with the measured values.

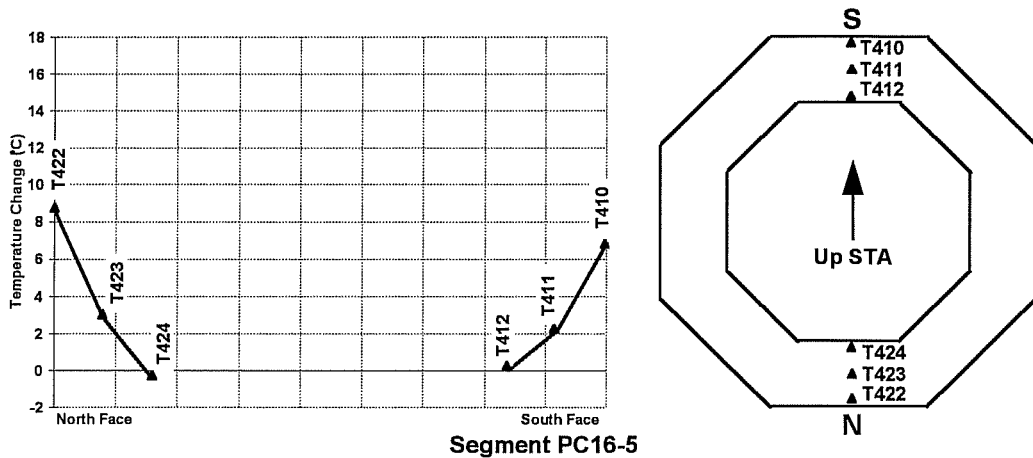


Figure 8.7: Temperature changes along the north-south cross-sectional axis recorded by thermocouples in segment PC16-5.

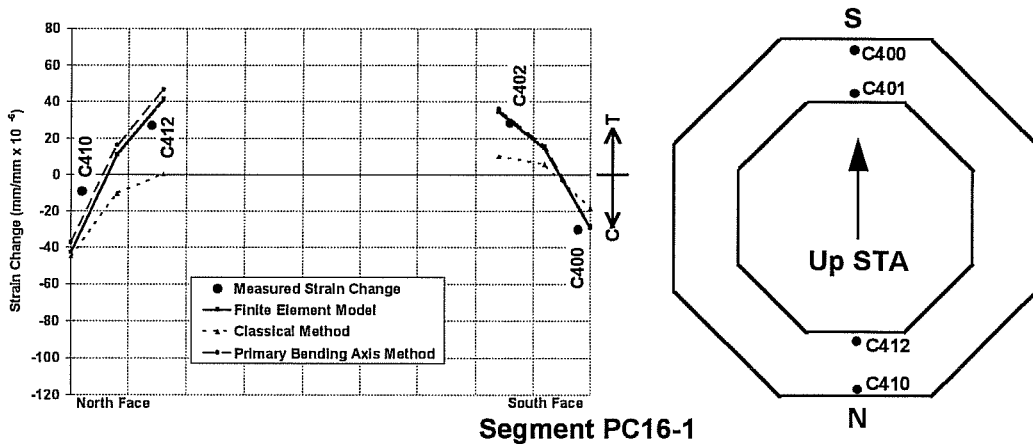


Figure 8.8: Calculated strain changes and strain changes recorded by concrete strain gauges in segment PC16-1, north-south cross-sectional axis.



Measured longitudinal strains located along the north-south axis again appear to confirm the calculated strain distributions. Slight differences in magnitude are most likely due to the differences in temperature distributions between the sunlit segment assumed for calculations and the shaded base segment PC16-1.

The measured strains on the east-west axis of segment PC16-5 are plotted in Figure 8.9. The interior gauges C441 and C435 show almost identical strain changes to those located in segment PC16-1 (C417 and C407). This may be due to the similarities in temperature at the interior faces of both segments. Although no measured temperatures are available at the interior faces of segment PC16-1, it is reasonable to assume that they would be similar to those measured at the same locations in the mid-height segment PC16-5. The exterior temperatures in the sunlit segment are influenced primarily by solar radiation, while exterior temperatures in the shaded segment are a function of ambient temperature changes. The interior temperatures, shielded in both segments by the thickness of the pier's concrete walls, may be insulated sufficiently so that they have similar magnitudes.

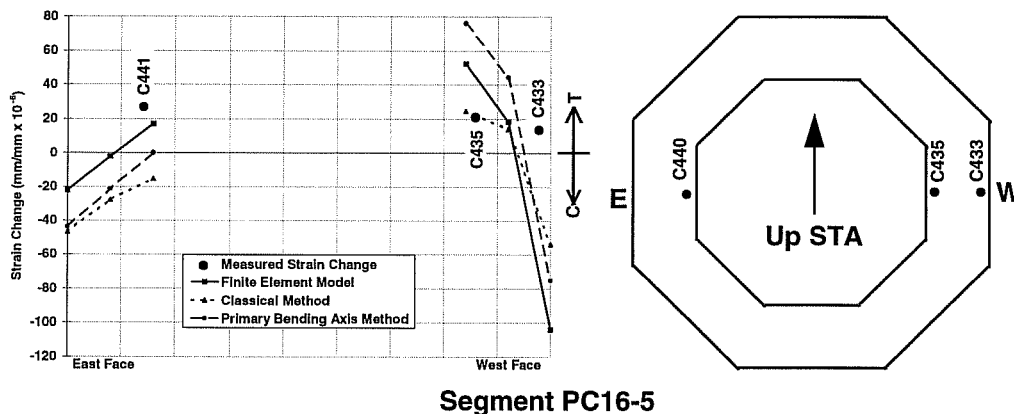


Figure 8.9: Calculated strain changes and strain changes recorded by concrete strain gauges in segment PC16-5, east-west cross-sectional axis.

Gauge C433, located near the west face of segment PC16-5, exhibits strain changes opposite in magnitude to those predicted by all three calculation methods. The daily cycles of strain change recorded by gauge C433 during three days in June exhibiting regular daily temperature patterns are shown in Figure 8.10. Unfortunately, a comparison of readings with gauges located near the west faces of the other instrumented segments was impossible because of damage sustained to those instruments. Both C405 in segment PC16-1 and C455 in segment PC16-7 produced large and erratic readings indicative of gauge damage most likely sustained during the casting process.

However, a comparison was possible with gauge C458 located near the northwest face of segment PC16-7. From the temperature cycles discussed in Chapter 5, it was shown that the west and northwest faces of the sunlit column segments experienced similar heating and cooling patterns and magnitudes. Therefore, C433 and C458 should show similar daily patterns of strain measurements. As seen in Figure 8.10, gauge C433 appears to produce an irregular cycle with magnitudes often opposite in sign to those exhibited by C458. Furthermore, the readings from C433 appear to “drift” from their initial position over time, an indication that the electronic strain gauge may be partially debonded from its steel bar and producing erroneous measurements. This may explain the unusual strain change recorded by C433 that was plotted in Figure 8.9. Note that the readings from T416 tend to confirm the cyclic pattern of C458 and further question the accuracy of C433.

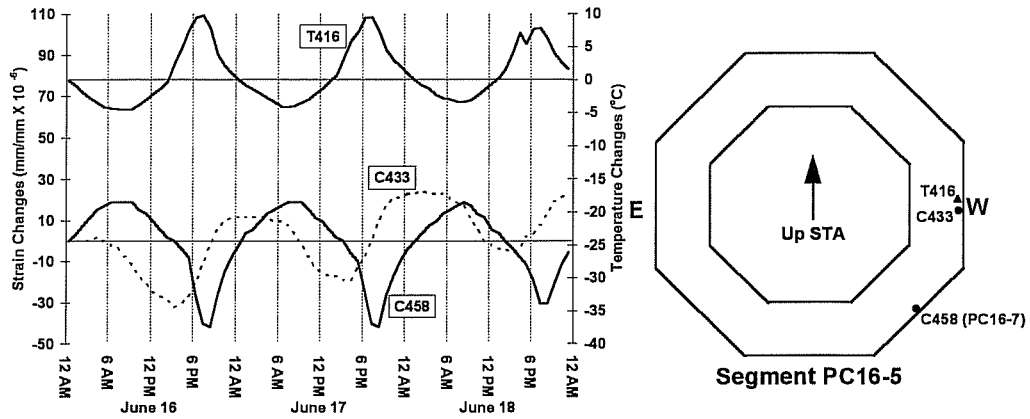


Figure 8.10: Comparison of C433 and C458 during several daily cycles of temperature.

Gauges located along the north-south axis of the mid-height segment PC16-5 appear to confirm the calculated strain values (see Figure 8.11). The magnitudes of strain changes recorded by instruments near both the north and south faces are quite close to the expected values. Interior strains vary somewhat from the calculated strains.

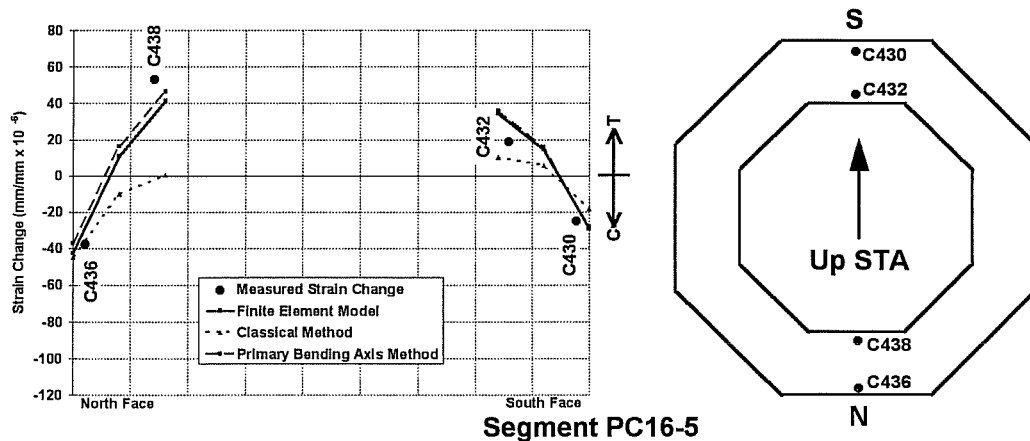


Figure 8.11: Calculated strain changes and strain changes recorded by concrete strain gauges in segment PC16-5, north-south cross-sectional axis.

A comparison of strain changes located along the east-west cross-sectional axis of the “top” segment PC16-7 is shown in Figure 8.12. Gauge C455, located near the west face, was unusable due to large and erratic readings. Strangely, the other gauges located along this axis produced strain changes with almost identical magnitudes.

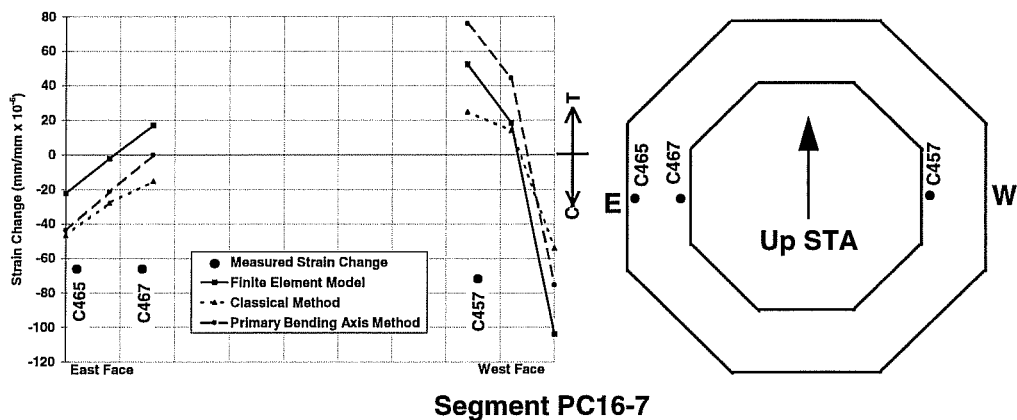


Figure 8.12: Calculated strain changes and strain changes recorded by concrete strain gauges in segment PC16-7, east-west cross-sectional axis.

A constant distribution of strains would indicate that all fibers in the cross-section were undergoing identical temperature changes. This is not the case, as Figure 8.5 clearly shows. After investigation of the readings produced by all strain gauges in segment PC16-7, it was found that nine gauges exhibited daily strain changes that were almost identical in their patterns and magnitudes (see Figure 8.13). This behavior could be caused by restraint provided by the solid capital segment. However, the random location of the gauges producing nearly identical readings suggests problems with the instrumentation wiring.

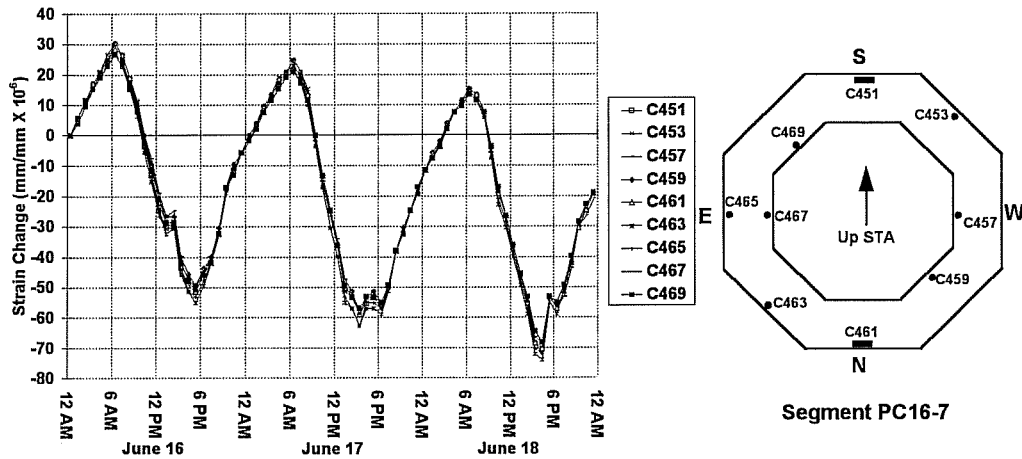


Figure 8.13: Nearly identical daily strain cycles for gauges in segment PC16-7 and their locations and orientations in the cross-section.

In contrast to the gauges located along the east-west axis, the strain readings from gauges on the north-south cross-sectional axis appeared to more closely agree with expected strains. Figure 8.14 shows the distribution of measured and calculated strains along the north-south axis of segment PC16-7. All four gauge readings appear to be “shifted” in tension away from the calculated strains, but their relative positions appear to be similar to those of the calculated strain levels. The nearby capital segment’s role as an anchorage zone may be affecting the apparent strains in this location. No significant changes in post-tensioning force occur over the short 11 hour time period of the temperature changes, but the capital may provide some axial restraint near the top of the pier’s hollow column section, affecting the apparent strains measured in the top segment PC16-7.

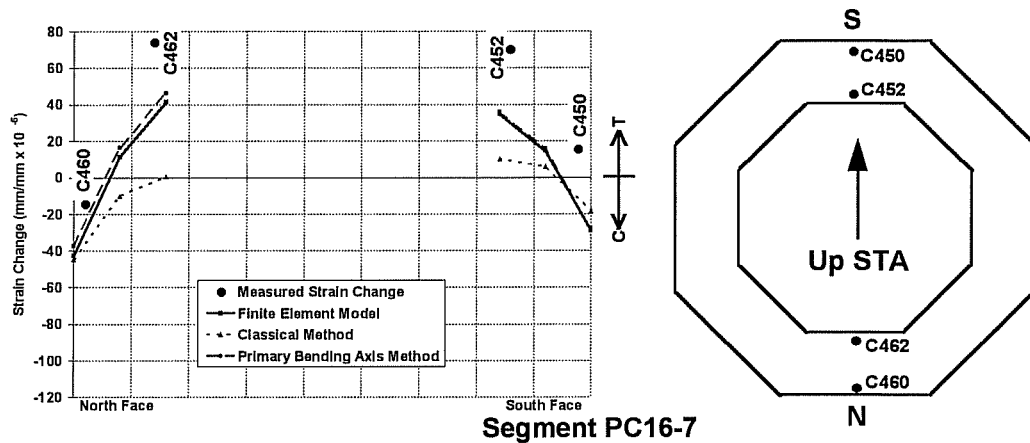


Figure 8.14: Calculated strain changes and strain changes recorded by concrete strain gauges in segment PC16-7, north-south cross-sectional axis.

### 8.1.2.2 Negative Gradient

The maximum negative temperature gradient for the month of June consisted of the temperature differences between 10:25 PM on June 3 and 5:25 AM on June 4. The temperatures present at 10:25 PM were still relatively high from heating during the previous day. At that time, the outer fiber temperatures had cooled while the slow heat flow into the interior of the pier continued to raise temperatures there. Thus, the temperatures were distributed evenly through the cross-section. By 5:25 AM the outer faces had cooled rapidly relative to the interior. At that time, the largest difference in temperatures between the outer and inner faces of the pier was present. A full discussion of the typical daily cycles of temperatures present in the pier can be found in Chapter 5.

Figure 8.15 shows the temperature changes recorded by the thermocouples located along the east-west axis of segment PC16-5 during the maximum negative gradient. Note the greater cooling of the outer fiber temperatures due to the influence of cool nighttime ambient temperatures. Again, these temperature changes are used for the calculations at all pier sections for maximum negative gradient strains. The tensile

changes in strain near the outer surfaces of segment PC16-1 along the east-west axis are illustrated in Figure 8.16. As discussed previously, the measured negative gradient effects on segment PC16-1 may be smaller in magnitude than those calculated due to the segments shaded location. The outer surfaces do not undergo the intense heating due to solar radiation, and therefore do not cool to the same extent that the sunlit segments do. In general, the calculated values on the east-west axis of segment PC16-1 match the measured strains quite well. In particular, the east face points are very close to the finite element analysis predictions.

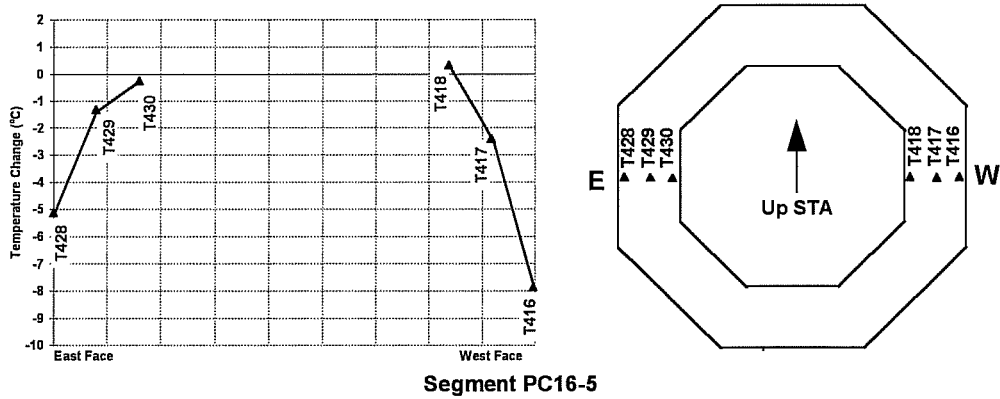


Figure 8.15: Temperature changes along the east-west cross-sectional axis recorded by thermocouples in segment PC16-5.

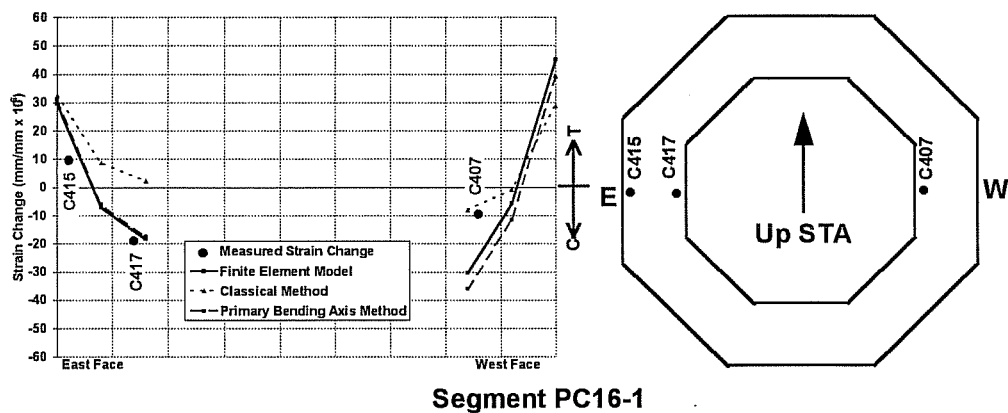


Figure 8.16: Calculated strain changes and strain changes recorded by concrete strain gauges in segment PC16-1, east-west cross-sectional axis.

The temperature changes recorded by the thermocouples located along the north-south axis of segment PC16-5 during the maximum negative gradient are shown in Figure 8.17. These were used for strain calculations along the north-south axis of all column segments. Excellent correlation between measured and calculated strains is apparent at points along the north-south cross-sectional axis of segment PC16-1 (see Figure 8.18). Again the agreement with the results of the finite element model is quite good. The calculated strain changes are slightly greater than those measured, reflecting differences in solar exposure. Note the distribution calculated by the classical method. The calculated values at the exterior faces are relatively close to those from other calculation methods. However, the strains located farther into the interior of the pier are heavily influenced by the tensile strains present at other exterior faces. The averaging techniques used to convert the two-dimensional temperature distribution to a one-dimensional graph for calculation purposes affects the accuracy of the values located away from the ends of the axis. This effect is apparent in Figure 8.18. For further discussion of strain calculation by the classical method, see Chapter 6.

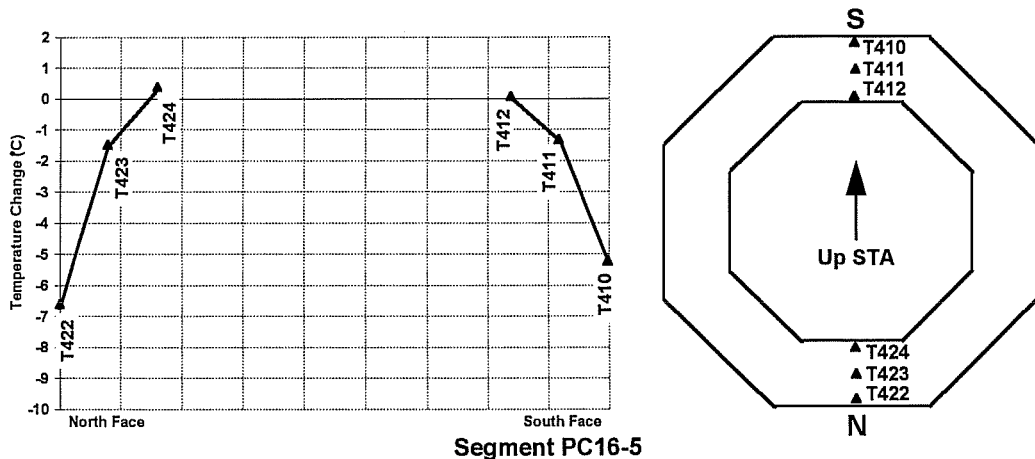


Figure 8.17: Temperature changes along the north-south cross-sectional axis recorded by thermocouples in segment PC16-5.



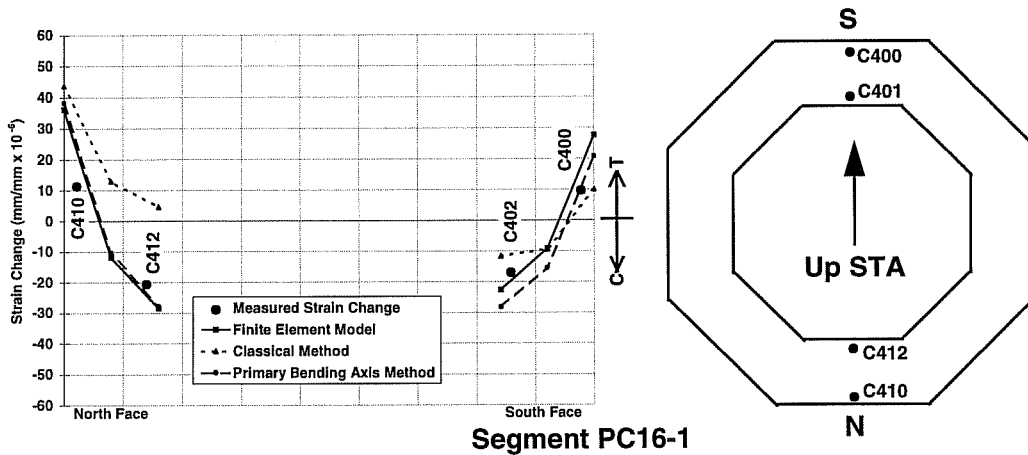


Figure 8.18: Calculated strain changes and strain changes recorded by concrete strain gauges in segment PC16-1, north-south cross-sectional axis.

The measured strains along the east-west axis of segment PC16-5 do not coincide as well with the calculated values, with the exception of gauge C441 (see Figure 8.19). As discussed earlier in this chapter, gauge C433, located near the west face of the segment, is probably not reliable. The strain change recorded by C435, located near the interior face of the pier's west wall, appears unusually small in magnitude. Figure 8.20 shows a plot of the strain measurements recorded by C435 over the course of three regular, typical summer days. For comparison, readings from C454, located in segment PC16-7, are also included. From the figure it can be seen that the magnitudes of strain recorded by C435 are much smaller than normally expected. The "stair-step" appearance of the data recorded by C435 indicates that the strain levels being recorded are close to the minimum strains the gauge is capable of sensing, and may be an indication that the gauge is partially debonded from its steel rod. Thus, both C435 and C433 appear to be unreliable.

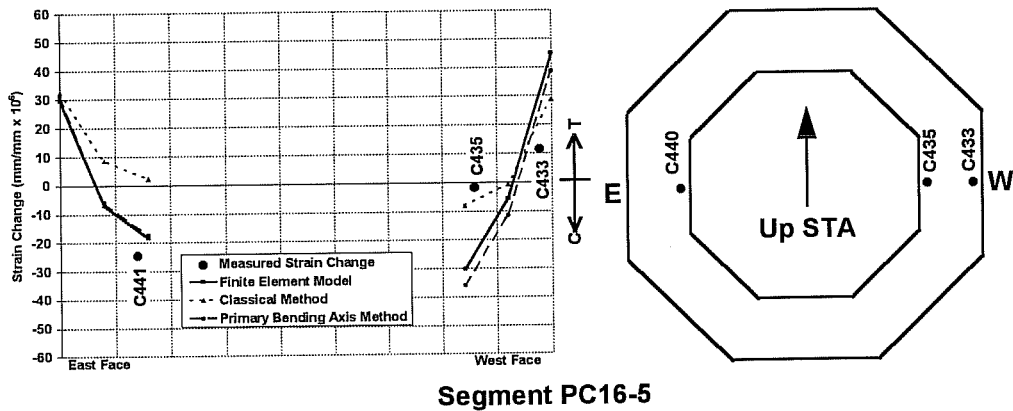


Figure 8.19: Calculated strain changes and strain changes recorded by concrete strain gauges in segment PC16-5, east-west cross-sectional axis.

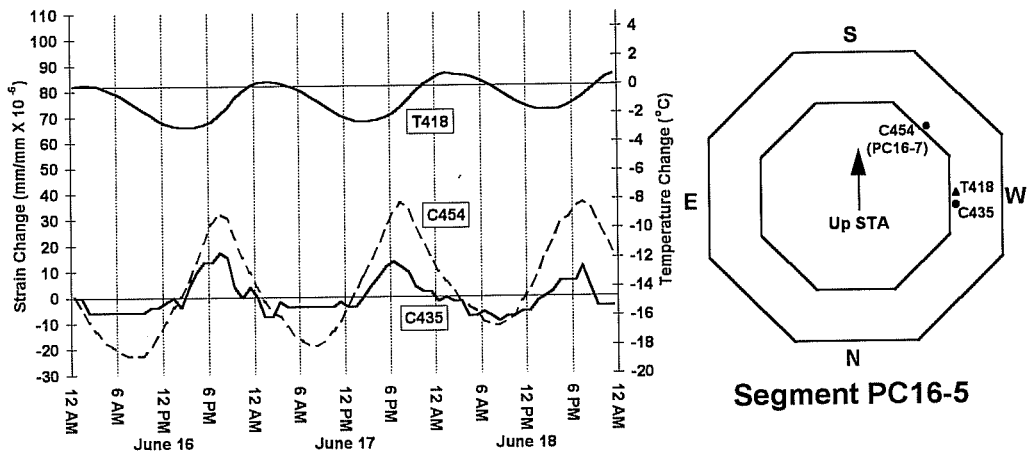


Figure 8.20: Daily cycles of strain recorded by C435 and C454.

In contrast to the troubled gauges along the east-west axis of segment PC16-5, excellent correlation between observed and calculated strains was found along the north-south axis of that segment. Figure 8.21 illustrates the similarities in measured and calculated strains. Both the finite element model and the primary bending axis method produced strains very close to those measured in the field.

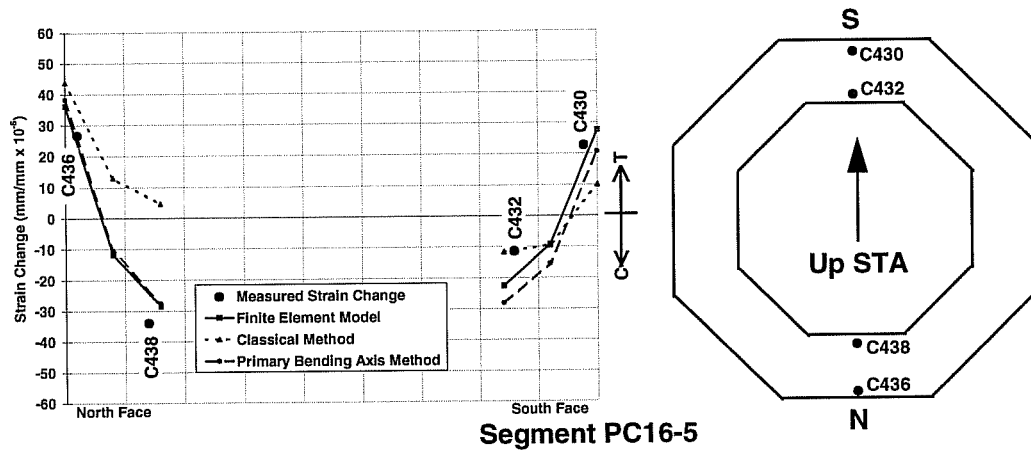


Figure 8.21: Calculated strain changes and strain changes recorded by concrete strain gauges in segment PC16-5, north-south cross-sectional axis.

Gauge measurements for the east-west and north-south axes of segment PC16-7 are plotted in Figures 8.22 and 8.23, respectively. Concerns about the measurements made by these gauges were expressed earlier in this chapter. However, it is notable that the same general trends in measurement apply for the negative gradient load case as for the positive gradient discussed earlier. In this case, the strain gauges produced readings different than those expected from strain calculations. Just as the measurements along the north-south axis were “shifted” in the direction of tension for the positive gradient (see Figure 8.14), so too are the negative gradient measurements “shifted” in the direction of compression (see Figure 8.23). Again, the north-south axis instruments exhibit strains that reflect the calculated distributions, but do not match the calculated magnitudes.

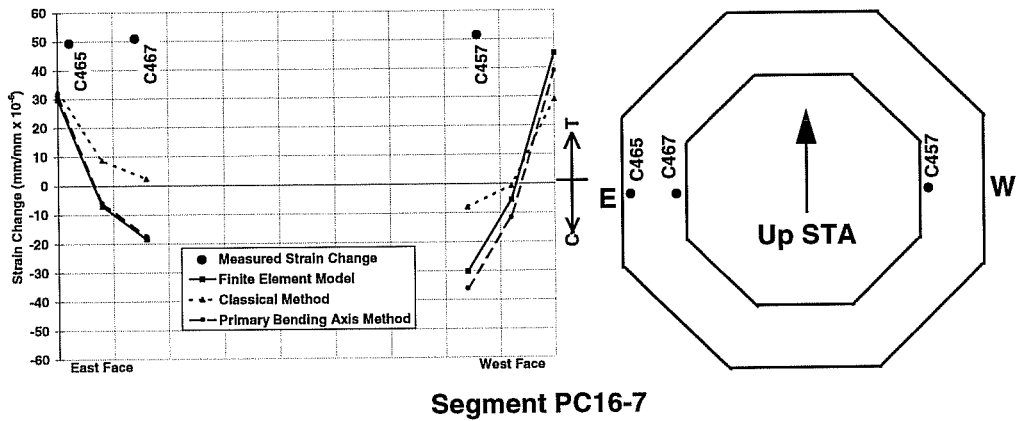


Figure 8.22: Calculated strain changes and strain changes recorded by concrete strain gauges in segment PC16-7, east-west cross-sectional axis.

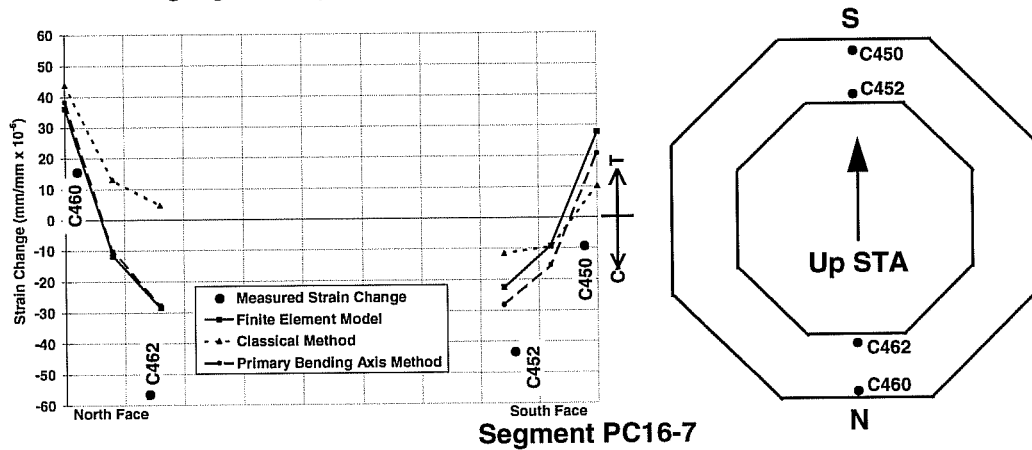


Figure 8.23: Calculated strain changes and strain changes recorded by concrete strain gauges in segment PC16-7, north-south cross-sectional axis.

### 8.1.3 Comments on Longitudinal Strains

In general, calculated strains compared favorably with strains measured in the pier. Unfortunately, the unreliability of several key concrete strain gauges prevented the determination of strains near the west face of the pier where the largest strains were expected to occur. Calculated and measured strains correlated well in locations where reliable strain gauges were operating. Strains in locations along the north-south axis of

base segment PC16-1 and mid-height segment PC16-5 agreed closely, as did many of those on the east-west axes. Thus, it appears that the calculation methods used to estimate self-equilibrating strains induced in the pier by non-linear temperature gradients are valid.

The strains measured in the top segment PC16-7 differ from those measured in the other column segments. They also do not match strains calculated using procedures outlined in Chapter 6 and determined from the finite element model discussed in Chapter 7. However, all three analytical models ignored the possible restraint effects on measured strains due to the presence of the monolithic capital segment less than 600 cm from the gauges located in PC16-7. The nonlinear strain effects due to the post-tensioning tendons anchored in the capital may be affecting apparent strains recorded by the strain gauges located near the capital. The unusual set of nearly identical strain measurements recorded by nine gauges in apparently random locations and orientations in segment PC16-7 also suggests the possibility of wiring errors.

## 8.2 *TRANSVERSE STRAINS*

Self-equilibrating strains also occur in the transverse direction (normal to the longitudinal axis of the pier). They are induced by temperature gradients through the thickness of the pier's walls but also depend on the geometry of the pier's cross-section (see Chapter 6 for a discussion of the calculation procedures to determine transverse strains).

Four strain gauges were installed in each column segment to verify the theoretical transverse strain calculations performed in Chapter 6 (see also the appendix). Gauges were located in the south, west, north, and east walls at a cover of approximately 65 mm and oriented parallel to the exterior faces. A full discussion of the pier instrumentation can be found in Chapter 3.

For comparison with measured strains, two calculation procedures were performed. The first involved hand calculations and the use of a computer frame

analysis program to determine redistribution of forces between walls of the pier's cross-section (see Chapter 6). Transverse strains were also determined using the finite element analysis discussed in Chapter 7. Both calculations assume that temperatures are known at three points through the thickness of the pier walls and that they vary linearly between known temperature locations. According to Imbsen, et al [5] temperatures can be assumed to vary linearly through walls about 250 mm or less in thickness. The distance between known temperatures located at points spaced approximately 200 mm apart is well within that limit.

Calculations of transverse strains were performed to determine the strain distribution through the pier wall thickness at mid-length of the wall. This location was chosen to coincide with the positions of the strain gauges. The figures in the following sections show strain distributions and points of measured strain for each of the four walls instrumented in each column segment.

### **8.2.1 Positive Gradient**

Transverse strains calculated by the methods described in Chapters 6 and 7 behaved in a similar fashion to the longitudinal strains. High temperatures tend to induce regions of compressive strain and vice versa as the pier maintains equilibrium with the temperature-induced expansions and contractions of the concrete. Thus, for the maximum positive gradient load case from June, where temperature increases occurred more rapidly at the outside face of the pier, transverse self-equilibrating strains were compressive near the outer faces and tensile in the pier's interior. The finite element model and the hand calculations produced virtually identical results. Both models were calculated with the full sunlit temperature distribution measured in segment PC16-5, and assumed no external restraints on the pier cross-section.

Figures 8.24 through 8.27 show the calculated and measured strains in each of the four walls of segment PC16-1 where transverse strain gauges were located. In general, except for gauge C416, calculated strains appear to correlate well with

measured strains. Slight differences in magnitude may be caused by the segment's shaded location. Gauge C401 located near the south face and C411 located near the north face both recorded strains within about 25% to 30% of those estimated by calculation. C406 and C411 recorded strains lower than those expected, while C401 recorded somewhat higher strains. Gauge C416, located near the east face, recorded a strain change exactly opposite in magnitude to the calculated strains at the same location.

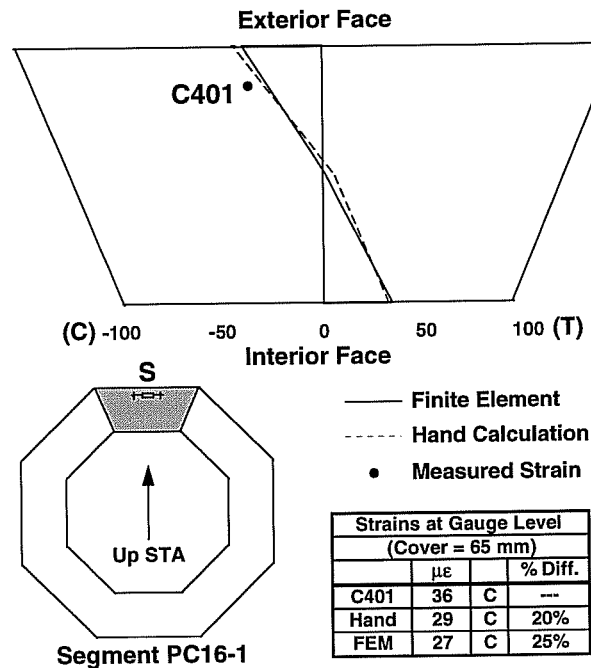


Figure 8.24: Transverse strain comparison in the south wall of segment PC16-1.

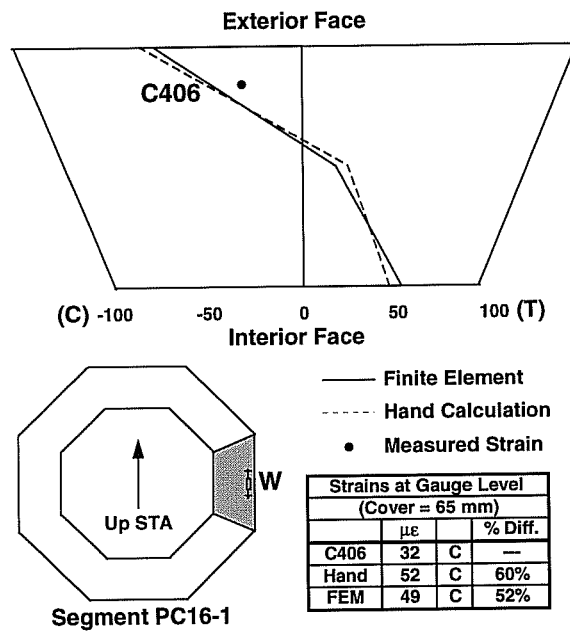


Figure 8.25: Transverse strain comparison in the west wall of segment PC16-1.

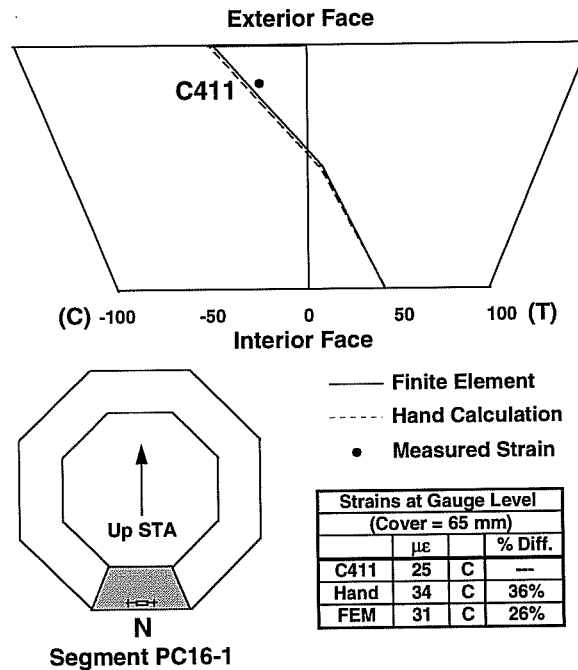


Figure 8.26: Transverse strain comparison in the north wall of segment PC16-1.



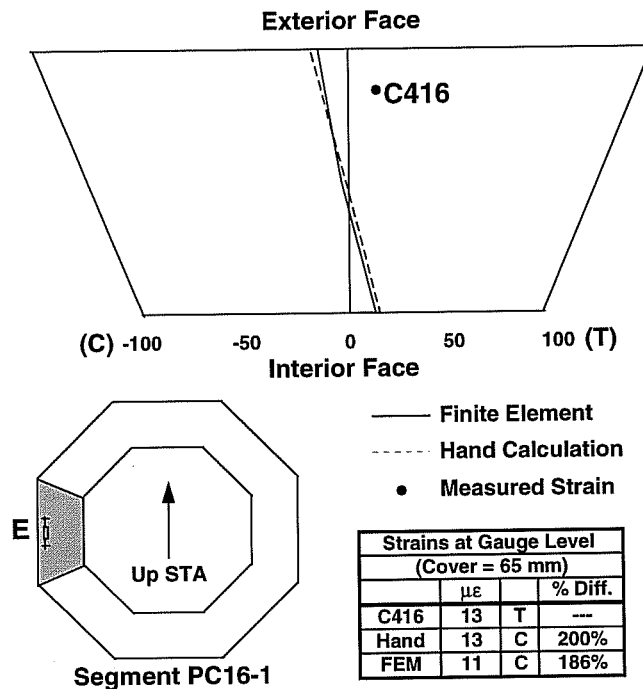


Figure 8.27: Transverse strain comparison in the east wall of segment PC16-1.

An examination of the behavior of gauge C416 over the course of several daily cycles of temperature revealed problems with the gauge hardware. Strain readings from C416, along with temperatures from thermocouple T428, located in a similar position in segment PC16-5, were plotted for several typical summer days in June (see Figure 8.28). Gauge C416 exhibited erratic behavior, and the readings tended to “drift” rather than following a regular cycle like the daily temperatures. Although there was a slight increase over the three day period of ambient temperature, this was not enough to account for the gauge drift and does not explain why C416 exhibits tensile strain changes during heating of the surrounding concrete. The plot in Figure 8.28 suggests that the electronic strain gauge is partially debonded from its steel rod.

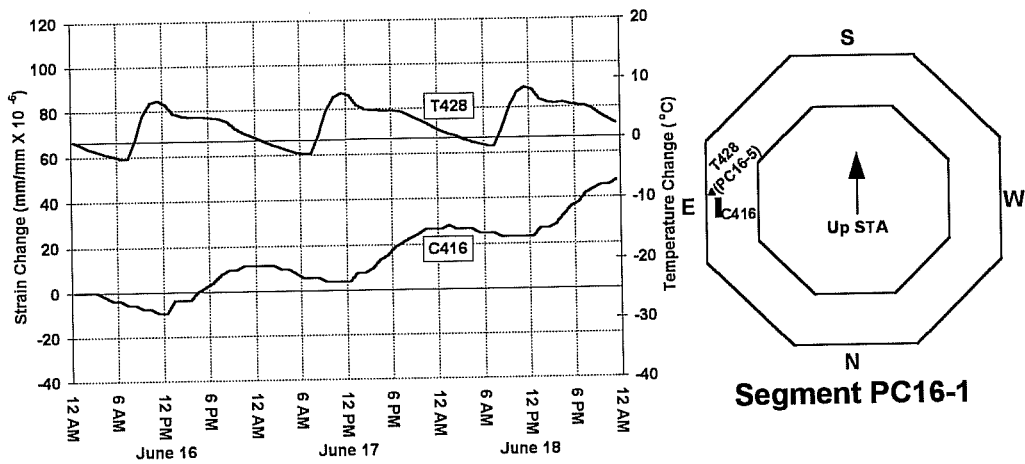


Figure 8.28: Several daily cycles of strain changes recorded by gauge C416.

Measured and calculated strains in the south and west walls of segment PC16-5 are similar in magnitude and direction (see Figures 8.29 and 8.30). Unfortunately, erratic behavior of gauge C437, located in the north wall, made a comparison of strains impossible there (see Chapter 5 for a discussion of gauge C437). Figure 8.32 shows the comparison of strains at the location of gauge C440. Calculated strains in the east face appear to be underestimated when compared to the strain change recorded by C440.

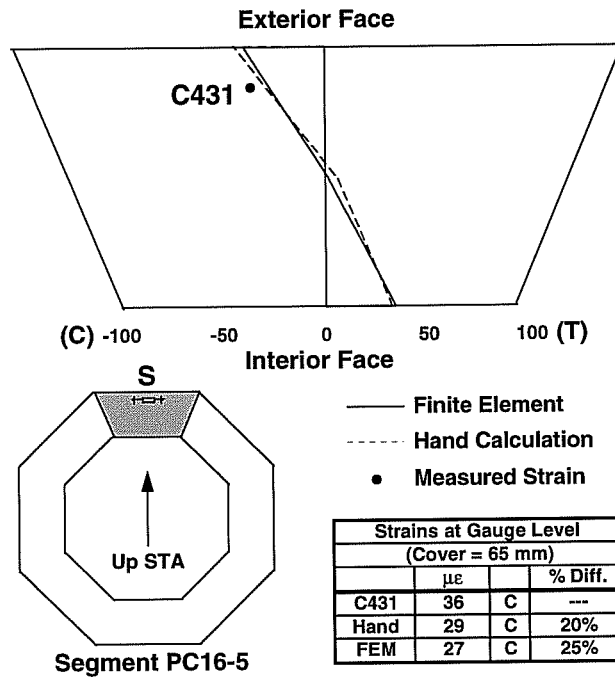


Figure 8.29: Transverse strain comparison in the south wall of segment PC16-5.

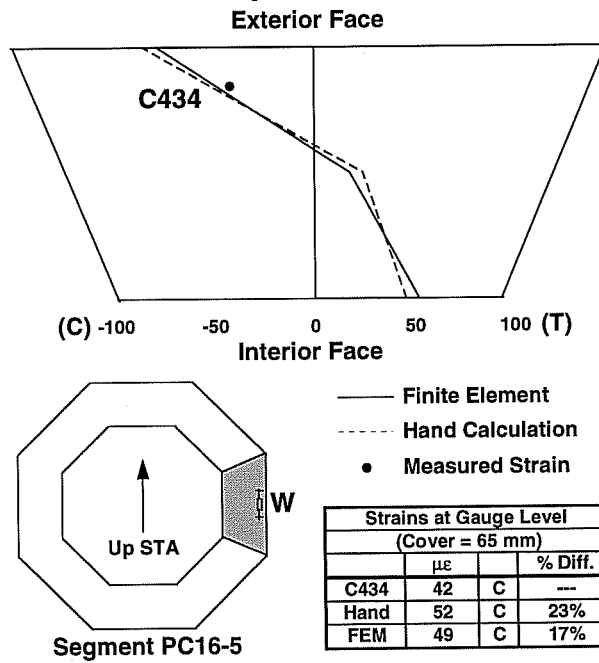


Figure 8.30: Transverse strain comparison in the west wall of segment PC16-5.

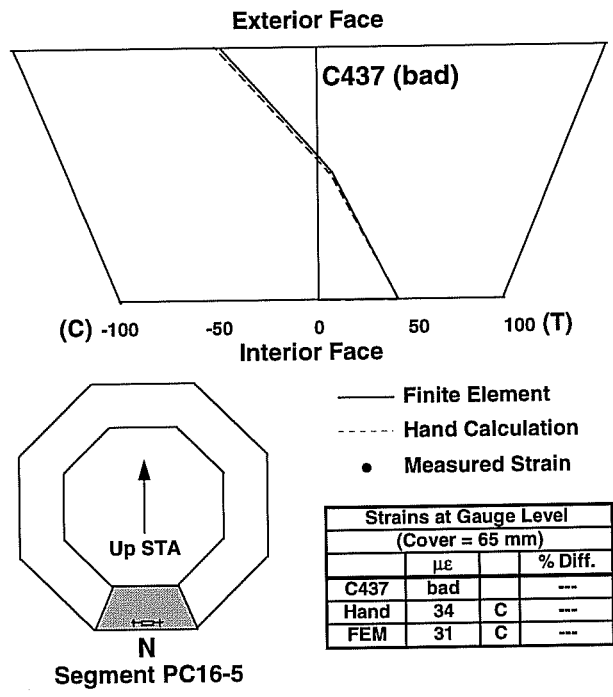


Figure 8.31: Transverse strain comparison in the north wall of segment PC16-5.

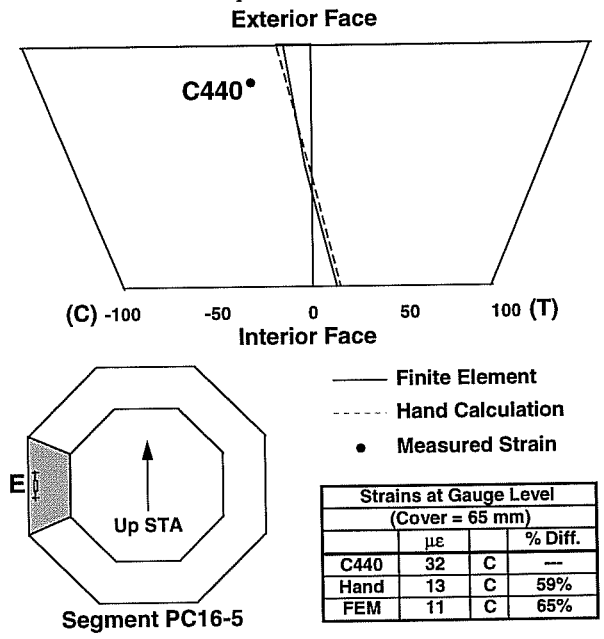


Figure 8.32: Transverse strain comparison in the east wall of segment PC16-5.

As discussed earlier in this chapter, longitudinal strain changes recorded by gauges located in segment PC16-7 appeared to be larger than those calculated. It was hypothesized that restraint provided by the nearby capital segment might be affecting the strain field at the location of the gauges. Transverse strain gauges in segment PC16-7 also recorded strain changes larger in magnitude than expected (see Figures 8.33 through 8.36). It is possible that the monolithic capital segment (which also serves as the anchorage zone for the pier's post-tensioning tendons) provides enough restraint to the top of the hollow column section to affect strain readings in that area. If the column was restrained sufficiently in the transverse direction, it could increase the strain levels induced by the temperature changes in the pier. In general, the strains recorded in segment PC16-7 were 40% to 60% greater than those calculated.

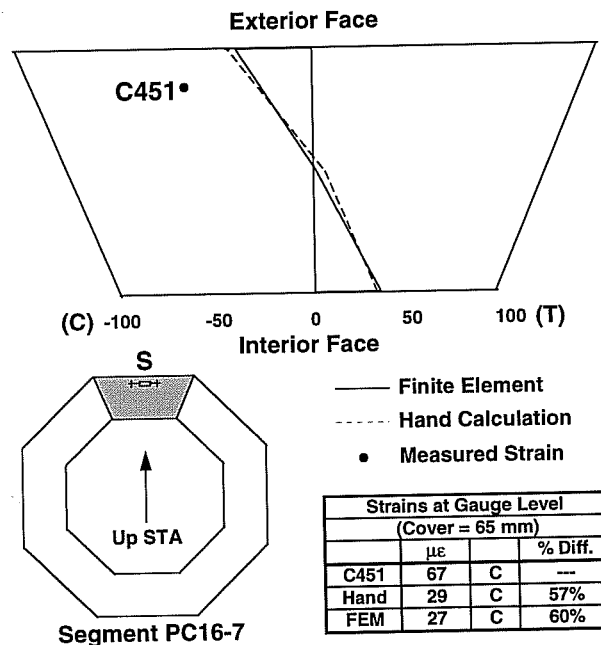


Figure 8.33: Transverse strain comparison in the south wall of segment PC16-7.

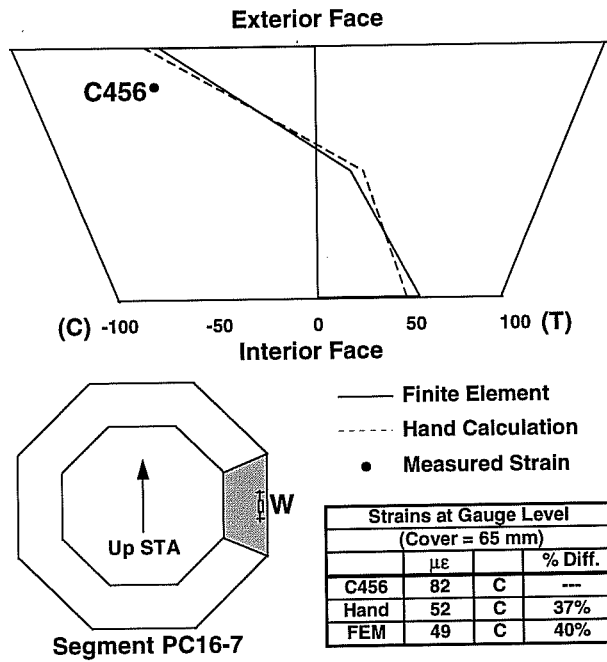


Figure 8.34: Transverse strain comparison in the west wall of segment PC16-7.

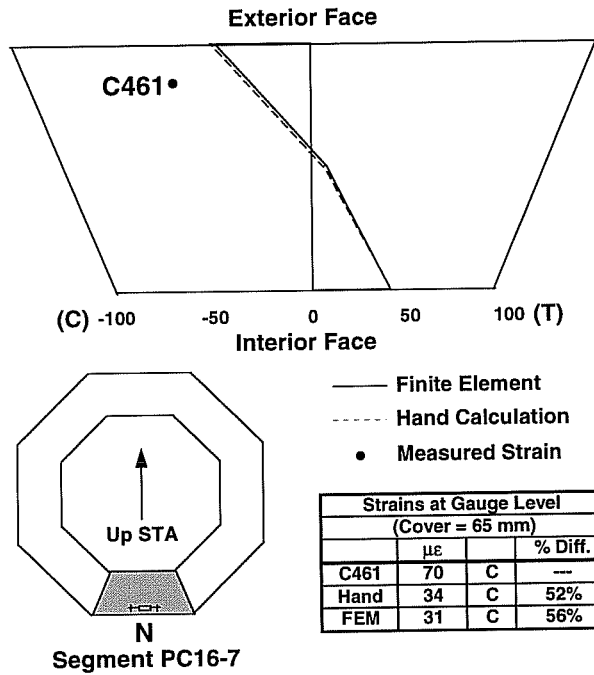


Figure 8.35: Transverse strain comparison in the north wall of segment PC16-7.

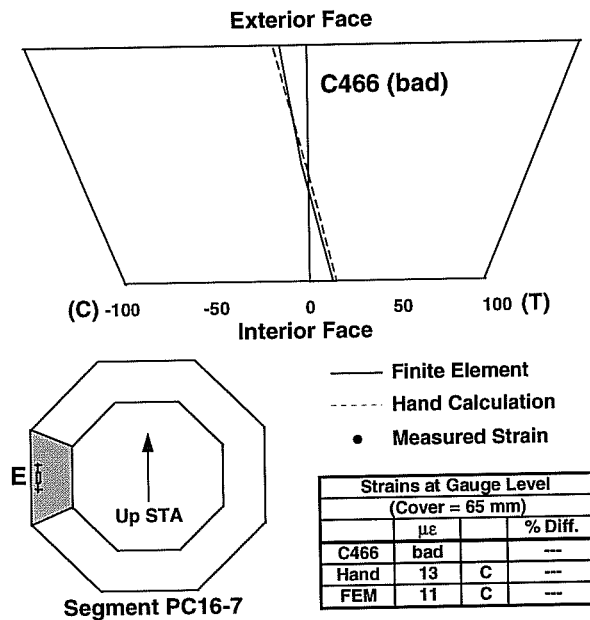


Figure 8.36: Transverse strain comparison in the east wall of segment PC16-7.

### 8.2.2 Negative Gradient

Transverse strains caused by the negative gradient temperature change during the early morning hours of June 4, 1996 were calculated using both hand calculations and the finite element analysis. The cooler temperatures in the exterior fibers of the pier's cross-section in theory produce tensile strains at those locations. Compressive strains occur near the interior faces of each wall of the pier. As with the transverse strains calculated for the positive gradients, the results from the hand calculations and the finite element model exhibited very close correlation.

With the exception of gauge C416 discussed earlier in this chapter, the measured strains in segment PC16-1 closely matched those predicted by theory. Figures 8.37 through 8.40 show the comparisons between calculated and measured strains for the four instrumented walls of segment PC16-1. Calculated strains varied from field measurements by 2% to 19%. Strains were calculated from temperatures

recorded at segment PC16-5, which for the negative gradient was not exposed to sunlight. Thus, temperature changes would be approximately the same magnitude in both the bottom segment PC16-1 and segment PC16-5. It should not be surprising, therefore, that the expected strain changes in both segments should be similar in magnitude compared to those which might occur during positive gradient temperature changes when only one of the segments is exposed to sunlight.

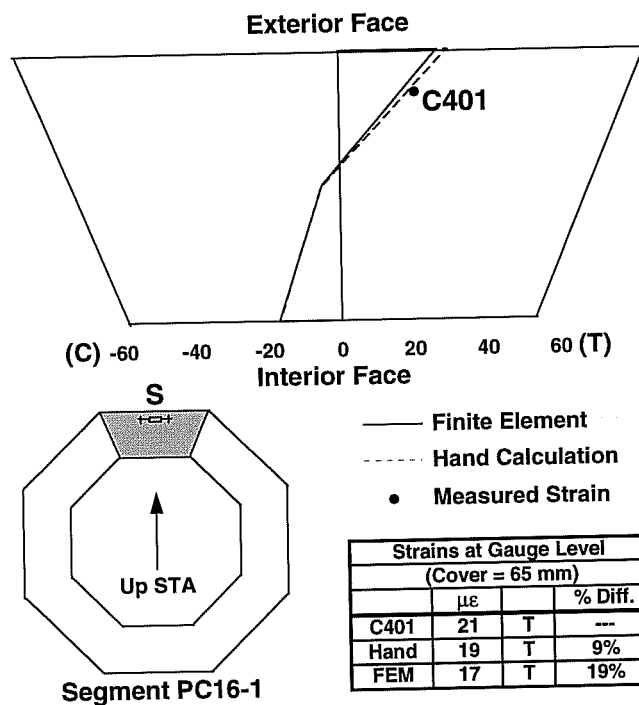


Figure 8.37 Transverse strain comparison in the south wall of segment PC16-1.



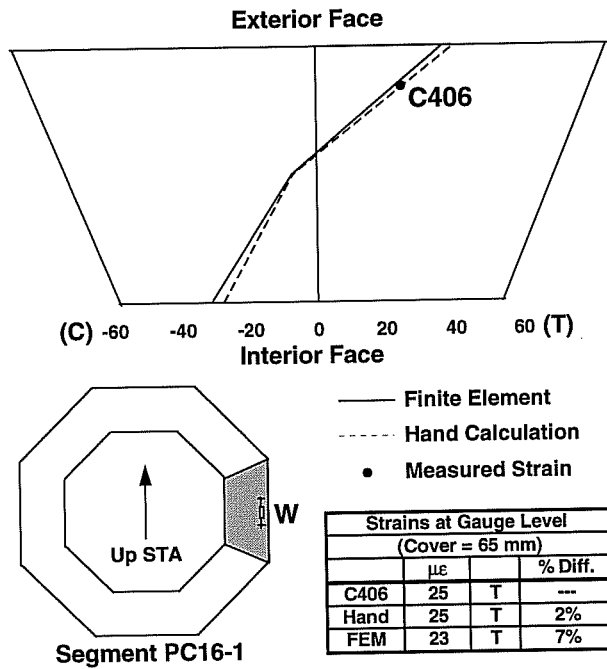


Figure 8.38 Transverse strain comparison in the west wall of segment PC16-1.

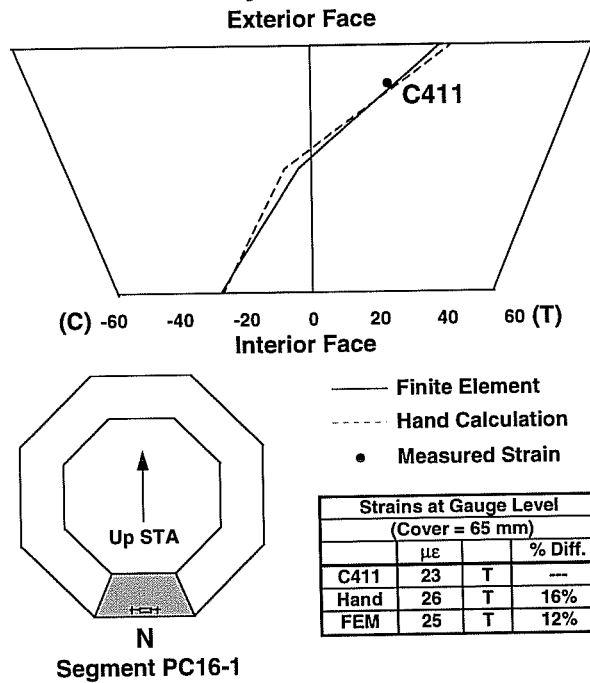


Figure 8.39 Transverse strain comparison in the north wall of segment PC16-1.

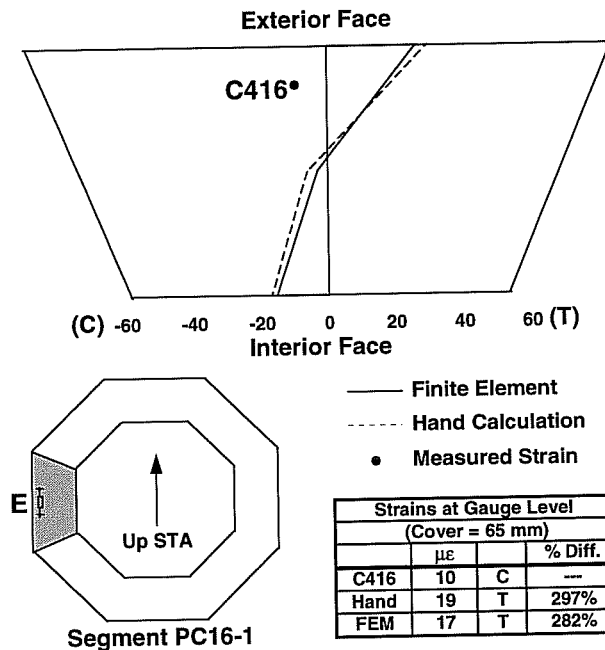


Figure 8.40 Transverse strain comparison in the east wall of segment PC16-1.

Strain changes recorded in segment PC16-5 also agreed very well with calculated strains. Figures 8.41 through 8.44 illustrate the calculated strain distributions and the corresponding measured strains in each of the four instrumented walls of the mid-height segment. The theoretical calculations appeared to predict the actual strains well, with differences ranging from 9% to 24%. As discussed in chapter 5, gauge C437 was unusable due to debonding of the electronic strain gauge from its steel rod.

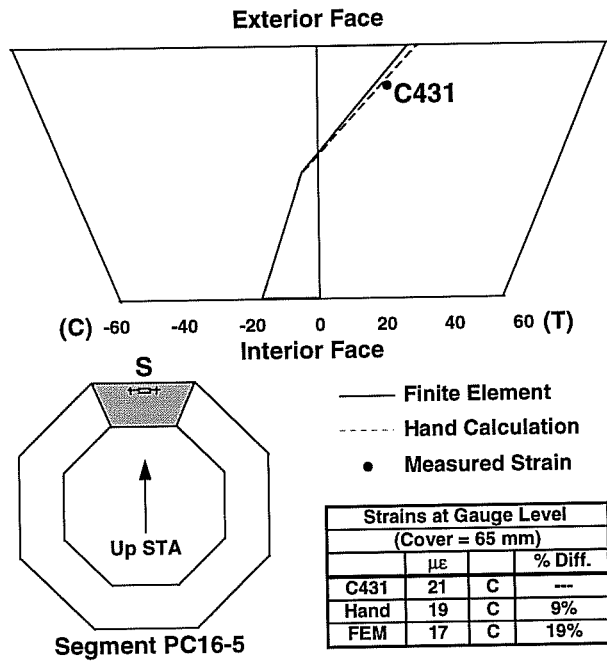


Figure 8.41 Transverse strain comparison in the south wall of segment PC16-5.

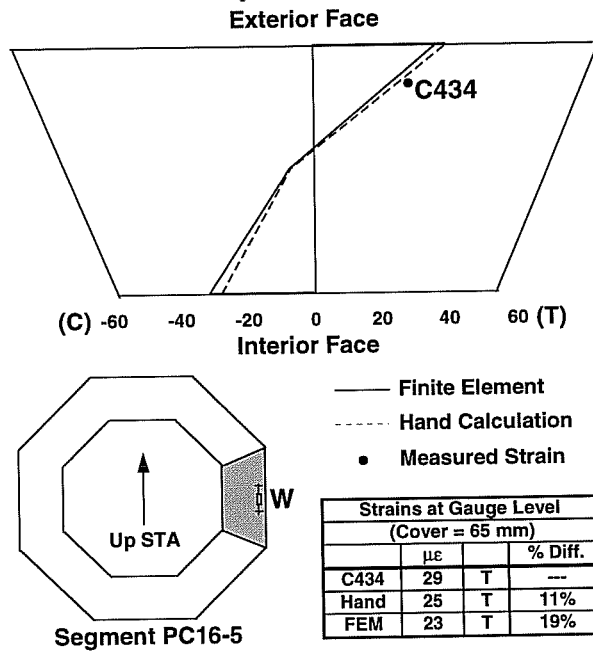


Figure 8.42 Transverse strain comparison in the west wall of segment PC16-5.

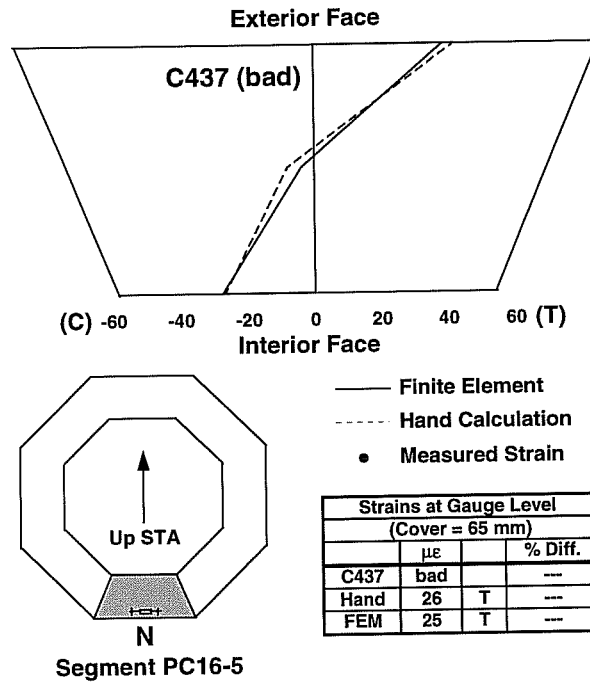


Figure 8.43 Transverse strain comparison in the north wall of segment PC16-5.

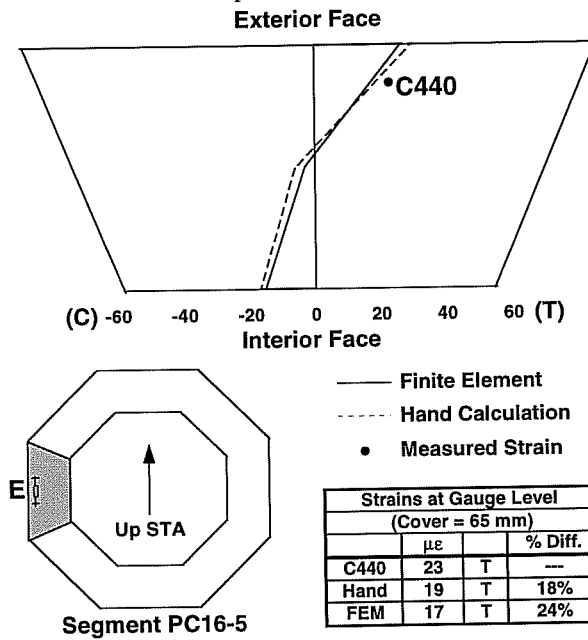


Figure 8.44 Transverse strain comparison in the east wall of segment PC16-5.

The three usable gauges in segment PC16-7 again recorded strains substantially larger in magnitude than those predicted. Predicted strains were calculated on the assumption that no external restraint of the pier's cross-section was present, but the measured strains indicate the possibility that the capital may act to restrain the column cross-section in the area just beneath the capital's bottom face. Such transverse restraint could cause an increase in the measured strains in this location. Figures 8.45 through 8.48 show the comparisons between calculated and measured strains in segment PC16-7.

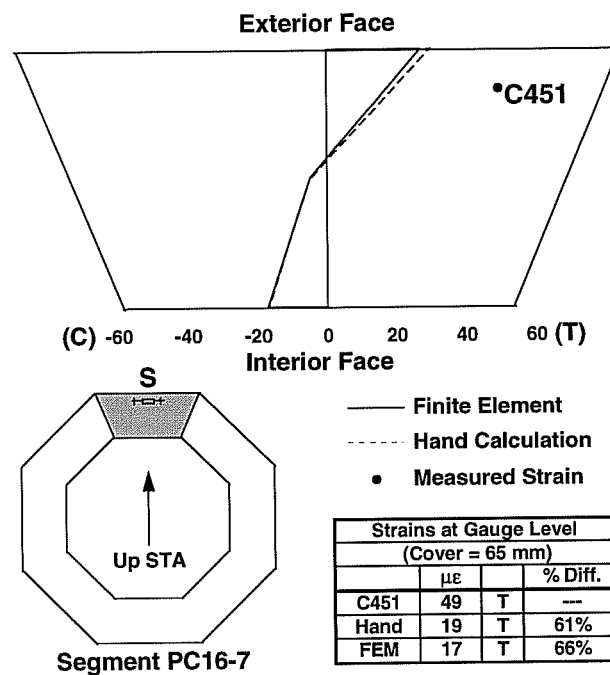


Figure 8.45 Transverse strain comparison in the south wall of segment PC16-7.

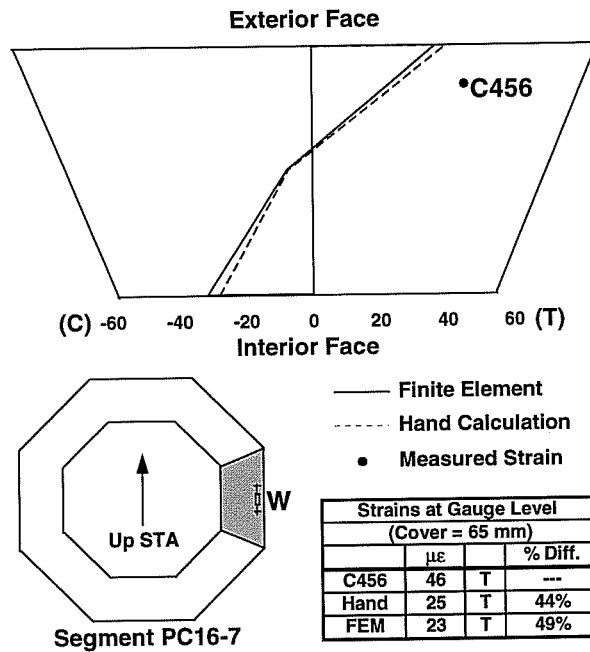


Figure 8.46 Transverse strain comparison in the west wall of segment PC16-7.

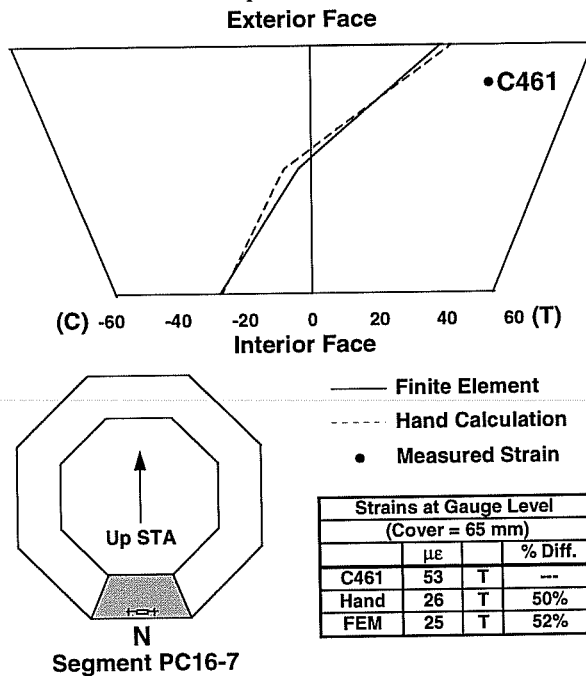


Figure 8.47 Transverse strain comparison in the north wall of segment PC16-7.

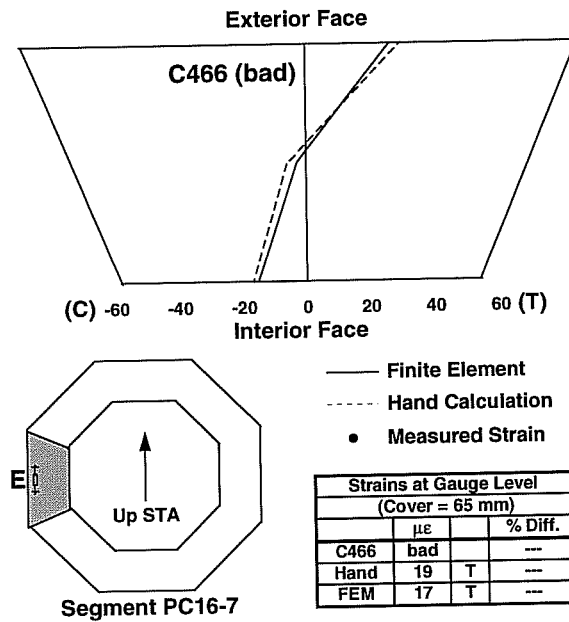


Figure 8.48 Transverse strain comparison in the east wall of segment PC16-7.

### 8.2.3 Comments on Transverse Strains

In general, calculated transverse strains due to the positive temperature gradient seemed to match the actual measured strains. For usable gauges located in segments PC16-1 and PC16-5, measured and calculated strains agreed to within approximately 25% on average. Negative gradient strain changes in these segments were even closer, with differences averaging less than 15%. These relatively minor differences indicate that the theoretical underpinnings of the transverse strain calculations are valid and applicable to the determination of effects due to temperature loading on transverse strains in hollow piers.

Like the longitudinal strains discussed earlier in this chapter, the transverse strains measured in segment PC16-7 were much larger than the calculated values. Restraint from the capital segment may affect the strain levels present at that location.

Transverse strain calculations performed for this project did not account for the possibility of transverse restraint at that location.

### 8.3 GENERAL COMMENTS

General trends are apparent from the comparisons of measured to calculated strains in pier P16. Calculations of longitudinal strains varied from measured longitudinal strains to a greater extent than strains compared in the transverse direction. The variation among analytical methods for determining longitudinal strain was also greater than the relative differences in the methods used for the calculation of transverse strains. This may reflect the difficulty of applying current methods of longitudinal strain calculations to the special case of bridge piers because the orientation of the pier with respect to solar radiation creates a much different temperature distribution than that present in bridge superstructures. Transverse strain calculations take into account the temperature distributions through each wall of the pier, as well as the geometry of the cross-section itself. This probably provides a more accurate estimation of the strains induced by the temperature distribution.

Strain comparisons agreed more closely for the negative gradient temperature change than for the positive gradient case. This may reflect a fundamental difference between the application of temperature loads to bridge piers and superstructures. The complex distribution of temperatures through the pier's cross-section changes during the course of the maximum positive gradient loading. As discussed in Chapter 5, certain faces of the pier experience heating *and* cooling over the time period corresponding to the maximum positive gradient temperature change (see Figure 5.2). The calculations used for this project assume that changes in strain between two times are path-independent. However, the change in actual strains in the pier from one time to another is not the same as the strain change calculated from the difference in temperatures between those same times.



If the entire pier cross-section experienced heating (albeit at different rates) between the times chosen for determination of the temperature gradient, the assumption of path-independent strains might be valid. However, because some areas of the pier undergo heating *and then cooling* during the chosen times (see Figure 5.2), a step-wise approach to the calculation of the strain differences may be necessary to more accurately estimate strain changes between the two times.

The comparison of measured to calculated strains for the negative gradient load case seems to confirm this hypothesis. During the period between the two times selected (10:25 PM and 5:25 AM) no significant rise in temperature occurs at any point in the cross-section. This is in contrast to a few locations which drop several degrees during the course of the positive gradient temperature changes. Because all of the fibers of the pier's cross-section cool during the period between the negative gradient times, less interaction between fibers occurs. Fibers are heated and, to a small extent, cooled during the course of the positive gradient temperature change, thus affecting the strain distribution in the pier as time progresses. The differences in characteristics of temperature change between the positive and negative gradient load cases may, in part, explain the more accurate calculated strains in the negative gradient case. Although the effects seem to be minor, step-wise calculations might better serve to accurately determine the effects of temperature changes over time on strains in the pier.

Strains measured in the top segment PC16-7 present a special problem. The large differences between measured and calculated strains in both the longitudinal and transverse directions suggest that the assumptions used during calculations for this project are not valid for all locations in the pier. It is unclear whether strains are influenced by the substantial restraint provided by the solid capital's interface with the top segment, the flow of post-tensioning forces from the capital to the top segment, or a combination of the two effects.

Small variations in measured strains may be accounted for by slight differences in the material properties present in the pier and those assumed during calculations.

Slight differences in pier geometry, particularly the presence of ducts, grout tubes, and electrical conduits could also affect the local strain fields near some of the strain gauges. However, every effort was made during instrumentation to avoid local discontinuities to minimize problems in gauge readings.

Overall, it appears that measured strain changes confirm the validity of calculation methods used to estimate self-equilibrating strains induced in the precast, hollow, segmentally-constructed pier by non-linear temperature distributions. The accuracy of the finite element analysis was best overall. A better understanding of the behavior in certain areas of the post-tensioned pier is needed, as well as a more accurate method for determining longitudinal strain changes caused by changes in temperature over time.

## CHAPTER 9

### *DESIGN IMPLICATIONS*

#### 9.1 *SAMPLE LOAD CASES*

##### **9.1.1 Construction Loads**

Construction loads produce some of the largest and most important effects on segmentally constructed bridges. Balanced-cantilever construction in particular has the potential to induce large tensile stresses on the associated substructure. To gauge the significance of the effects of non-linear temperature gradients on segmentally constructed piers, an estimate was made of the maximum effects of differential temperature on pier P16 during balanced-cantilever construction of the ramp superstructure.

Section 8.4.2 of the *AASHTO Guide Specification* [12] includes several load cases and allowable stresses related to special construction situations common in segmental bridges. Two of the load cases outlined in the Guide Specification Table 8-1 deal with stresses due to the placement of an unbalanced superstructure segment during balanced-cantilever erection. For illustration purposes, load case “b” is discussed here. This load case consists of the following (all load factors = 1.0):

$$DL + U + CLL + CE + IE + (R + S + T) \quad (9.1)$$

where: DL = Dead load of structure

U = Segment unbalance

CLL = Construction live load

CE = Construction equipment

IE = Impact load from equipment

R, S = Creep and Shrinkage

T = Temperature effects: thermal rise and fall (TRF) and differential temperatures (DT)

Allowable compressive stress =  $0.50 f_c$

Allowable tensile stress =  $7 \sqrt{f'_c}$  (where  $f'_c$  is in lb/in<sup>2</sup>)

The high amount of allowable tensile stress in the concrete, roughly equivalent to the modulus of rupture of concrete test prisms, reflects the extremely unlikely simultaneous occurrence of all of the factors present in the load case. It also recognizes the unusual construction procedures that the load case considers.

The largest moments produced in pier P16 due to an unbalanced segment occur during placement of the next-to-last segment in cantilever (see Chapter 4 for a discussion of the balanced-cantilever construction sequence). At this point, six ramp segments cantilever from the top of pier P16 in opposite directions. The seventh segment added to one cantilever produces the maximum unbalanced moment (see Figure 9.1). The application of a typical 285.5 kN ramp segment at a moment arm of 20.1 meters produces a bending moment of approximately 5740 kN-m at the base of the pier. Prestressing forces in the pier, construction live loads, and superstructure and pier dead loads were also included in the calculation of stresses for this load case (see the appendix).

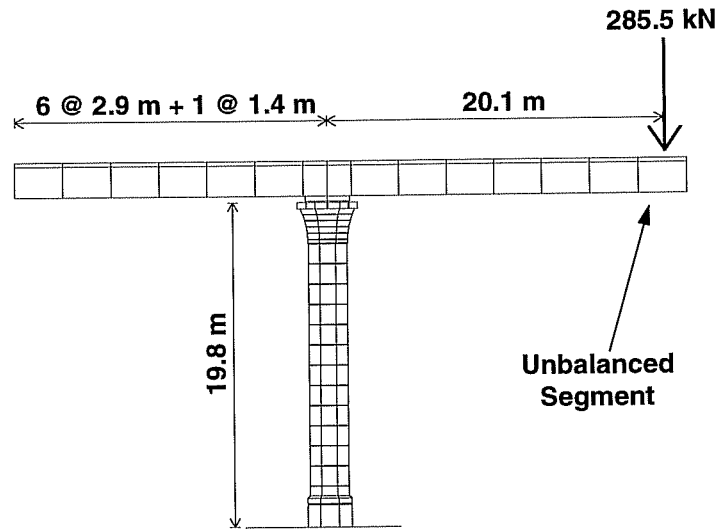


*Figure 9.1: Unbalanced segment construction load case.*

Figure 9.2 shows the magnitudes and distributions across the pier base segment of several of the load components calculated. The compressive stress of 5.24 MPa provided by the pier's post-tensioning counters most of the 5.84 MPa of tensile stress at the outer fibers of the pier produced by the unbalanced ramp segment. With the additional compressive stress provided by the superstructure and pier's own weight, the section in question located at the base of the pier remains completely in compression if temperature stresses are neglected.

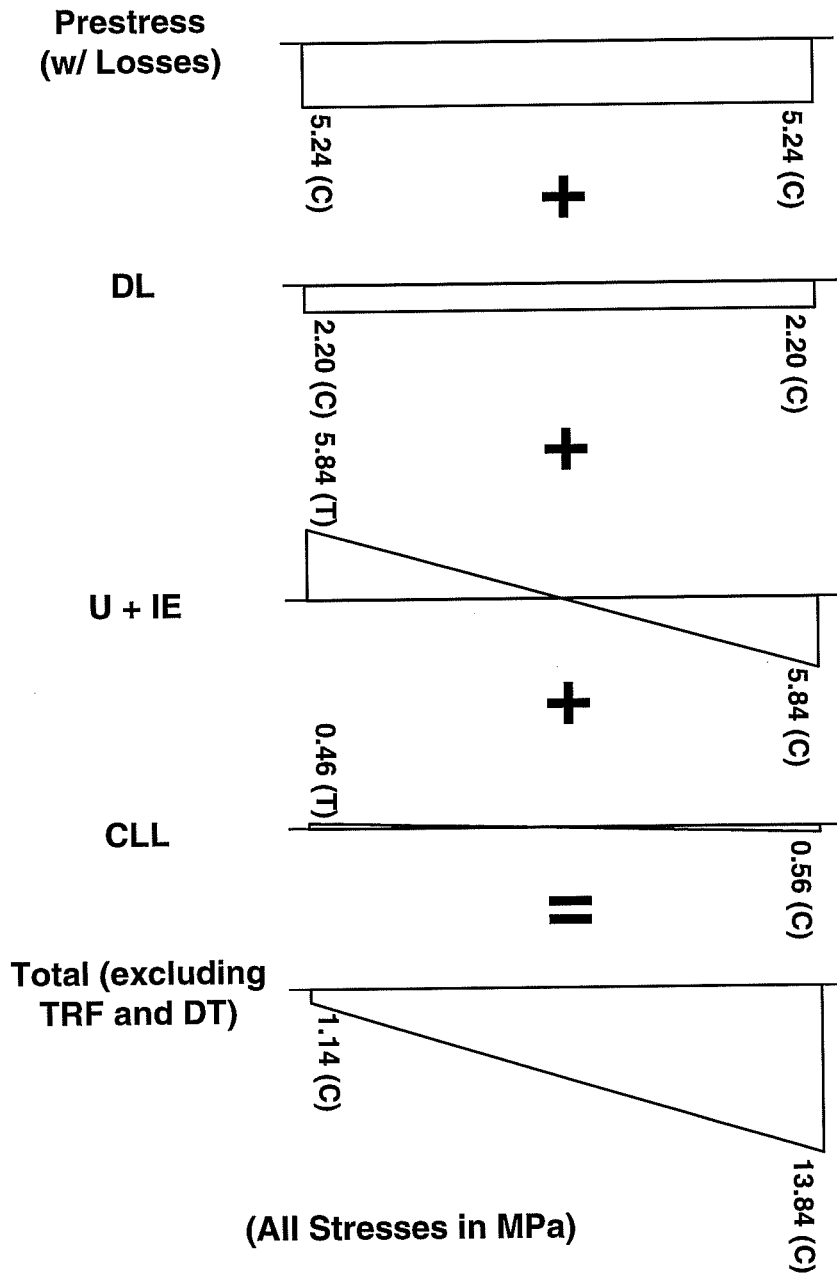


Figure 9.2: Stress components for load case excluding temperature effects.

Self-equilibrating stresses induced by the maximum measured positive temperature gradient for April 1996 are displayed with the other combined load effects in Figure 9.3. It should be noted that no restraint moments are induced in the pier at this point in the construction sequence because the structure is statically determinate. After closures are cast in the superstructure and continuity tendons have been stressed, the structure becomes indeterminate and some restraint moments due to differential temperature effects will be produced. See Chapter 2 for a discussion of moments induced by external restraint in a statically indeterminate structure.

Temperature induced self-equilibrating stresses calculated using the finite element analysis described in Chapter 7 are used for the effects of the maximum positive gradient. For comparison, the calculated stresses induced by the NCHRP Report 276 [5] positive design gradient as found using the finite element analysis are shown in Figure 9.4. To produce the maximum effect on the pier, the temperature gradients were applied to coincide with the bending moments due to the unbalanced segment.

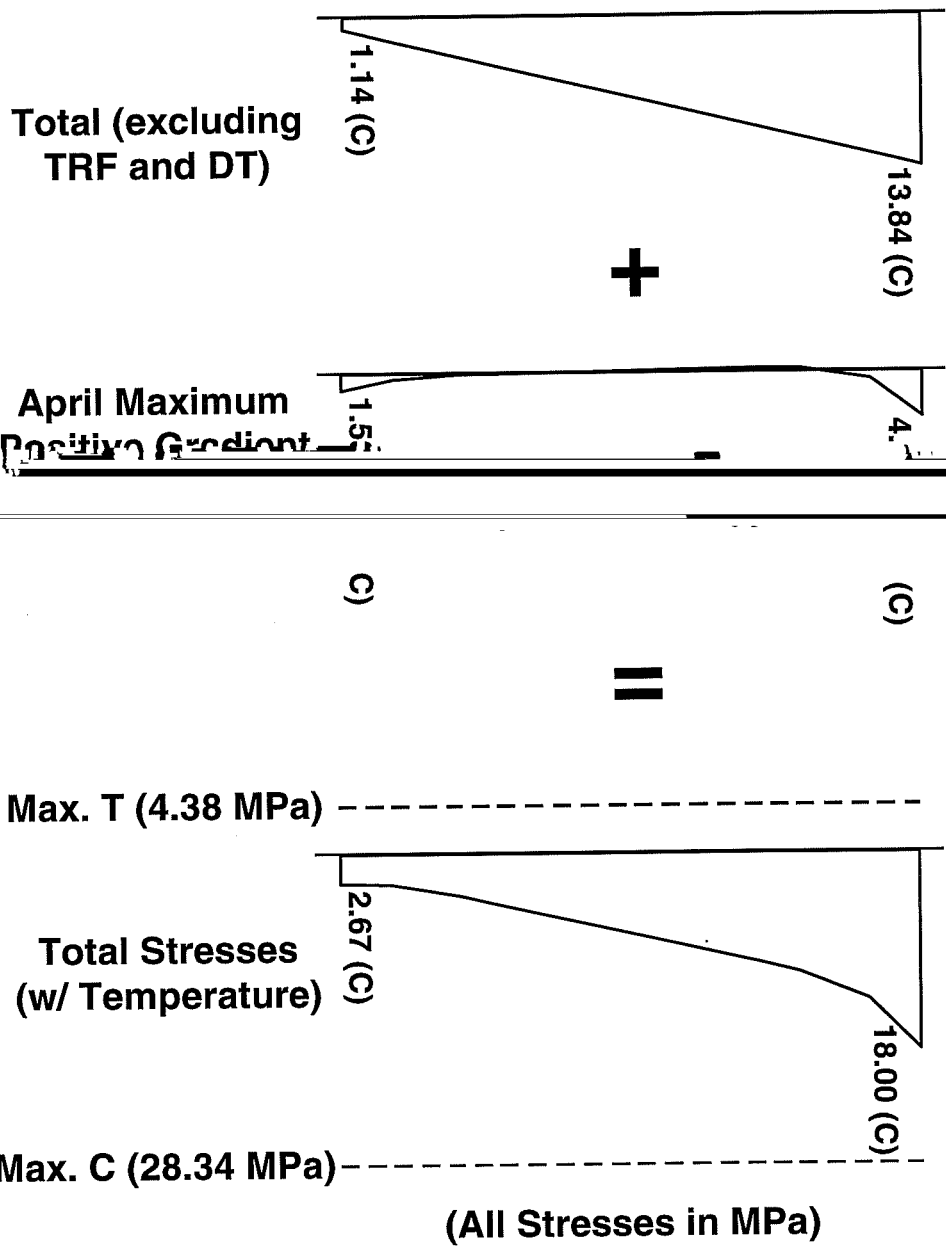


Figure 9.3: Additional sectional stresses due to the application of the April maximum measured positive temperature gradient.



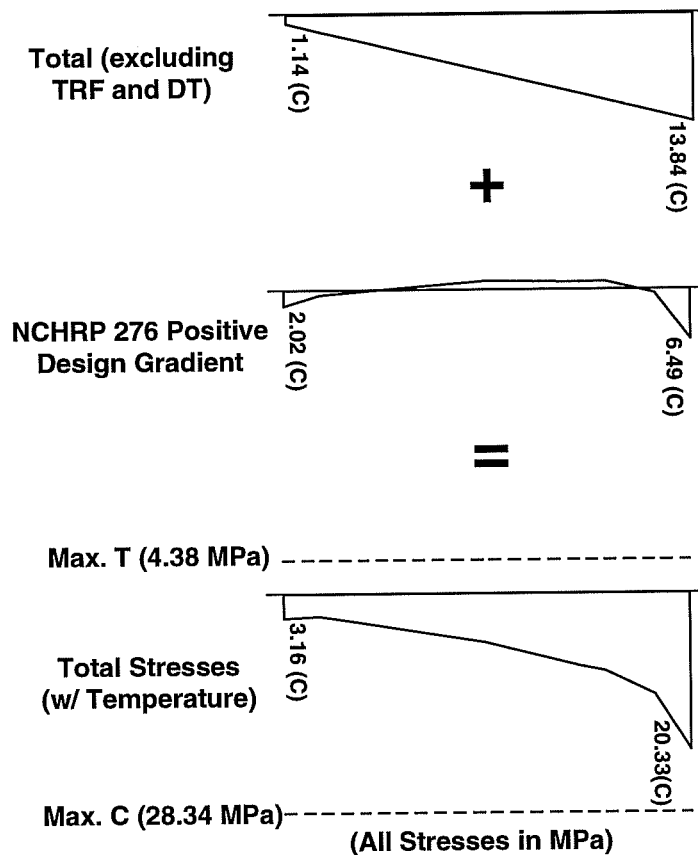


Figure 9.4: Additional sectional stresses due to the application of the NCHRP 276 positive design gradient.

As shown in Figure 9.3, the April positive gradient stresses increase the total compressive stresses due to non-thermal causes at the outer fibers of the pier by 230% and 130%, respectively. However, those compressive stresses are still well below the maximum allowable compressive stress of 28.34 MPa. No tension is developed in the pier's section due to this load case. The NCHRP positive design gradient shown in Figure 9.4 increases the total outer fiber compressive stresses to 280% and 150% of the non-thermal stresses, respectively. Clearly, the design gradient overestimates the

induced stresses in the pier. However, even for this case, the compressive stress levels are still well within the allowable limits.

Figure 9.5 illustrates the stresses induced by the maximum measured negative gradient for April, as determined using the finite element analysis. In this case, the negative gradient causes tensile stresses to develop at the outer fibers of one face of the pier. The compressive stresses at the opposite face are reduced to 87% of their previous level. The tensile stress of 1.13 MPa induced at the face of the pier is well below the design limit of 4.38 MPa for this construction load case. The maximum compressive stress for this case is also not critical.

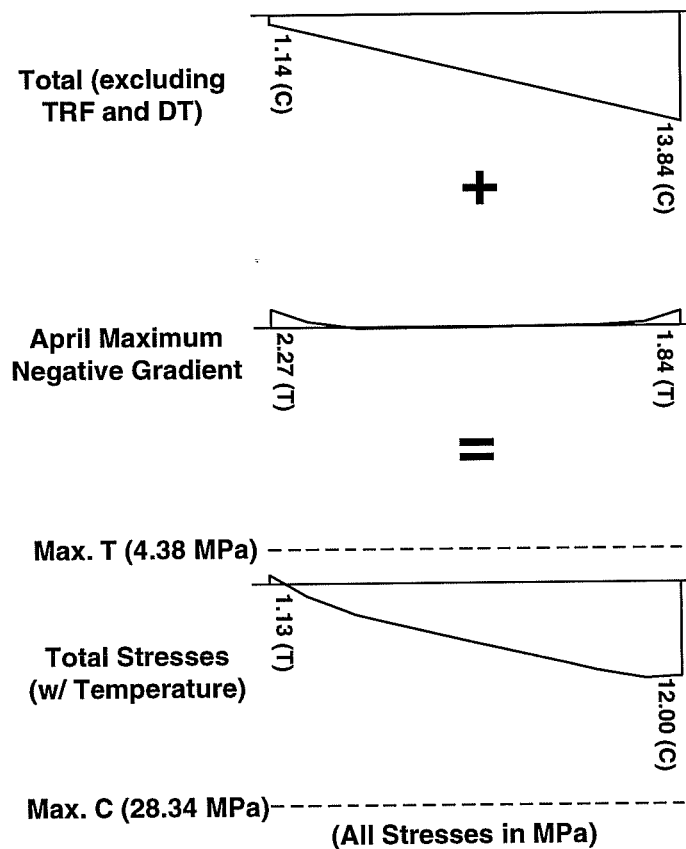


Figure 9.5: Additional sectional stresses due to the application of the April maximum measured negative temperature gradient.

The application of the NCHRP negative design gradient causes much greater tensile stresses at the outer face, reaching 64% of the maximum allowable tension (see Figure 9.6). The maximum compressive stresses in this case are reduced to 43% of the allowable level. The use of the negative design gradient in this case could potentially cause problems for designers attempting to meet the maximum tensile stress requirements during construction. This need not be the case, as it has been shown that the design gradients specified by NCHRP Report 276 [5] greatly overestimate the actual gradients measured in pier P16.

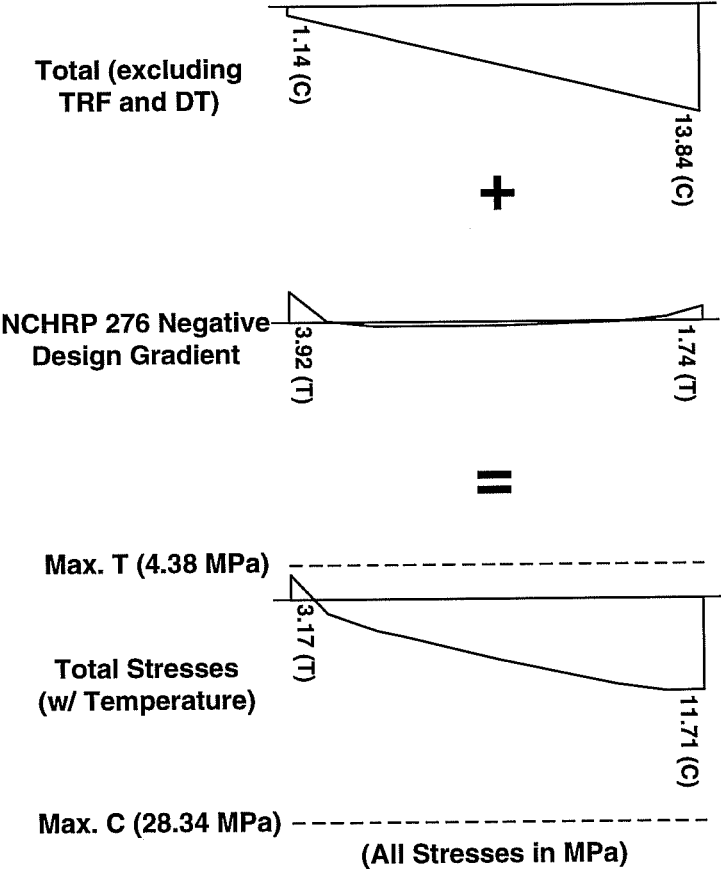


Figure 9.6: Additional sectional stresses due to the application of the NCHRP 276 negative design gradient.

### 9.1.2 Service Load Cases

The *AASHTO Guide Specifications* [12] also require the application of differential thermal stresses to several service limit state load cases. For load cases including live loads, the effects of differential temperature stresses may be reduced by 50%. The following service load cases include temperature effects:

$$\text{IV: } D + (L+I)_n + CF + \beta_E E + B + SF + R + S + (T + 0.5DT) \quad (9.2)$$

$$\text{V: } D + E + B + SF + R + S + (T + DT) \quad (9.3)$$

$$\text{VI: } D + (L+I)_n + CF + \beta_E E + B + SF + 0.3W + WL + LF + R + S + (T+0.5DT) \quad (9.4)$$

$$\text{Additional Thermal: } D + \beta_E E + B + SF + R + S + DT \quad (9.5)$$

where:  $D = DL + SDL + EL$

DL = structure dead load

S = shrinkage

SDL = superimposed dead load

DT = differential thermal

EL = erection loads

W = wind

$\beta_E E$  = earth pressure

LF = longitudinal live load forces

SF = stream flow

WL = wind load on live loads

R = creep

B = buoyancy

L = live loads

I = impact factor

CF = centrifugal force

SF = stream flow

T = temperature rise and fall

The maximum allowable compressive stress after all prestress losses is  $0.4 f'_c$ . For segmental members with epoxied joints (designated Type A) such as those in pier P16, no tensile stresses are allowed to occur at the service limit state. The design specifications allow a 25% increase in maximum allowable stresses for load case IV, and a 40% increase for cases V and VI. The additional thermal case from the *AASHTO Guide Specifications* [12] does not include an increase in allowable stresses. Unfortunately, the percentage increases allowed by the code do not relieve the requirement of zero tension for segmental members.

To gauge the importance of temperature effects in bridge piers, service loads are estimated for pier P16 after all estimated prestress losses have occurred. Structure dead loads were calculated through several phases of the balanced-cantilever construction (see Figure 9.7). This is necessary because the configuration of the structure that includes pier P16 at different times during construction affects the dead loads applied to the pier.

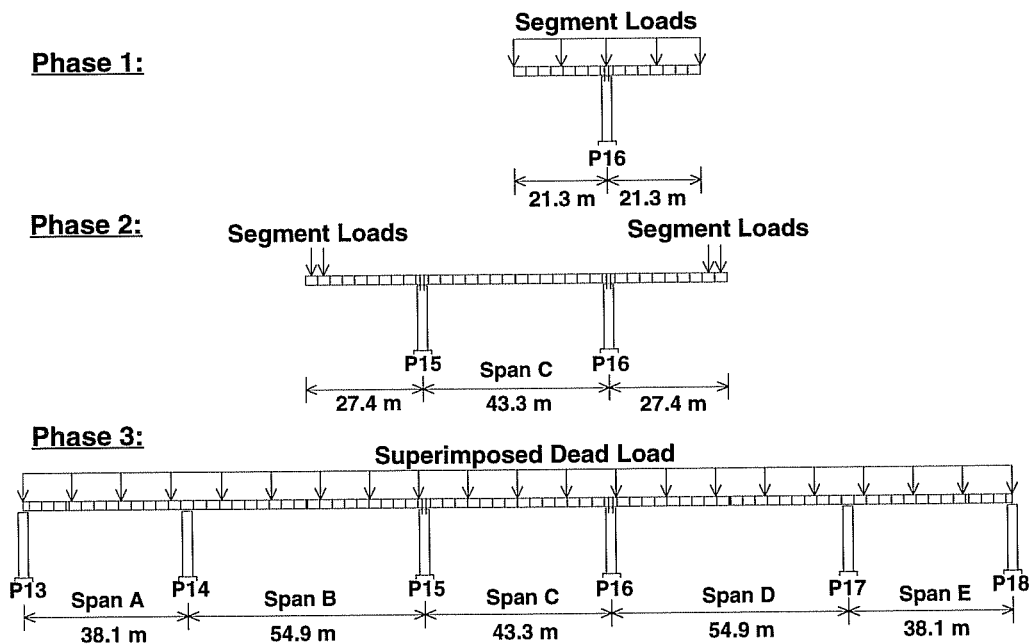


Figure 9.7: Dead loads at several phases during construction.

Prestressing effects in the superstructure and pier P16 were estimated and included in the total stress distributions calculated for the service load cases. Superimposed dead loads such as roadway overlays and barrier walls were determined, and the maximum effects due to AASHTO HS20-44 live loads were calculated (see the appendix for service load calculations). Figure 9.8 shows the estimated stress distributions across the segment at the base of pier P16 due to dead loads and prestressing as well as maximum live load effects. Note that the contribution from live loads is quite small compared to dead loads and prestressing. This is due in part to the use of balanced-cantilever construction and the large dead loads from the bridge superstructure. The maximum compressive stress on the pier's base is less than 40% of the allowable compressive stress.

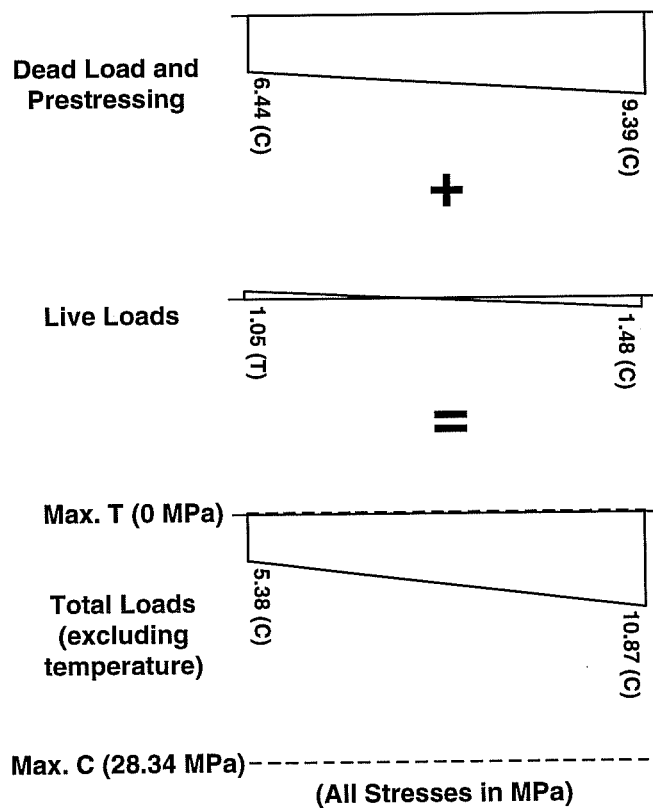


Figure 9.8: Relative contributions of dead and live loads to stress at the base of pier P16 for the service limit state.

To determine the contribution of thermal gradient stresses to the stress distribution in pier P16 at service loads, restraint moments and self-equilibrating stresses found using the classical method described in Chapter 6 were applied to the service load cases above (see the appendix for example calculations). The maximum measured positive and negative gradients (from April, 1996) as well as the NCHRP Report 276 [5] positive and negative design gradients were applied to two service load cases. Load case IV allows a 50% reduction in effects from temperature because it includes live and impact loads. The additional thermal case does not allow an increase in maximum stresses, but does not include live load effects.

Contributions from differential thermal gradients consisted of both self-equilibrating stresses and restraint moment stresses induced by the indeterminate nature of the five-span ramp unit to which pier P16 belongs (see Chapter 4). The magnitudes of self-equilibrating stresses used in these cases are slightly less than those used for the construction load cases in the previous section. As discussed in Chapter 8, the classical method of self-equilibrating stress calculation produced slightly lower values of longitudinal stress than the finite element analysis.

Figure 9.9 shows the maximum measured positive gradient stresses applied to the service load case IV. The maximum compressive stresses due to thermal effects for this case are about 14% of the total compressive stress. Even with the addition of the compressive stresses induced by the thermal gradients on the pier, the maximum compressive stress is only 45% of the largest allowable stress. No tension develops due to the temperature gradient.

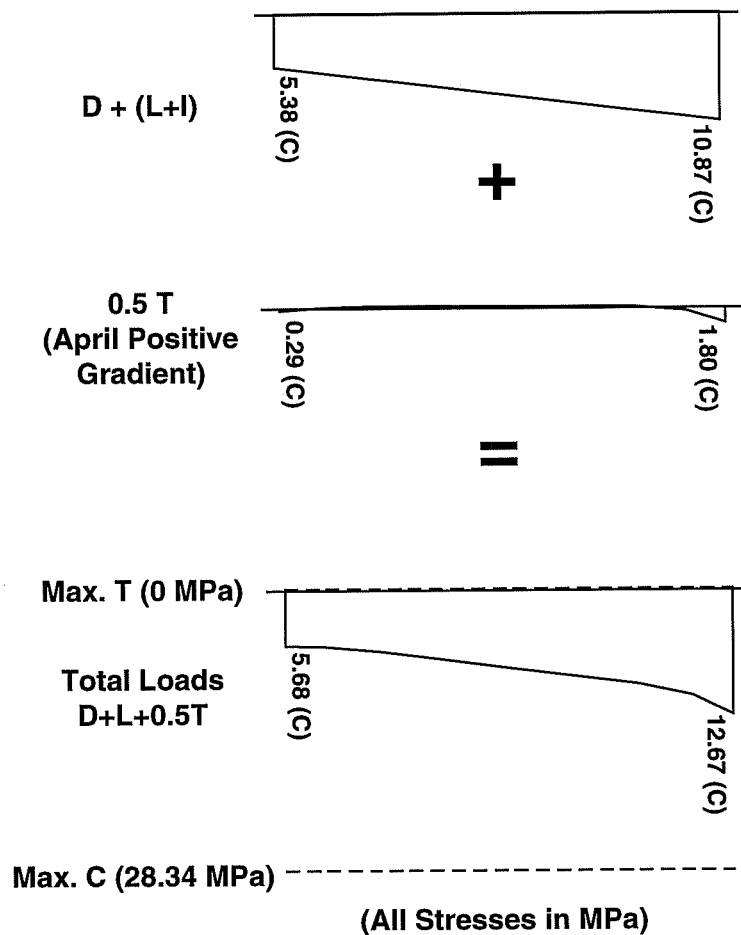


Figure 9.9: Service load case IV with maximum measured positive gradient effects.

The NCHRP positive design gradient also has little effect on the pier in service load case IV (see Figure 9.10). However, the design gradient stresses overestimate the stresses calculated from the measured gradient by 210%. Thermal compressive stresses in this case contribute only 26% of the maximum compressive stress on the pier's section. The majority of the thermal stresses occur near the outer fibers. Even with the larger thermal gradient, compressive stresses reach only 52% of the maximum allowable stress.



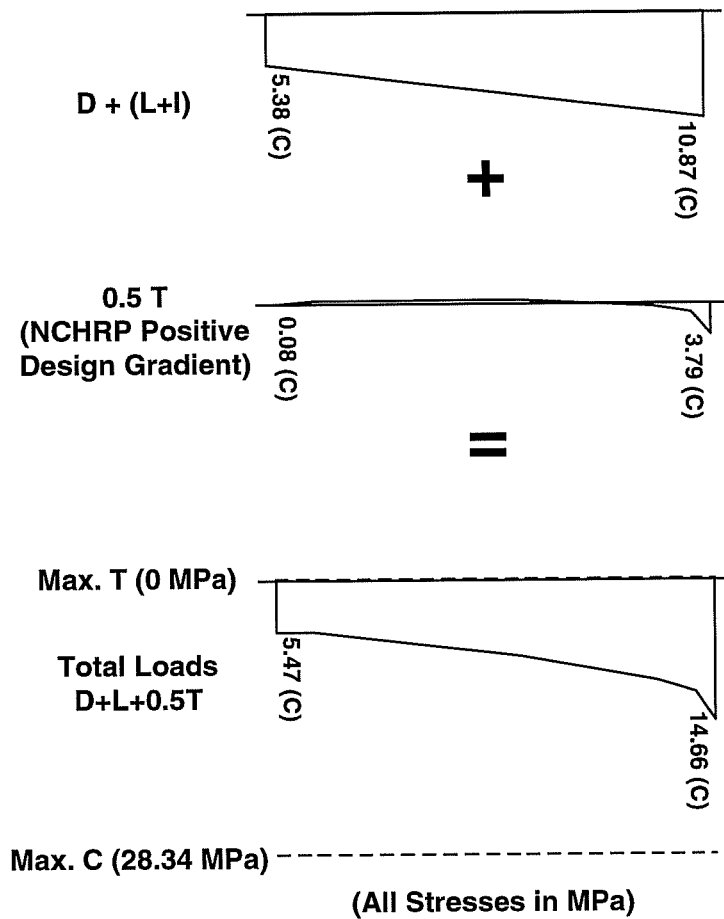


Figure 9.10: Service load case IV with NCHRP positive design gradient effects.

The positive thermal gradients have a somewhat greater effect on the cross-sectional stresses in the additional thermal load case. Figure 9.11 shows the increase in compressive stress due to the maximum measured positive temperature gradient. The contribution of thermal stresses to the total compressive stresses in the pier is less than 28% at the point of maximum compression. Figure 9.12 shows the contributions due to the positive design gradient on compressive stresses from the additional thermal case. Because of the steep change in temperature at the outer fiber specified by the design gradient, a relatively large amount of compressive stress occurs at that location. That

stress is approximately 45% of the maximum compressive stress calculated for this load case, which is in turn about 75% of the allowable compression. Note that the allowable stress for the additional thermal service load case is lower than the value for service load case IV because no increase in maximum stress is provided by the specifications.

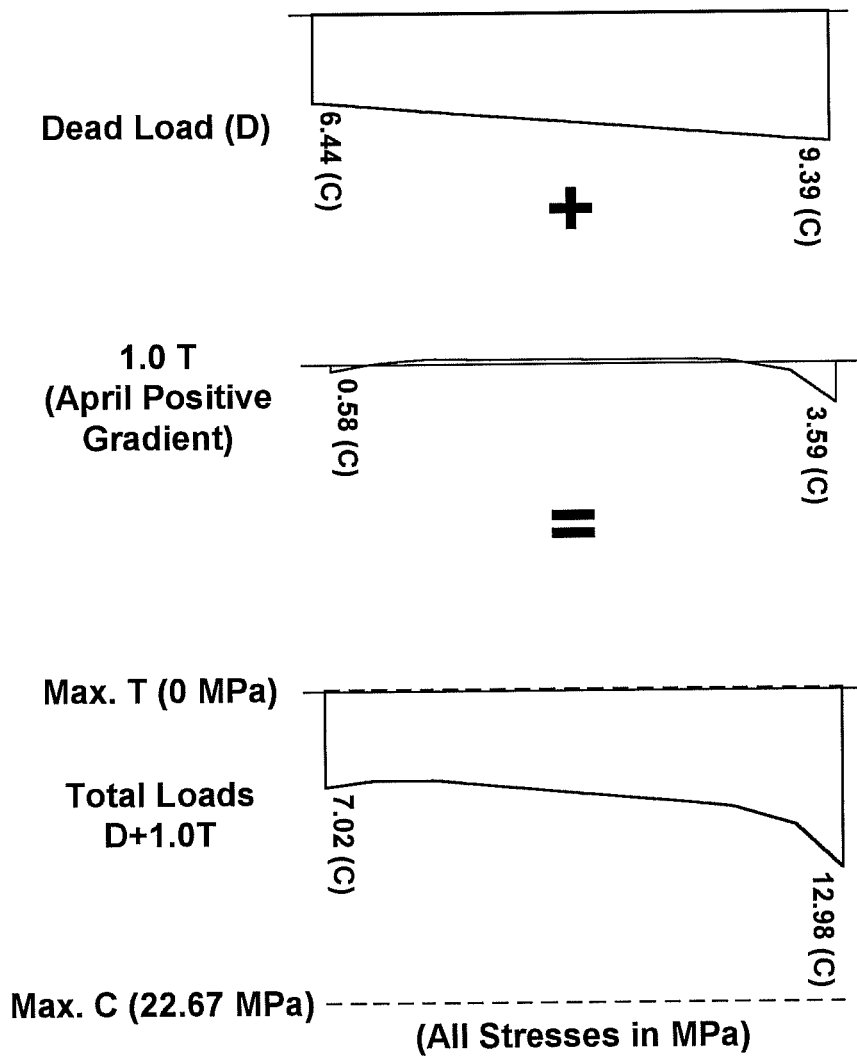


Figure 9.11: Additional thermal case with measured positive gradient effects.

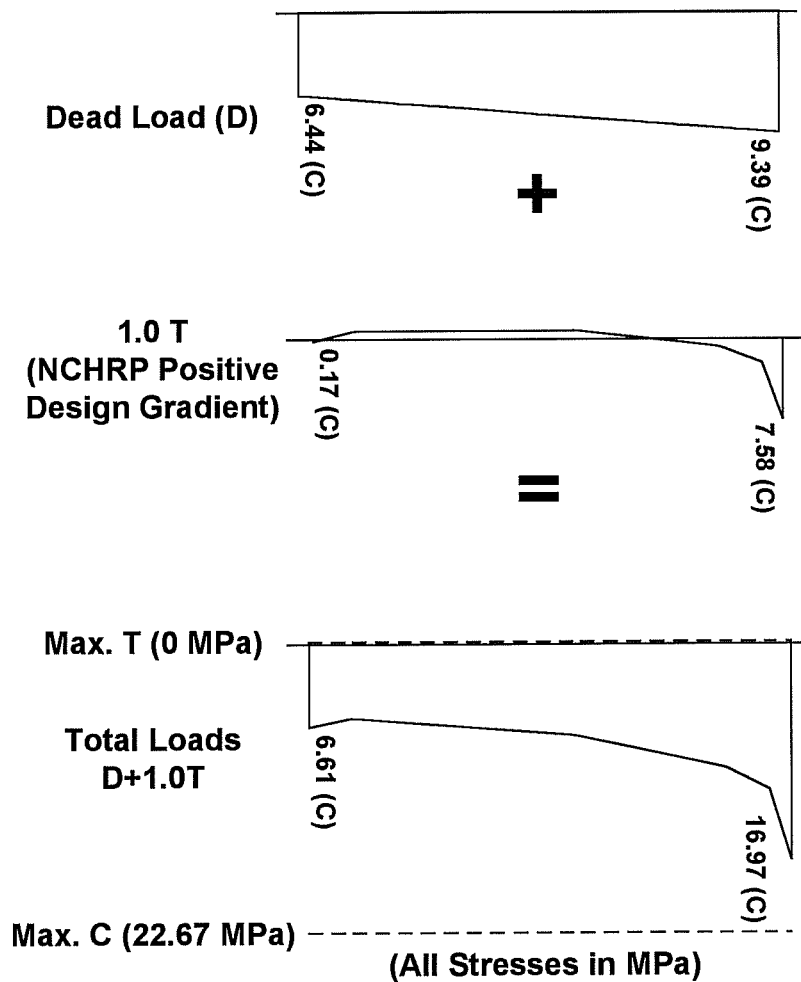


Figure 9.12: Additional thermal case with NCHRP positive design gradient effects.

Unlike the positive gradient effects, stresses due to negative temperature gradients are primarily tensile in nature. However, the large amount of compression on the pier from the dead loads and post-tensioning forces ensures that no tension develops due to thermal gradients. Figure 9.13 shows the small decrease in compressive stresses due to the maximum negative gradient effects. The negative gradient stresses cause a 20% reduction in compressive stress where the maximum thermal tensile stresses occur. Similarly, tensile stresses from the more severe NCHRP negative design gradient also

have little effect on the section for this load case (see Figure 9.14). The largest tensile stresses cause a 35% decrease in compression at the outer face. Still, neither gradient causes any tension at any depth of the section due to the large compressive stresses provided by other loads.

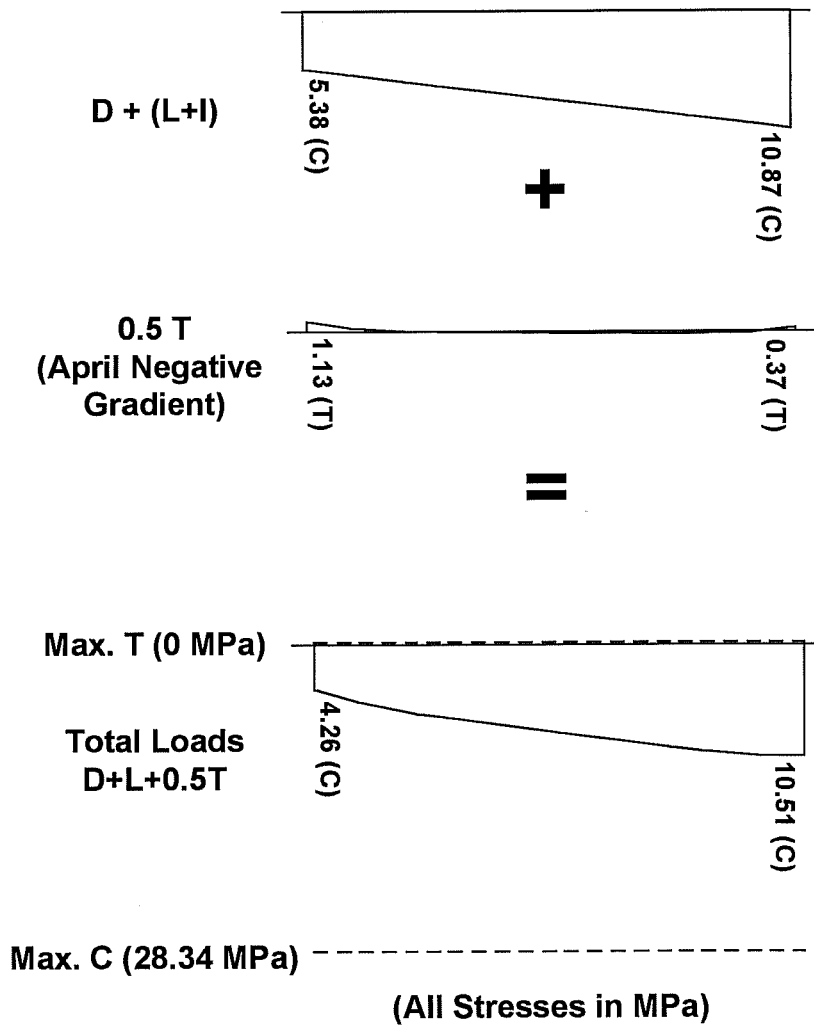


Figure 9.13: Service load case IV with measured negative gradient effects.

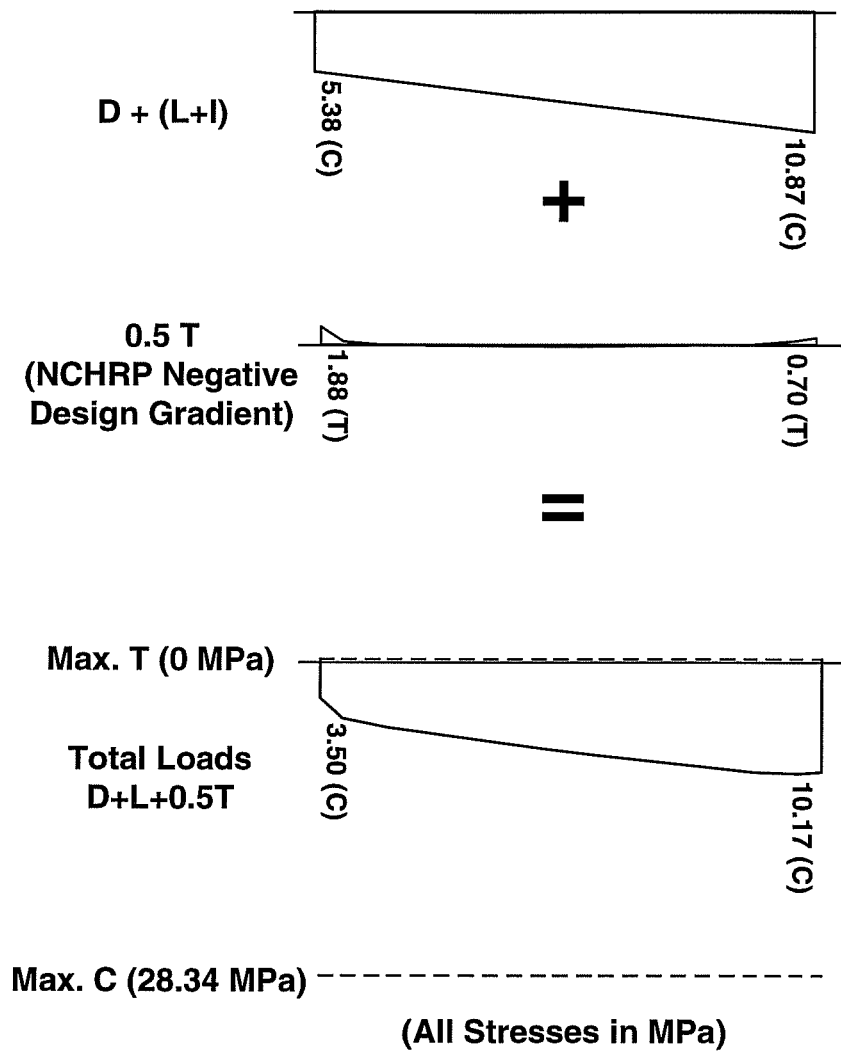


Figure 9.14: Service load case IV with NCHRP negative design gradient effects.

The additional thermal load case specified by the *AASHTO Guide Specification* [12] should produce the greatest effects on the section due to thermal gradients. Even so, neither the maximum measured negative gradient nor the much larger NCHRP negative design gradient induce any tension in the pier's cross-section (see Figures 9.15 and 9.16, respectively). The negative design gradient's maximum tensile stress does

reduce the compressive stresses due to dead loads by almost 60%, but most of the effect is localized within the first several centimeters of the depth, while the rest of the pier is affected very little. This is due to the relatively steep temperature gradient present near the outside fibers in the design temperature gradient's shape.

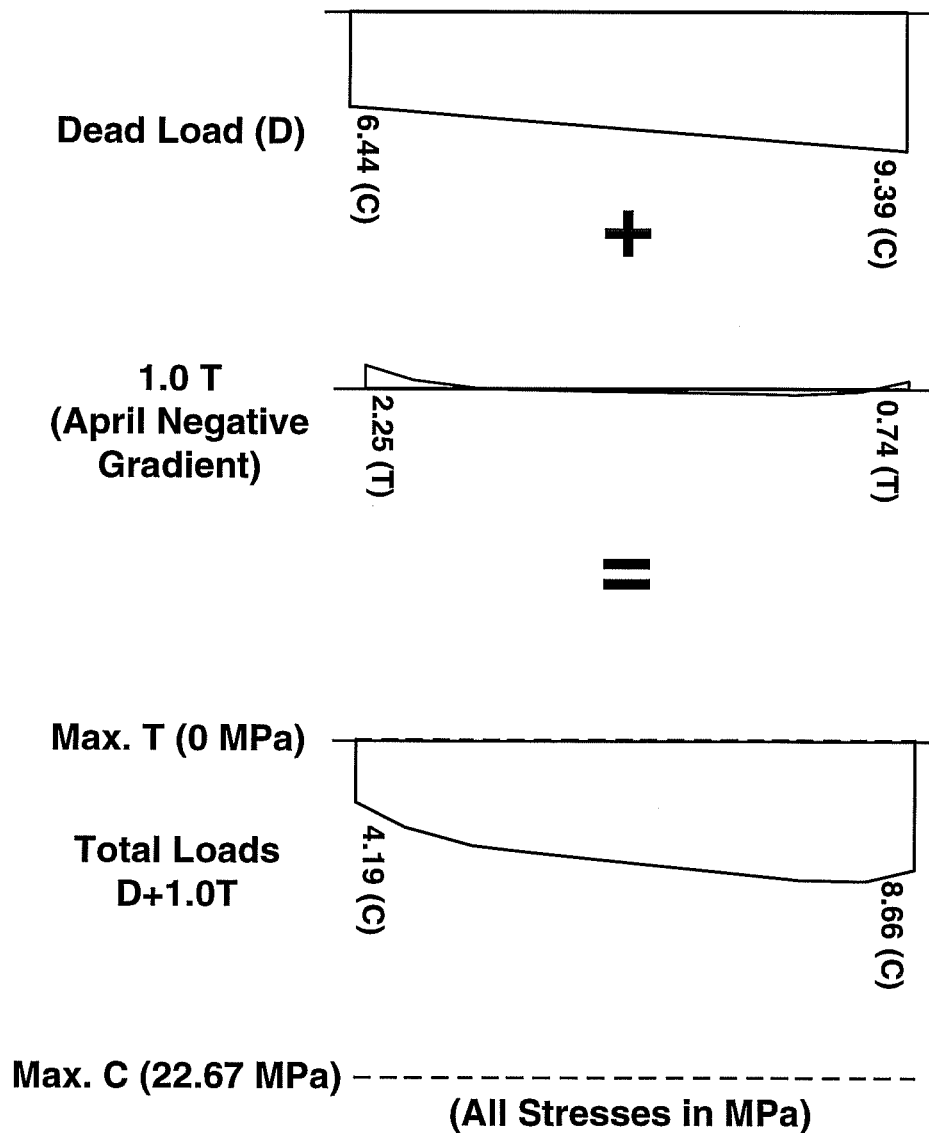


Figure 9.15: Additional thermal case with measured negative gradient effects.

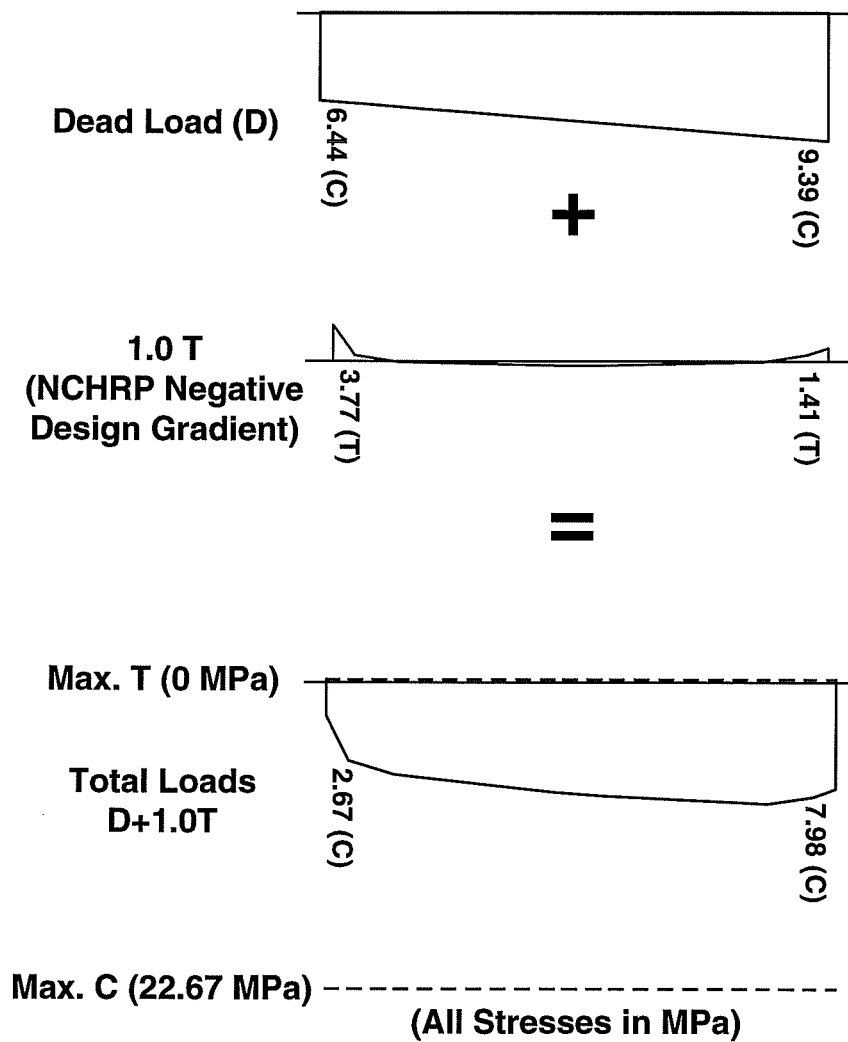


Figure 9.16: Additional thermal case with NCHRP negative design gradient effects.

### 9.1.3 Comments on Load Cases

In general, the measured temperature gradients have no profound effects on the stresses present in the pier during service conditions. The pier's post-tensioning forces appear to be adequate in preventing any tension from occurring at the interfaces between pier segments. The temperature gradients specified for design based on the

NCHRP Report 276 [5] produce larger effects on the pier, but no tensile stresses were calculated from the service load cases examined here. This is especially significant for the additional thermal load case, which has the greatest relative contributions due to thermal gradients and was designed to be the “worst case” service condition for the effects of temperature on a structure.

As can be seen in the appendix, the calculations performed here are only estimates of the service loads that might actually be used for design purposes. Still, it can be seen from these example load cases that the effects on cross-sectional stresses from thermal gradients are quite small in the post-tensioned pier.

On the basis of the magnitudes of stresses, it appears prudent to include the effects due to thermal gradients in the construction load cases. The measured negative gradient induced a significant amount of tensile stress in the pier’s cross-section. Because the negative gradient would likely occur during the night when most heavy urban construction work is in progress, designing for its affects is not unreasonable. The high level of allowable tension specified in Table 8-1 of the *AASHTO Guide Specifications* [12] accounts for the small likelihood of the simultaneous occurrence of the unusual construction loads and large negative thermal gradients. Compressive stresses from a positive temperature gradient in the pier would rarely significantly affect the stress distributions during construction.

## 9.2 *SUGGESTED REVISIONS TO AASHTO GUIDE SPECIFICATION [12]*

### **9.2.1 Thermal Gradients**

As discussed in Chapter 6, temperature distributions through the cross-section of pier P16 were measured using a comprehensive set of thermocouples. Pier temperatures were measured on an hourly basis for approximately four months during the spring and summer of 1996. Based on the temperatures recorded and their distributions in the pier, conclusions can be made regarding the positive and negative



design temperature gradients required for analysis by the *AASHTO Guide Specification* [12].

Measured temperature gradients projected onto a single axis for direct comparison to current superstructure design gradients appear to match the shape of those design gradients fairly well. The peak temperature from the maximum measured positive thermal gradient reached only 51% of the temperature specified for Austin, Texas (solar radiation Zone 2). These measurements also match very closely the shapes and magnitudes of thermal gradients measured by Roberts [7] on a segmental bridge superstructure with no asphalt topping. That fact strongly suggests that a bridge pier's vertical orientation does not necessarily protect it from large thermal gradients.

The shape of the maximum negative temperature gradient measured over the same time period also appeared to match the design gradient shape very closely. However, magnitude of the maximum measured temperature for this case was only 53% of the specified design value. Roberts [7] found measured negative gradient magnitudes to be around 80% of those specified for use in design.

In general, the temperature distributions measured in the segmental pier appear to be applicable for use in determining appropriate shapes and magnitudes for thermal gradients in bridge piers *and* superstructures. Roberts [7] suggested the following revisions to section 7.4.4 of the *AASHTO Guide Specifications* [12] (changes in italics):

#### **7.4.4 Differential Temperature**

Positive and negative differential superstructure temperature gradients *shall be taken as 80% of the values presented in Appendix A* of the National Cooperative Highway Research Program Report 276 "Thermal Effects in Concrete Bridge Superstructures" [5].

*Alternatively, site specific thermal gradients, developed based on the climatic conditions in the area and the actual material properties of the structure, may be substituted for the current design gradients.*

The magnitudes and distributions of temperatures measured in the segmental pier support this suggested change to the segmental bridge design code for superstructures. The similarities in gradient shapes and temperature magnitudes measured by this project and by Roberts [7] suggest that the temperatures measured in the hollow box, concrete segmental pier are an excellent match to those found in hollow box , concrete bridge superstructures.

### **9.2.2 Application of Thermal Gradients to Substructures**

Currently, there is no explicit reference to segmentally constructed bridge substructures with regards to the application of thermal differential loading in the *AASHTO Guide Specification* [12] for any service limit state load conditions. Segmental substructures are listed in Table 8-1 and thermal effects are included in load combinations applicable to them. Based on the load case described earlier in this chapter, it is prudent to include thermal gradient effects in segmental substructures for the construction load cases. However, no guidance is provided as to the application of non-linear thermal gradients to segmental piers for service load cases. Based on the thermal gradients measured in the field, the following section should be added to the *AASHTO Guide Specification* [12] (changes in italics):

#### ***8.2.3 Thermal Gradients in Substructures***

*When considering thermal gradient effects on bridge substructures, a load factor of zero (0) shall be applied to the differential temperature*

*load (DT) for the load combination described in section 8.2.2 and other AASHTO load combinations which include differential temperature gradient effects.*

In addition, the following statement concerning column (4) in Table 8-1 should be added to the notes for that table:

*\*\*\*\*\* When considering differential thermal effects in segmental substructures, a load factor of 0.65 shall be applied to the differential thermal term (DT).*

The following section should be added to the commentary:

### **8.2.3 Thermal Gradients in Segmental Substructures**

*Preliminary field research on the magnitudes and effects of non-linear thermal gradients in bridge piers suggests that gradients similar in shape but substantially less (50%) in magnitude to those measured in bridge superstructures [7] occur in hollow box, concrete piers. However, the thermal effects appear to be minor. For construction load cases in Table 8-1, temperature gradients for substructures need be only 65% of the values recommended in Appendix A of National Cooperative Highway Research Program Report 276 "Thermal Effects in Concrete*

*Bridge Superstructures” [5]. Generally, they need not be applied to substructures of this type for service load cases listed in section 8.0. Additional research is recommended to verify the importance of temperature gradient effects in hollow box, concrete bridge piers used for over-water crossings and piers with rectangular cross-sectional shapes.*

### 9.3 SUGGESTIONS FOR FUTURE STUDY

The field instrumentation of a segmentally constructed, hollow-box pier located on the U.S. 183 segmental viaduct provided important insights into the nature of temperature distributions in and their effects on substructures of this type. From the analyses performed, it is clear that standard, one-dimensional assumptions of temperature variations through the pier cross-section like those typically used in the analysis of bridge superstructures are inadequate to accurately describe the self-equilibrating strains and stresses induced by the pier’s temperature distribution. More accurate analysis of a pier’s response to temperature changes should account for the complex, two-dimensional distribution of temperatures caused by the shape of the cross-section and the orientation of the pier to solar radiation. A simplified method of analysis accounting for the measured temperature distributions was developed in Chapter 6, but additional development of that method is needed to verify its accuracy and increase its usefulness.

The instrumented pier was octagonal in cross-sectional shape, and its behavior was likely similar to that of a hollow, circular tube under differential temperature loading. However, as discussed in Chapter 2, most segmental piers constructed to date have rectangular cross-sections. The behavior of piers with this shape should be investigated to determine the influence of different cross-sectional shapes on the

temperature distributions produced in piers and their corresponding response. In addition, many segmental piers have been constructed as part of long, over-water crossings. The influence on pier temperature gradients from reflected sunlight as well as ambient humidity should be determined by the instrumentation of a pier constructed over water.

The large strains measured in the hollow cross-section of the pier near the solid capital segment were unexpected. Further clarification of the effects of restraint provided by the interface between hollow cross-sections and solid segments would provide a better understanding of structural response to temperature gradients. Similar increases in strain likely occur near heavy end anchorage segments in superstructures as well.

The effects of temperature gradients in piers that are rigidly connected to the superstructure should be investigated to determine the magnitude of induced moments in the superstructure members. This work could also be applied to multiple column bents with rigid connections between the columns and cross beams.

Most importantly, additional temperature and strain data should be recorded from the instruments installed in pier P16 to determine temperature characteristics during the fall and winter months at that location. Additional measurements would also aid in the verification of the magnitude and frequency of the largest temperature gradients that occur in the pier.

## CHAPTER 10

### *SUMMARY, CONCLUSIONS, AND RECOMMENDATIONS*

#### *10.1 SUMMARY*

This project represents one phase of the field instrumentation and monitoring of the new U.S. 183 segmental post-tensioned concrete viaduct in Austin, Texas. Other phases include the instrumentation of a mainlane superstructure span, mainlane cast-in-place pier [1], and balanced-cantilever ramp superstructure span. In this phase, concrete strain gauges, strain gauges attached to reinforcing bars, and thermocouples were installed in three precast column segments and one capital segment of a 20-meter high segmentally-constructed, post-tensioned, concrete, hollow box bridge pier. Data from the instruments were recorded hourly during the first four months after the pier's erection in April, 1996.

A set of 24 thermocouples was installed in a cross-section of the pier near mid-height to determine the shape and magnitude of any thermal gradients present. Three thermocouples were located through the thickness of each of the eight walls of the pier's octagonal cross-section. These instruments provided excellent data concerning the distribution of temperatures through the walls of the pier as well as across the cross-section as a whole. Smaller sets of thermocouples were installed in cross-sections near the base of the pier as well as the top segment. These instruments were used to confirm the temperature measurements recorded from the mid-height segment.

Strain gauges were embedded in the concrete of each of the three column segments and the capital segment during casting operations. Gauges located in the column segments were oriented longitudinally (vertically) to provide information on longitudinal self-equilibrating strains induced by the temperature changes in the pier over daily cycles of heating and cooling. A small number of gauges were also installed in the

transverse direction in each column segment to determine transverse strains due to temperature gradients through the pier walls. Chapter 3 provides a detailed discussion of the locations of all instruments installed in the pier.

Temperatures in the pier's concrete followed distinct daily cycles corresponding to both ambient air temperature changes and variations in solar radiation striking the pier's outer faces throughout the course of the day. The exterior faces of the pier experience the largest cycles of daily heating and cooling. The concrete's poor thermal conductivity prevented significant changes in the temperatures located in the interior. This also produced large thermal gradients between the inner and outer faces of the pier's walls, as well as thermal differentials between opposite faces of the pier. It was determined that solar radiation produced the largest and most rapid rises in temperature, while changes in ambient air temperature played an important, but secondary, role. A full discussion of the trends in the measured temperatures can be found in Chapter 5.

Daily fluctuations in differential or self-equilibrating strain readings also occurred due to the changing temperatures. Temperature compensated strain gauges were used to eliminate conventional linear expansion and contraction strain readings. Thus, the strain gauges reflect the stresses set up through the member by restrained thermal movements. So in general, a *rise* in temperature at the location of a strain gauge induced *compressive* strain changes in the gauge. Temperature *drops* produced *tensile* strains. Gauges were also monitored during post-tensioning operations to track forces in the column and capital, which served as the post-tensioning anchorage zone for the pier's tendons. Chapter 5 contains more information concerning the daily strain cycles.

From the temperature data, the maximum positive and negative temperature gradients were determined for each month. Positive gradients occurred when the outer faces of the pier were hotter than the insulated interior. The largest positive gradients typically occurred in the late afternoon as the sun almost directly struck the west face of the pier. Conversely, negative temperature gradients occurred when the outer faces of

the pier were cooler than the interior. The largest of these typically occurred during the early morning hours just before sunrise. The gradients measured were considerably smaller in magnitude than the applicable values recommended for box girder superstructures by the *AASHTO Segmental Bridge Guide Specifications* [11] and by the NCHRP Report 276 [5]. Chapter 6 includes a discussion of the maximum monthly temperature gradients.

The measured temperature gradients were then used to perform calculations to determine the distribution of self-equilibrating strains in the pier's cross-section. Two methods of hand calculations were used to determine longitudinal strains. A one-dimensional projection of the complex, two-dimensional temperature distribution was developed for the first hand calculation method. This "classical" method assumed that temperatures vary only through the depth of a member, even though temperatures in the pier actually varied throughout the cross-section. Therefore a second, more general, hand calculation method was developed to account for the more complicated temperature distribution associated with the maximum measured temperature gradients. Transverse strains were also calculated for each wall of the cross-section for each maximum monthly gradient. Information on the hand calculation procedures can be found in Chapter 6.

To confirm the hand calculations, a finite element model of the pier was constructed using ANSYS 5.0a. Using the measured temperatures associated with the maximum monthly gradients as input, this computer analysis calculated self-equilibrating stresses and strains across the entire pier cross-section in both the longitudinal and transverse directions. Chapter 7 describes the finite element analysis in detail.

Finally, the three analytical determinations of self-equilibrating strains were compared with the measured longitudinal strains from the embedded strain gauges. Good correlation between measured and calculated strains was found, and the finite element analysis typically provided the most closely matching results. Strains measured at the top of the column near the interface with the capital segment were much larger than those



calculated. This increase in apparent strain was probably due to partial restraint of the octagonal cross-section in that area by the solid capital. Transverse strains closely matched those calculated by hand as well as those from the finite element model. Transverse strain gauges located near the capital also measured larger strains than expected, further indicating possible restraint provided by the capital segment itself. A comparison of the measured and calculated strains can be found in Chapter 8.

Example load cases based on load combinations from the *AASHTO Guide Specification for Design and Construction of Segmental Concrete Bridges* [12] were calculated to determine the relative effects due to temperature-induced stresses on the pier. A construction load case and two typical service load combinations were evaluated. It was found that temperature gradients could potentially induce tensile stresses at the outer fibers of the pier's cross-section during construction. However, no net tension was calculated to occur from the service load combinations. The magnitudes of the stresses produced by temperature effects on the pier were found to be minor compared with stresses due to post-tensioning, superstructure dead loads, and design live loads (see Chapter 9).

## 10.2 CONCLUSIONS

Based on the instrumentation and analyses of the pier, several conclusions regarding thermal gradients in hollow box, segmentally constructed, post-tensioned concrete substructures can be made:

1. Temperature gradients in the hollow pier vary in magnitude and direction throughout the course of a typical day due to the changing position of the sun.
2. Pier temperatures fluctuate greatly at the outer surfaces of the cross-section, and do not vary as greatly in the interior.

3. Solar radiation produces the largest and most rapid changes in temperature at the outer faces of the cross-section. Ambient air temperature changes are a secondary mechanism of heat transfer.
4. Maximum differential temperature magnitudes measured in the pier were only 50% of the *AASHTO Guide Specification* [11] and the NCHRP Report 276 [5] design gradient magnitudes for both positive and negative gradients.
5. Maximum differential temperature magnitudes measured in the pier were similar to those found previously in bridge superstructures, suggesting that temperature distributions measured in hollow box piers can also be used to estimate temperatures in superstructures.
6. Unlike box girder superstructures, hollow box bridge piers experience a complex, two-dimensional distribution of temperatures throughout the cross-section. This makes conventional methods for the determination of self-equilibrating stresses inaccurate. More general methods which take into account the temperature at given points rather than discrete depths of the section should be used.
7. The analytical methods predicted the measured longitudinal and transverse strains fairly well. The finite element analysis produced strain results closest to those measured in the field. Of the two hand calculation methods used, the more accurate method accounted for the two-dimensional distribution of temperatures throughout the pier cross-section.
8. Calculated stresses due to thermal gradients contributed only a small amount to the total estimated stress on the pier from design code service load cases.
9. The amount of post-tensioning present in the pier was more than enough to counteract any tensile stresses induced by negative gradients, and the additional compression from the superstructure probably ensures that no tensile stresses will occur in the pier due to temperature effects.

### 10.3 RECOMMENDATIONS

The measured temperature gradients that occurred in the segmental pier were approximately 50% of those specified by design codes. Similar gradients were also measured by Roberts [7], who suggested the following revisions to the *AASHTO Guide Specification* [12] (changes in italics):

#### 7.4.4 Differential Temperature

Positive and negative differential superstructure temperature gradients *shall be taken as 80% of the values presented* in Appendix A of the National Cooperative Highway Research Program Report 276 “Thermal Effects in Concrete Bridge Superstructures” [5].  
*Alternatively, site specific thermal gradients, developed based on the climatic conditions in the area and the actual material properties of the structure, may be substituted for the current design gradients.*

The temperature gradient magnitudes measured during this research project support this suggested change to the code. Design gradients are much more severe than those measured during the course of this field research.

Clarification of the application of thermal gradients to bridge substructures should be provided in the commentary of the segmental bridge design code. Currently, design thermal gradients are explicitly designated for use in bridge superstructures, but

no mention is made of their possible application to piers. However, temperature effects are required to be analyzed for segmental substructures in the construction load cases outlined in Table 8-1 of the *AASHTO Guide Specification* [12]. To clarify the application of thermal gradients to bridge piers, the following section should be added to section 8.0 (changes in italics):

### ***8.2.3 Thermal Gradients in Substructures***

*When considering thermal gradient effects on bridge substructures, a load factor of zero (0) shall be applied to the differential temperature load (DT) for the load combination described in section 8.2.2 and other AASHTO load combinations which include differential temperature gradient effects.*

In addition, the following statement concerning column (4) in Table 8-1 should be added to the notes for that table:

*\*\*\*\*\* When considering differential thermal effects in segmental substructures, a load factor of 0.65 shall be applied to the differential thermal term (DT).*

The following section should be added to the commentary:

### **8.2.3 Thermal Gradients in Segmental Substructures**

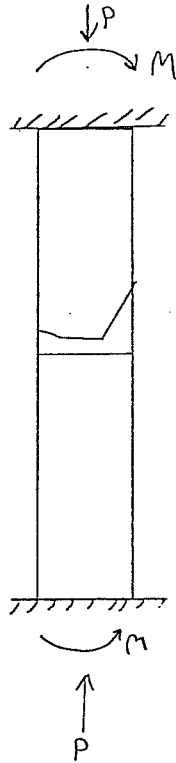
*Preliminary field research on the magnitudes and effects of non-linear thermal gradients in bridge piers suggests that gradients similar in shape but substantially less (50%) in magnitude to those measured in bridge superstructures [7] occur in hollow box, concrete piers. However, the thermal effects appear to be minor. For construction load cases in Table 8-1, temperature gradients for substructures need be only 65% of the values recommended in Appendix A of National Cooperative Highway Research Program Report 276 "Thermal Effects in Concrete Bridge Superstructures" [5]. Generally, they need not be applied to substructures of this type for service load cases listed in section 8.0. Additional research is recommended to verify the importance of temperature gradient effects in hollow box, concrete bridge piers used for over-water crossings and piers with rectangular cross-sectional shapes.*

## APPENDIX - CALCULATIONS

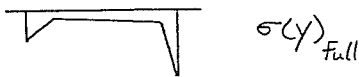
|   |     |
|---|-----|
| Self-Equilibrating Stresses - Classical Method .....            | 276 |
| Self-Equilibrating Stresses - Primary Bending Axis Method ..... | 282 |
| Transverse Stress Analysis .....                                | 286 |
| Construction Load Case - Unbalanced Segment.....                | 290 |
| Service Load Cases - Five-Span Unit .....                       | 293 |

## Self-Equilibrating Stresses - Classical Method

Classical Method of determination of self-equilibrating stresses from non-linear temperature gradients.

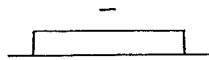


- pier restrained artificially
- non-linear gradient applied
- artificial restraint forces  $P$  and  $M$  we calculated. (see following pages)
- Fully restrained stress distribution determined with
 
$$\sigma(y) = E\alpha T(y)$$
- artificial restraining forces removed
- final stress distribution calculated



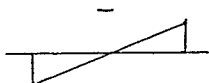
$$\sigma(y)_{Full}$$

$$P = \int_y E\alpha T(y) b(y) dy$$



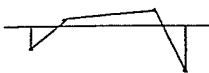
$$\sigma_{axial} = P/A$$

$$M = \int_y E\alpha T(y) b(y) y dy$$



$$\sigma_{bend} = \frac{Mc}{I}$$

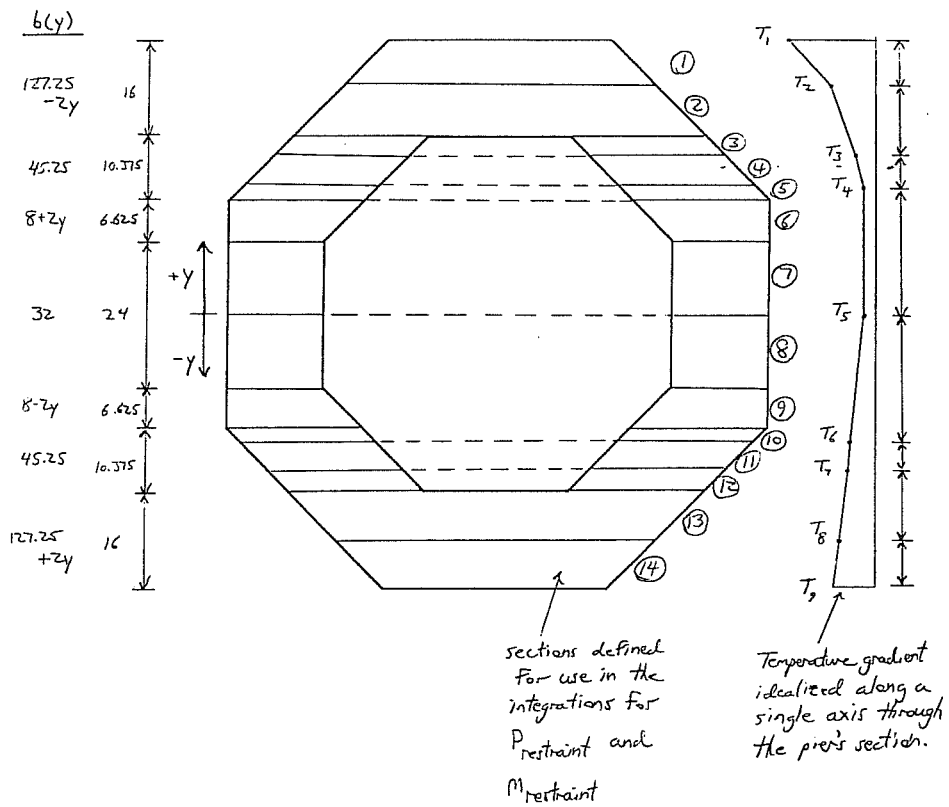
=



$$\sigma_{self-equilibrating}$$

## Self-Equilibrating Stresses - Classical Method

Discretization of pier cross-section  
for integration purposes:





### Self-Equilibrating Stresses - Classical Method

$$P1 := \int_{37}^{45} (127.25 - 2 \cdot y) \cdot \left[ T1 - (T1 - T2) \cdot \frac{45 - y}{8} \right] \cdot E \cdot \alpha \, dy$$

$$P2 := \int_{29}^{37} (127.25 - 2 \cdot y) \cdot \left[ T2 - (T2 - T3) \cdot \frac{37 - y}{10.8437} \right] \cdot E \cdot \alpha \, dy$$

$$P3 := \int_{26.1563}^{29} (45.25) \cdot \left[ T2 - (T2 - T3) \cdot \frac{37 - y}{10.8437} \right] \cdot E \cdot \alpha \, dy$$

$$P4 := \int_{20.5}^{26.1563} (45.25) \cdot \left[ T3 - (T3 - T4) \cdot \frac{26.1563 - y}{5.6563} \right] \cdot E \cdot \alpha \, dy$$

$$P5 := \int_{18.625}^{20.5} (45.25) \cdot \left[ T4 - (T4 - T5) \cdot \frac{20.5 - y}{20.5} \right] \cdot E \cdot \alpha \, dy$$

$$P6 := \int_{12}^{18.625} (8 + 2 \cdot y) \cdot \left[ T4 - (T4 - T5) \cdot \frac{20.5 - y}{20.5} \right] \cdot E \cdot \alpha \, dy$$

$$P7 := \int_{0}^{12} (32) \cdot \left[ T4 - (T4 - T5) \cdot \frac{20.5 - y}{20.5} \right] \cdot E \cdot \alpha \, dy$$

$$P8 := \int_{(-12)}^{0} (32) \cdot \left[ T6 - (T6 - T5) \cdot \frac{20.5 + y}{20.5} \right] \cdot E \cdot \alpha \, dy$$

### Self-Equilibrating Stresses - Classical Method

$$P_9 := \int_{(-18.625)}^{(-12)} (8 - 2 \cdot y) \cdot \left[ T_6 - (T_6 - T_5) \cdot \frac{20.5 + y}{20.5} \right] \cdot E \cdot \alpha \, dy$$

$$P_{10} := \int_{(-20.5)}^{(-18.625)} (45.25) \cdot \left[ T_6 - (T_6 - T_5) \cdot \frac{20.5 + y}{20.5} \right] \cdot E \cdot \alpha \, dy$$

$$P_{11} := \int_{(-26.1563)}^{(-20.5)} (45.25) \cdot \left[ T_7 - (T_7 - T_6) \cdot \frac{26.1563 + y}{5.6563} \right] \cdot E \cdot \alpha \, dy$$

$$P_{12} := \int_{(-29)}^{(-26.1563)} (45.25) \cdot \left[ T_8 - (T_8 - T_7) \cdot \frac{37 + y}{10.8437} \right] \cdot E \cdot \alpha \, dy$$

$$P_{13} := \int_{(-37)}^{(-29)} (127.25 + 2 \cdot y) \cdot \left[ T_8 - (T_8 - T_7) \cdot \frac{37 + y}{10.8437} \right] \cdot E \cdot \alpha \, dy$$

$$P_{14} := \int_{(-45)}^{(-37)} (127.25 + 2 \cdot y) \cdot \left[ T_9 - (T_9 - T_8) \cdot \frac{45 + y}{8} \right] \cdot E \cdot \alpha \, dy$$

$$P = \sum_{i=1}^{14} P_i$$

### Self-Equilibrating Stresses - Classical Method

$$M1 := \int_{37}^{45} (127.25 - 2 \cdot y) \cdot \left[ T1 - (T1 - T2) \cdot \frac{45 - y}{8} \right] \cdot E \cdot y \cdot \alpha \, dy$$

$$M2 := \int_{29}^{37} (127.25 - 2 \cdot y) \cdot \left[ T2 - (T2 - T3) \cdot \frac{37 - y}{10.8437} \right] \cdot E \cdot y \cdot \alpha \, dy$$

$$M3 := \int_{26.1563}^{29} (45.25) \cdot \left[ T2 - (T2 - T3) \cdot \frac{37 - y}{10.8437} \right] \cdot E \cdot y \cdot \alpha \, dy$$

$$M4 := \int_{20.5}^{26.1563} (45.25) \cdot \left[ T3 - (T3 - T4) \cdot \frac{26.1563 - y}{5.6563} \right] \cdot E \cdot y \cdot \alpha \, dy$$

$$M5 := \int_{18.625}^{20.5} (45.25) \cdot \left[ T4 - (T4 - T5) \cdot \frac{20.5 - y}{20.5} \right] \cdot E \cdot y \cdot \alpha \, dy$$

$$M6 := \int_{12}^{18.625} (8 + 2 \cdot y) \cdot \left[ T4 - (T4 - T5) \cdot \frac{20.5 - y}{20.5} \right] \cdot E \cdot y \cdot \alpha \, dy$$

$$M7 := \int_{0}^{12} (32) \cdot \left[ T4 - (T4 - T5) \cdot \frac{20.5 - y}{20.5} \right] \cdot E \cdot y \cdot \alpha \, dy$$

### Self-Equilibrating Stresses - Classical Method

$$M_8 := \int_{(-12)}^0 (32) \cdot \left[ T_6 - (T_6 - T_5) \cdot \frac{20.5 + y}{20.5} \right] \cdot E \cdot y \cdot \alpha \, dy$$

$$M_9 := \int_{(-18.625)}^{(-12)} (8 - 2 \cdot y) \cdot \left[ T_6 - (T_6 - T_5) \cdot \frac{20.5 + y}{20.5} \right] \cdot E \cdot y \cdot \alpha \, dy$$

$$M_{10} := \int_{(-20.5)}^{(-18.625)} (45.25) \cdot \left[ T_6 - (T_6 - T_5) \cdot \frac{20.5 + y}{20.5} \right] \cdot E \cdot y \cdot \alpha \, dy$$

$$M_{11} := \int_{(-26.1563)}^{(-20.5)} (45.25) \cdot \left[ T_7 - (T_7 - T_6) \cdot \frac{26.1563 + y}{5.6563} \right] \cdot E \cdot y \cdot \alpha \, dy$$

$$M_{12} := \int_{(-29)}^{(-26.1563)} (45.25) \cdot \left[ T_8 - (T_8 - T_7) \cdot \frac{37 + y}{10.8437} \right] \cdot E \cdot y \cdot \alpha \, dy$$

$$M_{13} := \int_{(-37)}^{(-29)} (127.25 + 2 \cdot y) \cdot \left[ T_8 - (T_8 - T_7) \cdot \frac{37 + y}{10.8437} \right] \cdot E \cdot y \cdot \alpha \, dy$$

$$M_{14} := \int_{(-45)}^{(-37)} (127.25 + 2 \cdot y) \cdot \left[ T_9 - (T_9 - T_8) \cdot \frac{45 + y}{8} \right] \cdot E \cdot y \cdot \alpha \, dy$$

$$M = \sum_{i=1}^{14} M_i$$

### Self-Equilibrating Stresses - Primary Bending Axis Method

Bending actually occurs along axis A-A,

therefore no bending occurs along B-B.

$$\therefore \left( \sum T \propto A_i \right)_{\text{south of AA}} = \left( \sum T \propto A_i \right)_{\text{north of AA}}$$

$$\left( \text{South Volume} \right) = \left( \text{North Volume} \right)$$

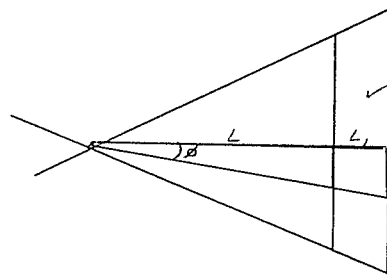
South Areas

$$A_1 = (35.04)(5.33) = 186.88 \text{ in}^2$$

$$A_2 = (30.625)(5.33) = 163.33 \text{ in}^2$$

$$A_3 = (26.21)(5.33) = 139.78 \text{ in}^2$$

North Areas



Total area = A

$$AT_1 = \frac{1}{2}(L+L_1)(L+L_1) \tan \theta$$

$$= \frac{1}{2}(L+b)(L)$$

$$AT_2 = \frac{1}{2}(L)(L) \tan \theta$$

$$A_L = \frac{A}{2} + (AT_1 - AT_2)$$

$$A_S = \frac{A}{2} - (AT_1 - AT_2)$$

A<sub>1</sub>:

$$AT_1 = \frac{1}{2}(45)(45) \tan \theta$$

$$AT_2 = \frac{1}{2}(35.0)(37.5) \tan \theta$$

$$A_{1L} = \frac{A_1}{2} + (1012.5 \tan \theta - 786.72 \tan \theta) = 93.44 + 225.78 \tan \theta = A_{1L}$$

$$A_{1S} = \frac{A_1}{2} - (1012.5 \tan \theta - 786.72 \tan \theta) = 93.44 - 225.78 \tan \theta = A_{1S}$$

A<sub>2</sub>:

$$A_{2L} = \frac{A_2}{2} + (786.72 \tan \theta - 589.39 \tan \theta) = 81.67 + 197.33 \tan \theta = A_{2L}$$

$$81.67 - 197.33 \tan \theta = A_{2S}$$

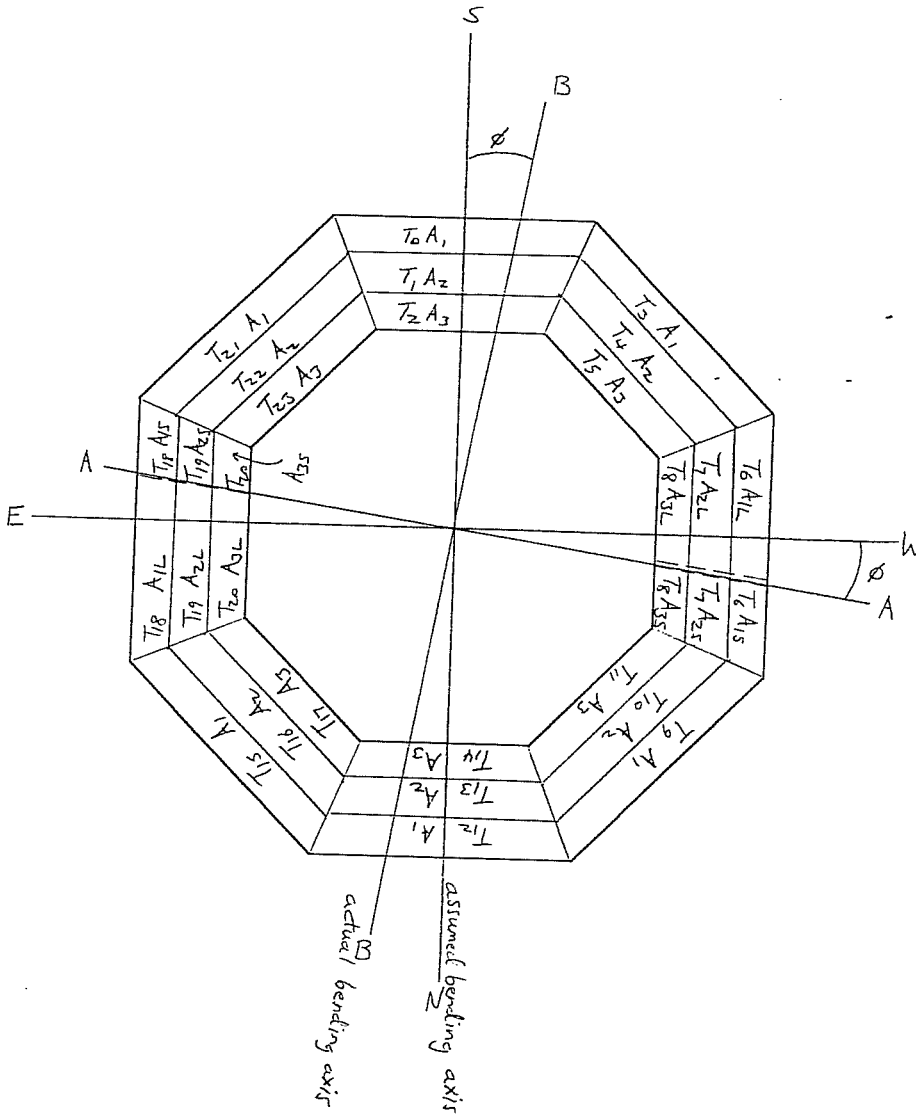
A<sub>3</sub>:

$$A_{3L} = \frac{A_3}{2} + (589.39 \tan \theta - 420.5 \tan \theta) = 69.89 + 168.89 \tan \theta = A_{3L}$$

$$69.89 - 168.89 \tan \theta = A_{3S}$$

## Self-Equilibrating Stresses - Primary Bending Axis Method

Discrete areas of constant temperature assumed for primary bending axis determination.



Self-Equilibrating Stresses - Primary Bending Axis Method

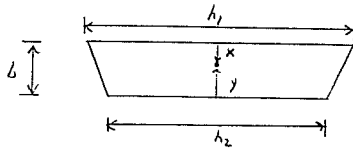
$$\sum_i T_i A_i \text{ south} = \begin{matrix} T_0 A_1 \\ T_1 A_2 \\ T_2 A_3 \\ T_3 A_1 \\ T_4 A_2 \\ T_5 A_3 \\ T_6 A_{1L} \\ T_7 A_{2L} \\ T_8 A_{3L} \\ T_{10} A_{15} \\ T_{19} A_{25} \\ T_{20} A_{35} \\ T_{21} A_1 \\ T_{22} A_2 \\ T_{23} A_3 \end{matrix} \quad \sum_i T_i A_i \text{ north} = \begin{matrix} T_9 A_1 \\ T_{10} A_2 \\ T_{11} A_3 \\ T_{12} A_1 \\ T_{13} A_2 \\ T_{14} A_3 \\ T_{15} A_1 \\ T_{16} A_2 \\ T_{17} A_3 \\ T_{18} A_{1L} \\ T_{19} A_{2L} \\ T_{20} A_{3L} \\ T_{21} A_{15} \\ T_{22} A_{25} \\ T_{23} A_{35} \end{matrix}$$

see 3DANAL.XLS for calc. of  $\phi$  angle

$$\text{Self. Equil.}_i = \frac{E \alpha T_i}{(\text{psi})} - \frac{\sum E \alpha T A_i}{\sum A_i (\text{psi})} - \frac{(\sum E \alpha T_i A_i y_i)(y_i)}{I_{\text{sect.}}}$$

self-equilibrating = Fully restrained - axial stress - bending stress

where  $y_i$  = centroidal distance to actual bending axis B-B



$$x = \frac{b(2h_2 + h_1)}{3(h_1 + h_2)} \quad y = b - \frac{b(2h_2 + h_1)}{3(h_2 + h_1)}$$

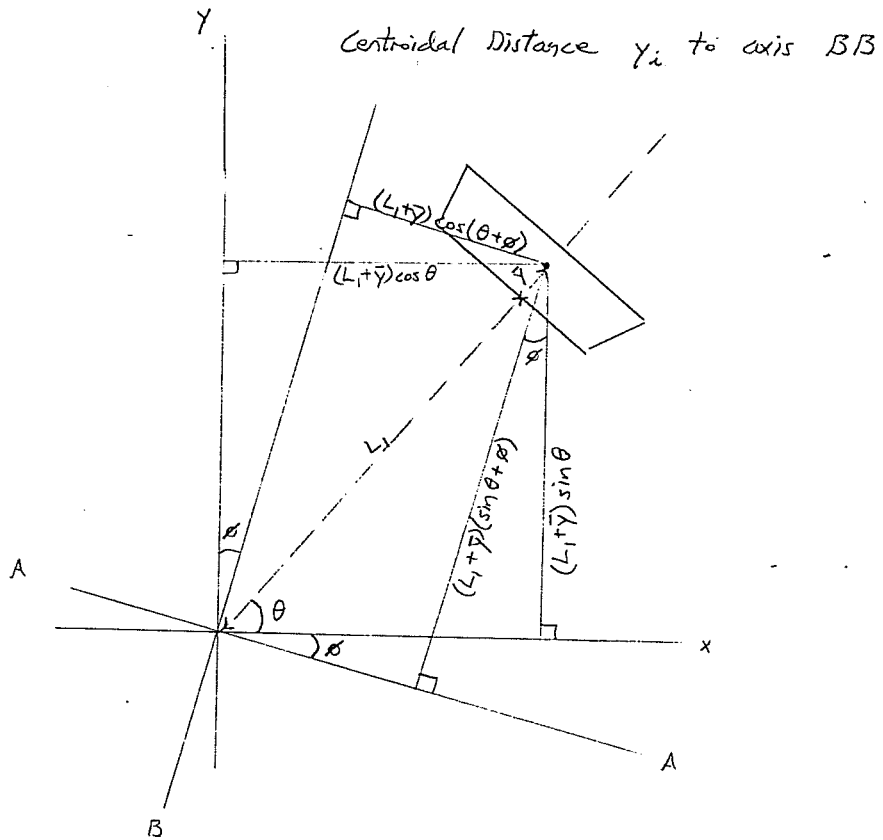
$$A_1: \quad x_1 = 2.6106 \quad y_1 = 2.7227$$

$$A_2: \quad x_2 = 2.6926 \quad y_2 = 2.7308$$

$$A_3: \quad x_3 = 2.5918 \quad y_3 = 2.7416$$

$$x_{\text{avg.}} = 2.60 \quad y_{\text{avg.}} = 2.73$$

Self-Equilibrating Stresses - Primary Bending Axis Method

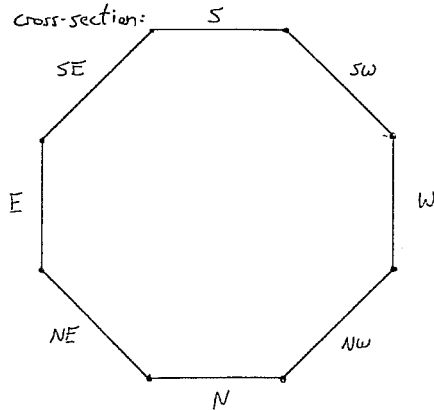




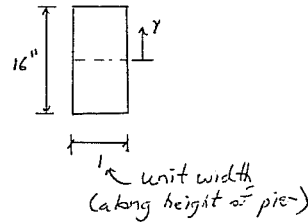
## Transverse Stress Analysis

### Transverse Stress Analysis:

Idealized cross-section:



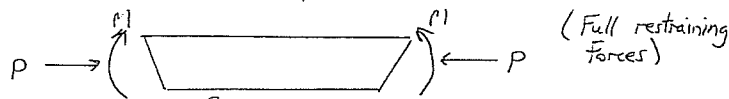
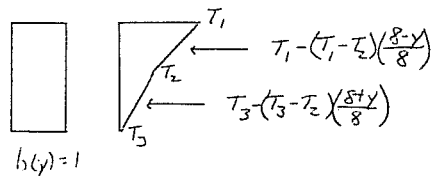
Each member has cross-section:



Member Length idealized as average of lengths of faces:

$$L = \frac{37.25' + 24.0'}{2} = 30.625'$$

Temperature variation through depth:



$$P = \int_0^8 E \alpha \left[ T_1 - (T_1 - T_2) \left( \frac{8-y}{8} \right) \right] dy$$

$$+ \int_{-8}^0 E \alpha \left[ T_3 - (T_3 - T_2) \left( \frac{8+y}{8} \right) \right] dy$$

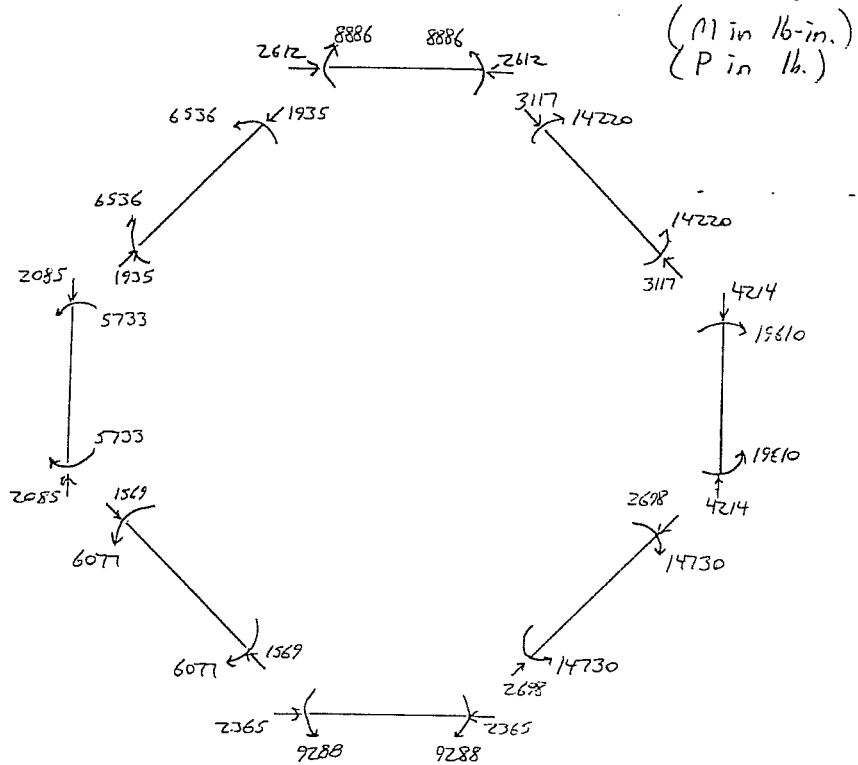
### Transverse Stress Analysis

$$M = \int_0^8 E \alpha [T_1 - (T_1 - T_2) \left(\frac{8-y}{8}\right)] y dy$$

$$+ \int_{-8}^0 E \alpha [T_3 - (T_3 - T_2) \left(\frac{8+y}{8}\right)] y dy$$

Integrations for each face and their temperatures performed using MathCAD.

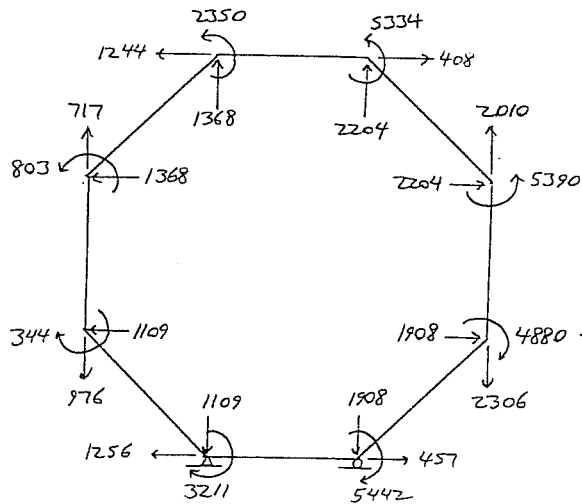
Fully restrained forces for April maximum positive gradient:



## Transverse Stress Analysis

Input for RISA-2D frame analysis:

(sum of the opposites of all restraint forces  
at each node)  
(16 and 16 in)



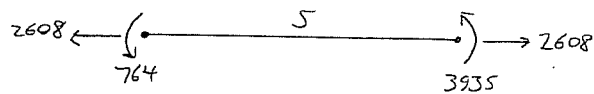
$$E = 5168000 \text{ psi}$$

$$\alpha = 5.2 \times 10^{-6} / ^\circ\text{F}$$

$$I = 341.3 \text{ in}^4$$

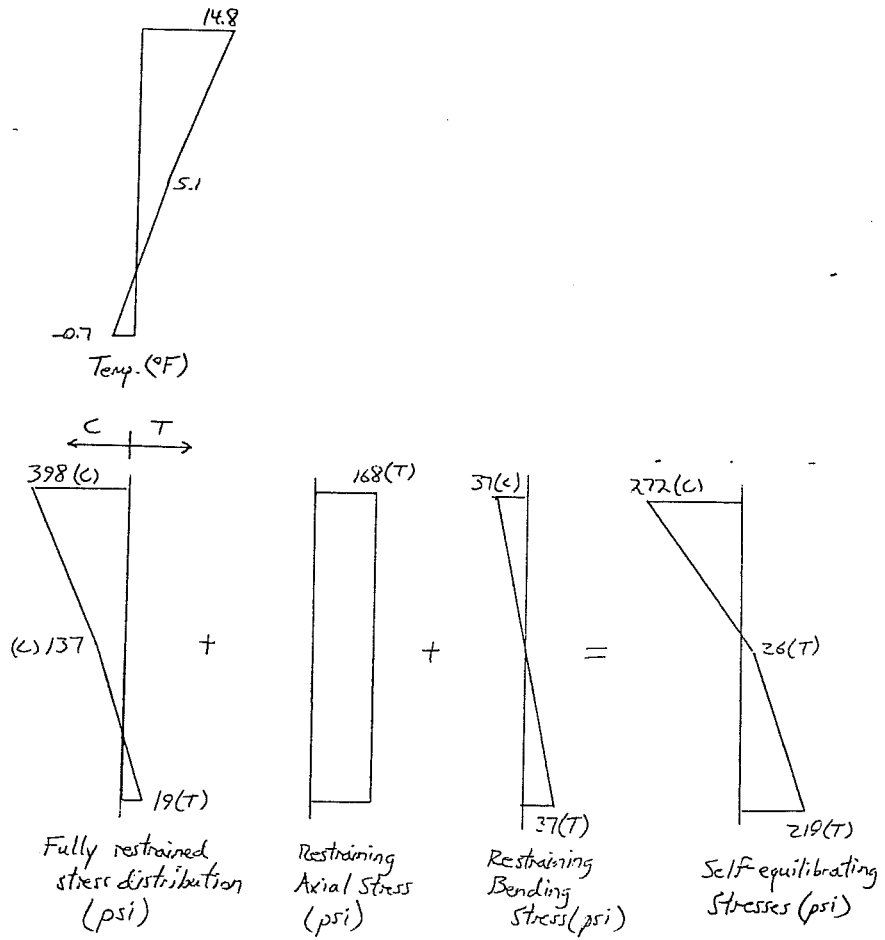
$$A = 16 \text{ in}^2$$

RISA output: end forces in south face (example)



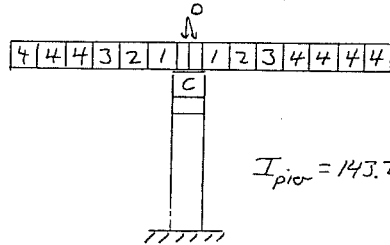
## Transverse Stress Analysis

Stress distribution in south face:



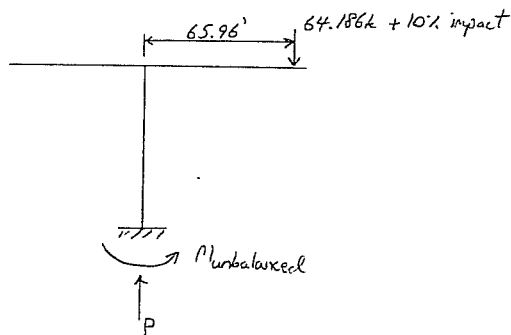
### Construction Load Case - Unbalanced Segment

Construction Load Case b) - Unbalanced segment



$$\rho = 155 \text{ pcf}$$

| Segment Type | A(ft <sup>2</sup> ) | L(ft) | Weight(k) |
|--------------|---------------------|-------|-----------|
| 0            | 86.828              | 4.75  | 63.927    |
| 1            | 45.318              | 9.417 | 66.148    |
| 2            | 44.849              | 9.417 | 65.463    |
| 3            | 44.401              | 9.417 | 64.809    |
| 4            | 43.974              | 9.417 | 64.186    |
| C (Capital)  |                     |       | ~ 60      |
| 4' Column    | 27.242              | 4.0   | 16.890    |
| 8' Column    | 27.242              | 8.0   | 33.780    |



$$M_{\text{unbalanced}} = (65.96)(1.10)(64.186) = \underline{4657 \text{ k}\cdot\text{ft}} \quad (U+I)$$

$$P = 2(63.927) + 2(66.148) + 2(65.463) + 2(64.809)$$

$$+ 7(64.186) + 60 + 16.89 + 6(33.78) \quad (DL)$$

$$P = \underline{1250 \text{ k}}$$

Load Combination b) from AASHTO Guide Specs Table 8-1:

$$DL + U + CLL + CE + IE + (R+T)$$

### Construction Load Case - Unbalanced Segment

Assume lump sum losses in pier post-tensioning = 35 ksi

$$A_{\text{steel}} = 4 \times 19 \times 0.217 \text{ in}^2 = 16.492 \text{ in}^2$$

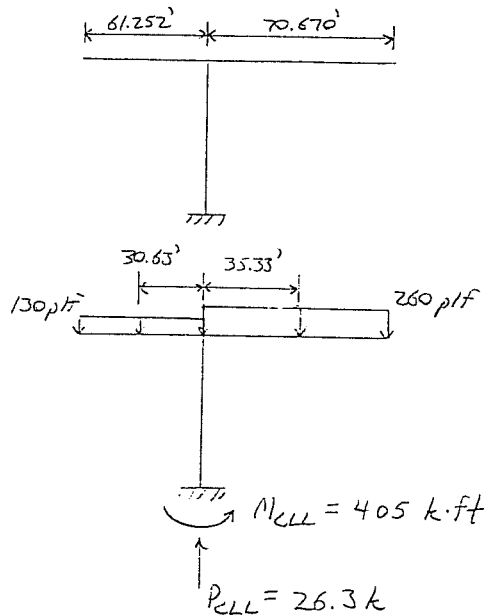
Initial stress @ 0.80 GUTS (279 ksi)

$$= 216 \text{ ksi}$$

Total PT force after losses:

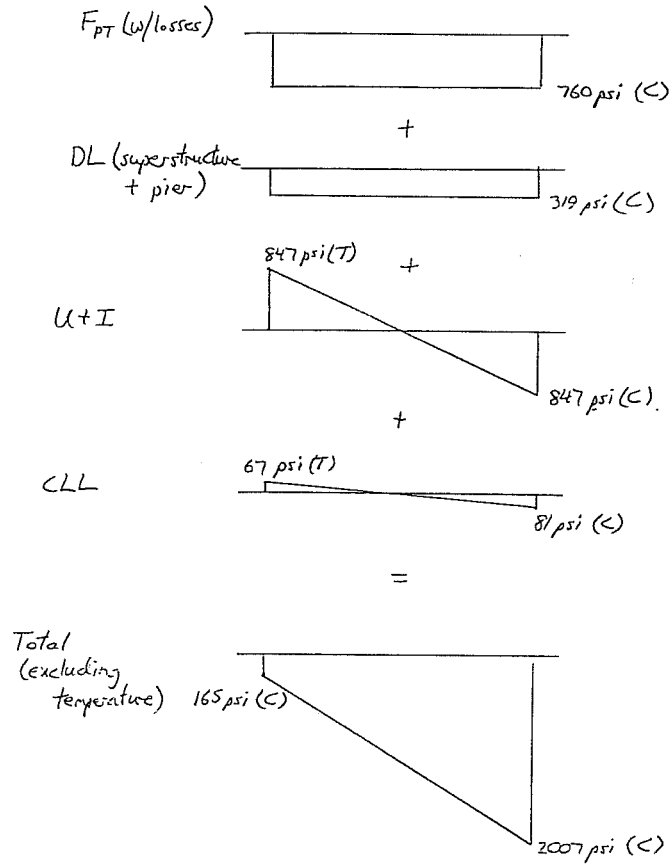
$$F_{\text{pt}} = (16.492)(216 - 35) = \underline{2985 \text{ k}}$$

CLL (Construction Live Load):  
 5 psf on short cantilever  
 10 psf on long cantilever  
 roadway width  $\approx 26'$



### Construction Load Case - Unbalanced Segment

#### Construction Live Load Stress Summary (2 pier base)



Self equilibrating stresses applied to maximum effect using spreadsheet.

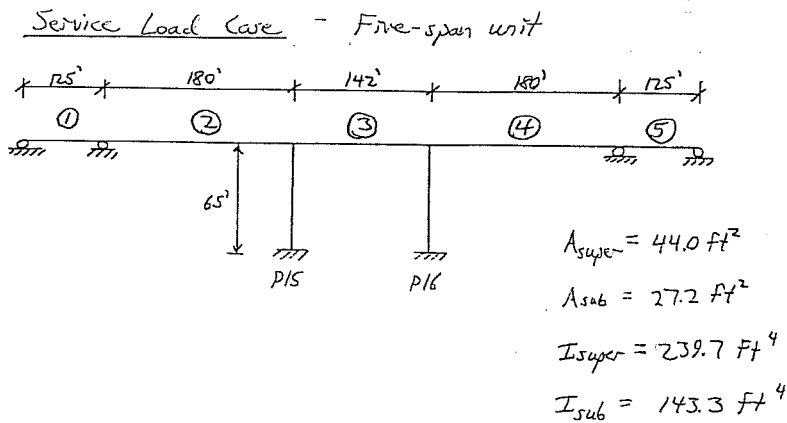
$$\text{Max allowable comp.} = 0.50 \bar{f}_c' \quad \bar{f}_c' = 8220 \text{ psi}$$

$$\text{Max. C} = 4110 \text{ psi} \quad (E = 5168 \text{ ksi})$$

$$\text{Max allowable tens.} = 7\sqrt{\bar{f}_c'}$$

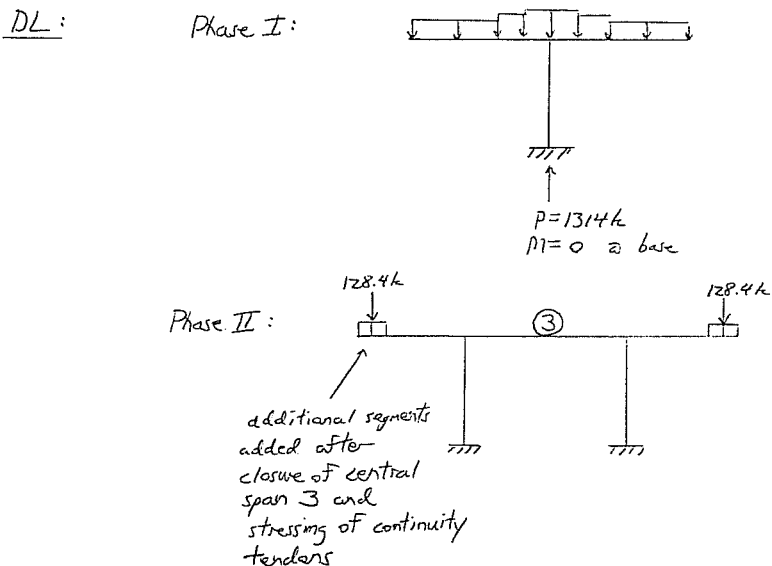
$$\text{Max. T} = 635 \text{ psi}$$

### Service Load Cases - Five-Span Unit



### Service Load Cases (AASHTO Guide Specs) - Allowable Stress

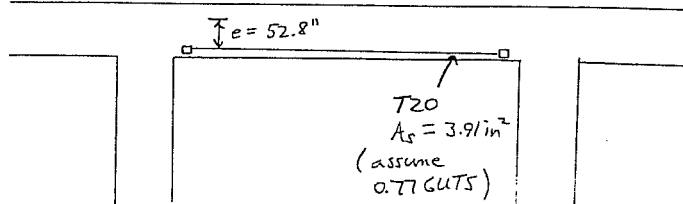
- IV:  $(DL+SDL+EL)+(L+I) + R+S+(TRF+0.5DT)$  125%
- II:  $(DL+SDL+EL) + R+S + (TRF+DT)$  140%
- VII:  $(DL+SDL+EL)+(L+I) + R+S+(TRF+0.5DT)$  140%
- Addition thermal:  $(DL+SDL+EL) + R+S + DT$  100%





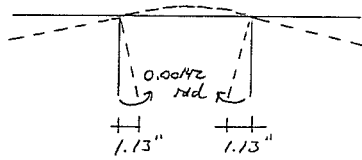
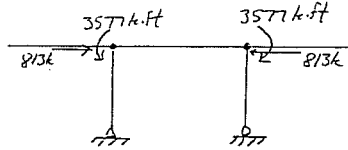
Service Load Cases - Five-Span Unit

Continuity tendons in span ③:

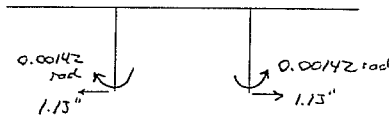


Tendon effects idealized as external loads for estimation

RISA-2D Input:



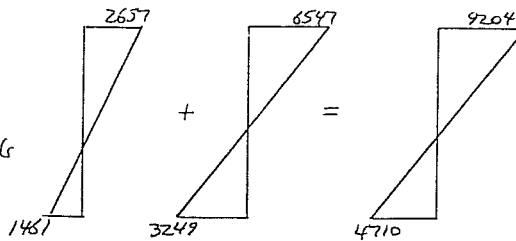
Prescribed deflections input to satisfy compatibility w/ external restraints.



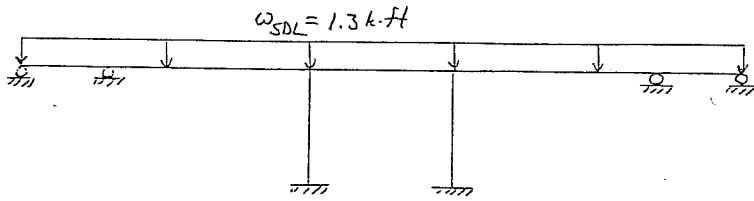
RISA Output

M diagram - pier P16 (k.ft)

T20 stressing + segment loads = Total



Service Load Cases - Five-Span Unit  
 Phase III: Superimposed dead loads:



barrier walls: 10" x 30" / Foot / wall

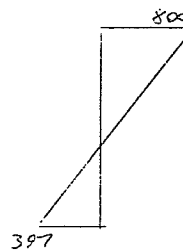
$$SDL_{walls} = 626 \text{ lb/ft}$$

2" over-lay:

$$SDL_{over-lay} = 670 \text{ lb/ft}$$

RISA-2D output

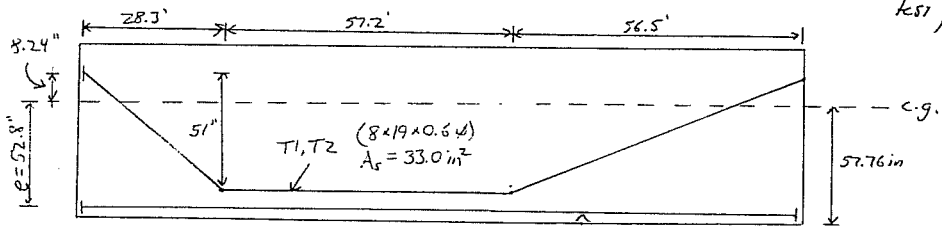
pier #16  
k-ft



Phase III: Pier-moments due to superstructure post-tensioning

Tendon Layout - Span ① (a1. (5))

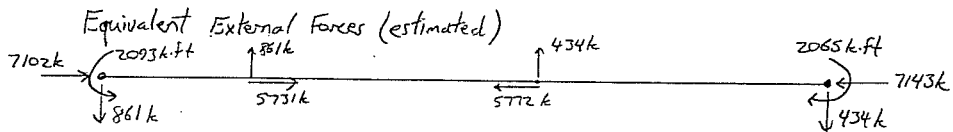
(Assume  $\sigma_s = 0.65(270) = 175.5 \text{ ksi}$ )



$$F_{1,2} = 5792 \text{ k}$$

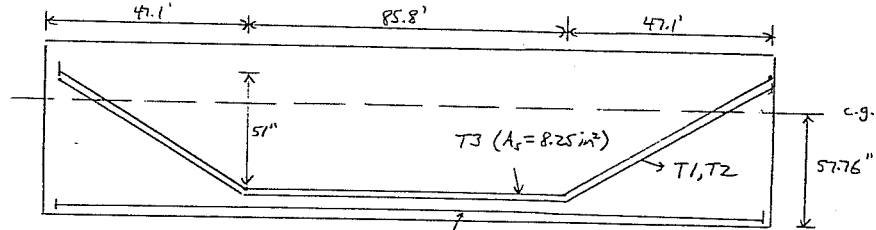
$$F_{19} = 1371 \text{ k}$$

$$T_{19} (4 \times 9 \times 0.6 \phi) \\ A_s = 7.81 \text{ in}^2$$



### Service Load Cases - Five-Span Unit

Tendon Layout - Span ② and ④



$$T2, T22 \quad A_r = 15.62 \text{ in}^2 \quad F_{2,22} = 2741 \text{ k}$$

$$F_x = 1447 \text{ k}$$

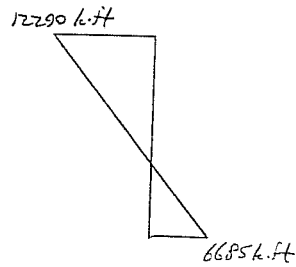
$$F_{y,z} = 5792 \text{ k}$$

equivalent external forces:



same procedure for span ③

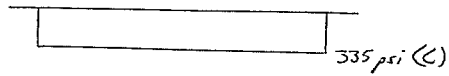
all equivalent external forces input as loads for frame analysis  
after satisfaction of compatibility, moments on pier P16 were:



## Service Load Cases - Five-Span Unit

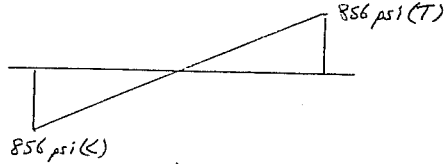
### Summary of Stresses - Pier Base

Phase I:  
DL



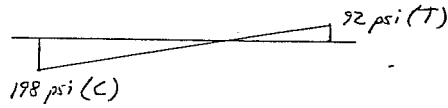
+

Phase II:  
DL + T20 continuity tendons



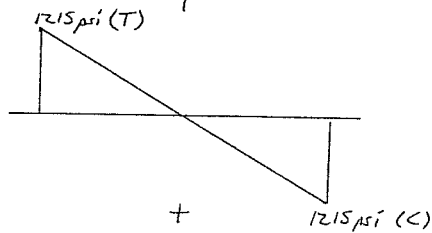
+

Phase III:  
SDL



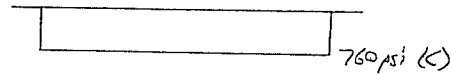
+

Phase III:  
Superstructure PT



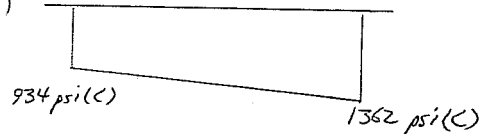
+

Pier-PT (w/losses)



=

Total (DL + prestress)

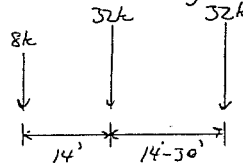


## Service Load Cases - Five-Span Unit

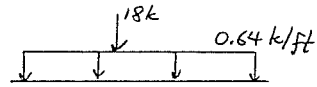
### Live Load Effects

Live load + impact effects were determined using:

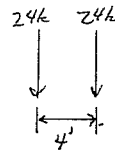
HS20-44 Truck Loading:



HS20-44 Lane Loading:



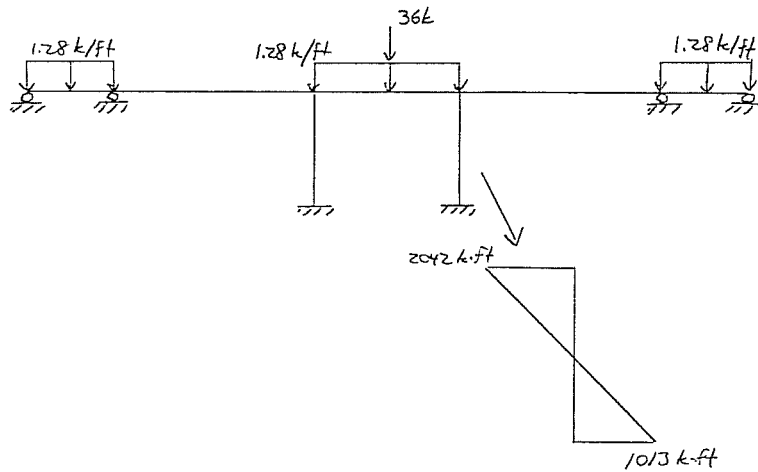
Military Loading:



(2 Design Lanes)

### RISA-2D Frame Analysis

Maximum moments @ pier base produced by:

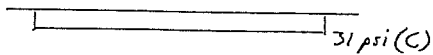


$$P_{LL} = 121.7 k$$

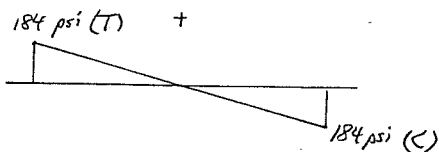
## Service Load Cases - Five-Span Unit

### Summary of stresses @ Pier Base

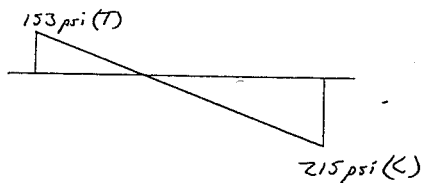
(LL+I) axial



(LL+I) bending

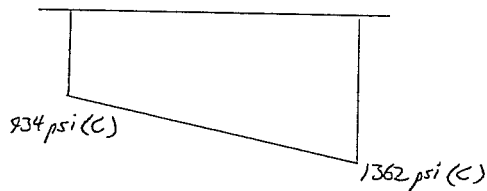


Total (L+I)

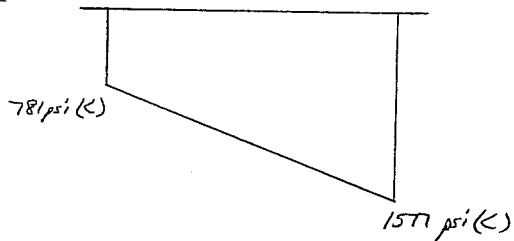


+

Total (D+prestressing)

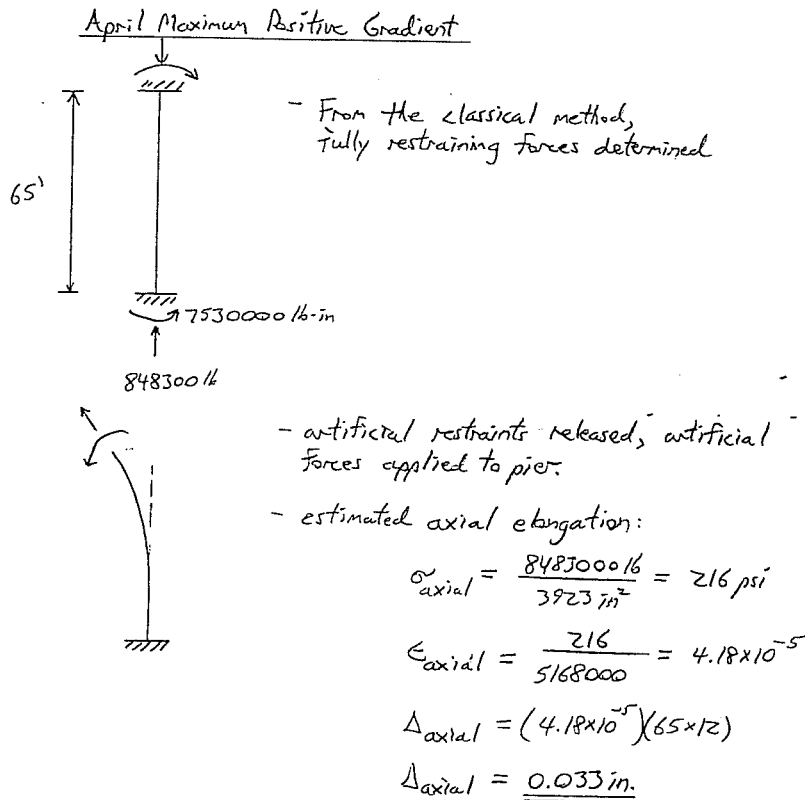


D+prestressing + L



## Service Load Cases - Five-Span Unit

Temperature Loads - sample calculation



Tip deflection and rotation:

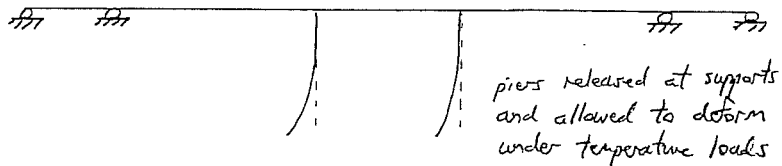
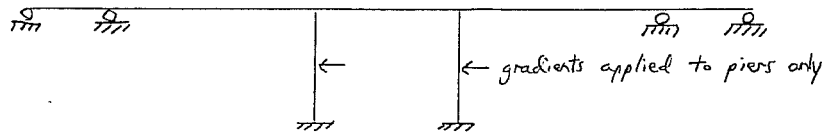
$$\text{curvature } \phi = \frac{M}{EI} = \frac{7530000}{(5.168 \times 10^6)(2970639)} = 4.905 \times 10^{-7} / \text{in.}$$

$$\theta_{tip} = \phi L = (4.905 \times 10^{-7})(65)(12) = \underline{\underline{3.826 \times 10^{-4} \text{ rad}}}$$

$$\Delta_{tip} = \frac{1}{2}(65)(12)(3.826 \times 10^{-4}) = \underline{\underline{0.149 \text{ in.}}}$$

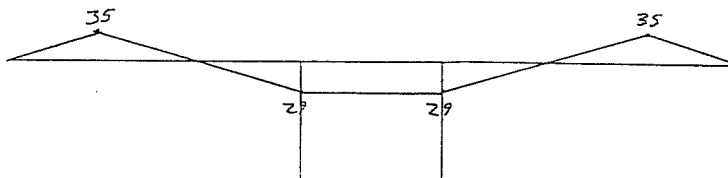
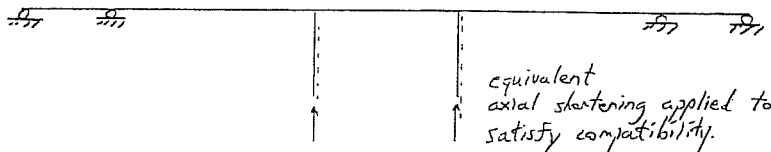
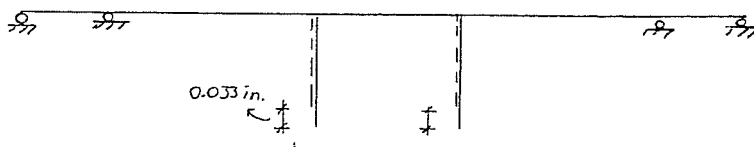
## Service Load Cases - Five-Span Unit

Frame analysis model



Total deformation consists of axial elongation and pier tip deflection and rotation.

Axial elongation component

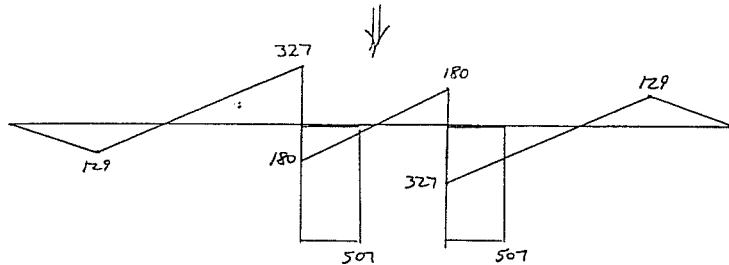
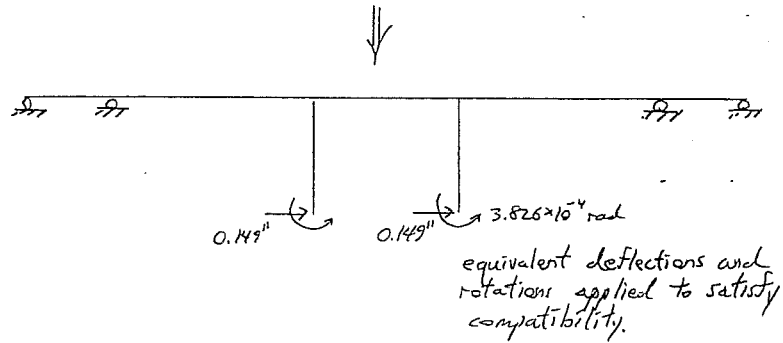
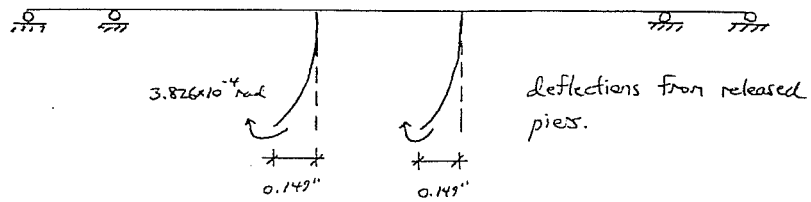


M diagram (k-ft) due to restrained axial elongation (From RISA)



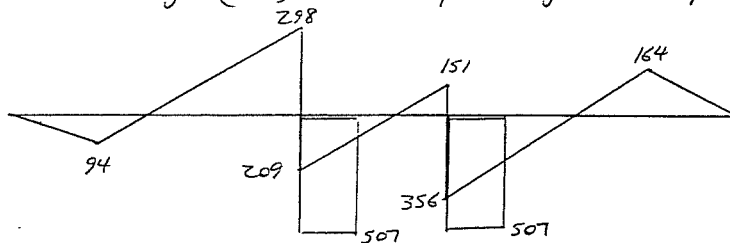
### Service Load Cases - Five-Span Unit

Tip deflection and rotation component



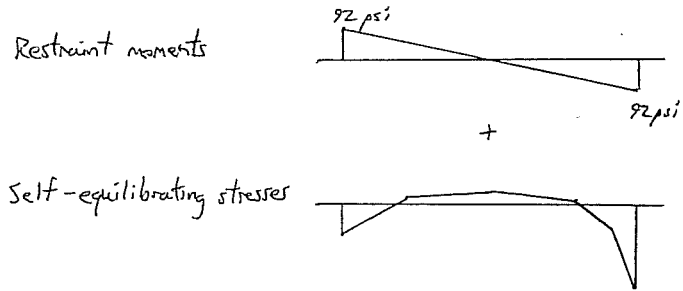
M diagram (k-ft) due to restrained rotation and deflection  
(From RISA)

Total M diagram (k-ft) due to temperature gradients in piers:



## Service Load Cases - Five-Span Unit

### Pier Stresses due to temperature



These thermal stresses are applied to produce the maximum effects for each load case.

## REFERENCES

1. Andres, V.A. "Verification of Force Distribution in an Innovative Bridge Pier." Master's Thesis. The University of Texas at Austin. Austin, TX. December, 1995.
2. Matejowsky, A. Letter to John E. Breen concerning precast substructures. March 19, 1996.
3. Branco, F.A. and Mendes, P.A. "Thermal Actions for Concrete Bridge Design." *Journal of Structural Engineering*. ASCE. V. 119, No. 8. August 1993, pp. 2313-2331.
4. Moorty, S. and C.W. Roeder. "Temperature Dependent Bridge Movements." *Journal of Structural Engineering*. ASCE. V. 118, No. 4. April 1992, pp. 1090-1105.
5. Imbsen, R.A., Vandershof, D.E., Schamber, R.A., and Nutt, R.V. "Thermal Effects in Concrete Bridge Superstructures". *NCHRP 276*. Transportation Research Board, Washington D.C. September 1985.
6. Poston, R.W., M. Diaz, and J.E. Breen. "Design Trends for Concrete Bridge Piers." *Journal of the American Concrete Institute*. January-February 1986, pp. 14-20.
7. Roberts, C.L. "Measurement Based Revisions for Segmental Bridge Design and Construction Criteria." Ph.D. Dissertation. The University of Texas at Austin. Austin, TX. December, 1993.
8. Potgieter, I.C. and W.L. Gamble. "Response of Highway Bridges to Nonlinear Temperature Distributions." Report No. FHWA/IL/UI-201. University of Illinois at Urbana-Champaign. April 1983.
9. Vecchio, F.J. and J.A. Sato. "Thermal Gradient Effects in Reinforced Concrete Frame Structures." *ACI Structural Journal*. V. 87, No. 3. May-June 1990, pp. 262-275.
10. Hoffman, P.C., R.M. McClure, and H.H. West. "Temperature Studies for an Experimental Segmental Bridge." Research Project 75-3 Interim Report. Pennsylvania State University. June 1980.

11. *AASHTO LRFD Bridge Design Specifications*. 1st ed. American Association of State Highway and Transportation Officials. 1994.
12. *AASHTO Guide Specifications for Design and Construction of Segmental Concrete Bridges*. American Association of State Highway and Transportation Officials. 1989.
13. *AASHTO Standard Specifications for Highway Bridges*. American Association of State Highway and Transportation Officials. 1989.
14. Stephenson, D.A. "Effects of Differential Temperature on Tall Slender Columns." *Concrete and Constructional Engineering*. V. 56, No. 5. May 1961, pp. 175-178.
15. Gallaway, T.M. "Design Features and Prestressing Aspects of Long Key Bridge." *PCI Journal*. V. 25, No. 6. November-December 1980, pp. 84-96.
16. Muller, J.M. "Construction of Long Key Bridge." *PCI Journal*. V. 25, No. 6. November-December 1980, pp. 97-111.
17. "Closing the Gaps with Assembly Line Span Placement." *Engineering News-Record*. V. 207, No. 10. September 3, 1981, pp. 26-28.
18. "Dauphin Island Bridge." *PCI Journal*. V. 29, No. 1. January-February 1984, pp. 128-147.
19. "Sunshine Skyway Bridge Closes the Gap." *PCI Journal*. V. 31, No. 6. November-December 1986, pp. 168-173.
20. Muller, J.M. and J.M. Barker. "Design and Construction of Linn Cove Viaduct." *PCI Journal*. V. 30, No. 5. September-October 1985, pp. 38-53.
21. Podolny, W., Jr. and J.M. Muller. *Construction and Design of Prestressed Concrete Segmental Bridges*. New York: John Wiley & Sons, Inc. 1982.
22. "Viaduct." *Civil Engineering*. American Society of Civil Engineers. V. 54, No. 7. July 1984, pp. 34-36.
23. Carr, F.H. and M.M. Charleston. "Precast Units Barged to Bridge." *Engineering News-Record*. V. 219, No. 2. July 9, 1987, pp. 32-34.

24. Hurd, M.K. "Cable-Stayed Bridge Completed Across James River." *Concrete Construction*. V. 34, No. 9. September 1989, pp. 775-779.
25. Pate, W. D. "The Chesapeake and Delaware Canal Bridge - Design-Construction Highlights." *PCI Journal*. V. 40, No. 5. September/October 1995, pp. 20-30.
26. Ralls, M.L. and R. Carrasquillo. "Texas High-Strength Concrete Bridge Project." *Public Roads*. V. 57, No. 4. Spring 1994, pp. 1-7.
27. Texas Department of Transportation, Division of Bridges and Structures. Bridge Plan: Louetta Road Overpass. June 1993, sheets 535-536.
28. "Precast Segmental Cantilever Bridges: The Northumberland Strait Crossing." JMI-Bridge Engineering Consultants Informational Pamphlet. 1995.
29. "Northumberland Strait Crossing Update." *Segments*. American Segmental Bridge Institute. V. 25. Spring/Summer 1995, pp. 8-12.
30. Arréllaga, J.A. "Instrumentation Systems for Post-Tensioned Segmental Box Girder Bridges." Master's Thesis. The University of Texas at Austin. Austin, TX. December, 1991.
31. Bergmeister, K, J.E. Breen, J.O. Jirsa, and M.E. Kreger. "Detailing for Structural Concrete." Center for Transportation Research Report 1127-3F. Austin, TX. May 1993.
32. Knight, Charles E. *The Finite Element Method in Mechinal Design*. Boston: The PWS-KENT Publishing Company, 1993.
33. Bathe, Klaus-Jürgen. *Finite Element Procedures*. Englewood Cliffs: Prentice-Hall, 1996.
34. Rowell, Randall B. "Behavior of Thin-Walled, Segmentally Constructed Post-Tensioned Bridge Piers", Master's Thesis, University of Texas at Austin, May 1990.
35. Mindness, Sidney, and J. Francis Young. *Concrete*. Englewood Cliffs: Prentice-Hall, Inc., 1981.
36. Beer, Ferdinand P. and Russell Johnston, Jr. *Mechanics of Materials*. 2nd ed. New York: McGraw-Hill, Inc., 1992.

## VITA

Wade Sterling Bonzon was born in Albuquerque, New Mexico on February 27, 1972, to Lloyd Louis Bonzon and Jessica Reed Bonzon. He attended Eldorado High School in Albuquerque and graduated from there in May of 1990. He entered New Mexico State University in Las Cruces, New Mexico in August of 1990. In December of 1994 he graduated from New Mexico State with honors. He entered The University of Texas at Austin in January of 1995. While at The University of Texas, he was awarded the Phil M. Ferguson Endowed Presidential Scholarship and the Joe M. Coffield Endowed Graduate Fellowship.

Permanent Address: 9629 Pebble Beach Dr. NE  
Albuquerque, New Mexico 87111

This thesis was typed by the author.